Coupled modelling of land surface microwave interactions using ENVISAT ASAR data

Dissertation der Fakultät für Geowissenschaften

der Ludwig Maximilians Universität München

vorgelegt von:

Alexander Löw

Eingereicht: 25.08.2004

Abstract

In the last decades microwave remote sensing has proven its capability to provide valuable information about the land surface. New sensor generations as e.g. ENVISAT ASAR are capable to provide frequent imagery with an high information content. To make use of these multiple imaging capabilities, sophisticated parameter inversion and assimilation strategies have to be applied. A profound understanding of the microwave interactions at the land surface is therefore essential.

The objective of the presented work is the analysis and quantitative description of the backscattering processes of vegetated areas by means of microwave backscattering models. The effect of changing imaging geometries is investigated and models for the description of bare soil and vegetation backscattering are developed. Spatially distributed model parameterisation is realized by synergistic coupling of the microwave scattering models with a physically based land surface process model. This enables the simulation of realistic SAR images, based on bio- and geophysical parameters.

The adequate preprocessing of the datasets is crucial for quantitative image analysis. A stringent preprocessing and sophisticated terrain geocoding and correction procedure is therefore suggested. It corrects the geometric and radiometric distortions of the image products and is taken as the basis for further analysis steps.

A problem in recently available microwave backscattering models is the inadequate parameterisation of the surface roughness. It is shown, that the use of classical roughness descriptors, as the rms height and autocorrelation length, will lead to ambiguous model parameterisations. A new two parameter bare soil backscattering model is therefore recommended to overcome this drawback. It is derived from theoretical electromagnetic model simulations. The new bare soil surface scattering model allows for the accurate description of the bare soil backscattering coefficients. A new surface roughness parameter is introduced in this context, capable to describe the surface roughness components, affecting the backscattering coefficient. It is shown, that this parameter can be directly related to the intrinsic fractal properties of the surface.

Spatially distributed information about the surface roughness is needed to derive land surface parameters from SAR imagery. An algorithm for the derivation of the new surface roughness parameter is therefore suggested. It is shown, that it can be derived directly from multitemporal SAR imagery.

Starting from that point, the bare soil backscattering model is used to assess the vegetation influence on the signal. By comparison of the residuals between measured backscattering coefficients and those predicted by the bare soil backscattering model, the vegetation influence on the signal can be quantified. Significant difference between cereals (wheat and triticale) and maize is observed in this context.

It is shown, that the vegetation influence on the signal can be directly derived from alternating polarisation data for cereal fields. It is dependant on plant biophysical variables as vegetation biomass and water content.

The backscattering behaviour of a maize stand is significantly different from that of other cereals, due to its completely different density and shape of the plants. A dihedral corner reflection between the soil and the stalk is identified as the major source of backscattering from the vegetation. A semiempirical maize backscattering model is suggested to quantify the influences of the canopy over the vegetation period.

Thus, the different scattering contributions of the soil and vegetation components are successfully separated. The combination of the bare soil and vegetation backscattering models allows for the accurate prediction of the backscattering coefficient for a wide range of surface conditions and variable incidence angles.

To enable the spatially distributed simulation of the SAR backscattering coefficient, an interface to a process oriented land surface model is established, which provides the necessary input variables for the backscattering model. Using this synergistic, coupled modelling approach, a realistic simulation of SAR images becomes possible based on land surface model output variables. It is shown, that this coupled modelling approach leads to promising and accurate estimates of the backscattering coefficients. The remaining residuals between simulated and measured backscatter values are analysed to identify the sources of uncertainty in the model. A detailed field based analysis of the simulation results revealed that imprecise soil moisture predictions by the land surface model are a major source of uncertainty, which can be related to imprecise soil texture distribution and soil hydrological properties.

The sensitivity of the backscattering coefficient to the soil moisture content of the upper soil layer can be used to generate soil moisture maps from SAR imagery. An algorithm for the inversion of soil moisture from the upper soil layer is suggested and validated. It makes use of initial soil moisture values, provided by the land surface process model. Soil moisture values are inverted by means of the coupled land surface backscattering model. The retrieved soil moisture results have an RMSE of 3.5 Vol %, which is comparable to the measurement accuracy of the reference field data.

The developed models allow for the accurate prediction of the SAR backscattering coefficient. The various soil and vegetation scattering contributions can be separated. The direct interface to a physically based land surface process model allows for the spatially distributed modelling of the backscattering coefficient and the direct assimilation of remote sensing data into a land surface process model.

The developed models allow for the derivation of static and dynamic landsurface parameters, as e.g. surface roughness, soil texture, soil moisture and biomass from remote sensing data and their assimilation in process models. They are therefore reliable tools, which can be used for sophisticated practice oriented problem solutions in manifold manner in the earth and environmental sciences.

Zusammenfassung

Die Erkenntnisse der letzten Jahrzehnte haben gezeigt, dass sich aus Daten von Mikrowellensensoren wertvolle Informationen über Eigenschaften und Prozesse der Landoberfläche ableiten lassen. Neue Sensoren, wie beispielsweise der ENVISAT ASAR, ermöglichen die häufige Abdeckung und Beobachtung eines Gebietes. Damit werden sie für operationelle und insbesondere auch zeitkritische Anwendungen, wie beispielsweise die Hochwasservorhersage interessant. Um dieses Potential nutzen zu können ist es notwendig, die Effekte der daraus resultierenden unterschiedlichen Aufnahmegeometrien zu kompensieren. Dazu sind problemorientierte, anspruchsvolle Lösungsansätze notwendig. Grundlage hierfür sind Erkenntnisse über die Rückstreumechanismen an der Landoberfläche unter verschiedenen Aufnahmegeometrien.

Ein Schwerpunkt der vorliegenden Arbeit liegt in der Analyse und quantitativen Beschreibung der Rückstreumechanismen von offene Böden, sowie vegetationsbestandenen Flächen. Neue Ansätze zur theoretischen und semiempirischen Beschreibung des Radarrückstreukoeffizienten werden hierzu entwickelt. Unterschiedlichste Aufnahmegeometrien finden dabei Berücksichtigung. Eine Grundvoraussetzung zur flächenhaften Modellierung der Radarrückstreuung ist die flächige Bereitstellung der notwendigen Modelleingabeparameter. Dies wird durch die Kopplung der Radarrückstreumodelle mit einem physikalisch basierten Prozessmodell erreicht, welches die notwendigen bio- und geophysikalischen Eingabeparameter flächig verteilt bereitstellen kann.

Unabdingbare Grundlage für die quantitative Auswertung der SAR Daten ist eine adäquate und genaue geometrische und radiometrische Vorprozessierung der Datensätze. Insbesondere den reliefbedingten geometrischen und radiometrischen Einflüssen auf das Bildprodukt muss hierbei Rechnung getragen werden. Ein entsprechendes, anspruchsvolles Korrekturverfahren zur Eliminierung der reliefbedingten Lagefehler sowie radiometrischen Unterschiede wurde daher auf Basis eines vorhandenen Verfahrens weiterentwickelt. Es ist die Grundlage für alle weiteren quantitativen Auswertungen der Bilddaten.

Die Trennung des Bodens- und Vegetationssignals ist zum Verständnis und zur Modellierung der Rückstreuung von z.B. Ackerflächen, unabdingbar. Ein Schwerpunkt der vorliegenden Arbeit bildet daher die Trennung dieser unterschiedlichen Rückstreuanteile.

Die korrekte Parametrisierung der Oberflächenrauhigkeit stellt bei den derzeit verfügbaren theoretischen Rückstreumodellen eines der Hauptprobleme dar. Durch den Vergleich mit Bilddaten wird gezeigt, dass die klassische Parametrisierung der Rauhigkeit durch die RMS Höhe (vertikale Rauhigkeit), sowie die Autokorrelationslänge (horizontale Rauhigkeit) zu unzureichenden und mehrdeutigen Modellparametrisierungen führen kann. Durch ein neu entwickeltes Bodenrückstreumodell, welches lediglich zwei Eingabeparameter benötigt, kann dieses Problem gelöst werden. Das neue Bodenmodell erlaubt die genaue und eindeutige Modellierung der Radarrückstreuung auf Basis von Landoberflächenparametern. In diesem Zusammenhang wird ein neuer Parameter zur Beschreibung der Oberflächenrauhigkeit eingeführt. Es wird gezeigt, dass sich dieser Parameter direkt auf die fraktalen Eigenschaften einer Oberfläche zurückführen lässt. Ein Verfahren zur flächendeckenden Ableitung dieses Rauhigkeitsparameters wird entwickelt und validiert. Auf Basis multitemporaler SAR Bilddaten, lassen sich somit flächenhafte Informationen über die Oberflächenrauhigkeit von Böden gewinnen. Die so gewonnenen Rauhigkeitsinformationen werden für die weitere Verarbeitung der Daten und Modellentwicklungen verwendet.

Durch einen Vergleich der Ergebnisse des entwickelten Bodenmodells und der gemessenen Bilddaten, sowie der daraus resultierenden Residuen, kann der Einfluss der Vegetation auf das Gesamtsignal quantifiziert werden. Hierbei wurden deutliche Unterschiede zwischen Getreide- und Maisfeldern festgestellt.

Der Einfluss der Vegetation kann im Fall von Getreideflächen (Weizen und Tritikale) direkt aus den Bilddaten abgeleitet werden. Durch die Verwendung verschiedener Polarisationen ist es möglich, diesen Effekt zu parametrisieren. Es wird aufgezeigt, dass ein starker Zusammenhang zwischen den Polarisationsunterschieden und pflanzenphysiologischen Parametern wie Biomasse und Wassergehalt bestehen. Dies kann zur quantitativen Beschreibung der Vegetationsrückstreuung genutzt werden.

Aufgrund der deutlich geringeren Bestandesdichte, sowie der unterschiedlichen Pflanzengeometrie, ist die Rückstreuung von Maisbeständen anders, als jene von Getreide. Der Einfluss der Vegetation lässt sich hier vor allem durch den starken Einfluss der Interaktion zwischen dem Stängel der Maispflanze, sowie der Bodenoberfläche erklären. Ein semiempirisches Rückstreumodell wurde entwickelt, um die Rückstreuung eines Maisbestandes im Laufe der phänologischen Entwicklung adäquat beschreiben zu können.

Die somit erfolgreiche Trennung und separate quantitative Beschreibung von Boden- und Vegetationsanteilen ermöglicht durch die Kopplung beider

Modellkomponenten die Simulation der Radarrückstreuung von Vegetationsbeständen. Hierbei sind unterschiedlichste Aufnahmegeometrien, sowie Oberflächenzustände denkbar.

Zur flächenverteilten Modellierung der Radarrückstreuung ist es notwendig, die für das Modell notwendigen Eingabeparameter flächig zur Verfügung zu stellen. Dies wird durch die Kopplung mit einem physikalisch basierten Prozessmodell erreicht. Dieses kann zeitlich und räumlich verteilte Eingabeparameter wie beispielsweise Bodenfeuchte, Biomasse und Vegetationshöhe bereitstellen. Durch die synergetische Nutzung von Prozess- und Rückstreumodell, wird eine realistische Simulation von SAR Bildern möglich. Es wird gezeigt, dass die Simulationsergebnisse die vom Satelliten tatsächlich gemessene Radarrückstreuung gut wiederspiegeln. Die verbleibenden Residuen können zur Detektion und Beschreibung von Fehlern und Unzulänglichkeiten in den Modellen und Parameterdatensätzen verwendet werden. Auf Basis einer feldbasierten Detailanalyse wird aufgezeigt, dass unzureichende Bodenfeuchtesimulationen aus dem Prozessmodell eine wesentliche Fehlerquelle darstellen können. Hierbei spielt vor allem die oft unzulängliche Parametrisierung der hydrologischen Bodeneigenschaften eine Rolle. Der beschrittene gekoppelte Modellansatz bietet demnach Möglichkeiten zur verbesserten flächenverteilten Parametrisierung von Eigenschaften der Landoberfläche.

Die Bodenfeuchte der obersten Bodenschicht hat einen wesentliche Einfluss auf die Radarrückstreuung, was zur Ableitung flächenverteilter Bodenfeuchteinformationen aus SAR Daten verwendet werden kann. Unter Zuhilfenahme des entwickelten gekoppelten Modellansatzes wird ein Verfahren zur Ableitung der Bodenfeuchte vorgestellt. Dieses verwendet *a priori* Informationen des Prozessmodells über den initialen Bodenfeuchtezustand. Der Vergleich mit Referenzmessungen ergab eine Genauigkeit des Verfahren von 3.5 Vol. %.

Die in der vorliegenden Arbeit entwickelten Verfahren ermöglichen die genaue Vorhersage des Radarrückstreukoeffizienten auf Basis flächenverteilter Eingabeparameter des Zustandes der Landoberfläche. Hierbei können unterschiedlichste Aufnahmegeometrien berücksichtigt werden. Die verschiedenen Einflüsse der Boden- und Vegetationsanteile an der Radarrückstreuung können dabei getrennt betrachtet werden. Die direkte Kopplung mit einem Landoberflächenprozessmodell ermöglicht hierbei die flächige Modellierung und direkte Assimilation von SAR Bilddaten. Die vorgestellten Modelle und Invertierungsansätze ermöglichen die anspruchsvolle und praxisorientierte Verwendung von Mikrowellendaten für unterschiedlichste Fragestellungen.

Preface

The increasing demand of spatially distributed information about the land surface, at various spatial and time scales, can be fulfilled, using remote sensing techniques. Application oriented image analysis techniques and remote sensing assimilation strategies are a prerequisite for the successful operational use of these datasets.

Microwave remote sensing has become a reliable and valuable information source in this context. During my master thesis, I had the chance to get an insight into the details of this fascinating technique. After my graduation, I had the possibility to join the Chair of Geography and Geographical Remote Sensing at the Ludwig-Maximilians-Universität in Munich (Germany), held by Prof. Dr. Wolfram Mauser. He gave me the chance to participate in an application oriented project with the objective of derivation of land surface parameters from ENVISAT ASAR data. It was a great pleasure for me, to be involved with the development of new parameter inversion models for microwave remote sensing data. I would like to thank Prof. Mauser cordially for his support and the trust he placed in me. With his obliging help, it was possible for me to realize my own ideas. He supported not only the progress of this thesis, but also gave me the chance to make new experiences as lecturer at the University.

Parts of this thesis, especially the field campaign, were sponsored by the DLR (German Aerospace Centre) funded project InFerno[+]. I would like to thank the DLR for the support.

The ENVISAT ASAR data was provided by the European Space Agency (ESA) within their PI programme, which is gratefully acknowledged. Thanks also to the ESA helpdesk and technical staff for the support of my - sometimes complicated - technical questions.

This thesis is closely associated to the competence of the remote sensing and hydrology working group of the Chair of Geography and Geographical Remote Sensing of the University of Munich. Many thanks to all actual and former members of this group for the pleasant working atmosphere and the support in the solutions of various small and big problems.

Cordial thanks to my colleague and project partner Dr. Ralf Ludwig, who supported me in various technical and hydrological questions. It was a pleasure for me to work

Table of Contents

List of Figures

List of Tables

List of Abbreviations

ACF	Autocorrelation function
ACL	Autocorrelation length
AP	Alternating polarisation
ASAR	Advanced Synthetic Aperture Radar
dB	Decibels
DOY	Day of year
DWD	Deutscher Wetterdienst = German Weather Service
EM-wave	Electromagnetic wave
ERS	European remote sensing satellite
GCP	Ground control point
IEM	Integral equation model
LAI	Leaf area index
LUT	Look up table
PDF	Probability density function
PRF	Pulse repetition frequency
RCS	Radar cross section
RMSE	Root mean square error
RT-model	Radiative transfer model
SAR	Synthetic aperture radar
SM	Soil moisture
SSM	Simplified scattering model (bare soil)
SVAT	Soil vegetation atmosphere transfer
TDR	Time domain reflectrometry
VWC	Vegetation water content
WSM	Wide Swath mode

List of Symbols

β^0	image brightness
CP	copol ratio
CP_N	normalized copol ratio
c, c_0	speed of light; in vacuum
D	fractal dimension
DN	digital number
$\in_r, \in_r', \in_r''$	relative dielectric constant, real and imaginary part
$\varepsilon_r, \varepsilon_r', \varepsilon_r''$	absolute dielectric constant, real and imaginary part
f_D	doppler frequency
f	frequency
G	antenna gain
Γ, Γ_0	fresnel reflectivity; in nadir
H	Hurst Exponent
K	wavenumber
K_e	extinction coefficient
L	antenna size
l	surface autocorrelation length
λ	wave length
m_v	volumetric soil moisture
$\vec{v}$	velocity vector
P	power
ψ	projection angle
Θ	look angle

θ, θ_i	incidence angle, local incidence angle
μ_r	magnetic permeability
R	range distance
$\rho_a, \rho_{r,} \rho_G$	azimuth, slant range and ground range resolution
s	surface rms height
σ	radar cross section
σ^0	backscattering coefficient; if not explicitly mentioned otherwise, the value of the backscattering coefficient is always linear (and not in decibels)
σ_S^0	bare soil backscattering coefficient
σ_V^0	vegetation backscattering coefficient
$\sigma_{V/G}^0$	backscattering coefficient, resulting from vegetation-ground interactions
σ_{pp}^0	polarisation dependant backscattering coefficient; p=H or V
τ	optical depth or pulse length

Chapter 1
Introduction

A prerequisite for sustainable development and management of the limited natural resources of the Earth are integrative analysis and monitoring tools and techniques. Decision support systems are needed to provide necessary data about the global environment and realistic future scenarios.

Recent Global Change research therefore focuses on the development of integrative and interdisciplinary strategies to describe the complex linkages between man and its natural environment (ENGELEN, 2000; MAUSER, 2003; LUDWIG *et al.*, 2003). Geospatial datasets are mandatory input variables to such systems. Geospatial datamining has therefore increasing significance in the fields of natural, and recently social sciences.

Earth observation by means of remote sensing techniques has become a powerful tool for the characterization and description of the biosphere system at regional and global scales. It enables the spatially distributed, systematic monitoring of the environment by means of various imaging and non imaging techniques, over a broad range of the electromagnetic spectrum. It is therefore an ideal tool to provide the necessary geospatial datasets.

The permanent, weather independent, monitoring capacities of microwave remote sensing systems, underline their importance in this context. The high sensitivity of the microwaves to key parameters of the land surface energy and water fluxes, as e.g. vegetation biomass and soil moisture, make them an ideal monitoring instrument in addition to sensors operating in other frequency ranges.

1.1 New sensors – new challenges

An increasing demand of these valuable datasets leads to the development of new sensor systems with more sophisticated imaging capabilities. Recent operational spaceborne SAR systems as e.g. ENVISAT ASAR and RADARSAT and forthcoming systems as e.g. RADARSAT-II or TerraSAR, allow frequent, multipolarised observations of the Earth surface. Contrary to their predecessors, as e.g. the ERS and JERS satellites, the new sensor generation is capable to acquire data under different imaging geometries. This enables the frequent observation of an area of

interest, which is crucial for operational applications as e.g. flood forecasting or disaster management. Figure 1.1 gives an overview about actual and forthcoming spaceborne SAR systems and their temporal and spatial resolution capabilities, compared to the user requirements in various fields of applications (SCHRÖDER *et al.*, 2004).
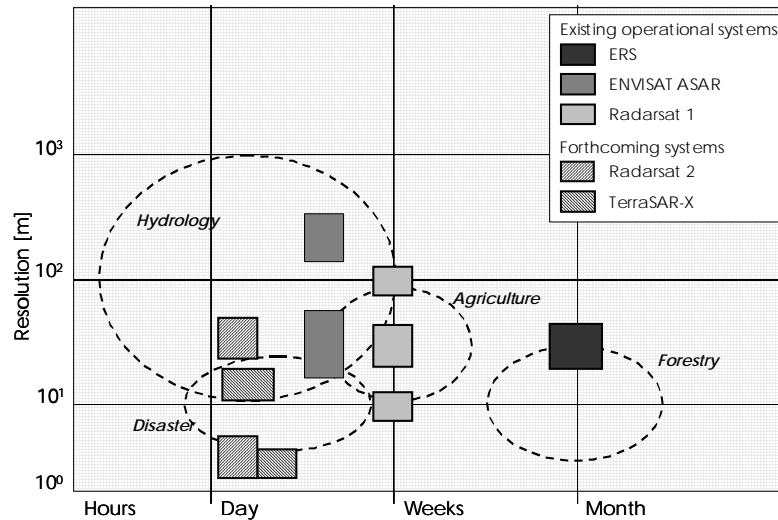
Figure 1.1: **Observation frequencies and spatial resolutions of recent and forthcoming spaceborne SAR systems, compared to specific user requirements.**

A profound understanding of the interactions between the electromagnetic waves and the land surface parameters is crucial for a quantitative analysis of these datasets. Due to the different imaging geometries and highly variable surface characteristics the interpretation of these multiple datasets becomes more complicated than that of a system with a unique geometry.

Sophisticated models and analysis tools, applicable for various sensor types, are therefore needed. The availability of validated electromagnetic models that describe the interactions between the microwaves and natural surface characteristics is critical to comprehend and exploit the dependence of the SAR signal to geophysical parameters. They help to understand the complex mechanisms and simplify the transfer of inversion procedures to global scales.

Adequate interfaces between remote sensing data and land surface process models, describing the energy and mass fluxes at the atmosphere-biosphere boundary layer, are needed to make use of these valuable geospatial datasets. The assimilation of remote sensing products into physically based process models is therefore another important topic in recent research (e.g. WALKER, WILGOOSE and KALMA, 2001; CROSSON *et al.*, 2002; BACH and MAUSER, 2003; BACH, MAUSER and SCHNEIDER, 2003).

1.2 Scientific objectives and outline of the thesis

The launch of the ENVISAT platform in March 2002, started a new era in operational microwave remote sensing. The onboard ASAR sensor enabled the acquisition of new and challenging image datasets.

It is the objective of the present thesis to develop methods and strategies for the understanding and wise use of this microwave SAR imagery for the description of land surface processes. It is therefore situated at the linkage between theoretical remote sensing sciences and the development of practical applications.

The microwave backscattering coefficient is the result of complex interactions between electromagnetic waves and the land surface (Figure 1.2). It is dependant on various sensor and intrinsic object specific parameters. Under different imaging geometries, the interactions between the various constituents within a resolution cell are different. To relate the object characteristics to the backscattering coefficient, a separation of the different contributing scattering terms, as e.g. soil, vegetation, topography is needed.

Recent theoretical backscattering models share the problem of an ambiguous model parameterisation. Different surface roughness parameter combinations result in the same backscattering coefficients. Especially for multiple geometries, this makes parameter inversion much more difficult. Current theoretical vegetation scattering models are often not practicable due to the necessity of large input parameter sets and unsatisfactory prediction results, related to limited model accuracies.
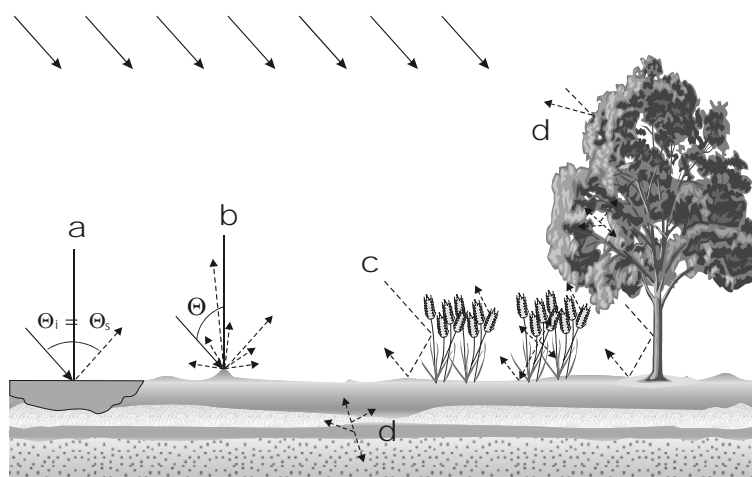
Figure 1.2: Examples for the complex interactions between microwaves and the land surface: a) specular, b) diffuse, c) corner reflection, d) volume scattering

The presented work therefore concentrates on the understanding, separation and quantitative description of the various scatter contributors. A theoretical land surface microwave backscattering model is suggested for bare soil and vegetated areas. By means of a synergistic coupling approach with a land surface process model, it enables the derivation of geophysical datasets from SAR imagery of various imaging geometries.

After a brief introduction into the basic principles of microwave remote sensing in *Chapter 2*, the important interactions of the electromagnetic waves with the land surface parameters are described in *Chapter 3*. The state of art of the scientific research in the field of backscatter modelling and inversion of bio- and geophysical parameters from SAR imagery is summarized. The chapter concludes with the main research needs and scientific objectives for the operational use of ENVISAT ASAR data.

Sophisticated preprocessing steps are mandatory for the derivation of quantitative information from SAR imagery. Especially the terrain influences on the geometrical and radiometrical properties of the image data have to be compensated. A sophisticated preprocessing chain, including a rigorous terrain geocoding approach, is therefore introduced in *Chapter 4*.

Field measurements are necessary to calibrate and validate the information derived from remote sensing data. The testsite and field campaign, carried out within this work, is presented in *Chapter 5*.

A two parameter bare soil backscattering model, valid over a wide range of imaging geometries and surface conditions, is proposed in *Chapter 6*. It enables the unambiguous derivation of surface properties of bare soils. A new surface roughness parameter is suggested in this context, which can be directly related to intrinsic surface properties. A soil roughness inversion procedure, based on multitemporal and multipolarised SAR imagery, is developed and validated.

Based on the bare soil backscatter model results, a vegetation model for agricultural fields is developed and calibrated in *Chapter 7*. It allows the prediction of the backscattering coefficient, based on bio- and geophysical input variables. The model is applied to predict the backscattering coefficients of various agricultural fields.

For spatially distributed modelling, several input variables are needed for the backscatter model parameterisation. These can be obtained from a land surface process model. An interface between a physically based land surface process model and the developed bare soil and vegetation backscattering model is proposed in *Chapter 8*. It allows for the realistic simulation of SAR images and the spatially distributed comparison with real image datasets. By using this interface, a direct model based assimilation and derivation of land surface parameters from SAR imagery becomes possible. The capabilities and accuracies are outlined, using the example of soil moisture inversion.

The thesis concludes in *Chapter 9* with a summary of the achievements and an outlook for future remote sensing data use and assimilation strategies.

Chapter 2
SAR basics and imaging principles

The chapter gives a brief overview about the SAR technique and system inherent properties which are important for an understanding of the interactions between the imaging system and an object. The focus lies hereby on the properties of an active SAR system in the microwave region of the electromagnetic spectrum, as it is realized by the ENVISAT ASAR sensor used within this work. An amount of good introductions to SAR imaging techniques can be found in the literature (e.g. BAMLER and SCHÄTTLER, 1993; KLAUSING and HOLPP, 2000; OLMSTED, 1993; LEWIS and HENDERSON, 1998). The introduction therefore concentrates on important features for the presented investigation.

2.1 SAR principle

An air- or spaceborne synthetic aperture radar system scans the Earth surface in a sidelooking manner as depicted in Figure 2.1. While the sensor is moving on its orbit it transmits and receives electromagnetic pulses at the rate of the pulse repetition frequency. The flight direction provides the azimuth and the perpendicular direction the range coordinate. From each object, illuminated within the systems footprint, it receives information at different times and from different pulses. By measuring the travel time of a pulse between transmission and reception, the range distance of an object can be determined.

Contrary to a real aperture radar (RAR), the received echoes from various pulses are used within a SAR system to generate a synthetic antenna length (*synthetic aperture*). By time integrating over different subapertures, the systems spatial resolution can be significantly improved.

Hence a SAR system is an active system which illuminates the Earths surface with an own source of electromagnetic waves. Being independent from external sources of illumination makes it possible to operate the system day and night.
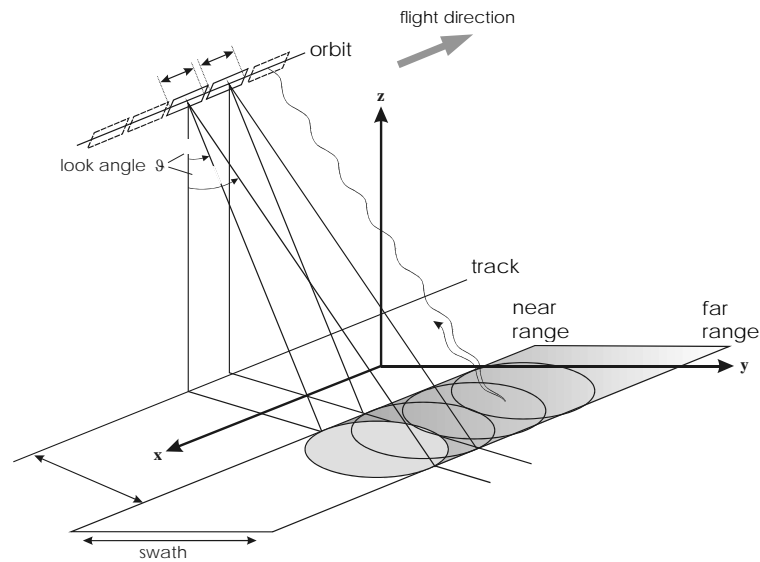
Figure 2.1:   SAR imaging principle

The atmosphere is almost transparent for microwaves. Contrary to the optical part of the electromagnetic spectrum the influence of the atmosphere on the signal is negligible. This should not mislead to the assumption that there is no influence of the atmosphere. For several applications, e.g. weather radar, short microwaves are used to detect heavy rain or hail. The phase of the electromagnetic wave is also influenced by the atmospheric water content, which can even be used for inversion approaches (HANSSEN *et al.*, 1999).

The commonly used frequency bands in the microwave region are given in Table 2.1. Dependant on the sensor configuration of a SAR system, different interactions of the electromagnetic wave with an object can be observed. This is discussed in Chapter 3.

Table 2.1:   Microwave frequency bands

FREQUENCY BAND	WAVELENGTH [CM]	FREQUENCY [GHZ]
K	0.8 … 2.4	40. … 12.5
X	2.4 … 3.8	12.5 … 8.0
C	3.8 … 7.5	8.0 … 4.0
S	7.5 … 15.0	4.0 … 2.0
L	15.0 … 30.0	2.0 … 1.0
P	30.0 … 100.0	1.0 … 0.3
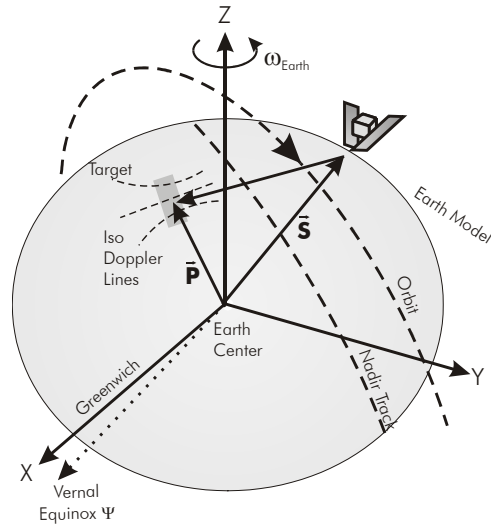
Figure 2.2:   General SAR imaging geometry

2.2 SAR imaging model

2.2.1 Imaging model

The position of a SAR system on an orbit at time *t* is given by its Earth centred state vector $\vec{S}(t)$. Assuming the imaging geometry given in Figure 2.2, the range distance $R_s(t)$ to a target $\vec{P}$ can be calculated by

$$R_S = \sqrt{(\vec{S} - \vec{P}) \cdot (\vec{S} - \vec{P})} \qquad (2.1)$$

As already mentioned, a SAR system receives the echoes of an object within multiple pulses. The footprint of a system with a small beamwidth of 0.3 ° (e.g. ERS) gives a footprint on the Earth's surface of about 5 km. At a pulse repetition frequency of 1680 Hz, the beams footprint moves only ~4 m between the pulses. This means that each object is seen more than 1000 times by the radar (OLMSTEDT, 1993).

The coherently recorded echoes of an object have to be integrated during the image formation process to estimate the objects position within the image plane. For that the Doppler frequency shift f_D can be calculated for each orbit position by

$$f_D = \frac{2f_0}{c} \frac{(\vec{v}_P - \vec{v}_S)\vec{R}_S}{|R_S|} \qquad (2.2)$$

with the carrier frequency f_0 and the target and sensor velocities $\vec{v}_P$ and $\vec{v}_S$.

The Doppler frequency is higher for objects approaching the sensor, than for objects the sensor is moving away from. The point, where the object is perpendicular to the sensors position, corresponds to the Zero-Doppler position. For any given object the corresponding Zero-Doppler position can be calculated iteratively using (2.1) and (2.2) (e.g. MEIER, FREI and NÜESCH, 1993; LÖW and MAUSER, 2003).

2.2.2 SAR image properties

2.2.2.1   Local imaging geometry

The angle between the incident wave and the normal vector on the geoid is defined as the incidence angle θ. It has a major influence on the radar backscatter. While θ is defined for a flat Earth the local incidence angle θ_i takes the local terrain slope into account. It is defined as the angle between the incident ray and the local surface normal. This is illustrated in Figure 2.3.
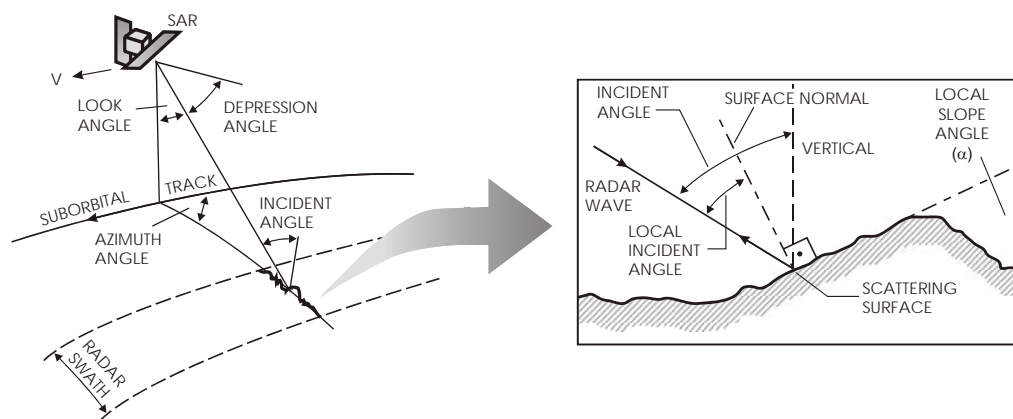
Figure 2.3:   **Global and local imaging geometries**

2.2.2.2   Azimuth resolution

The geometric resolution of an imaging system determines the spatial extent of a resolution cell on the Earth surface. The azimuth resolution ρ_a of a SAR system is the resolution of the system in flight direction, given as

$$\rho_a = \frac{L}{2} \tag{2.3}$$

where L is the length of the physical antenna. Note, that ρ_a is independent from range distance. Theoretically the azimuth resolution is therefore not influenced by the targets distance to the sensor.
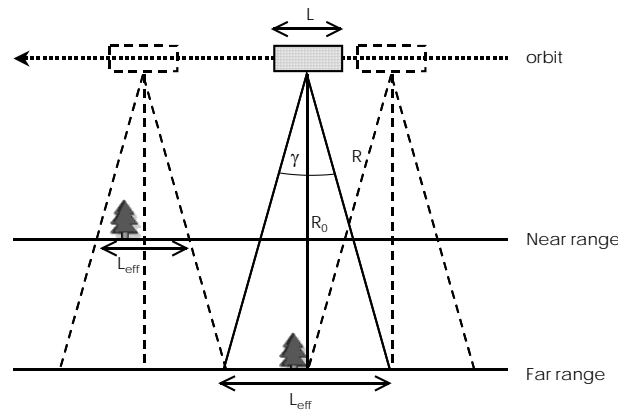
Figure 2.4:   SAR azimuth resolution

This can be explained by the concept of the SAR, which integrates information gathered within a certain time interval. For a physical antenna, the angular beamwidth γ is directly proportional to the antenna size L and the wavelength λ as (OLMSTED, 1993)

$$\gamma = \frac{\lambda}{L} \tag{2.4}$$

The corresponding footprint L_{eff} is a function of the range distance R as

$$L_{eff} = \gamma R = \frac{\lambda R}{L} \tag{2.5}$$

For a synthetic aperture radar, L_{eff} corresponds to the distance, the target is within the beam. For targets in near range this integration time is shorter than for targets in far range, as can be seen from Figure 2.4. The effective angular beamwidth of a SAR system is then given by

$$\gamma_{eff} = \frac{\lambda}{2L_{eff}} \tag{2.6}$$

which is similar to (2.4), except for the factor 2, which is caused by the different collecting of phase shifts (MOREIRA, 1992). Using (2.5) the azimuth resolution can then be calculated as

$$\rho_a = \gamma_{eff} R = \frac{\lambda R}{2L_{eff}} = \frac{\lambda R}{2\frac{\lambda R}{L}} = \frac{L}{2} \tag{2.7}$$

which is equal to (2.3).

2.2.2.3 Range resolution

The range resolution of a SAR system depends on the pulse length τ of the transmitted signal. Two objects, illuminated by the same pulse, can not be distinguished, whereas objects with a distance larger than the resolution cell can be separated (Figure 2.5). The slant range resolution ρ_r is given by

$$\rho_r = \frac{c\tau}{2} \tag{2.8}$$

where c is the speed of light. Assuming a flat Earth surface, the corresponding ground range resolution ρ_G for an incidence angle θ is given by

$$\rho_G = \frac{c\tau}{2\sin(\theta)} \tag{2.9}$$

Thus, the geometric ground resolution is dependant on the incidence angle. In the Far Range region, the resolution is better than in the Near Range of the footprint. This is shown in Figure 2.5, where the points P_1 and P_2 can not be separated by the SAR system whereas P_3 and P_4, which have the same ground distance, can be separated due to the better spatial resolution.
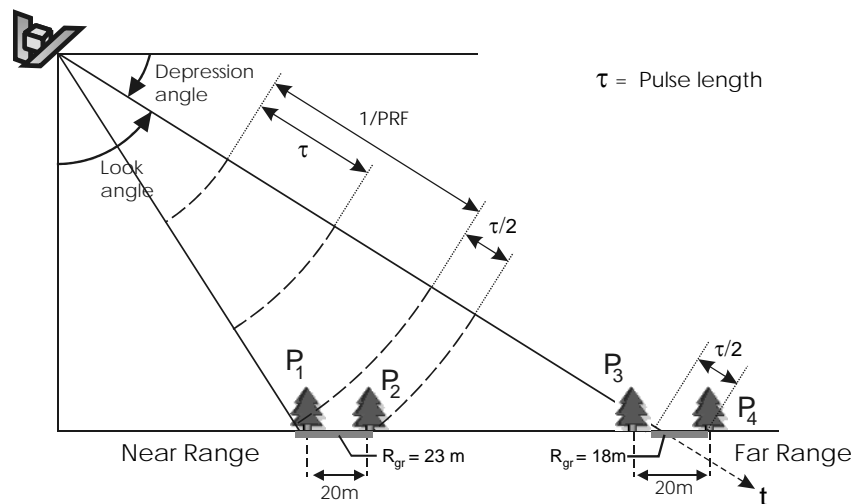
Figure 2.5: Range resolution of a SAR system: The ground range resolution is increasing from Near to Far Range

2.2.2.4 Relief distortions

Due to the side looking geometry of a SAR, the relief can induce significant geometric and radiometric distortions to the image product. Scattering occurs from sloping and faceted surfaces, which creates local distortions that depend on the surface to beam orientation. As will be shown later in Chapter 4, these distortions can be corrected using rigorous image processing techniques.

Figure 2.6 shows the slant and ground range planes for rugged terrain as seen by a SAR system. Slopes, facing towards the sensor cause a displacement of the elevated parts of the terrain towards the sensor. This *foreshortening* is the reason why surfaces, directing towards the sensor, appear bright in SAR images. The energy of many scatters is compressed within few image pixels. The extreme foreshortening, where the signal from the top of a mountain reaches the sensor before that of the base is named *layover*. Areas aspecting away from the sensor or lying behind the top of a mountain are not illuminated. No backscatter return is therefore received from that *shadow* region.
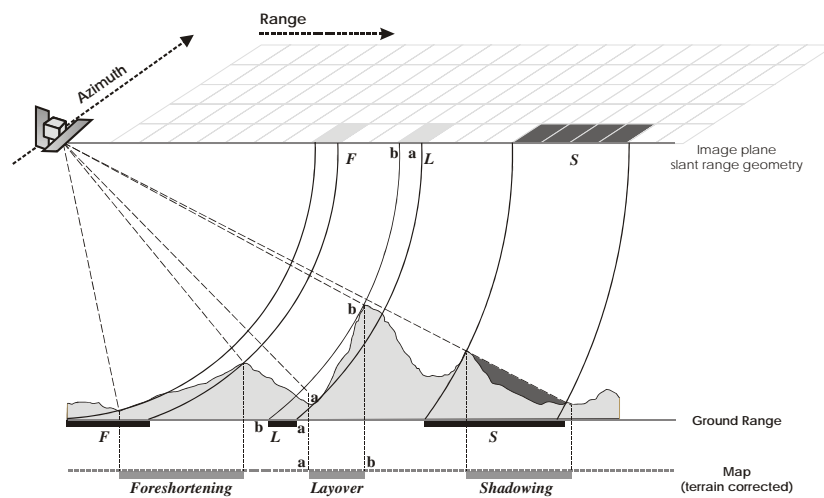
Figure 2.6: Geometric and radiometric relief distortions

In along track direction, the radial velocity between the sensor and the target changes with changing terrain height, which introduces an additional Doppler frequency shift. For the ERS configuration, this terrain introduced shift causes a misalignment of 110 m or 9 azimuth pixels for a height difference of 1000 m and targets in the mid-latitudes (MEIER, FREI and NÜESCH, 1993).

For slopes, facing the incident wavefront, a larger ground area contributes to the returned signal of a slant range resolution cell, than for slopes lying in the opposite direction. The slope and aspect of the scattering surface produces significant changes of the scattering area among neighbouring resolution cells. The correction of this effect is crucial. It is shown in Chapter 4 that it can be compensated in a rigorous way.

2.3 Radar equation and backscattering coefficient

The power, received at the antenna of a SAR system, is recorded and can be processed to a two-dimensional image (e.g. BAMLER and SCHÄTTLER, 1993; CURLANDER and MCDONOUGH, 1991; MOREIRA, 1992).

The received power is given by (ULABY *et al.*, 1982; KLAUSING and HOLPP, 2000):

$$\overline{P}_R = \frac{\lambda^2}{(4\pi)^3} \int \frac{P_T G^2}{R^4} \cdot \sigma^0 dA \qquad (2.10)$$

$\overline{P}_R$, P_T	=	average received power, transmitted power
G	=	antenna gain
A	=	illuminated area
R	=	range distance
λ	=	wavelength
σ^0	=	backscattering coefficient

Equation (2.10) is known as the *radar equation*. A derivation of the formula is given in Appendix A. The target scattering characteristics are comprised by the backscattering coefficient σ^0. It describes the ratio of the energy scattered by the target compared to the energy scattered by a lambertian isotropical surface. The relevant backscattering processes contributing to the backscattering coefficient are described in Chapter 3. For distributed targets, σ^0 is the normalized radar cross section (RCS) of the scatterers within a resolution cell:

$$\sigma^0 = \frac{\sigma}{A} \left[\frac{m^2}{m^2} \right] \qquad (2.11)$$

Thus for the derivation of σ^0, the scattering area must be known. As will be seen in Chapter 4, the scattering area is strongly influenced by terrain undulations. During the image generation procedure, the local terrain slopes are not known. Therefore image products are not normalized to the ground surface. The normalization of the grey values is done in the slant range geometry, which means that the unit area is given by the azimuth and slant range resolution of the imaging system. Thus, the image is directly proportional to the received power and is called a *brightness* image. Contrary to the backscattering coefficient on the ground σ^0, it is abbreviated by β^0. A third possibility exists, where the image is normalized to the area perpendicular to the incident ray. In Figure 2.7 the three different possible normalization methods are shown. The only backscattering coefficient, being independent from the local imaging geometry is β^0. This is the reason why SAR image products are always delivered as β^0 images (LAUR *et al.*, 1998; SHEPARD, 2000; ROSICH and MEADOWS, 2004).
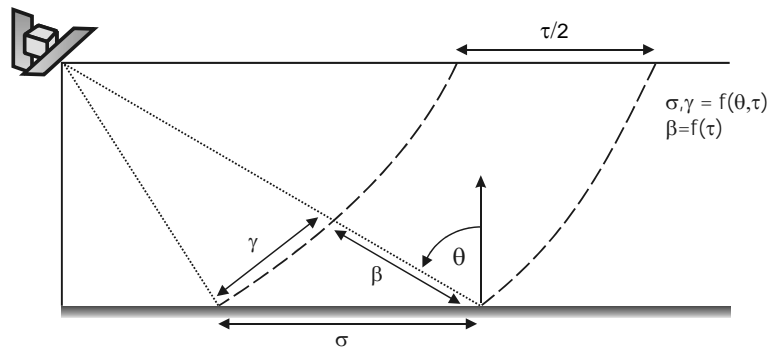
Figure 2.7: Definition of the backscattering coefficients σ^0, β^0, γ^0

2.4 ENVISAT ASAR

The <u>A</u>dvanced <u>S</u>ynthetic <u>A</u>perture <u>R</u>adar (ASAR) is the biggest instrument of the payload, boarded on the ENVISAT platform. It was built to continue and extend Earth observation using SAR. Figure 2.8 shows the ASAR antenna on board of the satellite and in the laboratory. The deployed antenna has a size of about 10 meters.
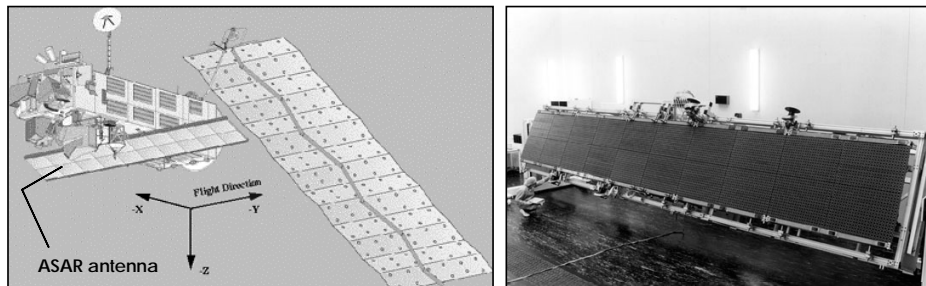
Figure 2.8: ASAR sensor onboard (left) and antenna in the laboratory (right); (modified after ESA, 2002)

Based on the experience with ERS-1/2, several enhancements have been made for ASAR. Most important is the replacement of a central power amplifier for the antenna, by an active phase array antenna system with distributed elements. The whole antenna consists of 320 independent Transmit/Receive (T/R) modules, organized in 32 rows of 10 modules, which can be adjusted each individually (ROSICH *et al.*, 2003). As a result, the instrument can be used in a very flexible manner. It allows different polarisation combinations, incidence angles and imaging modes. Table 2.2 summarizes the main characteristics of the sensor. More detailed technical information can be found in ESA (2002).

The innovative concept of the sensor allows for new acquisition modes with different image content. The major improvements are presented next.

Table 2.2:   Main ASAR configuration parameters

PARAMETER	ASAR CONFIGURATION
Orbit altitude	~799 km
Orbit inclination angle [°]	98.55
Incidence angle range[x]	14 – 45 °
Swath width[x]	58 – 109 km
Frequency / wavelength	5.331 GHz / 5.6224 cm (C-band)
Polarisation	HH / VV / VH / HV
Calibration accuracy	± 0.5 dB
Range sampling rate [MHz]	19.21
Pulse repetition frequency [Hz] [x]	1709 – 2067

[x] dependant on the selected configuration

2.4.1 Selectable imaging modes and incidence angle

ENVISAT ASAR has different selectable imaging modes which can be chosen by the user prior to the acquisition. Additionally the possibility to control the direction of the antenna lobe allows for the acquisition of images with different incidence angles.
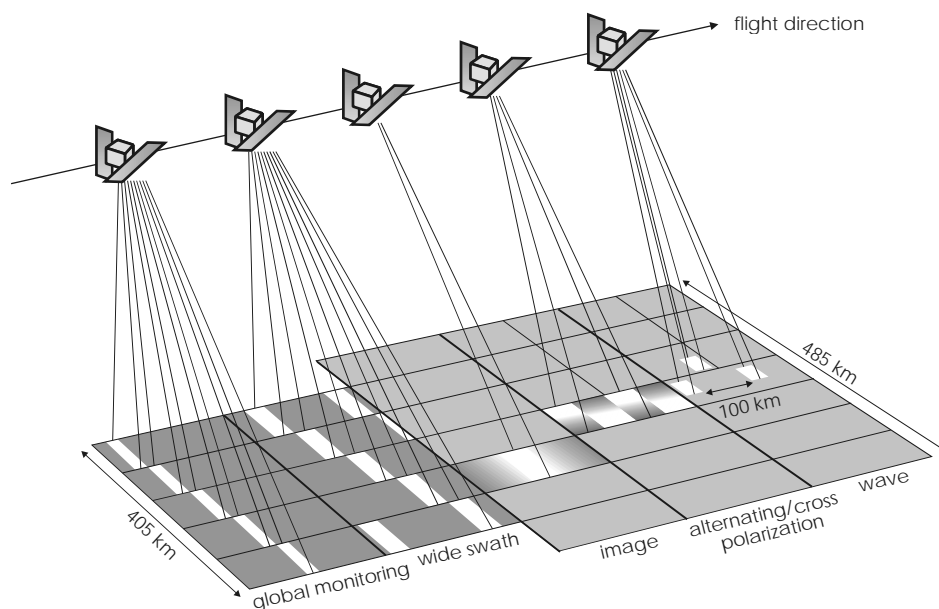
Figure 2.9:   ASAR imaging modes (modified after ESA, 2002)

The different imaging modes of ASAR, shown in Figure 2.9, are (ESA, 2002):

- Image Mode (IM)

  VV or HH polarisation images from any of 7 selectable swaths. Swath width between approximately 56 km (swath 7) and 100 km (swath 1) across track. Spatial resolution of about 30 m (for precision product).

- Alternating Polarisation (AP)

  Two co-registered images per acquisition, from any of 7 selectable swaths. HH/VV, HH/HV or VV/VH polarisation pairs possible. Spatial resolution of approximately 30 m (for precision product).

- Wide Swath (WM)

  400 x 400 km² wide swath image. Spatial resolution of approximately 150 m. VV or HH polarisation. The image is acquired using the ScanSAR technique where 5 subswaths form the whole image.

- Global Monitoring Mode (GM)

  same acquisition technique as for the wide swath mode, but with reduced spatial resolution. Spatial resolution of approximately 1 km. HH or VV polarisation

- Wave Mode (WV)

  A small imagette is acquired at regular intervals of 100 km along track. The imagette can be positioned anywhere in an image mode swath. HH or VV polarisation may be chosen. Imagettes are converted to wave spectra for ocean monitoring.

The different imaging modes allow to use the sensor in a very flexible manner. It can switch between the different modes within a few seconds. The main achievements of these new imaging capabilities are:

- *frequent observations* - the different swaths allow to observe an area of interest from different orbit paths, which increases the observation frequency. For areas in the mid-latitudes, coverages from two up to four times a week are possible. The different ENVISAT ASAR swathes and their properties are summarized in Appendix A.

- *Multi-incidence observations* - The radar backscatter has an angular dependency. The programmable incidence angles allow to chose the best incidence angle for a certain application

- *Wide area coverage* - For many applications it is important to cover a wide area with an acceptable spatial resolution. In hydrological applications it can be of interest to retrieve surface parameters (e.g. soil moisture, snow covered area) for a whole watershed. The wide swath mode with an area extent of 400 x 400 km² is well suited for these needs, when the corresponding loss in spatial resolution remains acceptable. It provides homogeneous, temporal consistent datasets for large areas. Figure 2.10 shows an example of an WSM image in southern Germany.
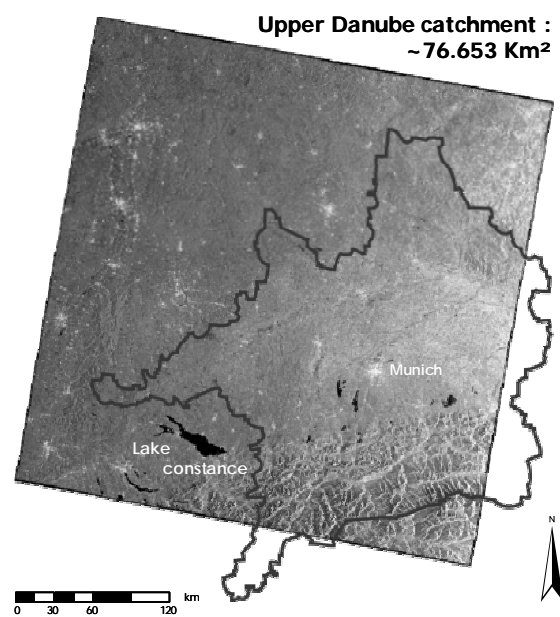
Figure 2.10:   Example of a WSM image, covering the upper Danube watershed

2.4.2 Dual polarisation

Imaging radars can transmit and receive differently polarised electromagnetic waves. The electric field can be polarised horizontally (H) or vertically (V) with respect to the incident wave on the surface. Each possible combination of transmit/receive configuration is abbreviated by the H and V characters. The first character corresponds to the transmit, the second to the receive polarisation (e.g. VH stands for vertical transmit and horizontal receive). A SAR system with the same transmit/receive combination (VV or HH) is a copolarised system, contrary to the crosspolarised case (VH or HV).

ENVISAT ASAR is the first operational spaceborne sensor which provides a dual-polarisation channel. In its alternating polarisation mode (AP mode), one of three different channel combinations are possible:

- VV and HH

- HH and HV

- VV and VH

The different polarisation combinations contain different information about the scattering processes and therefore allow to invert land surface parameters with less degrees of freedom, which might simplify inversion strategies (ESA, 2002).

Chapter 3
Microwave interactions with natural surfaces

Complex interactions take place between the incident electric field of a SAR system and an object on the Earth's surface. Along with the system related parameters, the geometrical and electrical properties of the objects as well as the local imaging geometry have an influence on the radar backscatter (Table 3.1). The understanding of the interplay between the sensor and object parameters is therefore needed for the retrieval of land surface parameters from SAR data.

Table 3.1: **Fundamental system and target parameters influencing the radar backscatter**

SYSTEM PARAMETERS	TARGET PARAMETERS
Wavelength or Frequency	Surface Roughness
Polarisation	Dielectric properties
Look angle	Slope and orientation
Resolution	

The chapter outlines the main backscattering mechanisms and their dependency on the surface and sensor characteristics. After that, the state of art in land surface parameter retrieval from SAR data is briefly summarized. The new imaging capabilities of ENVISAT ASAR have implications on the inversion strategies to retrieve land surface parameters. The challenges and potentials are discussed and a strategy for the modelling of microwave land surface interactions is outlined.

3.1 Sensor parameters

3.1.1 Frequency / Wavelength

The selection of the operating frequency of a radar system is dependant on the application. For example, the appearance of vegetation or soils changes with changing frequency. Generally, lower frequencies are capable to penetrate deeper into a medium. Figure 3.1 shows the differences in information content of various frequencies. The same area was imaged with two frequencies (X- and P-Band). It can be seen, that there is predominant structural information in the X-band image. Field boundaries can be distinguished easily and the backscatter of the forest in the image center is comparable to that of the agricultural areas.

In the P-band image on the other hand, field boundaries are not visible any more. The forest appears very bright instead. The reason is, that the P-band is not influenced by scatterers smaller than the wavelength such as leaves or stalks. It can therefore penetrate into the forest canopy and the high backscatter results from corner reflections between the trunks and the underlying surface.

In addition, technical considerations are a major constraint for the decision of the frequency of a SAR system. The radar equation (2.10), implies, that larger antenna sizes are needed for lower frequency systems, which is a major constraint for spaceborne SAR systems.
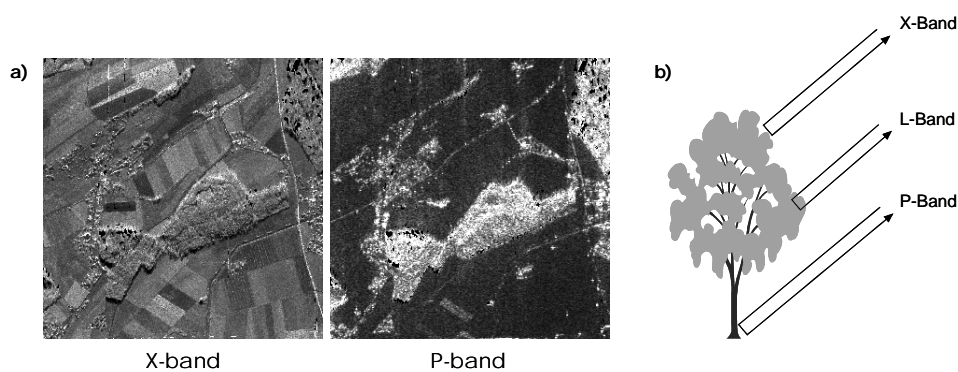
Figure 3.1: **Frequency dependant information content of a SAR image (a) and schematic penetration depth for vegetation canopies (Löw, 2000)**

3.1.2 Polarisation

The polarisation of an EM-wave is defined by the direction of its electric field vector. Radar systems can have single, multiple or full polarised configurations. A single polarised system records information only in one transmit/receive polarisation combination, while a multiple system, as ENVISAT ASAR, has different possible channel combinations. A fully polarimetric SAR system stores the full scattering matrix which allows to reconstruct the depolarisations caused by a target. The basics of polarimetry and its applications are e.g. discussed by VAN ZYL *et al.* (1987), ZEBEKER *et al.* (1987) and BOERNER *et al.* (1998).

Depolarisation of the transmitted signal is primarily a consequence of

a) quasi specular reflection from corner reflectors,

b) multiple scattering from rough surfaces and

c) multiple volume scattering.

Targets with a characteristic geometrical shape with regard to the incident polarisation, influence the signal return significantly. Features having a linear vertical shape, as e.g. a wheat field, have stronger influence on a VV polarised EM-wave than a comparable HH-polarised field. The stalks of the plants behave like small dipoles which influence the signal return.

The incorporation of multiple-polarisation radar datasets in the analysis of SAR images raises the understanding of the signal/target interactions and can simplify surface parameter retrieval.
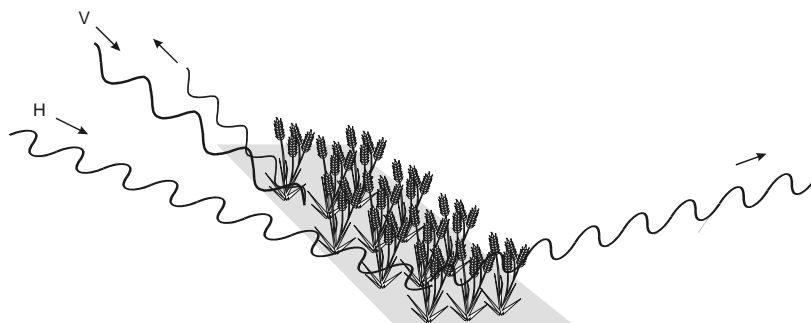
Figure 3.2:   **Definition of the polarisation vector**

3.1.3 Incidence angle

The definition of the local imaging geometry was given in section 2.2.2.1. It is dependant on the sensor's look angle and the target's local slope and aspect, with regard to the incident wave. Local terrain slopes have significant influence on the backscattering coefficient, making quantitative image analysis difficult. Therefore a systematic correction of the terrain induced grey value changes has to be applied on the image data. This prerequisite preprocessing steps are discussed in Chapter 4.

The interaction between the target and the EM-wave also depends on the incidence angle. The sensitivity of the signal to surface roughness or the contribution of a vegetation canopy to the signal increases with increasing incidence angle.

3.2 Object parameters

Several target parameters have an influence on the backscattering process. They are directly interrelated with the sensor parameters. The returned signal from a resolution cell is the sum of different backscatter contributions within that cell.

3.2.1 Surface roughness

Roughness is a very important target characteristic that influences the appearance of a feature on radar images. Roughness in this context means the "smoothness" of the target with respect to the wavelength and incidence angle (LEWIS and HENDERSON, 1998). Thus, the same surface has a different *effective* roughness in different frequencies and under different incidence angles.

When a surface is smooth, the impinging energy is reflected away from the surface, governed by Snell's law. As the roughness increases, the directional component of the scattered energy becomes more diffuse. For a perfect lambertian surface, the energy is scattered isotropically. The scattered component increases, while the reflected component of the signal decreases (Figure 3.3).
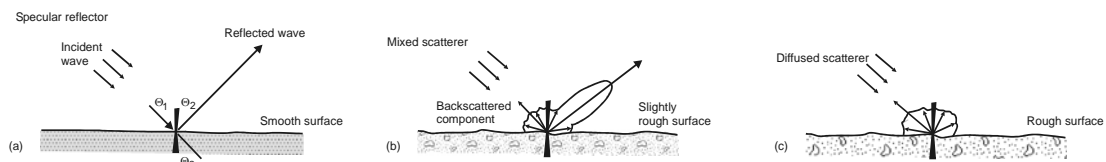
Figure 3.3: **Specular reflection and diffuse scattering from a smooth (a), medium rough (b) and very rough lambertian (c) surface**

In a first approximation, a surface can be treated as rough if it meets the *Rayleigh* criterion (ULABY *et al.*, 1982):

$$h > \frac{\lambda}{8\cos\theta}$$

(3.1)

where h is the average height variation of the surface and λ is the wavelength. For natural surfaces, the Rayleigh criterion is often not strict enough because the surfaces have roughness spectra similar to the wavelength, resulting in frequent scattering. A more stringent criterion is therefore needed. ULABY *et al.* (1982) therefore propose the *Fraunhofer* criterion. It is defined as:

$$h > \frac{\lambda}{32\cos\theta}$$

(3.2)

3.2.1.1 Surface roughness characterization

The description and derivation of surface roughness parameters is important for the understanding of the backscattering mechanisms. They are needed as input variables for theoretical electromagnetic models.

Commonly, the surface roughness is expressed in terms of the rms height s and autocorrelation length l (DAVIDSON *et al.*, 2000; DOBSON and ULABY, 1998). The rms height describes the vertical roughness of the surface as the deviation from the average height $\bar{h}$. It is defined as

$$s = \sqrt{\frac{\sum_{i=1}^{n}\left(h_i - \bar{h}\right)^2}{n}}$$

(3.3)

The surface autocorrelation function is a measure of the degree of correlation between the height $h(x)$ and the height $h(x+\xi)$, where ξ is the displacement factor. The horizontal roughness is expressed by the autocorrelation length l, which is defined as the distance where the value of the autocorrelation function is less than e^{-1} (Figure 3.4). For a perfectly smooth surface l is ∞. To approximate the shape of the autocorrelation function $p(\xi)$ by theoretical functions, exponential or gaussian distributions are commonly used. They are given as (DOBSON and ULABY, 1998)

$$p(\xi) = \exp\left(-\frac{\xi^2}{l^2}\right) \qquad \textit{Gaussian}$$

(3.4)

$$p(\xi) = \exp\left(-\sqrt{2}\frac{|\xi|}{l}\right) \qquad \textit{Exponential}$$

(3.5)
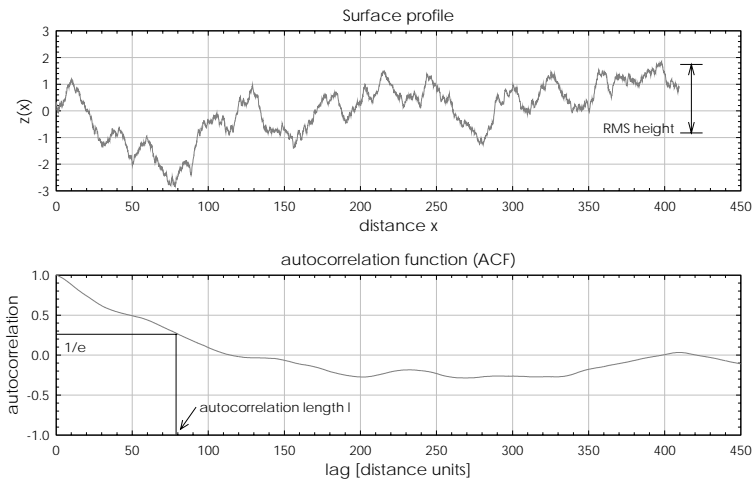
Figure 3.4: **Derivation of rms height and autocorrelation length from surface roughness profiles**

Unfortunately, neither of these is capable to satisfactorily describe the shape of the autocorrelation function of natural surfaces. Several other theoretical autocorrelation functions have therefore been proposed, trying to mediate between the gaussian and exponential shape (FUNG, 1994; LI, SHI and CHEN, 2002; CHANZY, MOLINEAUX and ZRIBI, 2003)

The roughness of a surface is commonly derived from one dimensional surface profiles. These can be generated using simple mesh grids, needle-like profilers or laser profilers. The derivation from high resolution elevation models is also possible (ZRIBI *et al.*, 2000).

The derivation of roughness parameters from field measurements has shown that their estimation can be difficult due to several reasons:

1) The autocorrelation length is not a measurable parameter. It is calculated from the autocorrelation function. Its estimate is strongly influenced by the profile length, used for the measurements (CHANZY, MOLINEAUX and ZRIBI, 2003; MATTIA *et al.* 2003; DAVIDSON *et al.*, 2000; OH and KAY, 1998).

2) Once the autocorrelation length has been defined for the characterization of the surface roughness, it can only be used in combination with the definition of the shape of the corresponding theoretical autocorrelation function (ACF). The simple shapes of the ACF are an inaccurate, nevertheless necessary, approximation to the true ACF estimates.

3) One dimensional surface profiles can only characterize a small subset of surface roughness characteristics. Many measurements in different directions are needed to get an estimate of the surface roughness. This is especially important for surfaces with characteristic linear macro scale variations as e.g. potato fields.

4) Natural surfaces have different roughness frequency components. This has to be taken into account when calculating the autocorrelation length. CHANZY, MALINEAUX and ZRIBI (2003) therefore propose a decomposition of the roughness spectra in low and high frequency components.

5) Compared to the resolution cell of a SAR system, the measured profiles are short and not absolutely a representative for the characteristic roughness component affecting the backscattered signal.

To overcome these drawbacks and to come to a more realistic description of natural surfaces, power spectral indices or self-affine fractal surfaces have been used for the surface roughness characterization (DAVIDSON *et al.*, 2000; LOUIS *et al.*, 2003; POWER and TULLIS, 1995; ZRIBI *et al.*, 2000).

3.2.2 Dielectric properties

The scattering and absorption of EM waves by a media is strongly dependant on its dielectric properties. These are described by the complex dielectric constant which is a measure for the polarisability of the media.

The complex permittivity ε_c, often called the dielectric constant, is the principal description of the medium's response to the presence of an electric field. It is given as (RANEY, 1998)

$$\varepsilon_c = \varepsilon' - j\varepsilon'' = \varepsilon_o\left(\in_r' - j\in_r''\right) \tag{3.6}$$

where $\varepsilon_0 = 8.85 \times 10^{-12}$ [farad/m] is the permittivity of free space, ε' is the *absolute* and $\in_r'$ the *relative* dielectric constant. Both, ε' and $\in_r'$ can be found in the literature, but the distinction between the absolute and relative values are not always reliable. The *relative* dielectric constant, representing an intrinsic property of the media, is often cited in the literature simply as *dielectric constant*. To be consistent with other publications (e.g. DOBSON and ULABY, 1998; ULABY *et al.* 1982; HALLIKAINEN *et al.*, 1985), $\in_r$ is also referred as *dielectric constant* within this work.

The real part of the dielectric constant $\in_r'$ defines the relative permittivity of the media. It influences the wave propagation and depolarisation and defines the amount of scattered energy. The polarisation of the molecules at the boundary layer between two media produces a separation of the electrical charges.

The force of this separation is expressed by $\in_r'$. The imaginary part $\in_r''$ is a measure for the absorption properties of the media. It is common to express the loss properties in terms of the loss tangent

$$\tan\delta = \frac{\in_r''}{\in_r'} \tag{3.7}$$

Most natural materials have dielectric constants ranging from 3 to 8 when dry, while liquid water has a high dielectric constant due to its dipole character (TIPLER, 1994). For frequencies below 5 GHz the dielectric constant of water is about 80. For higher frequencies, it decreases but remains significantly larger than that of other natural materials (MÄTZLER, 1987). Thus, the dielectric constant is strongly influenced by the water content of the media. A high moisture content implies a high radar reflectivity and a high signal return. Therefore the penetration depth of the EM-wave into a media is inversely proportional to the water content. High moisture contents lead to high reflection at the top of the surface, resulting in low penetration depths. Subsurface contributions to the signal have therefore a higher probability under dry conditions. The penetration depth D_{pen} is defined as the depth, at with $I(D_{Pen})/I(0) = e^{-1}$, where $I(0)$ is the intensity of the transmitted wave at the interface between two media. It is dependant on the radar wavelength and the local incident vector. The intensity of the wave at a given depth is then given by

$$I(r) = I(0) \cdot e^{-\alpha \vec{r}} \tag{3.8}$$

where $\vec{r}$ is the vector of the incident field and α is the attenuation factor which is defined as (RANEY, 1998):

$$\alpha = \frac{2\pi}{\lambda} \sqrt{0.5\sqrt{1 + \tan^2\delta} - 0.5} \tag{3.9}$$

Figure 3.5 shows the penetration depth for the ENVISAT ASAR sensor configuration (C-band) for various surface moisture contents and incidence angles. For most cases, the penetration depth is within the upper 1-2 centimetres. This uppermost soil layer may have a significant different moisture content than the lower soil layers.
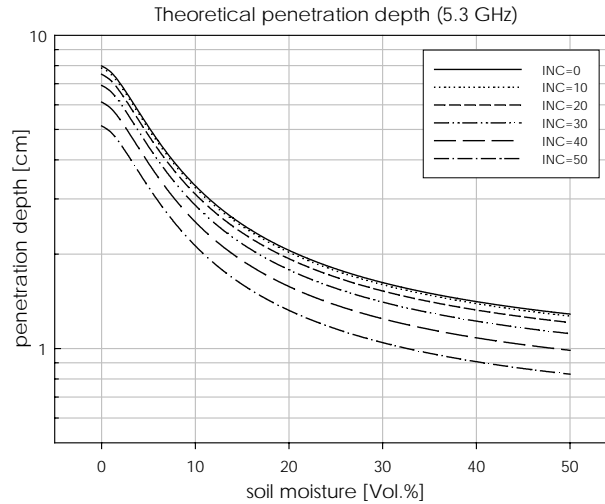
Figure 3.5: **Penetration depth at 5.3 GHz for different incidence angles**

3.2.2.1 Dielectric models

Natural surfaces, as soils or vegetation, consist of heterogeneous materials. In contrast to pure media (e.g. water and ice) or electrolytic solutions, their dielectric constant has to be calculated using dielectric mixture models. There are many theoretical or semi-empirical models which describe the dielectric behaviour of natural materials as a function of moisture content (e.g. WANG, 1980; DOBSON *et al.*, 1985; HALLIKAINEN *et al.* 1985; PEPLINSKI, ULABY and DOBSON, 1995; SERBIN, OR and BLUMBERG, 2001). The most commonly used, in the field of remote sensing, are the dielectric models of HALLIKAINEN *et al.* (1985) for soils and the Dual Dispersion model of ULABY and EL-RAYES (1987) for vegetation. They describe the dielectric constant as a function of the soil and vegetation volumetric water contents as follows:

Soil (HALLIKAINEN *et al.*, 1985)

$$\in_r = (a_0 + a_1 S + a_2 C) + (b_0 + b_1 S + b_2 C)m_v + (c_0 + c_1 S + c_2 C)m_v^2 \qquad (3.10)$$

where m_v is the volumetric soil moisture, S and C are the sand and clay textural components of the soil in percent by weight and a_n, b_n, c_n are empirically determined model coefficients. The coefficients are given for the real and imaginary part of $\in_r$.

Vegetation (ULABY and EL-RAYES, 1987)

The Dual Dispersion model treats the dielectric constant of vegetation $\in_v$ as the additive mixture of a nondispersive residual component $\in_r$, a free water component $\in_f$ and a bulk vegetation bound water component $\in_b$ as

$$\in_v = \in_r + v_{fw} \in_f + v_b \in_b \tag{3.11}$$

where v_{fw} and v_b are the volume fractions of the free water and bulk vegetation bound water components respectively. The different components of (3.11) are given by (3.12) – (3.17) as follows:

$$\in_r = 1.7 - 0.74 m_g + 6.16 m_g^2 \tag{3.12}$$

$$v_{fw} = m_g (0.55 m_g - 0.076) \tag{3.13}$$

$$\in_f = 4.9 + \frac{75.0}{1 + if/18} - i \frac{18\sigma}{f} \tag{3.14}$$

$$v_b = \frac{4.64 m_g^2}{\left(1 + 7.36 m_g^2\right)} \tag{3.15}$$

$$\in_b = 2.9 + \frac{55.0}{1 + \left(if/0.18\right)^{0.5}} \tag{3.16}$$

$$\sigma = const = 1.27 \tag{3.17}$$

where f denotes the frequency and m_g the gravimetric moisture content of the vegetation. The influence of the water content on the dielectric constant for 5.3 GHz is shown in Figure 3.6 for both models.
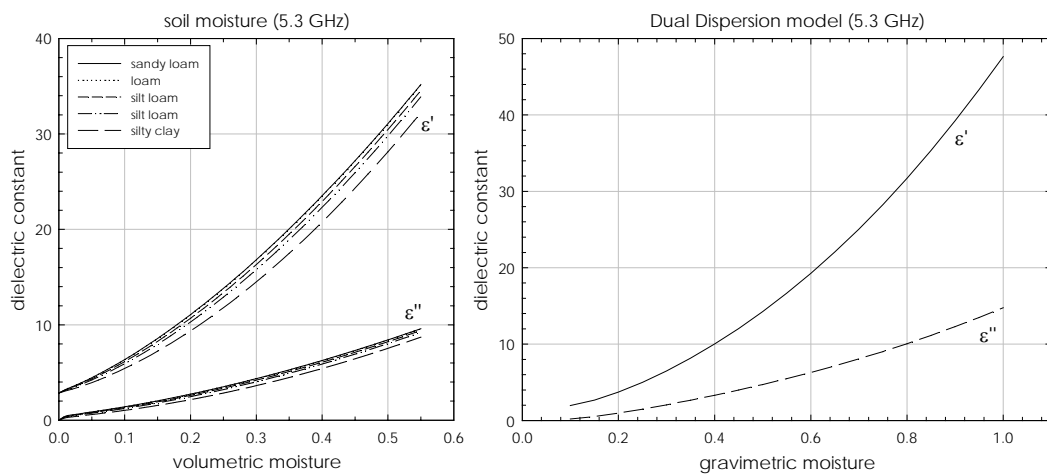
Figure 3.6: Dielectric constant for soils (left) and vegetation (right) as a function of water content

3.3 Modelling land surface backscattering

The availability of electromagnetic models which describe the complex interactions between EM-waves and the object properties and their interrelationships is critical for a better understanding of the scattering processes and the retrieval of geophysical parameters. FUNG (1994) gives an overview about existing scattering models and their wide field of applications. The main motivations for using theoretical models are (FUNG, 1994):

1) assist data interpretation, by permitting the calculation of signal return, dependant on biogeophysical object properties

2) study the signal sensitivity to biogeophysical or system parameters

3) provide an interpolation or extrapolation tool for filling gaps in existing datasets

4) to simulate the signal by "forward modelling", dependant on biophysical parameters, leading to the inversion of those

5) to aid experimental design

While trying to build up such models and use them for practical applications one particular difficulty is to provide an accurate and complete set of input variables, describing the properties of the object. Furthermore, the validity of each model is restricted to a limited range of each input parameter.

A brief overview about existing electromagnetic models, suitable for the description of the microwave land surface interactions, is given in the following. All models use the rms height, autocorrelation length and dielectric constant as input variables.

3.3.1 Theoretical surface scattering models

The complex geometry of bare soil surfaces has to be approximated by simpler geometries to describe electromagnetic wave scattering. Each scattering model is therefore constrained to a certain validity range of surface roughness.

If the surface irregularities are large compared to the wavelength, commonly expressed by the wavenumber k, the *Kirchhoff approximation* is applicable (OH, SARABANDI and ULABY, 1992). Such a rough surface is characterized by a large radius of curvature at each point of the surface. Various types of modifications and improvements have been made to the *Kirchhoff* model. The most commonly used are the geometric optics model (GOM) and the physical optics model (POM).

Geometric optics model (GOM)

The geometric optics model (BECKMANN and SPIZZICHINO, 1987), also known as the Kirchhoff method under the stationary phase approximation, is based on the assumption that $\sigma_{hh}^0 = \sigma_{vv}^0$ at all incidence angles for rough surfaces. It is only defined for the copolarised case. Thus an adequate parameterisation of the depolarisation is missing because it is assumed that $\sigma_{hv}^0 = 0$. Following DOBSON and ULABY (1998) this assumption is applicable up to an incidence angle of 60 °. For higher incidence angles the backscattering coefficient is highly underestimated by the GOM.

Physical optics model (POM)

The physical optics model is also known as the Kirchhoff approach under the scalar approximation. It is defined for medium rough surfaces with an autocorrelation length larger and a rms height smaller than the wavelength. Both copolarisations can be sufficiently described. It shows good agreement with measured datasets up to an incidence angle of 30 °. For higher incidence angles, the backscattering coefficient is underestimated (DOBSON and ULABY, 1998).

Small Perturbation Model (SPM)

For smooth surfaces with only slight profile deviates from the mean height, perturbation solutions can be used. The small perturbation model (RICE, 1951) is defined for smooth surfaces, where the rms height is small compared to the wavelength. The surface should have an isotropical character. Therefore the range of validity is reduced and the model application is mainly restricted to longer wavelengths in L- or P-band (DOBSON and ULABY, 1998)

Integral Equation Model (IEM)

The validity ranges of the models introduced above are shown in Figure 3.7. It must be noted that there remains a gap, especially for $ks < 2.0$ and $kl < 6.0$, where none of the models is valid. The surface roughness of most natural surfaces is situated within this region. This limits the applicability of the models introduced above significantly. To overcome this problem, FUNG, LI and CHEN (1992) proposed a model, namely the Integral Equation Model (IEM), which is valid over a wide range of surface roughnesses, as can be seen from Figure 3.7. It is especially applicable to model the backscattering behaviour of natural surfaces. The IEM is one of the most popular backscattering models for Earth science applications, where it has proven its capability to reproduce the backscattering coefficient of natural surfaces (e.g. BINDLISH and BARROS, 2000; ZRIBI and DECHAMBRE, 2000; BAGHDADI *et al.*, 2002; WIGNERON *et al.*, 1999; ZRIBI *et al.*, 2003). A detailed model description of the IEM is given in Chapter 6.
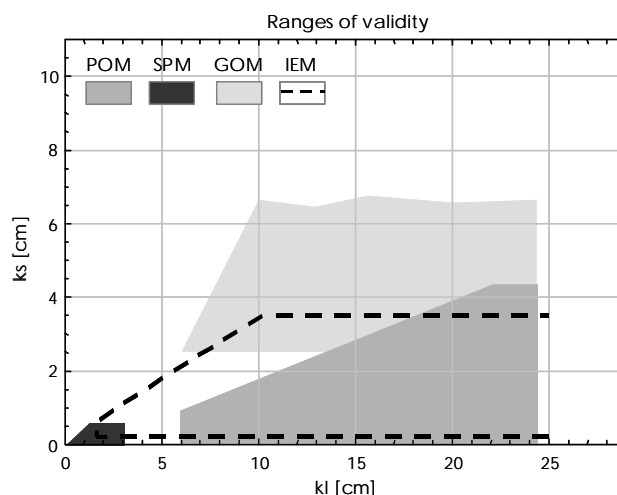
Figure 3.7: **Roughness validity ranges of electromagnetic models, dependant on the frequency and surface rms height s and autocorrelation length l (after O**H *et al.***, 1992; F**UNG**, L**I **and C**HEN**, 1992; D**OBSON **and U**LABY**, 1998)**

3.3.2 Vegetation interactions

Attempts to describe the backscattering from vegetation covered areas have been made since the late 1970s. They have evolved from the simple "cloud" model of ATTEMA and ULABY (1978) over multilayered, multi-constituent models as the MIchigan MIcrowave Canopy Scattering Model (MIMICS) proposed by ULABY *et al.* (1990) or the radiative transfer model of KARAM *et al.* (1992). Recent approaches become more sophisticated, using 3-dimensional parameterisations of the canopy (FLOURY, 1999; MARTINEZ *et al.*, 2000; DISNEY, SAICH and LEWIS, 2003; LEWIS *et al.*, 2003). The different kinds of vegetation representations are shown in Figure 3.8.
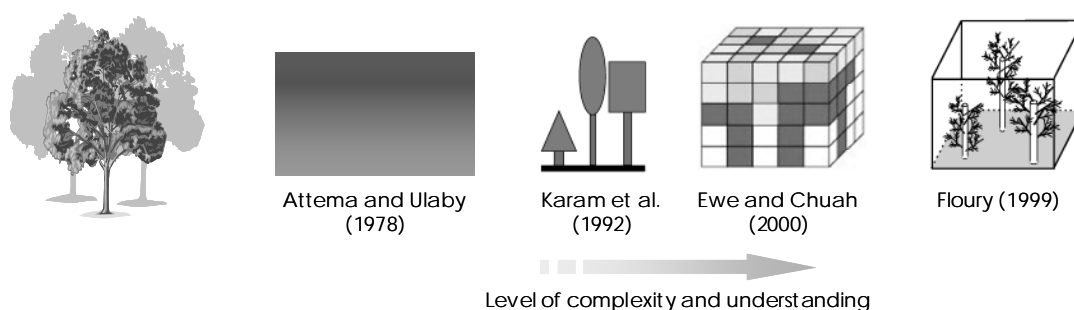
Figure 3.8: **Different vegetation representations for electromagnetic modelling**

Despite the progress which has been made in understanding the complex interactions between electromagnetic waves in the microwave region and the vegetation and soil properties, the scattering models still represent a simplified description of the underlying physical process. This has several reasons:

- The backscattering coefficient of a resolution cell is the result of the contributions of independent scatters which add incoherently to the returned signal. The electromagnetic models describe this by randomly distributed independent scatterers with specific scattering and attenuation properties. These are summarized to calculate the final backscattering coefficient. The independent scatterer assumption is valid, if the distance between the scatterers is large compared to the wavelength. If the scatterers have a distance within or below a wavelength, the single contributions add coherently, resulting in positive or negative interference. In first order radiative transfer models (e.g. KARAM *et al.*, 1992) multiple scattering between the different sources is often neglected.

- As a consequence of the assumption of independent scatterers, the attenuation by the vegetation canopy is often over- and the vegetation and bare soil scattering terms are underestimated. This effect increases with increasing incidence angle, which is a problem if the model should be used for various imaging geometries.

- Each scatterer has to be characterized by its location within the resolution cell and its geometrical and dielectric properties. Commonly this is realized by randomly distributing the scatterers within a volume and define their dielectric properties. For more sophisticated 3D-models the exact position of each scatterer has to be known, which leads to large and sophisticated parameter sets, being not available for operational tasks.

- Heterogeneities within the resolution cell can not be taken into account.

- The scatterers are assumed to satisfy azimuthal symmetry which may not correspond to natural appearance (e.g. sunflowers)

- The geometric shape of the scatterers has to be approximated by simplified geometric structures, such as needles, disks or cylinders for which the extinction and polarisation properties can be calculated using electromagnetic equations. The curvature of e.g. leaves is not taken into account when using these simple geometries.

Recently, electromagnetic models have been developed to overcome the drawback of the independent scatterer assumption (MARLIANI *et al.*, 2002; PICARD, LETOAN and MATTIA, 2003; PICARD and LETOAN, 2002; LIN and SARABANDI, 1999; COOKMARTIN *et al.*, 2000). These coherent models preserve the phase information and take into account interference of all scatterers within a resolution cell, defined by their size, position and orientation. Nevertheless, they are still based on a simplified description of the three-dimensional structure of the vegetation by a discrete set of primitives.

To provide the necessary input parameters for the radiative transfer models a coupling of vegetation growth models, based on the description of specific physiological processes of plant growth, in combination with geometrical plant vegetation models, as L-systems, is helpful (LINDENMAYER, 1975; PRUSINKIEWICZ and LINDENMAYER, 1990; FOURNIER and ANDRIEU, 1999). While radiative transfer models have been established in the optical domain for appropriate inversion of plant parameters (BICHERON and LEROY, 1999; BACH *et al.*, 2000; WEISS *et al.*, 2000; COMBAL *et al.*, 2002; BACH and MAUSER, 2003), they are seldomly used to understand the microwave backscattering of vegetated surfaces. The main reasons are the difficulties in model parameterisation and the limitations of the electromagnetic models mentioned above. First approaches in this direction were made by LEWIS *et al.* (2003) who coupled the coherent, Monte Carlo based backscattering model of LI and SARABANDI (1999) with an L-system based geometrical and physiological plant model (FOURNIER and ANDRIEU, 1999).

Thus empirical models are still often used for operational questions, where the amount of required input parameters is limited. The obtained inversion accuracies are not necessarily worse than those of theoretical models. The following section summarizes the state of art of land surface parameter retrieval from SAR data with a focus on the parameterisation of agricultural surfaces.

3.4 Retrieval of land surface parameters from SAR data

The retrieval of bio- and geophysical parameters from SAR imagery has been subject to many investigations. During the mission of the European Remote Sensing Satellite (ERS), manifold approaches have been developed to gather information about the Earth surface from microwave remote sensing in different scientific disciplines. Concerning the land surface, different groups of applications and parameters can be distinguished. A subset of studies and parameters related to the retrieval of land surface parameters from SAR data is given in Figure 3.9 and Table 3.2 without any claim of completeness. A good summary of land surface parameter retrievals can be found in HENDERSON and LEWIS (1998).
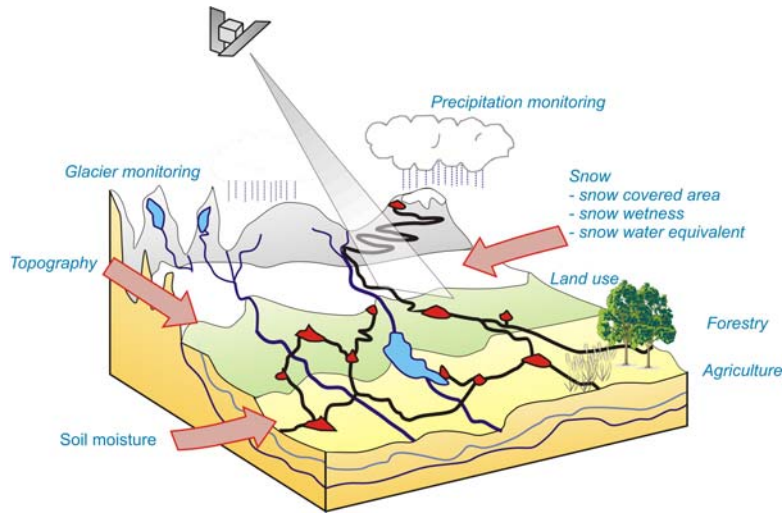
Figure 3.9:   Land surface parameters from SAR data

The new and flexible imaging capabilities of ENVISAT ASAR offer new potentials for the retrieval of bio- and geophysical parameters from SAR data. The multiple incidence angles allow for frequent observations of an area. The variable polarisations help to gather multichannel information about objects and may simplify inversion strategies, whereas the ENVISAT wide swath mode allows for the acquisition of larger areas as e.g. mesoscale watersheds ($\sim$100.000 km²).

One key parameter for the interactions between the solid Earth surface, vegetation and the atmosphere is the *soil moisture*. It has an impact on the energy and water fluxes at the boundary layer between the solid Earth and the atmosphere. Accurate and spatially distributed estimates of the current soil moisture state near the land surface are needed, to make this information available for modelling purposes in Earth sciences and practical applications as e.g. flood forecasting. The possibility of monitoring soil moisture patterns with help of SAR imagery has incited a large number of studies dealing with its retrieval strategies.

For the derivation of soil moisture information in agricultural areas, the effect of the vegetation cover on the backscattering coefficient has to be known to quantify its influence in the soil moisture inversion process. On the other hand, the vegetation contribution to the signal can also be used to gather information on plant parameters. Thus both, soil moisture as well as plant properties, are important for surface parameter inversion strategies in agricultural areas.

The previous section has summarized theoretical modelling approaches. In the following an overview about the derivation of soil moisture and the knowledge of scattering from vegetated surfaces is given.

Table 3.2: **Land surface parameters from SAR data**

PARAMETER	SELECTED REFERENCES
Soil moisture	DUBOIS, VAN ZYL and ENGMAN (1995)
	OH, SARABANDI and ULABY (1992)
	ROMBACH and MAUSER (1997)
	QUESNEY *et al.* (2000)
	DAVIDSON *et al.* (2001)
	ZRIBI and DECHAMBRE (2002)
	LÖW, LUDWIG and MAUSER (2003a)
Soil roughness	BENALLEGUE *et al.* (1995)
	DUBOIS, VAN ZYL and ENGMAN (1995)
	MAGAGI and KERR (2001)
	LE HEGARAT-MASCLE *et al.* (2003)
Snow covered area	KOSKINEN, PULLIAINEN and HALLIKAINEN (1997)
	STROZZI, WEGMÜLLER and MÄTZLER (1999)
	NAGLER and ROTT (2000)
	LÖW, LUDWIG and MAUSER (2003)
Snow water equivalent	PULLIAINEN and HALLIKAINEN (2001)
	SHI and DOZIER (2000a,b)
Vegetation biomass	DOBSON *et al.* (1992)
	RANSON and SUN (1994)
	DOBSON *et al.* (1995)
	SAATCHI and MOGHADDAM (1999)
	KURVONEN, PULLIAINEN and HALLIKAINEN (1999)
	RIEGLER (2000)
Vegetation height	ULANDER, DAMMERT and HAGBERG (1995)
	DAMMERT and ASKNE (1998)
	GABRIEL *et al.* (1999)
	RIEGLER (2000)
Classifications	SAATCHI, SOARES and ALVES (1996)
	RIGNOT, SALAS and SKOLE (1997)
	STROZZI *et al.* (1998)

3.4.1 Soil moisture

An optimal SAR system configuration, applicable for the retrieval of soil moisture patterns, would be a C-band SAR system with HH polarisation and steep incidence angles between 7 and 20 ° (AUTRET, BERNARD UND VIDAL-MADJAR, 1989; DOBSON and ULABY, 1998; BENALLEGUE *et al.*, 1995). Operational SAR systems all have shallower incidence angles to improve the range resolution. Thus backscattering models and inversion techniques have been developed, based on the available experimental, as well as operational sensor systems. These include studies using scatterometer and space- and airborne SAR systems with various configurations (DOBSON and ULABY, 1998; ENGMAN and CHAUHAN, 1995). While most studies are dealing with the retrieval of soil moisture for bare soil conditions, only a few studies investigated vegetated areas, compensating the canopy effect on the signal using empirical or theoretical approaches.

3.4.1.1   Bare soil models

An empirical surface scattering model and inversion technique was proposed by OH, SARABANDI and ULABY (1992) based on multifrequency polarimetric scatterometer data. The soil moisture was inverted with an RMSE of 4 Vol.%. The model was simplified for rougher surface conditions (ks>1.5) by WEIMANN (1996) to make it applicable to the ERS system configuration. The errors of the retrieved soil moisture values ranged from 2.7 to 4.5 Vol.%.

DUBOIS, VAN ZYL and ENGMAN (1995) presented an empirical scattering model for both copolarisations. It is valid for three frequencies (1.25, 4.75, 9.5 GHz) and can easily be inverted to derive soil roughness and moisture from copolarised datasets. The soil moisture was inverted with an accuracy of 3.5 Vol.%.

Based on numerical simulations of the backscattering coefficient for various soil roughness and moisture conditions, DAVIDSON *et al.* (2001) suggested a soil moisture inversion algorithm for bare soil conditions. The most *probable* soil moisture value is calculated, using the conditional probabilities of the backscattering coefficients for defined surface roughness conditions.

A synergistic approach using ERS-AMI and ERS-scatterometer data was proposed by ZRIBI *et al.* (2003). They used the multiincidence angle configuration to invert soil moisture patterns for sparse vegetated or bare soils. The achieved accuracies are within ±4 Vol.%.

3.4.1.2 Vegetation effect

The backscattering coefficient σ^0 of a vegetated surface can be described as a function of attenuated ground backscatter and vegetation, as well as vegetation ground interactions as (TSANG, KONG and SHIN, 1985)

$$\sigma^0 = \sigma_S^0 \cdot e^{-2\tau} + \sigma_V^0 + \sigma_{V/S}^0 \qquad\qquad (3.18)$$

where σ_S, σ_V and $\sigma_{V/S}$ are the soil, vegetation and interaction terms respectively. The soil signal is attenuated as function of the optical depth τ which is expressed as

$$\tau = \frac{\kappa_e \cdot h}{\cos(\theta)} \qquad\qquad (3.19)$$

where κ_e is the extinction coefficient [np/m] and h is the canopy height.

Thus the vegetation contributes to the total signal by the attenuation of the underlying soil layer and an intrinsic scattering term. A good summary of existing theoretical and (semi)empirical vegetation backscattering models can be found in BINDLISH and BARROSS (2001).

One of the most popular vegetation models is the CLOUD model of ATTEMA and ULABY (1978), which treats the canopy as a cloud of small dipoles, randomly distributed within a volume. It has been used successfully in numerous studies (e.g. MAGAGI and KERR, 2001; MORAN *et al.*, 1998; STOLZ *et al.*, 2000; XU *et al.*, 1996).

WIGNERON *et al.* (1999) used a combined bare soil surface scattering (FUNG, LI and CHEN, 1992) and a radiative transfer model (KARAM *et al.*, 1992) to investigate the backscattering behaviour of soybeans. They were able to show, that there is a stable relationship between the backscattering coefficient and the optical depth τ as well as between the vegetation water content and τ. Hence it was possible to replace the complex radiative transfer model by a simpler model and predict the backscattering coefficient in dependency of the soil moisture and vegetation water content.

Based on the work of TACONET *et al.* (1996), who stated that soil moisture can be retrieved from wheat fields, a soil moisture index was proposed on the watershed scale by QUESNEY *et al.* (2000) using ERS data. The vegetation contribution to the signal is calculated, using the radiative transfer model of KARAM *et al.* (1992). Using *a priori* knowledge of the current state of the vegetation, the attenuation and vegetation backscattering terms could be calculated and used to derive the soil backscatter contribution. From that, the soil moisture could be retrieved, using empirical relationships.

The method was extended to other crop types and an operational inversion methodology was suggested by LE HÉGARAT-MASCLE *et al.* (2001; 2002). The approach was tested for three catchments with rms errors between 1.7 and 7.4 Vol.%. On the watershed scale, soil roughness effects could be neglected. On the other hand, the coarse spatial resolution doesn't provide information about the spatial distribution of the soil moisture patterns within the watershed, which is crucial for e.g. predicting runoff generation (SCHULZ *et al.*, 2002).

An empirical soil moisture inversion algorithm for heterogeneous landscapes was proposed by ROMBACH and MAUSER (1997). It is based on the empirical compensation of the vegetation contributions on the signal. It assumes, that the vegetation effect is constant after reaching a certain phenological state. Thus the dielectric constant can be inverted from the backscattering coefficient and then be compiled to soil moisture values, using existing dielectric models (see 3.2.2.1).

The model was developed for different crop types and grassland. It was successfully applied in several studies (SCHNEIDER and OPPELT, 1998; BACH *et al.*, 2000; BACH and MAUSER, 2003; STOLZ *et. al.*, 2000; STRASSER, SCHNEIDER and MAUSER, 1999). LÖW, LUDWIG and MAUSER (2003a) have shown, that it is also applicable to mesoscale SAR imagery, using subscale land use information.

The sensitivity of the different models to soil moisture m_v is shown in Figure 3.10. The dielectric constant, which is needed as input parameter for most models, was calculated from m_v using (3.10) for a loamy sand. The gain of the relationship between soil moisture and backscattering coefficient ranges from 0.25 to 0.4 for the chosen models. The models for bare soil (DAVIDSON *et al.*, 2001; ROMBACH and MAUSER, 1997) have a lower gain than the other models, where the bare soil backscatter was calculated, by eliminating the vegetation contribution from the total signal. This might be interpreted as an indication, that the calculated bare soil backscattering coefficients of those models still contain information about the vegetation contribution to the signal. The different offsets of the functions may be caused by slightly different imaging geometries and surface roughness conditions between the studies.

soil moisture vs. backscattering coefficient VV polarization
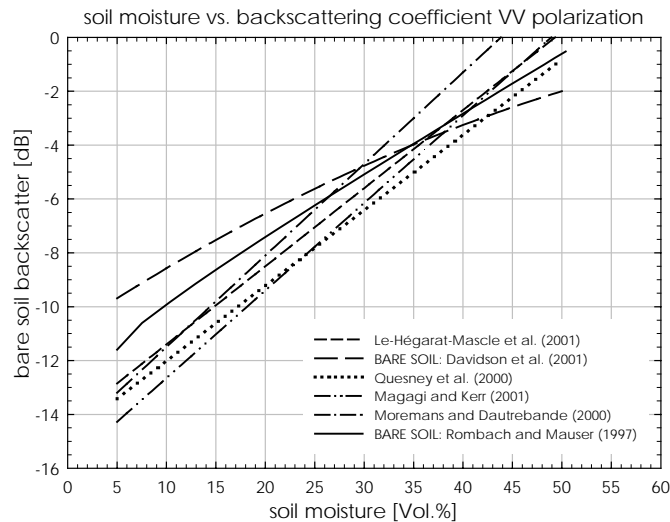
Figure 3.10: Relationship between volumetric soil moisture and bare soil backscattering coefficient (as reported in the literature)

3.4.2 Scattering signatures of agricultural crops

Theoretical modelling approaches need a profound understanding of the intrinsic scattering mechanisms of a medium. The models, described in section 3.3, were mainly developed based on high resolution scatterometer observations or theoretical solutions of the Maxwell equations with respect to the scattering problem of vegetation canopies. Direct observations of the scattering within the canopy were not available. To investigate the intrinsic scattering mechanisms of a canopy, BROWN *et al.* (2003) conducted high resolution imaging of a wheat canopy in an indoor campaign. The radar cross section σ was measured during the vegetation period under different imaging geometries and with different frequencies.

Figure 3.11 shows an example for the measured backscattering behaviour of a wheat stand in C-band for both copolarisations. The vertical distribution of the radar cross section, which is the appropriate measure at very high resolutions, is shown dependant on the incidence angle.

It can be seen, that most of the signal comes from the ground and the subsurface. The main backscattering mechanism for wheat is the double bounce reflection between the stalk of the plant and the underlying surface. Thus, soil ground interactions play an essential role (MARLIANI *et al.*, 2002).

The vegetation backscatter is lower than the soil contribution. It can be stated, that the attenuation of the vegetation is higher for VV, where the signal from the ground is less than that in HH. An incidence angle dependency can also be observed. As expected, the vegetation contribution increases with increasing incidence angle, whereas the soil signal is lower for shallower imaging geometry.
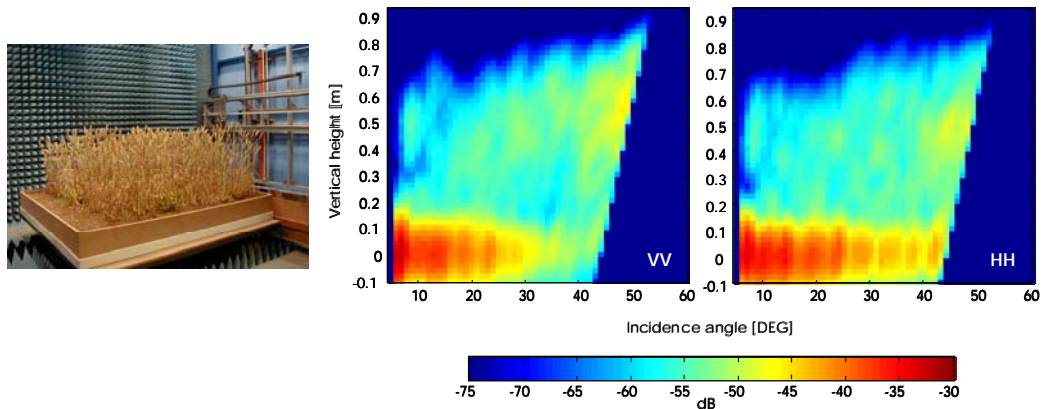
Figure 3.11: Wheat canopy radar cross section in C-band for VV and HH polarisation (after BROWN *et al.***, 2003)**

These observations confirm, that the soil contributes significantly to the signal. The backscatter differences between the polarisations contain information about the vegetation structure and biomass. This can be exploited to estimate plant biomass from the copolarisation ratio HH/VV. A strong relationship between plant properties and the copol ratio was reported by MATTIA *et al.* (2003).

3.4.3 Requirements and research needs

Theoretical models lead to a better knowledge of the backscattering mechanisms, but they still fail to describe the temporal behaviour of the SAR backscattering coefficient as a function of biophysical parameters in a satisfying manner. On the other side, empirical models have proven their applicability to invert land surface parameters from SAR data without a complex description of the soil and vegetation.

The research needs in the field of microwave remote sensing of the land surface are after BRISCO and BROWN (1998), the accurate ecological modelling of plant growth and coupling of these models with microwave backscattering models, to gather information on crop development, biophysical parameters and soil properties from SAR imagery. To provide information for practical applications at short time scales, the influence of different imaging geometries has to be compensated.

With the launch of ENVISAT ASAR, a sensor is available which can be used in a very flexible manner. The various imaging modes and different swathes allow for frequent observations of an area of interest. It is therefore especially interesting for time critical applications and monitoring of rapid changing landsurface variables as e.g. soil moisture patterns.

Frequent observations can only be achieved, using different imaging geometries. Backscattering and parameter inversion models have therefore to account for the incidence angle effect on the soil and vegetation interactions with the electromagnetic waves. The questions to be addressed in this context are:

- *Which effects have different imaging geometries on the signal, and how can these be described by models?*

- *How can the vegetation and soil backscatter contributions be separated for different imaging geometries?*

- *How can bio- and geophysical data be inverted from multitemporal ENVISAT ASAR data to provide frequent observations for time critical applications?*

To make use of the spatially distributed informations of remote sensing data, assimilation strategies have to be developed which allow for the quantitative assimilation of remote sensing data into land surface process models. State variables in the land surface process model may not be identical with those derived from remote sensing data. For instance, the sensitivity of a SAR system to surface soil moisture content is limited to the uppermost 2-5 centimetres (Figure 3.5), while informations about the water content of the whole root zone (up to 250 cm) are needed for water balance modelling. A direct linkage between models, describing the interactions of electromagnetic waves with the land surface, and land surface process models enable a consistent and physically based assimilation strategy. For instance, the water fluxes within the root zone can be described using a multi layer soil model within the land surface process model. The uppermost soil layer corresponds to the sensitivity region of a SAR system and enables direct comparisons between the simulated soil moisture values and observed backscattering coefficients.

BACH and MAUSER (2003) proposed to use the 4DDA (four dimensional data assimilation) technique in this context to adjust parameters of the land surface process model based on remote sensing data. A further question to be addressed is therefore:

- *How can ASAR derived products be assimilated in land surface process models? How could an automated interface look like?*

Empirical parameter inversion and backscattering models are difficult to calibrate in this context. To develop an empirical soil moisture model for ASAR data, numerous field measurements, combined with ASAR acquisitions would be needed. Even for a minimal specification, the number of necessary measurements exceeds the capabilities for ground based data acquisitions.

Figure 3.12 images the case, in which a soil moisture model should be developed for just one land use on only one field with the following constraints: Nine different phenological stages of the plant should be taken into account. The model should be valid for ten soil moisture classes, corresponding to an accuracy of ~5 Vol.% and for six incidence angle classes with 5° each.

This simple example leads to a total number of 540 necessary samples for the model calibration. To develop a generalized approach, even more fields and land use classes would be necessary. This could only be achieved with intensive field campaigns over several years.
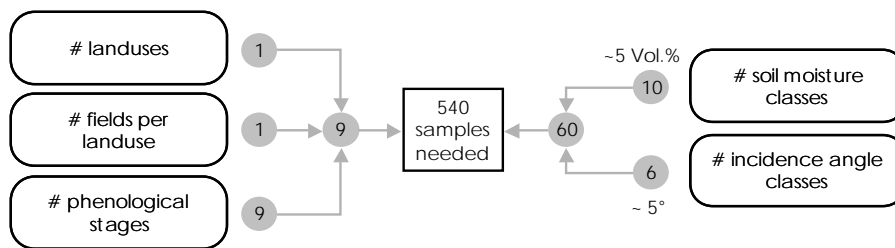
Figure 3.12: Development of an empirical soil moisture model from ENVISAT ASAR data: a minimal configuration

To overcome this problem, a combination of empirical with theoretical backscattering models might be helpful. These can be calibrated, using a reduced number of ground measurements, and then used for the generalized prediction of the backscattering coefficient for various imaging geometries and ground conditions. Together with a plant growth model, which can predict the plant and soil parameters for each instant, the number of field measurements can be reduced significantly. Such a model can also be used, to provide spatially distributed time series of land surface parameters, needed as input variables for a backscattering model.

3.4.4 Conceptual approach of the thesis

A model based approach was therefore chosen for this work to address the research needs mentioned above with relevance for the derivation of soil and vegetation parameters from ENVISAT ASAR data. A separation of the soil and vegetation contributions to the signal is crucial in this context. A combination of a theoretical bare soil, with a semiempirical vegetation backscattering model was chosen to quantify and separate the different contributions to the signal. The approach and its structure is shown in Figure 3.13. The thesis is mainly separated into two major parts.

The first deals with the derivation and calibration of soil and vegetation backscattering models for various imaging geometries. The models are calibrated and validated using ground measurements and image data. To reduce the number of necessary model input parameters, a bare soil backscattering model is recommended, which requires only two input parameters. This helps to simplify the description of bare soil surfaces and allows the accurate prediction of the bare soil backscatter. A vegetation backscattering model is then calibrated and validated, using available ground measurements and SAR image data. The resulting forward backscattering model allows for a precise prediction of the backscattering coefficient of vegetated areas, based on bio- and geophysical variables.

The second part of the thesis transfers the developed backscattering models for spatially distributed simulation of the backscattering coefficient in heterogeneous areas. The necessary spatially distributed backscattering model input parameters are provided as output of a physically based land surface process model. The coupling of the backscattering and process models is realized by an appropriate interface. This enables the spatially distributed prediction of the backscattering coefficient based on bio- and geophysical parameters. This coupled model is used, to derive land surface parameters from remote sensing data and assimilate it in the same step into the land surface process model.
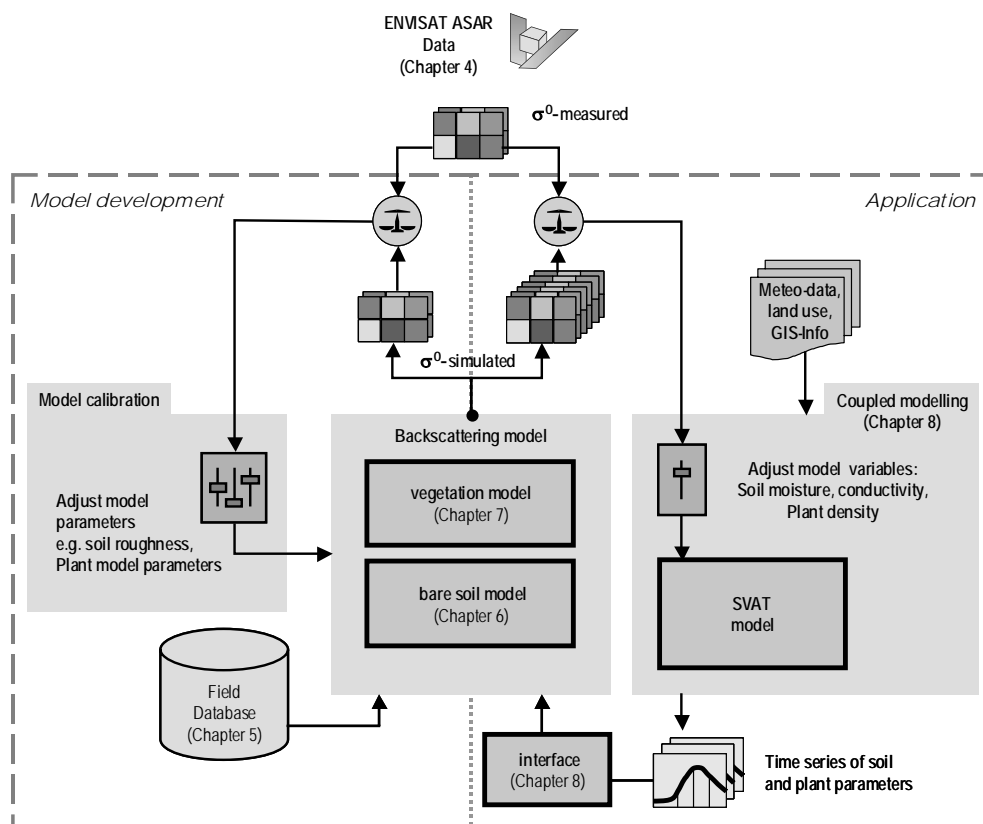
Figure 3.13:   Conceptual approach and structure of thesis

Chapter 4
Remote sensing data

An overview about the ENVISAT ASAR data used in this work and the required preprocessing steps is given in this chapter. The SAR images used are already processed slant or ground range image products. The discussion of their generation is beyond the scope of this work and the reader is referred to the literature. A good introduction into the topic of SAR image formation is given e.g. by BAMLER and SCHÄTTLER (1993), OLMSTED (1993), HENDERSON and LEWIS (1998) and CURLANDER and MCDONOUGH (1991).

The importance of a rigorous geometric and radiometric terrain correction is emphasized and a sophisticated correction algorithm is presented. Figure 4.1 gives an overview of the main processing steps, discussed in this chapter.
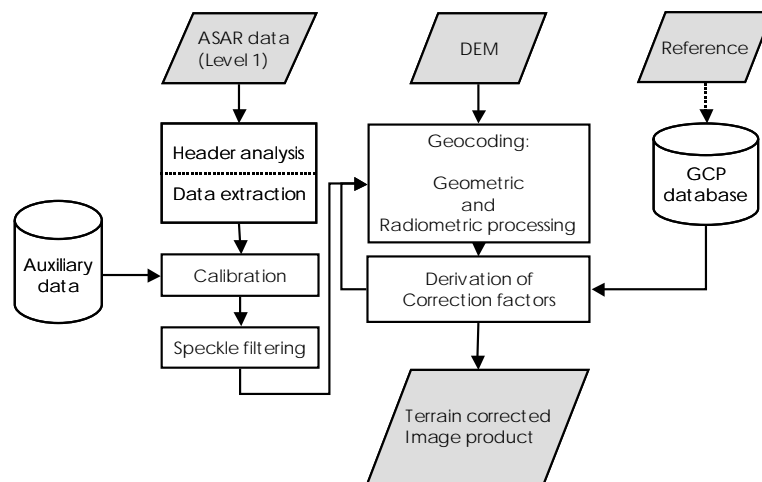
Figure 4.1: **Flowchart of preprocessing steps for the generation of terrain corrected SAR image products**

4.1 Header and data extraction

In addition to the recorded backscattering values, each image product contains important information on the sensor configuration and image processing parameters which were used to generate the image product. A subset of this header information has to be extracted from the product, to be available for further processing steps. It contains information about the actual sensor configuration and sensor position as well as information on corrections applied to the image product.

The binary image data has to be extracted from the image product and converted to an image processing software data format. The various ASAR image products are stored in different formats. The format, used to generate the product, is specified in the product header. ENVISAT ASAR alternating polarisation data (AP) for example, are complex values, where the real and imaginary components are each stored as SIGNED integer (16-bit). After the calculation of the pixel intensity value, the image can be converted and used for further processing.

4.2 Radiometric calibration

4.2.1 ASAR image calibration

As discussed in Chapter 2, the radar backscattering coefficient σ^0 can be derived from recorded intensity values, using the radar equation (2.10). For ENVISAT ASAR, the procedures to derive the backscattering coefficient are given by ROSICH AND MEADOWS (2004). The relationship between the image pixel grey values (DN) and the radar backscattering coefficient is given by

$$DN^2 = \beta^0 \cdot const = const \cdot \sigma^0 \cdot \sin^{-1}\theta \qquad (4.1)$$

Ground range products
For ground range detected products, such as the wide swath image product, the backscattering coefficient σ^0 is calculated as

$$\sigma^0 = \frac{DN^2}{K} \cdot \sin(\theta) \qquad (4.2)$$

and from (4.1) β^0 is derived as

$$\beta^0 = \frac{DN^2}{K} \qquad (4.3)$$

where θ is the incidence angle and K the absolute calibration constant.

Slant range products

For complex slant range products, the image intensity for each resolution cell can be derived from the complex input data as follows:

$$DN^2 = \sqrt{I^2 + Q^2}$$

(4.4)

where I and Q represent the real and imaginary parts of the complex samples. The backscattering coefficient is then given by

$$\sigma^0 = \frac{DN^2}{K} \cdot \frac{1}{G(\Theta)} \cdot \left(\frac{R}{R_{\mathrm{Ref}}}\right)^N \cdot \sin(\theta)$$

(4.5)

with N=3 for image mode products and N=4 for alternating polarisation data. The two-way antenna gain pattern *G(Θ)* changes with the look angle Θ. The image brightness value is then written as

$$\beta^0 = \frac{DN^2}{K} \cdot \frac{1}{G(\Theta)} \cdot \left(\frac{R}{R_{\mathrm{Ref}}}\right)^N$$

(4.6)

For each ASAR imaging mode, different antenna gain patterns are provided by the European Space Agency (ESA). They are updated several times a year. Figure 4.2 shows recent antenna gain patterns for different ASAR imaging modes.

All ASAR image products used in this work were calibrated to β^0 values. The backscattering coefficient σ^0, representing the intrinsic scattering properties of a ground range resolution cell, was obtained after the terrain geocoding process, which is discussed in section 4.4.
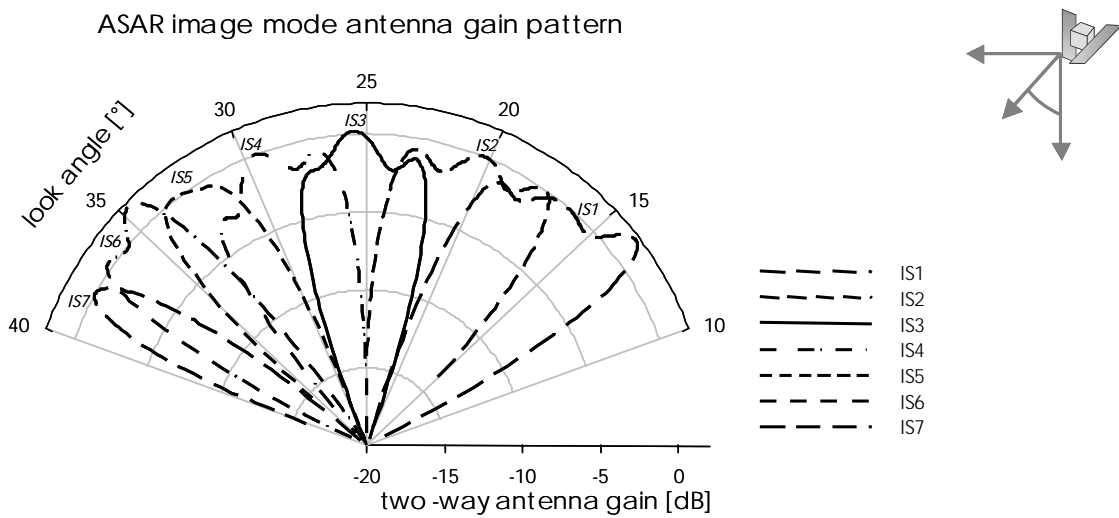
Figure 4.2:   ASAR two-way antenna gain patterns for different swathes

4.2.2 Radiometric Accuracy

The relative and absolute radiometric accuracies of the image products can be derived from measurements over homogeneous distributed targets as rain forests and by calibrating the image against external references. This is normally done, by using man made objects with a well defined radar cross section, as corner reflectors or transponders. The stability of the ASAR sensor is checked continuously in a special calibration mode by several scientific groups. The actual radiometric accuracy range for different imaging modes is given in Table 4.1.

Table 4.1:   ASAR calibration accuracies

MODE	RADIOMETRIC ACCURACY [dB]	REFERENCE
Alternating polarisation	0.47 – 0.51	MEADOWS and WRIGHT (2002)
Wide Swath	0.33 – 0.59	ROSICH (2002a)
Image mode	0.31 – 0.56	ROSICH (2002b)

4.2.3 Calibration problems

In the case of alternating polarisation data products, several SAR images were acquired in the steep looking IS1 mode. In this mode, calibration uncertainties, resulting from inaccurately estimated antenna gain patterns were observed. Figure 4.3 shows a calibrated IS1 image. The grey value undulations in the near range region can clearly be detected.

After a recalibration of the antenna gain pattern by ESA, the problem was reduced, but there were still remaining calibration errors, ranging up to several decibels. Figure 4.3b shows the column statistics of an IS1 image after calibration with the refined antenna gain pattern provided by ESA, still showing significant deviations in the near range region.

To ensure that all backscattering coefficients, used within this work, are reliable, the affected first 1400 image columns in near image were excluded from further investigations.
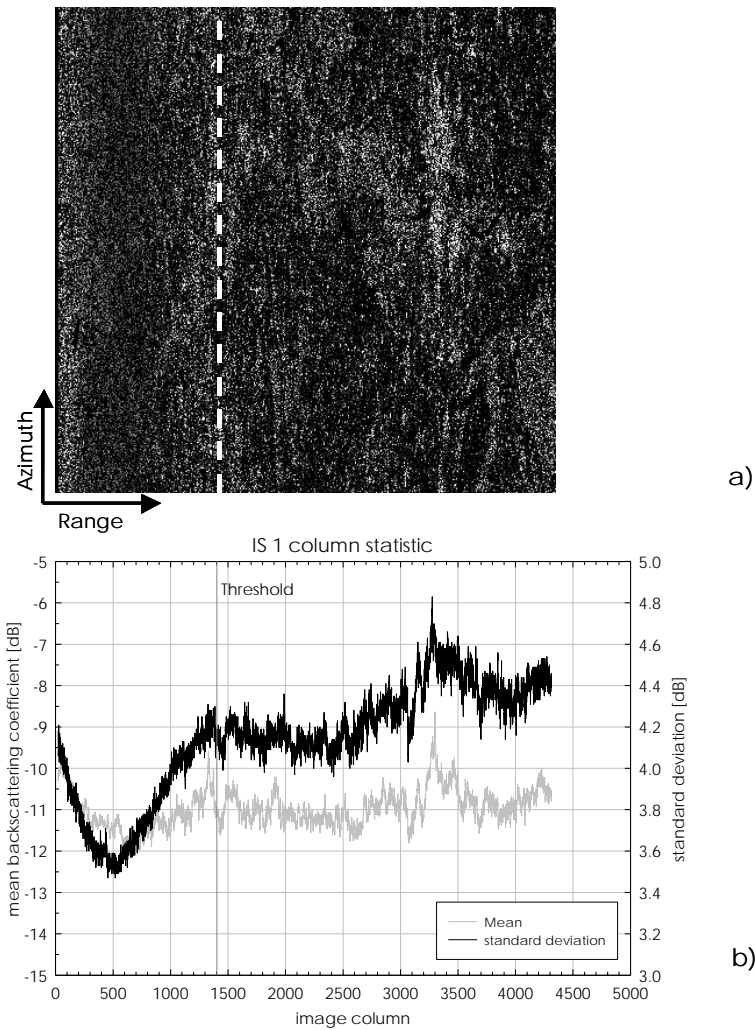
Figure 4.3: **IS1 calibration problem: a) image example showing grey value undulations in the near range region, b) image column statistics after recalibration by new antenna gain pattern**

4.3 Speckle Filtering

The resolution cell size of a SAR system is always much larger than the signal wavelength and also significantly larger than the size of individual scatterers contributing to the returned signal. Because of commonly random orientation of different scatterers within a resolution cell, the contributions of each scatterer add incoherently (random phase), giving a net backscattering coefficient with a random distribution in the image plane (Figure 4.4). This phenomena is well known as *speckle*.
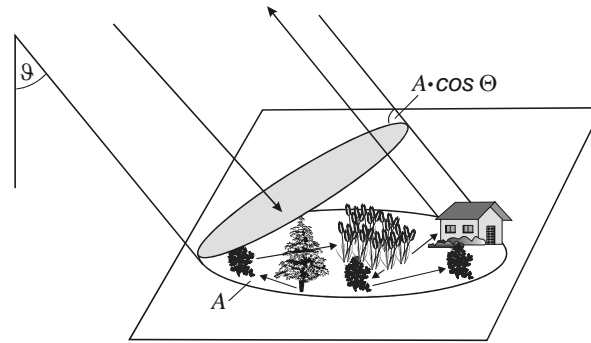
Figure 4.4: Scattering within a SAR system resolution cell

A reduction of the speckle effect is crucial for an adequate estimate of the backscattering coefficient σ^0. Statistical estimates of the backscattering coefficient can be improved, by averaging several samples. As a consequence, the spatial resolution of the image is reduced. Several image processing and filtering techniques have been developed to reduce the speckle, while preserving as much of the spatial resolution of the image product as possible (LAWS, 1980; LEE, 1981; LEE, 1986; FROST *et al.*, 1982; KLAUSING and HOLPP, 2000).

To obtain a reliable estimate of the backscattering coefficient, the speckle in the ENVISAT ASAR data, used within this work, is reduced by applying a special speckle filter to the slant range image and by a local adaptive spatial integration over several image pixels during the geocoding process introduced in the following section. Best results are obtained using a 7x7 Frost filter (FROST *et al.*, 1982). The filtering process is applied to the slant range image before geocoding. Figure 4.5 shows the statistics for single look and speckle filtered images. It can clearly be seen, that the exponentially distributed single look histogram converges to a Rayleigh distribution due to speckle filtering. The filtered images make object identification much easier compared to the single look image and result in reliable estimates of the backscattering coefficient.

Single look   Frost 3x3   Frost 7x7
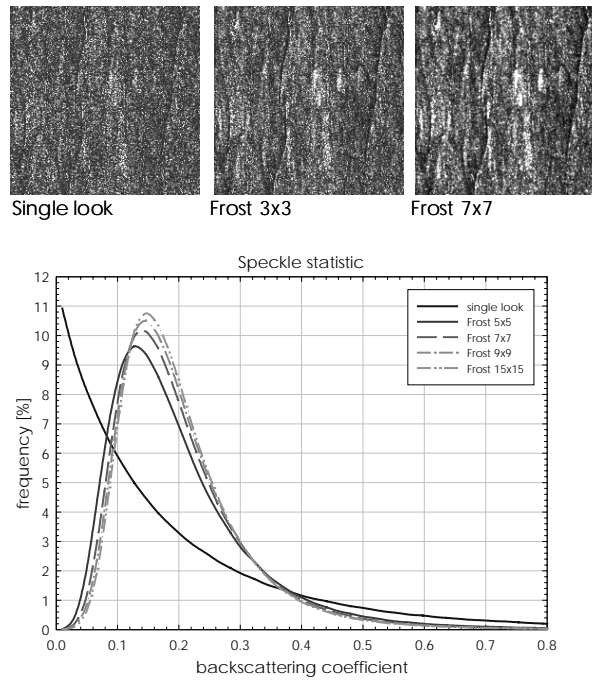
Figure 4.5: Image statistics for single look and speckle filtered images: image examples (above) and backscatter frequency distributions (below)

4.4 Precise terrain geocoding

Topography has a significant influence on the geometric and radiometric properties of SAR images. Standard geocoded image products refer to a flat Earth ellipsoid and do not take into account local terrain undulations (ROSICH and MEADOWS, 2004; SMITH, 2003). Relative calibration accuracy on a flat Earth is below 1.0 dB (LAUR *et al.* 1993; SRIVASTAVA *et al.*, 1999; MEADOWS and ROSICH, 2003). In rugged terrain, the changing local imaging geometry can result in backscatter changes up to ± 5 dB (BEAUDOIN *et al.*, 1995). This is unacceptable for quantitative analysis of the image data, which is one of the main objectives of this work.

A sophisticated geocoding approach is therefore described in the following, to derive relief independent backscatter values in roughed terrain. The algorithm was developed by MAUSER (see RIEGLER and MAUSER, 1998) for ERS data and was extended within this work to be applicable for multiple sensors and image data products, including already geocoded products as e.g. wide swath images (LÖW and MAUSER, 2003). The main objective is to eliminate relief induced geometric and radiometric distortions, which have to be compensated to obtain images, only containing information about the surface backscattering process. The presented rigorous approach is applicable to single-look-complex, as well as to geocoded image products. The method accounts for energy-preservation and compensates the disturbing effects.

4.4.1 Geocoding procedure

For precise terrain geocoding, a high resolution digital elevation model (DEM) and additional information about the orbit of the sensor platform are needed. The orbit informations are normally provided in terms of orbit state vectors in the image product header or are available as separate orbit files. The orbit state vectors can be provided in a Cartesian Inertial (ECI) or Earth Centred Fixed rotating (ECF) reference frame, with respect to a geodetic datum (MONTENBRUCK and GILL, 2000; SEEBER, 1989). The DEM is given in a defined projection with corresponding ellipsoid and local geodetic datum. To relate each image pixel to the DEM, the imaging geometry has to be reconstructed, using the Range-Doppler equation, given by (2.1) and (2.2). Therefore a common reference system is required and geodetic transformations have to be applied to the orbit vectors as well as to the DEM coordinates. The reference system used in this work is the commonly used WGS84 system (NIMA, 2000).

Generally there are two possibilities to geocode an image pixel, namely *forward* and *backward* geocoding (CURLANDER and MCDONOUGH, 1991). In a forward geocoding approach, the position of each image pixel on the Earth surface is calculated, using the Range-Doppler equation separately. This is usually realized by using the Newton iteration method (PRESS *et al.*, 1992, HOLECZ, 1993) which determines the location of each pixel from the sensor's perspective. The backward scheme is vice versa. Here, the image pixel with the nearest range-doppler coordinate is calculated for each DEM element. The main advantage is the significant reduction of necessary calculation steps. The range-doppler equation has to be solved only for the number of DEM elements and not for the whole amount of image pixels. For a standard image product of ENVISAT ASAR, this reduces the number of necessary iterations by a factor of approximately ten. The main processing steps consist of (Figure 4.6)

A.) transformation of coordinates to a common reference frame,

B.) performing adequate orbit integration

C.) iterative solution of the range Doppler equation to find appropriate image pixel and DEM pairs.

D.) mapping of the image pixels on the DEM; including calculation of local imaging geometry

E.) in cases of ground range products: reconstruction of the slant range ground range mapping procedure.
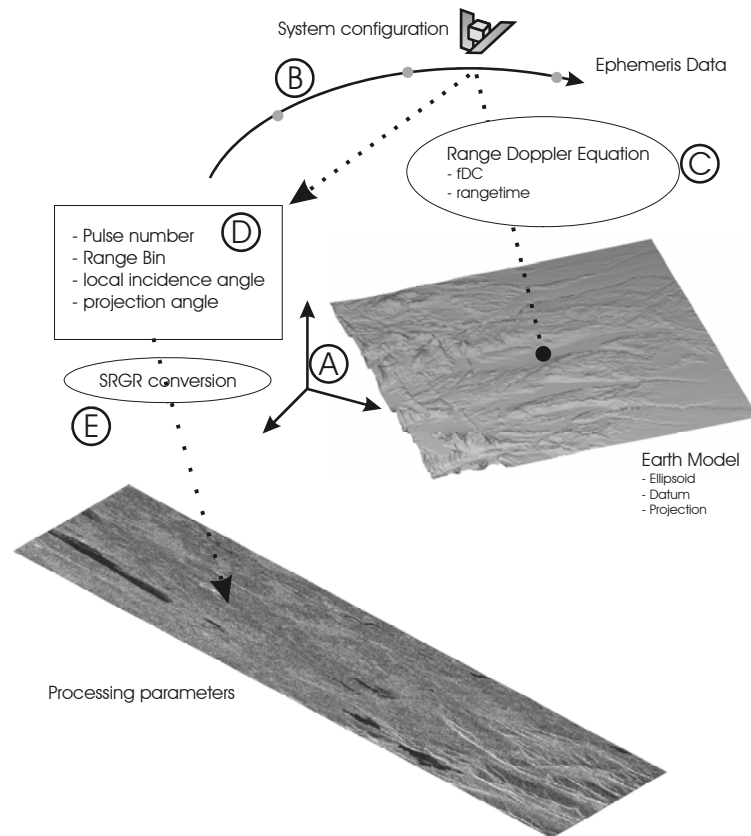
Figure 4.6: **Backward geocoding scheme**

4.4.1.1 Coordinate transformations

Both, DEM and sensor positions, have to be transformed to the WGS84 system, by reprojecting the data. The main transformation steps, consist of:

1. Transformation of the map coordinates (E, N) to geographic coordinates (λ, φ)
   BENZING and KIMMIG (1989)
   BUGAYEVSKIY and SNYDER (1995)

2. Transformation of geographic coordinates (λ, φ) and height h to local Cartesian coordinates
   FREI, GRAF and MEIER (1993)

3. Datum Shift correction to WGS84 datum for the DEM as well as for the orbit state vectors.
   NIMA (2000)
   SCHWÄBISCH (1995)

The DEM and sensor coordinates are then given in a Cartesian Earth fixed coordinate system with a common geodetic datum. This enables the calculation of the look vector from the sensor to the target and the appropriate Doppler frequency shift.

4.4.1.2   Orbit Integration

The orbit state vectors, given in the image product header, are acquired at discrete time intervals. For the estimation of the position of each image pixel on the Earth surface, the exact sensor position and velocity vectors have to be known for each azimuth time t (*slowtime*). Therefore an orbit model being dependant on slowtime t has to be built up which integrates the sensors position and velocity vectors. The accuracy of the orbit measurements varies within a wide range, depending on the sensor type and the quality of the orbit type used (RUFENACHT, PROULX and CEFOLA, 1997; ESA, 2004). The positioning accuracy can vary between a few centimetres and several hundred meters. Lower order polynomials are often used to establish the orbit model. For small images, 3rd order polynomials were found to be accurate enough to describe the orbit (OLMSTED, 1993; RAGGAM *et al.*, 1993). For ENVISAT ASAR, this was also confirmed in this work.

A more sophisticated approach is the numerical integration of the differential equations for position and velocity by a 4-th order Runge-Kutta method (MONTENBRUCK and GILL, 2000; PRESS *et al.,* 1992). For each integration step, the acceleration due to the changing gravity field of the Earths geoid is taken into account, using the gravity force terms J_2, J_3 and J_4 (SEEBER, 1989). This makes it possible to predict the sensors orbit with an accuracy of a few meters. Especially for sensors which have a low state vector frequency, the Runge-Kutta integration leads to much better results than simpler approaches. The algorithm was implemented in the geocoding procedure and can be used in addition to the simple polynomial interpolation method.

Orbit correction

The set up orbit model describes the form of the orbit. Nevertheless, timing errors can result in significant positioning errors in along and across track direction. The orbit can be adjusted using ground control points (GCP) (e.g. RAGGAM, STROBL and HUMMELBRUNNER, 1993; SMITH, 2003). The coordinates of a GCP are transformed to image space, where they are compared to the position of the respective image coordinates. A shift in terms of rows and columns can be transformed to time differences in slow- and fasttime for along and across track direction respectively, as shown in Figure 4.7. If the orbit is integrated accurately and the coordinate transformations are performed strictly, one GCP is enough to correct the orbit. It can be either chosen by user interaction or by automatic image coregistration techniques using a reference image.

The estimated correction terms Δr and Δt, expressed in fast- and slowtime, can be used to correct the orbit and calculate the new range and azimuth position of a pixel in terms of image coordinates.
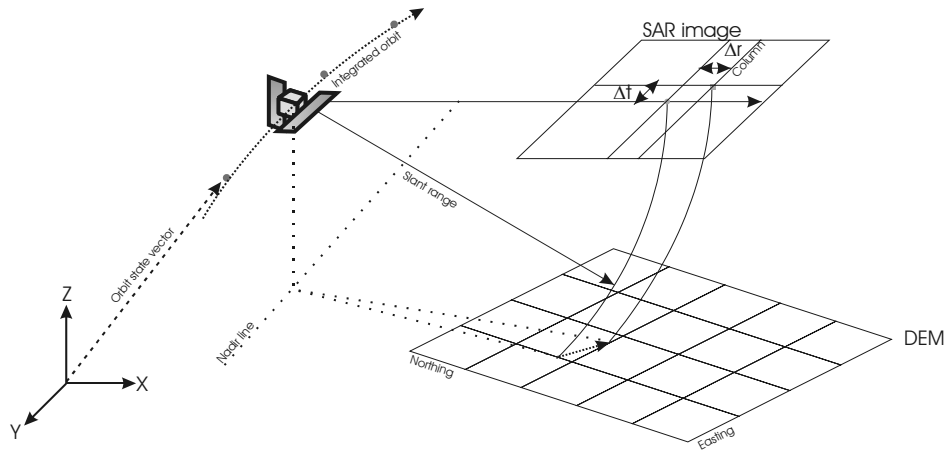
Figure 4.7: Orbit correction: From an observed shift of a GCP point in the geocoded image, two correction terms for azimuth (Δt) and range (Δr) can be calculated to adjust the orbit

4.4.1.3 Geometric rectification

To obtain the image coordinates for a given DEM element, the Range-Doppler equation given by (2.1) and (2.2), is solved iteratively. For images, processed to Zero-Doppler Shift, the zero Doppler position f_{DC} is found, when

$$f_{D(i)} \leq f_{DC} \leq f_{D(i+1)} \tag{4.7}$$

where $f_{D(i)}$ is the Doppler frequency at pulse i. The pulse satisfying (4.7) is the corresponding image line. The range resolution cell j is found, using the slant range distance R_s from (2.1) by

$$j = \frac{R_S - R_0}{\Delta R} \tag{4.8}$$

with the slant range distance to the first range pixel R_0 and the slant range pixel spacing ΔR.

Geocoded image products, as precision images or ScanSAR images, acquired by RADARSAT or ENVISAT ASAR are only available in ground range geometry. The geocoding was performed using an n-th order slant range ground range polynomial of the form

$$R_S = \sum_{i=0}^{n} c_i \cdot R_G \quad with \ R_G = j \cdot \Delta G \tag{4.9}$$

where R_G is the ground range distance, j is the image column and ΔG is the ground range pixel spacing (ESA, 2002; Shepard, 2000). With the knowledge of the polynomial coefficients c_i, provided in the image header, the image column in the ground range image can easily be found from the slant range distance R_S. Thus the correct grey values can be extracted from the image product.

4.4.1.4 Application and accuracies

Using the algorithm described above, the range distance and Zero Doppler position can be calculated for each DEM element using the backward geocoding approach. These are converted to image coordinates of the calibrated image. For ground range images, the corresponding image column is found by applying the slant-range-ground-range polynomial given by (4.9). The currently supported sensors, image product types and geodetic reference systems are given in Table 4.2 and Table 4.3.

Table 4.2: SAR sensors and image products, supported by the geocoding software (✓✓=enhancements within this work)

SENSOR	IMAGE PRODUCT	SUPPORTED
ERS	SLC	✓
	PRI	
Radarsat	ScanSAR Narrow	✓✓
	ScanSAR Wide	✓✓
	Standard Beam Path Image	✓✓
ENVISAT	ImageMode	✓✓
	WideSwathMode	✓✓
	Alternate Polarisation	✓✓

Table 4.3: Ellipsoid and Geodetic datum combinations supported by the Geocoding software (✓✓= enhancements within this work)

	ELLIPSOID		
DATUM	HAYFORD INTERNATIONAL	BESSEL	WGS 84
ED 50	✓		
DHDN (Potsdam)		✓✓	
WGS 84			✓
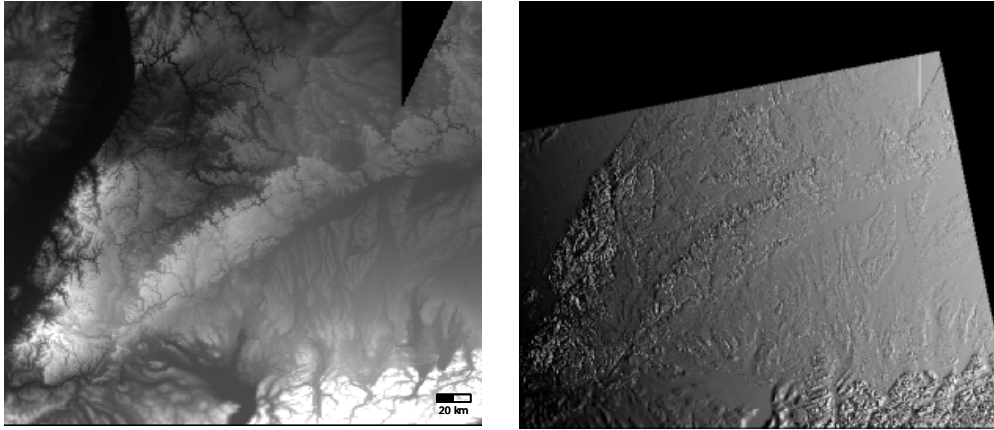
Figure 4.8: DEM (left) and calculated local incidence angle (right) for southern Germany. The imaging geometry is calculated for an ENVISAT ASAR WSM image with ascending orbit

Additional information, such as the local incidence angle or regions of layover and shadow can be calculated for each DEM cell. Figure 4.8 shows a DEM and a calculated local incidence angle map for southern Germany. On the left side is the upper Rhine valley with the Black Forest. The flat area in the lower mid image is Lake Constance.

The geometric accuracy of the geocoded data products are validated, using tiepoints or vectorized linear features as reference data. A vector dataset, digitised from topographic maps with an accuracy of approximately 20 m was available for the testsite of this study. Figure 4.9 shows an example of an image subset, geocoded to 30 m with overlaid vector data. It can be seen, that the image fits very well with the reference dataset.
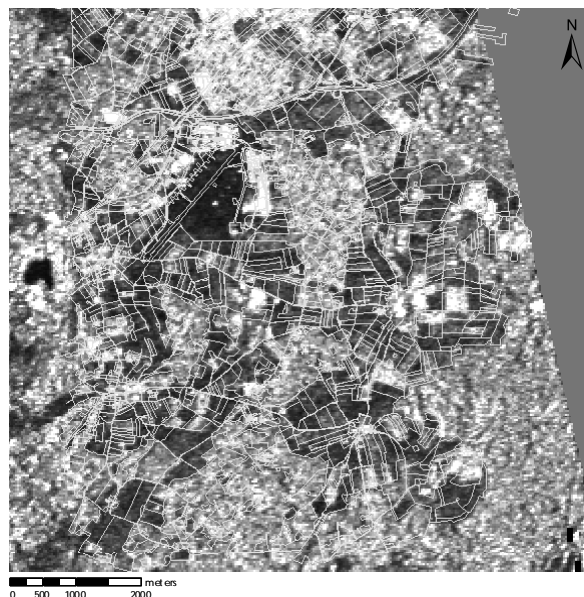
Figure 4.9: Geocoded SAR image (30 m) with overlaid field boundaries
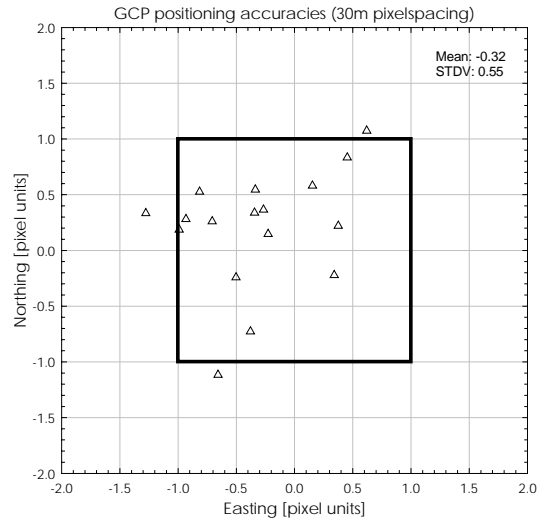
Figure 4.10: Residuals of GCPs after geocoding; ENVISAT ASAR image, 30 m

For quantitative geocoding accuracy estimation, GCPs were chosen to calculate the positioning residuals. Figure 4.10 shows a residuals plot of the GCP points. Detailed results are given in Appendix B. The obtained geometric accuracy is better than the resolution cell size of the DEM. With the help of more than one tiepoint for the orbit correction, these results could still be improved (HELLWICH and EBNER, 2000; SMITH, 2003).

4.4.2 Radiometric terrain correction

After an accurate description and reconstruction of the local SAR imaging geometry, these informations can be used for a precise radiometric correction of the SAR image.

Assuming a SAR system with a better spatial resolution than the DEM, the result of the backward geocoding approach is the Zero-Doppler position, centred within the DEM pixel. Adjacent image pixels also correspond to the same DEM element as shown in Figure 4.11. They are found by mapping the image pixels to the closest Zero-Doppler position. Care has to be taken, that each image pixel is assigned once to a DEM pixel only.

To calculate the radar brightness for each DEM element, the corresponding image pixels have to be integrated. The averaged radar brightness $\bar{\beta}$ is then given by

$$\bar{\beta} = \frac{1}{n} \iint_k \beta_k \qquad (4.10)$$

where k corresponds to an image position $(i, j) \in N$.
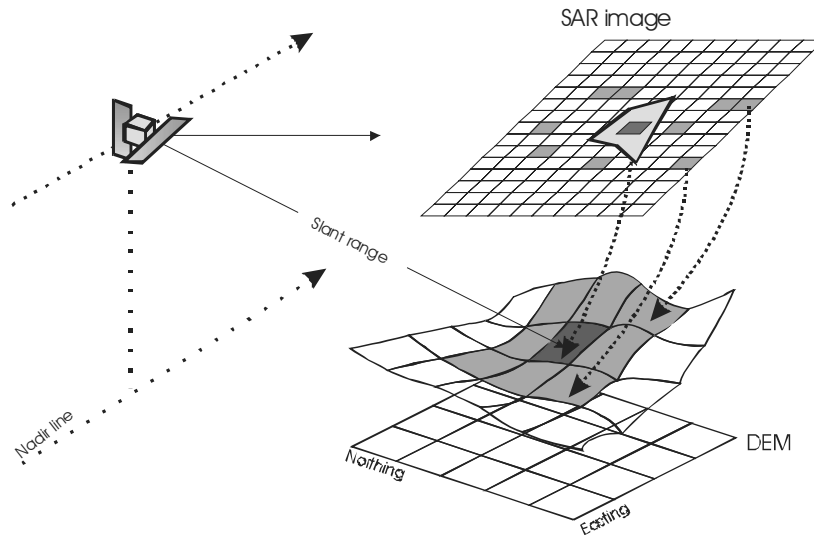
Figure 4.11: Radar brightness integration. Dark greyed pixels indicate calculated Zero-doppler positions for each DEM cell element, while light grey indicates all adjacent pixels corresponding to the same surface scattering area

All n image pixels share the same Zero-Doppler coordinate on the ground. This method guarantees that the integrated backscatter intensity, measured for each pulse, is preserved throughout the geocoding process. This is essential for the generation of geocoded products, which are comparable to the original SAR image and is the basic requirement for a successful terrain correction.

To compensate for the changing scattering area, caused by rugged terrain, the projection angle ψ, proposed by ULANDER (1996), is calculated from the local imaging geometry (Figure 4.12). It is more suitable for the correction of the scattering area than other approaches, especially for steeper incidence angles (DEDIEU et al., 2003). It is defined as the complementary angle to the smallest angle between the surface normal and the image plane and can be derived from the SAR systems look vector and local terrain slopes and aspects as

$$\cos(\Psi) = \sin(\theta)\cos(u) + \cos(\theta)\sin(u)\sin(v) \tag{4.11}$$

where θ is the local incidence angle, and u and v are the terrain slope and aspect, within the defined coordinate system.
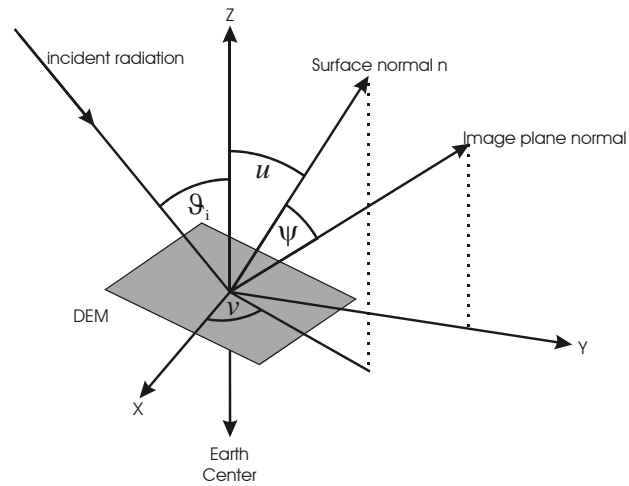
Figure 4.12: Definition of the projection angle ψ (after ULANDER, 1996)

The terrain corrected radar backscattering coefficient σ^0 is related to the radar brightness as (ULANDER, 1996)

$$\sigma^0 = \overline{\beta} \cos \psi \qquad\qquad (4.12)$$

Thus the output of the geocoding procedure is an backscatter image (σ^0) which contains no terrain induced geometric and radiometric distortions.

4.4.2.1 Radiometric Accuracy

The effect of the radiometric terrain correction on a SAR image is shown in Figure 4.13. An ENVISAT ASAR WSM image was geocoded with and without radiometric terrain correction. As can be seen clearly, the relief induced brightness changes are well corrected. The resulting image product has a "flat" appearance.
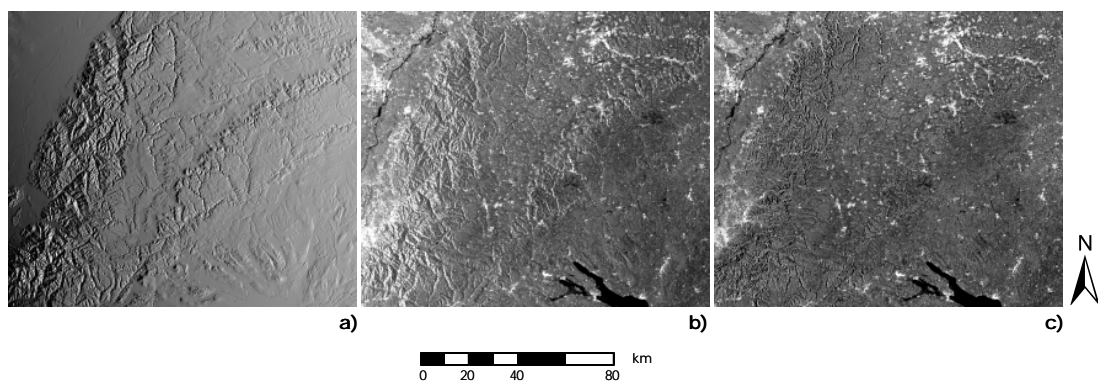
Figure 4.13: Image subsets of ENVISAT ASAR Wide Swath image showing the South-Western part of Germany. The mountainous areas are the Black Forest and Swabian Alb. (a) local incidence angle map, (b) uncorrected, (c) corrected image

To quantify the radiometric correction results, the mean backscattering coefficient for the corrected and uncorrected case is calculated for each local incidence angle. This is shown in Figure 4.14. The uncorrected data show a clear decrease of the average backscatter with increasing local incidence angle, whereas the corrected data remain almost constant over the incidence angle range, as is expected for a large number of image pixels. A comparison of the histograms in Figure 4.14b, calculated for the corrected and uncorrected images, shows the improvement obtained by the correction procedure. The Rayleigh distributed intensity values of the uncorrected image converges to a Gaussian distribution. The narrower histogram is an indicator for a better radiometric accuracy, defined as the separability of objects with different backscattering behaviours (HENDERSON and LEWIS, 1998; KLAUSING and HOLPP, 2000).
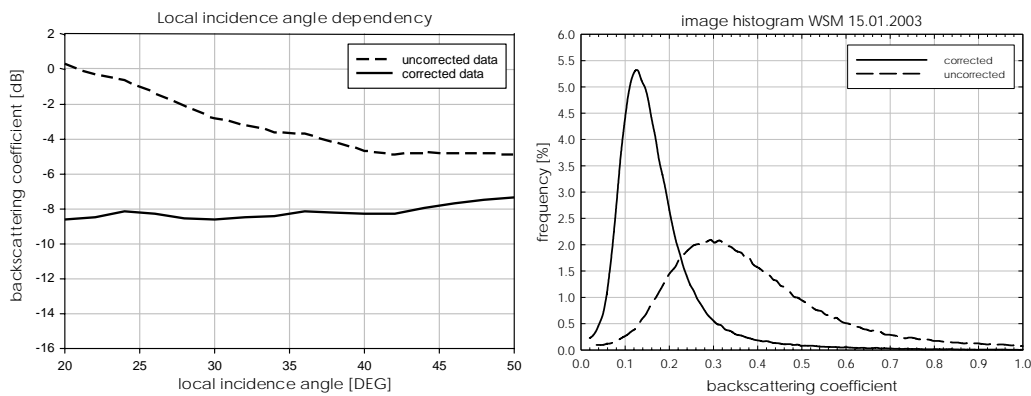
Figure 4.14: Local incidence angle statistics (left) and global image statistics (right) before and after terrain correction

4.5 ENVISAT ASAR datasets

The ENVISAT ASAR data, used within this work, were acquired in the year 2003. Primarily it was planned to use datasets from the year 2002 on. The delayed launch of ENVISAT and the unavailability of ENVISAT ASAR data during the commissioning phase was the reason, that the first dataset over the testsite was acquired in late autumn 2002 after the vegetation period. The image data for this work were provided by ESA within two principal investigation projects dealing with the derivation of biophysical parameters from ENVISAT ASAR data and their assimilation into physically based landsurface process models[1].

---

[1] ENVISAT principal investigation projects (PI: Prof. Mauser, University of Munich, Germany):
  #475: Improved surface soil moisture determination using ASAR dual-polarization data
  #477: Synergistic use of ENVISAT data to model land surface processes

To be comparable with field measurements, high resolution SAR images are needed. The alternating polarisation image products are best suited for the objectives of this work. They provide information at a spatial scale of 30 m, which guarantees, that most agricultural fields are covered by several image pixels. Additionally, multiple polarisation acquisitions are possible. An overview about the processed image datasets for the vegetation period 2003 is shown in Figure 4.15. Additional information about the *in situ* measured plant and soil parameters, which are introduced in the next chapter, is included in the diagram.
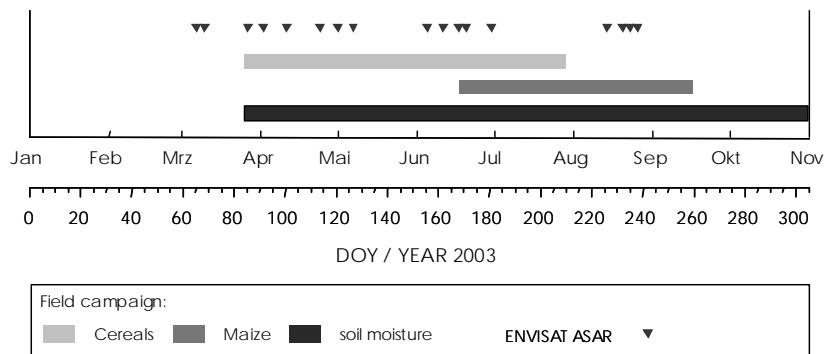
Figure 4.15: **ENVISAT ASAR data coverage during the vegetation period 2003**

The temporal coverage of the datasets is reasonable for this study. Two gaps, one in May and the other in July can be observed. No image data were acquired over the testsite during these periods. An example of a multitemporal and a dual-polarisation image dataset of the testsite, is shown in Figure 4.16. The high geometric quality of the multitemporal image datasets is a result of the rigorous geocoding procedure. The multitemporal dataset contains much information about the actual land use and land use dynamics of the area. Additional information about the different scattering behaviour in the various polarisation channels can also be observed. Examples of areas with a high copolarisation ratio (HH:VV), corresponding to the bright red areas in Figure 4.16b, are mainly cereals with vertical oriented stalks.

24.04.2003 / 01.05.2003 / 11.06.2003   VV / HH / HH:VV
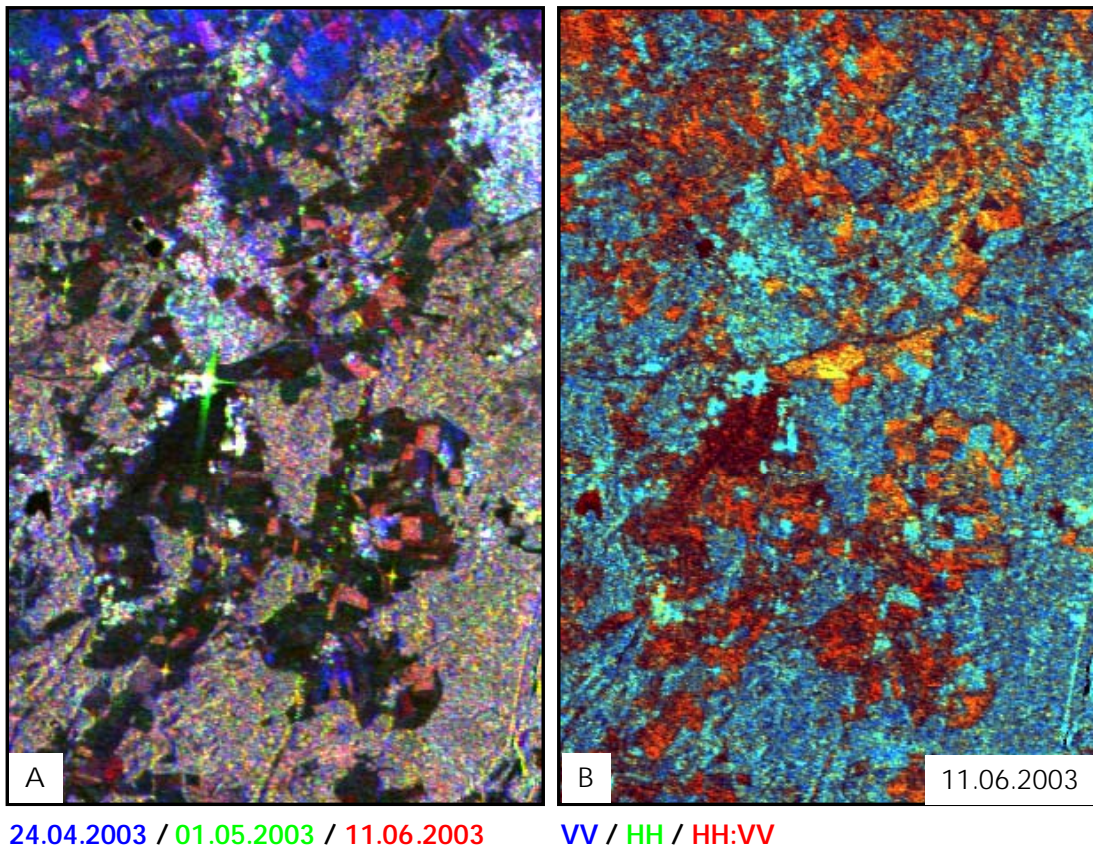
Figure 4.16:   Multitemporal HH polarised (left) and dual polarised (right) image dataset of the Gilching testsite (Alpine Foreland, Germany)

Chapter 5
Testsite and Field Measurements

Ground based measurements are essential for the calibration and validation of remote sensing data products. They are used to validate the accuracy of existing models and are essential for the adaptation or development of new models for new sensor systems.

Within the scope of this work, field measurements of land surface parameters play an essential role for the development of an inversion strategy for ENVISAT ASAR data. Therefore, intense field campaigns were carried out to collect the necessary ground truth data. In the following, the testsite, the investigated plant species and measured parameters are presented.

5.1 Testsite Gilching

The testsite is located in Southern Germany, 25 km southwest of the Bavarian Capital Munich, between the lakes "Ammersee" in the West and the "Starnberger See" in the East (Figure 5.1). It is a part of the alluvial plain of Munich, formed in the last ice-age, fringing to the young moraine region of the Isar-Loisach glacier (MEYNEN and SCHMITHÜSEN, 1953; MICHLER, 1994).

The southern and western boundaries are delineated by the hills of the young moraines. In the East, the boundary is given by remains of the older moraines of the Riß Diluvium. In the North the testsite is limited by the town of Gilching. Its location and boundaries are shown in Figure 5.1 and Table 5.1.

Table 5.1:   Corner coordinates of the testsite Gilching

CORNER	GEOGRAPHICAL		GAUSS KRÜGER (ZONE 4)	
	LONGITUDE [°]	LATITUDE [°]	EASTING [m]	NORTHING [m]
Upper left	11° 15′	48° 8′	[4]444000	5333000
Lower right	11° 20′	48° 2′	[4]450000	5322000
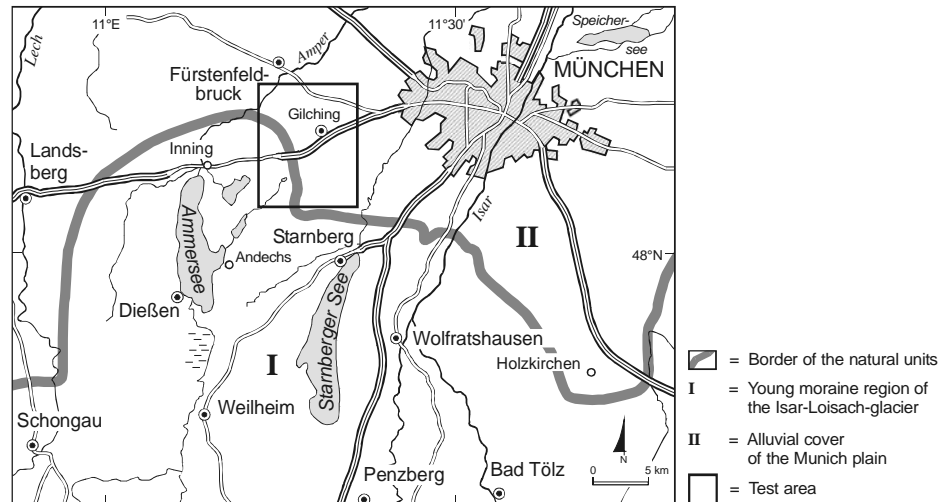
Figure 5.1: Location of the testsite and borders of natural landscape units

There are several reasons why this testsite was chosen for the field measurements:

- The area is characterized by a large variability of land use in similar climate condition. Different soil types occur within the testsite, which is important for the examination of soil texture effects on the backscattering coefficient.

- A practical reason is the accessibility of the testsite. It can be reached from Munich within half an hour, which makes ground measurements very flexible and cost effective.

- Based on the experience from former projects (OPPELT, 2002), it was possible to use the good relationships to the farmers to get the permission to investigate the test fields.

- An automatical agrarmeteorological weather station is situated nearby the investigated test fields. It provides hourly measurements of precipitation, temperature, air humidity, total radiation and soil temperature. This is a main advantage for the investigations, because changes in soil moisture can be directly related to measured precipitation with a minimum of spatial or temporal interpolation errors.

- The field campaign was embedded within a framework of different projects conducted by the University of Munich. These included hyperspectral remote sensing of agricultural areas (OPPELT and MAUSER, 2004) as well as the interdisciplinary modelling of the water cycle by the GLOWA-DANUBE framework (MAUSER and LUDWIG, 2002; LUDWIG *et al.*, 2003) and the use of remote sensing data in the InFerno$^+$ project (SCHULZ *et al.*, 2002). The testsite provided ideal prerequisites for the synergetic use of the sampled data for the various projects.

5.1.1 Characteristics

The testsite's landscape was formed by the pleistocene ice-ages. Being located at the boundary between the formerly glaciered regions of the young moraines and the adjacent alluvial plains, it can be divided in two parts which can easily be delineated regarding the topography.

The gravel alluvial plain of Munich covers the biggest part of the testsite. The relief energy is low and the plain rises from 530 m in the North to 630 m in the South. In the southern and eastern part, the moraines with height differences greater than 10 meters form the second part. The moraines result from the Würm and Riß diluvium. A glacier spillway, surrounded by the moraines, is located in the centre of the testsite (Figure 5.2).

The soil texture distribution shows a strong dependency on topography. Meanwhile the alluvial plain and the spillway are dominated by paddy field soils, the moraines are covered by silt and silty loam, sometimes influenced by damming wetness.

The main land uses within the area are forests, grassland, maize and cereals. Land cover mappings in 2003 (see 5.2.3) resulted in 26 % of forests, 19 % of grassland and 38 % of cropland. The distribution of the different crop types is dominated by winter cereals. Generally, the forests are mostly situated on the top and hillslopes of the moraines while the arable land is located on the soils of the alluvial plain with its high agricultural potential. Thus the fraction of arable land increases northwards.
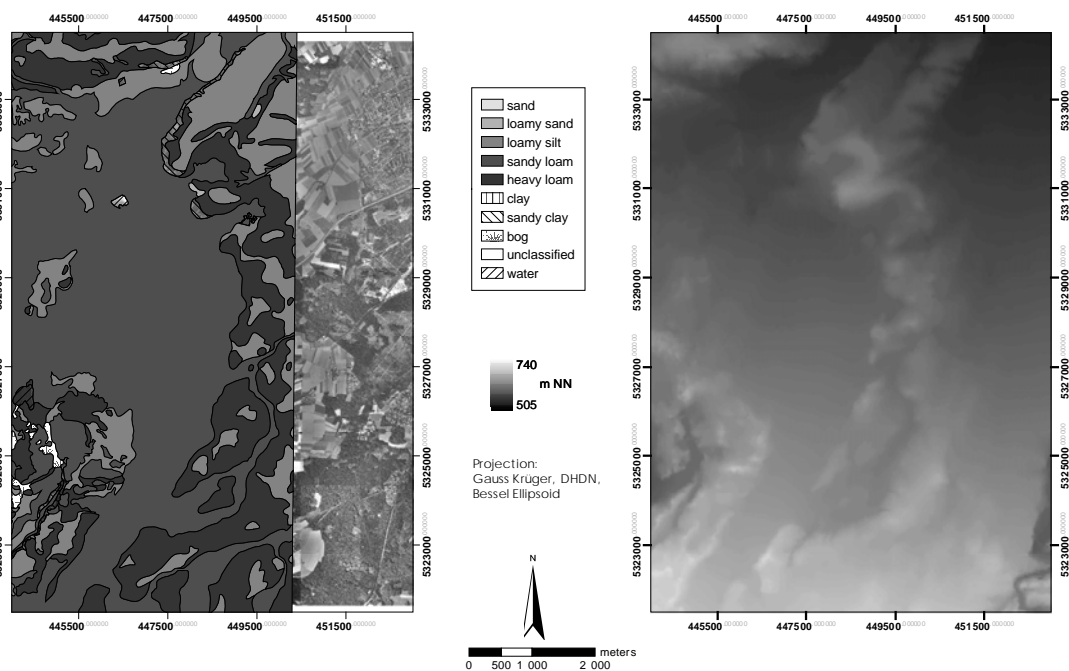
Figure 5.2: **Soil texture map (left) and digital elevation model (right) of the Gilching testsite**
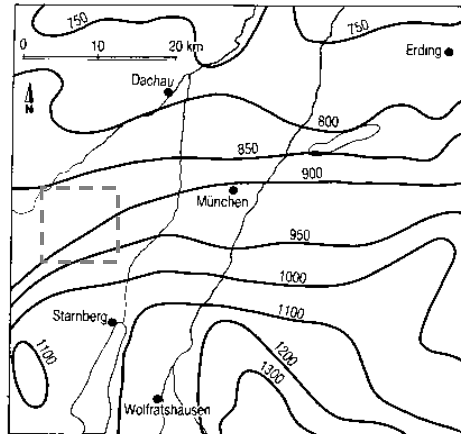
Figure 5.3: Distribution of mean annual precipitation (after Mɪᴄʜʟᴇʀ, 1994)

Climate conditions

Following the climate classification of Kᴏ̈ᴘᴘᴇɴ and Gᴇɪɢᴇʀ (1961), the testsite belongs to the cool and ever moist climate (*Cfb*) of the mid-latitudes. The mean annual temperature amounts to 7 – 8 °C (Mɪᴄʜʟᴇʀ, 1994; Bᴀʏꜰᴏʀᴋʟɪᴍ, 1996), with only slight spatial variations. The mean annual temperature amplitude is 14 – 16 K (Mɪᴄʜʟᴇʀ, 1994). The precipitation distribution is mainly influenced by the orographic convection at the Alps. As can be seen from Figure 5.3 the precipitation increases southwards. The annual precipitation varies between 900 and 1100 mm for the testsite. The maximum rainfall is reached during June and July.

5.1.2 Geographical information system

A geographical information system (GIS), with a spatial resolution of 30 m, was built up from the available datasets. The Universal Transversal Mercator projection (UTM zone 32), with the Hayford International ellipsoid and the European Datum 1950 served as cartographic reference system. The reason was that most data available for the testsite were given in that projection. Another reason was that the SAR geocoding software (see Chapter 4) at the beginning of this work only supported geographic or UTM coordinates. The GIS consists of

- DEM: 30 m resolution

- Soil texture map

- Land cover map 2003 (see 5.2.3)

- Additional meteorological information

  o DWD weather stations (3 times a day)

  o Agrometeorological stations (hourly)

- 17 ENVISAT ASAR alternating polarisation images

5.2 Ground measurements

Ground measurements were carried out in the years 2002 and 2003, with the objective to build up a reference database of plant and soil conditions during ENVISAT ASAR acquisitions. Different land use types were investigated. In 2002 three crop, three maize and two fields of grassland were investigated. In 2003, the campaign enclosed two crop, two maize and one rape field (see Table 5.2). An overview of the test fields is given in Figure 5.4.

The variable imaging modes of the ASAR sensor need a careful planning of image acquisition and field measurements. The satellite is programmed by the European Space Agency (ESA) on user request. This was done for both investigation periods. Due to the delayed launch of ENVISAT in March 2002 and to the following commissioning phase, ESA was not able to guarantee the acquisition of user requested datasets in 2002. In result, although several images were requested over the vegetation period 2002, the first image acquired from the Gilching testsite is from October 2002. Thus no image data is available for a comparison with field measurements in 2002.

Table 5.2:   Investigated test fields

YEAR	FIELD NUMBER	NAME	CROP TYPE	SIZE [ha]
2002	1/02	Stürzer wheat	winter wheat	5.2
2002	2/02	Stürzer grassland	grassland	4.8
2002	3/02	Oberbrunn grassland	ext. grassland	2.8
2002	4/02	Mitterwies wheat	winter wheat	12.4
2002	5/02	DLR maize	maize	1.0
2002	6/02	Wastian maize	maize	1.4
2002	7/02	DLR wheat	winter wheat	0.9
2002	8/02	St. Gilgen maize	maize	1.0
2003	1/03	Stürzer triticale	triticale	6.1
2003	2/03	Stürzer wheat	winter wheat	5.3
2003	3/03	Stürzer rape	rape	8.2
2003	4/03	Tiefenbrunn maize	maize	15.4
2003	5/03	Argelsried maize	maize	2.5
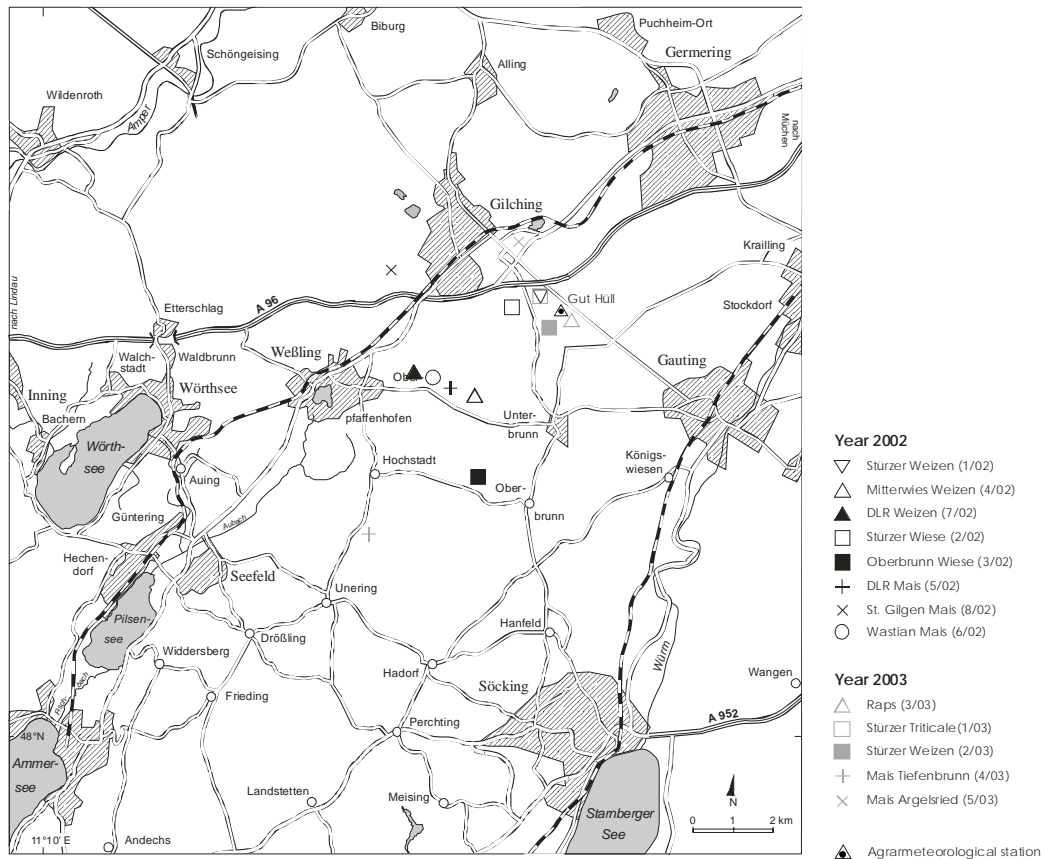
Figure 5.4: **Investigated test fields of the Gilching Testsite for 2002/2003 and location of the agrarmeteorological weather stations**

After the commissioning phase had finished in late autumn 2002, the image acquisitions of the testsite became more regular. In the year 2003 it was expected that the number of acquired images would increase. Therefore the field campaign was concentrated on a smaller number of test fields, while increasing the sampling frequency. At each confirmed acquisition by ESA, ground truth measurements were carried out. A summary of the field measurements and derived backscattering coefficients from the image data is given in Appendix E for each test field.

5.2.1 Investigated land use types

The investigations, made in this work, were focused on maize, wheat and triticale. They are the most important crop types in the study area. A brief summary of the needs and properties of the different crop types is given in the following.

5.2.1.1 Wheat (*Triticum aestivum*)

Wheat is the most important cultivated crop in the world. The cultivated area (~33 % of all agricultural area), as well as the production (~30 % of total production) is larger than for rice or maize (ZIMMERMANN, 1998) . The reason is the high yield potential and the ability to adapt to different climate conditions.

Wheat is an annual, mostly non-aristated spiky grass. The two main groups are winter and summer wheat. They differ in their frost resistance. Winter wheat is typically sowed between 1st and 20th of October in the most regions in the mid-latitudes, while summer wheat is sown as early as possible in spring (ZIMMERMANN, 1998).

The cultivated area is mainly limited by the local climate conditions. Best yields are obtained in regions with mild winters and warm summers. The mean average annual temperature should exceed 7.5 °C (STOLZ, 1998). The plant is nevertheless capable to suffer longer periods with temperatures below 0 °C. For the germination wheat needs a stimulus of daily temperatures below 5 °C for several weeks (ZIMMERMANN, 1998).

The water storage capacity of the soil is a very important factor for the yield income. Nutritious soils with a good drainage and a large available water storage capacity are more suitable. After DERMIRCAN (1995), 50-60 % of the used water comes from the upper 30 cm of the soil. Another 20-25 % are withdrawn from the next 30 cm. The storage capacity of the upper soil layer is therefore more important for wheat growth than regular precipitation. High precipitation rates limit the cultivation. The annual precipitation should not exceed 1000 mm. Especially during anthesis (mid of June – begin of July for the testsite), the precipitation should not exceed 35-40 mm, otherwise yield is reduced (STOLZ, 1998).

5.2.1.2   Triticale (*Triticosecale Wittmack*)

Triticale represents a new kind of cereal, which was developed in the course of the last hundred years. It is an hybrid of wheat (*Triticum*) as male plant and rye (*Secale*) as female. It combines the yield capacity of wheat with the frost resistance, undemanding nature and disease resistance of rye. Triticale mediates between the needs of rye and wheat. While rye is best suited for sandy soils, triticale yields better than wheat on soils with a medium water storage capacity. For soils with a high water storage capacity, wheat and triticale yields are comparable. Thus it is suitable for a wider range of climate and soil conditions. This explains why the cultivated area increases while that for other crops as wheat, rye or barley stagnates or decreases (DOLESCHEL, 1998). Triticale is mainly used as fodder corn. The typical sowing dates are between 25th of September and 10th of October.

5.2.1.3   Maize (*Zea mays*)

Concerning the cultivated area, maize is the third important crop in Germany. Worldwide it takes the second place behind wheat. Maize is a tropical plant, belonging to the family of grasses (*Graminaceae*). Due to its tropical origin, it is sensitive to low temperatures. Especially late frost in spring is unfavourable for its

development. During the vegetation period it needs mean daily temperatures above 13.5 °C (EDER, 1998; STOLZ, 1998). For germination the soil temperatures must not drop below 9-10 °C. While maize is undemanding concerning the amount of precipitation, it is sensitive to the precipitation distribution. During anthesis approximately 150 mm are needed (EDER, 1998).

Production is possible on all well drained soils. Damming wetness can be a limiting factor when the soil is too dense. Especially in cooler regions, maize grows better on soils with balanced temperature conditions. The major uptake of soil water originates from the uppermost 1 m which contains most of the plant roots.

In the region, maize can be differentiated between grain and silage maize. After EDER (1998), only 2 % of the production in Germany in 1994/96 were used for grain production. The rest was cultivated as silage maize for fodder production.

5.2.2 Field database

The objective of the field campaign was the sampling of ground data, suitable for the validation and calibration of remote sensing models. The sampling of the plant parameters was carried out weekly, while soil moisture measurements were performed during ENVISAT ASAR acquisitions. A time interval of a week is enough to guarantee that the plant biophysical parameters can be interpolated sufficiently between two sampling dates to ensure the reconstruction of the plant development for each sensor pass (DERMIRCAN, 1995; OPPELT, 2002). Due to the high variability of the soil moisture, the volumetric moisture content was measured for each ENVISAT ASAR acquisition.

Three sampling points were selected along a diagonal across each test field (Figure 5.5). This was done to reduce measurement errors and to get a measure of the variance within the field. The position of each sampling point was determined by GPS measurements.

Figure 5.5:   Sampling points within a test field

The plant and soil parameters, discussed below, were taken at each sampling point. The plant samples were either taken from 25 cm of one grain row or three plants for maize respectively. Once in the vegetation period, the row distance and the plants per meter were estimated to calculate the plant parameters for 1 m², which is the unit area. A direct sampling of one square meter was not possible, due to limiting facilities in the laboratory and unacceptable yield loss for the farmers. In the following the different plant and soil parameters are described.

5.2.2.1   Plant Parameters

The following plant parameters were measured regularly during the field campaign:

Plant height | The aboveground crop height was measured for the *shoot* and *leaf* separately. The shoot corresponds to the maximum height of the plant above the ground, whereas the leaf height is given by the height of the uppermost leaf.

Phenological status | The phenological development of the plants was recorded using the EUCARPIA (EC) code for cereals and maize (ZADOKS, CHANG and KONZAK, 1974). The different growth stages are represented by a two digit decimal number. The principal growth stages are characterized by the first and the continuous growth of the plants within these stages by the second digit. The digit code for the principal stages is given in Table 5.3.

Table 5.3:   EC principal growth stages

CODE	DESCRIPTION
0	Germination
1	Seeding growth
2	Tillering
3	Stem-elongation
4	Booting
5	Inflorescence emergence
6	Anthesis
7	Milk development
8	Dough develoment
9	Ripening

Biomass	The freshly harvested plants were separated in the laboratory into their different components (stalk, leaf, fruit). These were weighted on a dial balance and then dried in desiccators at 105 °C for 20 hours. The dry probes were weighted again.
	Thus, the wet and dry biomass were measured for each component. The biomass per m² was then calculated using the known row distance and sampling length or the number of plants per meter for maize respectively.
LAI	The leaf area index (LAI) was measured in a non destructive way using the LI-COR LAI2000 sensor (LiCor, 1991; Welles and Norman, 1991). Using the gap fraction analysis, the attenuation of the sunlight by a vegetation canopy can be estimated and related to the LAI. Systematic analyses of destructive LAI measurements and LI-COR LAI2000 results have shown good agreement and hence allow for fast and non destructive measurements in equivalent quality (Holzhauser, 2002).
Photographs	Photographs were taken for each stand, to record the current phenological development and stand conditions. Especially at the beginning of the vegetation period the photographs contain valuable information about the areal fraction covered by the plant. A general overview picture and detailed photographs were taken from each stand to gather information about the internal structure.

5.2.2.2 Soil moisture

The volumetric soil moisture was measured, using the time-domain-reflectrometry technique (TDR) which has developed into a reliable method for soil water content determination (Brandelik and Hübner, 1996; Mojid, Wyseure and Rose, 1997; Jones, Wraight and Or, 2002). It is based on the measurement of the travel time of an electromagnetic pulse in the media, which is then related to its relative dielectric constant $\in_r$ by (Fundinger and Köhler, 1992)

$$c = \frac{c_0}{\sqrt{\in_r \mu}} \tag{5.1}$$

where c_0 is the speed of light in vacuum, c the speed of the electromagnetic pulse and µ the magnetic permeability. If the length of the probe and cables are known, the travel time can be used to invert $\in_r$.

The volumetric soil moisture m_v can then be calculated from $\in_r$ using the commonly used formula of TOPP, DAVIS and ANNAN (1980):

$$m_v = -0.053 + 0.29 \in_r -5.5 \cdot 10^{-4} \in_r^2 +4.3 \cdot 10^{-6} \in_r^3 \qquad (5.2)$$

The probe used in the field measurements was an IMKO-Trime system, which allows measurements with accuracies of 1-2 Vol.% (FUNDINGER and KÖHLER, 1992).

A major drawback is, that the measurement result is only representative for a very small soil volume (<dm³). This makes it sensitive to small-scale soil water content variations (e.g. macropores, air gaps due to TDR insertion) within this volume (FERRÉ, RUDOLPH and KACHANOSKI, 1996).

Thus, there is a scale gap, between the TDR measurements on the ground and the resolution cell size of a remote sensing system. Two dimensional measurement techniques as ground penetrating radar (GPR) are capable to solve this problem. A good overview and comparison of both techniques is given in HUISMAN et al. (2003) and HUISMAN (2002). Nevertheless, the GPR technique is not applicable on agricultural fields. Frequent measurements would lead to intolerable yield losses for the farmers. Therefore other strategies have to be applied. The experience has shown, that using multiple TDR sampling points within a field provides good results when comparing remote sensing data with in situ soil moisture measurements (ROMBACH and MAUSER, 1997; DUBOIS, VAN ZYL and ENGMAN, 1995; SCHNEIDER and OPPELT, 1998; MOEREMANS and DAUTREBANDE, 2000; LE HÉGARAT-MASCLE et al., 2002). Thus the TDR measurements are a practicable and cost effective measurement technique, applicable on agricultural fields.

The soil moisture was measured three times at each sampling point. The probe was plunged vertically into the soil bulk and horizontally in a depth of 2 cm. Hence, the moisture content within the possible range of the probe (~12 cm) can be estimated by the vertical and that within the penetration depth of the electromagnetic waves by the horizontal measurement. For each field a total of 18 (9 vertical, 9 horizontal) soil moisture values were collected at each date. To get an appropriate field average for the vertical and horizontal measurements, the median of each sampling point was calculated and the three median values were then averaged. This ensures, that extreme values don't effect the averaged soil moisture value.

5.2.3 Land cover mapping

The land cover of the whole test area was mapped on the field scale during the vegetation period. The mapping was done in June before harvesting, where the different land covers could be distinguished easily. A complete list of differentiated land cover classes is given in Appendix C. The resulting land cover map and the fractions of the various land covers are shown in Figure 5.6.
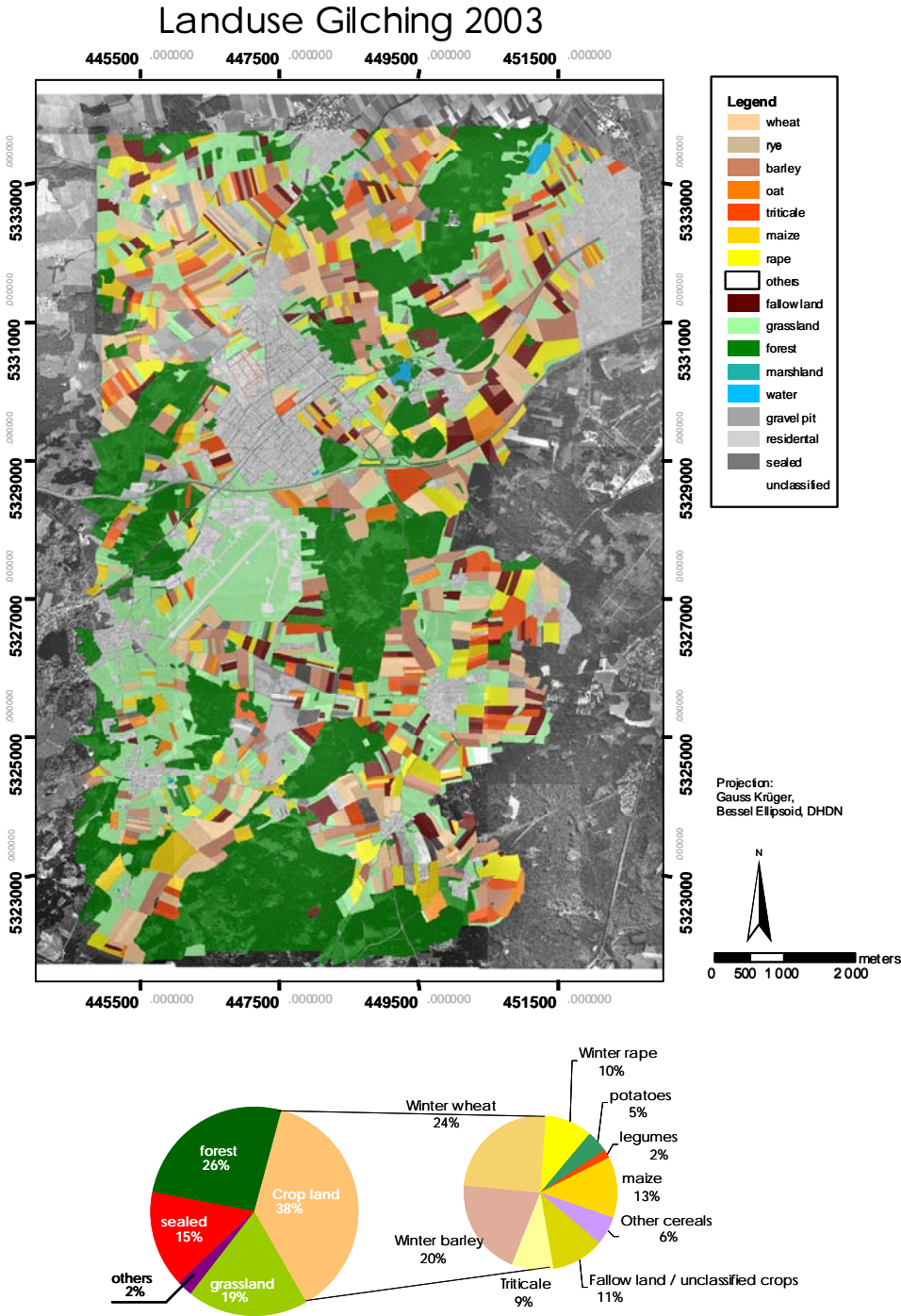
Figure 5.6:   Land cover map 2003 and statistics of the different land cover fractions
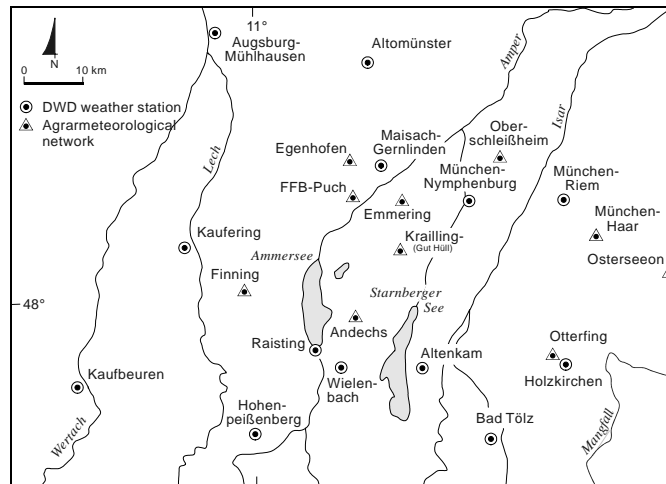
Figure 5.7: Location of the climate stations near the Gilching testsite

5.2.4 Additional information

5.2.4.1 Meteorological data

Meteorological datasets are mandatory input parameters for hydrological models. Combined with the physiogeographical conditions, they are responsible for the evapotranspiration process on the land surface and the growth of vegetation. Meteorological data are needed in the context of this work to estimate whether it was raining during or prior to an ENVISAT ASAR image acquisition and as input parameter for the land surface process model used in Chapter 8.

Two meteorological measurement networks exist in and around the test area. The first is the agrometeorological network, which hourly records various meteorological parameters. The data is available free of charge via the word wide web (STMLF, 2004). One station (Gut Huell) is situated nearby the test fields. The second network is operated by the German Weather Service (DWD). It provides different meteorological variables which are measured three times a day. The network of climate stations of both networks, surrounding the test area is shown in Figure 5.7. Table 5.4 lists the meteorological parameters of both networks as needed for this study.

Table 5.4: Meteorological variables measured by DWD and AGRO network

PARAMETER	STMLF	DWD	PROCESS MODEL INPUT VARIABLE
Precipitation	✓	✓	✓
Air temperature (2m)	✓	✓	✓
Air humidity		✓	✓
Wind speed		✓	✓
Cloud coverage		✓	✓
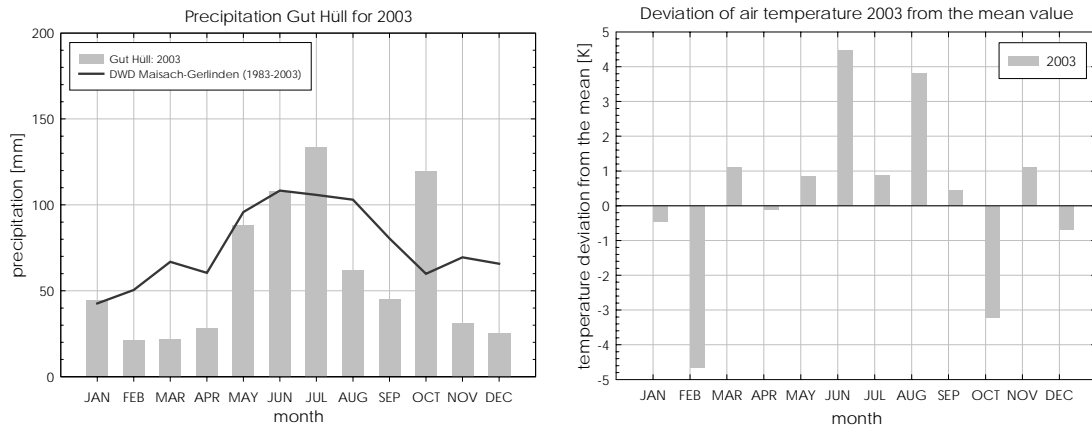
Figure 5.8: **Monthly precipitation distribution for year 2003 (Gut Huell) and a long term period (Maisach Gerlinden, 1983-2003)**

Climatic conditions during the investigation period

The year 2003 was the warmest year ever recorded in Germany since the start of systematic meteorological observations. The spring was dominated by stable high-pressure weather, resulting in below average precipitation. After a dry and warm first half, May ended with plentiful rainfall. Starting from June the course of the weather showed an extremely dry and hot summer (GIETL, 2004). A stable high-pressure belt lead to very warm and dry conditions with low precipitation and high evapotranspiration rates. The deviation of the monthly temperatures from the average value was several Kelvin from June to August (Figure 5.8). As can be seen in Figure 5.8, the precipitation in the testsite was even higher than the average value. This was caused by several isolated thunderstorms. Generally, the high temperatures and low rainfall persisted until the end of September, followed by plentiful rainfall in October. The low precipitation rates on the one side and the high evapotranspiration rates on the other side lead to a decrease of the available water surplus in the test area from 400-600 mm to 0-100 mm (DWD, 2004). The climatic conditions of the test area for a long term period (1983-2003), as well as for 2003 are summarized in Table 5.5.

Table 5.5: **Climatic conditions of the testsite for a long term period (1983-2003, Maisach-Gerlinden) and the investigation period (Gut Huell), (STMLF, 2004; DWD, 2004)**

PARAMETER	1983-2003	GUT HUELL 2003
Precipitation [mm]	910	728
Month of precipitation minimum	JAN	FEB
Month of precipitation maximum	JUN / JUL	JUN
Mean temperature [°C]	8.0	8.8

Chapter 6
Bare soil backscatter modelling

As discussed in Chapter 3, the Integral Equation Model (IEM), proposed by FUNG, LI and CHEN (1992) is one of the most common theoretical models for predicting the backscattering coefficient of rough surfaces. Contrary to other surface models it is applicable to a wide range of roughness scales. Within this work it is used to parameterise bare soil backscattering.

After a brief description of the IEM and its sensitivity to surface parameters, the theoretical model results are compared with ENVISAT ASAR observations. It is shown, that realistic backscattering values can only be obtained through an empirical model calibration. To overcome this drawback, a simplified bare soil model is derived from IEM simulations, which reduces the number of necessary input parameters. The model is used to derive surface roughness information from multitemporal ENVISAT ASAR data.

6.1 The Integral Equation Model (IEM)

The theoretical formulation and derivation of the IEM is described by FUNG, LI and CHEN (1992), as well as by FUNG (1994). The model description is summarized in the following, in the way it was implemented for the simulations within this work.

6.1.1 Model description

The single scattering term of the IEM is given for a polarisation combination p, q by (FUNG, 1994)

$$\sigma_{pq}^0 = \frac{k^2}{2} e^{-2s^2 k_z^2} \sum_{n=1}^{\infty} s^{2n} \left| I_{pq}^n \right|^2 \frac{W^n(-2k_x, 0)}{n!} \tag{6.1}$$

where

$$I_{pq}^n = (2k_z)^n f_{pq} e^{-2s^2 k_z^2} + \frac{k_z^n \left[F_{pq}(-k_x, 0) + F_{pq}(k_x, 0) \right]}{2} \tag{6.2}$$

with k: wavenumber $\qquad k = 2\pi/\lambda, \cong 1.1\,cm^{-1}$ for C-Band

s: rms height [cm]

θ: local incidence angle

$$k_z = k\cos(\theta_i)$$

$$k_x = k\sin(\theta_i)$$

$W^n(\ldots)$ is the Fourier transform of the *n*-th power of the surface autocorrelation function $\rho(x,l)$. It is defined by

$$W^n = \int \rho^n(x,l)\,e^{-i\omega x}\,dx \qquad (6.3)$$

For efficient computing it is necessary to minimize the number of iterations n. FUNG (1994) gives a formula for the calculation of the number of necessary iteration steps n_{max}. For $n > n_{max}$ the backscattering coefficient saturates. The number of necessary iterations varies between 2 and 50, depending on the soil roughness (FUNG, 1994).

The Kirchhoff field coefficients f_{pq} and the sum of the complementary field coefficients F_{pq} are given for the like polarised case as (FUNG, 1994)

$$f_{hh} = \frac{-2R_h}{\cos(\theta)} \qquad (6.4)$$

$$f_{vv} = \frac{2R_v}{\cos(\theta)} \qquad (6.5)$$

$$F_{hh}(-k_x,0) + F_{hh}(k_x,0) = -\frac{2\sin^2\theta(1+R_h)^2}{\cos(\theta)} \cdot \left[\left(1 - \frac{1}{\mu_r}\right) + \frac{\mu_r \in_r -\sin^2\theta - \mu_r \cos^2\theta}{\mu_r^2 \cos^2\theta} \right] \qquad (6.6)$$

$$F_{vv}(-k_x,0) + F_{vv}(k_x,0) = -\frac{2\sin^2\theta(1+R_v)^2}{\cos(\theta)} \cdot \left[\left(1 - \frac{1}{\varepsilon_r}\right) + \frac{\mu_r \in_r -\sin^2\theta - \in_r \cos^2\theta}{\in_r^2 \cos^2\theta} \right] \qquad (6.7)$$

The Fresnel power reflection coefficients R_h and R_v are given by

$$R_h = \frac{\mu_r \cos(\theta) - \sqrt{\mu_r \in_r -\sin^2\theta}}{\mu_r \cos(\theta) + \sqrt{\mu_r \in_r -\sin^2\theta}} \qquad (6.8)$$

$$R_v = \frac{\in_r \cos(\theta) - \sqrt{\mu_r \in_r -\sin^2\theta}}{\in_r \cos(\theta) + \sqrt{\mu_r \in_r -\sin^2\theta}} \qquad (6.9)$$

where $\in_r$ is the relative dielectric constant and μ_r the magnetic permeability (μ_r = const = 1.0 for most natural medias). Thus the surface is characterized by its roughness components rms height s and autocorrelation length l and the shape of the autocorrelation function (ACF), as well as its dielectrical properties given by $\in_r$.

6.1.2 Roughness parameterisation

As shown by FUNG (1994), the shape of the applied ACF strongly influences the model results. Standard models for the ACF, used for the description of natural surfaces, have a gaussian, exponential or modified exponential form (FUNG, 1994; DAVIDSON *et al.* 2000; WEIMANN, 1996; ULABY *et al.*, 1982).

None of these theoretical models are capable to sufficiently describe the complex roughness statistics of natural surfaces. It implies that the surface can be characterized for a unique spatial scale whose vertical and horizontal properties are represented by the rms height and autocorrelation length. A main problem is the inaccurate estimate of the autocorrelation length in field measurements (see 3.2.1). Because it is not a direct measurable parameter as the rms height, it has to be calculated from the roughness profiles (e.g. DAVIDSON *et al.*, 2000; OH and KAY, 1998; BAGHDADI *et al.*, 2002).

Despite the problems of an accurate statistical description of natural surfaces, empirical observations have shown, that best backscatter simulation results are achieved, using an exponential ACF (OH and KAY, 1998; DAVIDSON *et al.*, 2000; BAGHDADI *et al.*, 2002). For that reason, the exponential ACF is used for the further investigations.

Figure 6.1 shows experimentally measured ACFs and theoretical gaussian and exponential ACFs. The experimental ACFs were derived using a laser profiler system. The shown ACFs are based on 25 individual 1 m profiles which were averaged after calculating the individual autocorrelation function. It can be seen clearly, that the exponential ACF fits best to the experimental dataset.
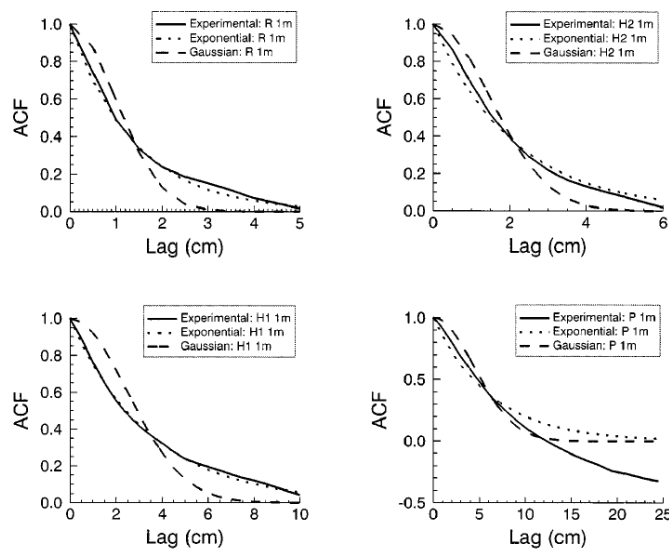
Figure 6.1: Fit between experimental and theoretical autocorrelation functions for different surface roughness (DAVIDSON *et al.*, 2000)

Figure 6.2 shows IEM simulation results assuming a gaussian and an exponential autocorrelation function. The differences can amount up to several tens of decibels. It becomes clear that the gaussian model is much more sensitive to incidence angle effects. Because of the high dynamic range of the backscattering coefficient, associated with the surface roughness, it is desirable to accurately estimate the roughness terms, for modelling the SAR backscattering coefficient.
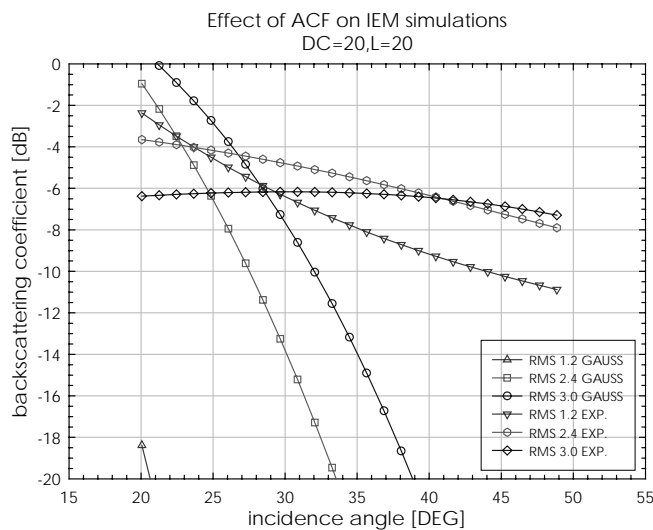
Figure 6.2: IEM simulations for differently shaped surface correlation functions: dielectric constant=20, autocorrelation length=20cm; GAUSS=gaussian, EXP=exponential autocorrelation function

6.1.3 Sensitivity of the IEM

The sensitivity of the IEM to different model input parameters is analysed in the following. These are the incidence angle, dielectric constant and the surface roughness.

6.1.3.1   Dielectric constant

Figure 6.3 shows the sensitivity of the backscattering coefficient for different rms heights s and a constant autocorrelation length l of 20 cm, with regard to the dielectric constant $\in_r$. A high sensitivity can be observed for low dielectric constants. For $\in_r$ greater than 20, which corresponds to a soil moisture content of approximately 40 Vol.%, the backscattering coefficient saturates. Further it can be seen, that the surface roughness has no significant influence on the sensitivity of the signal to $\in_r$.
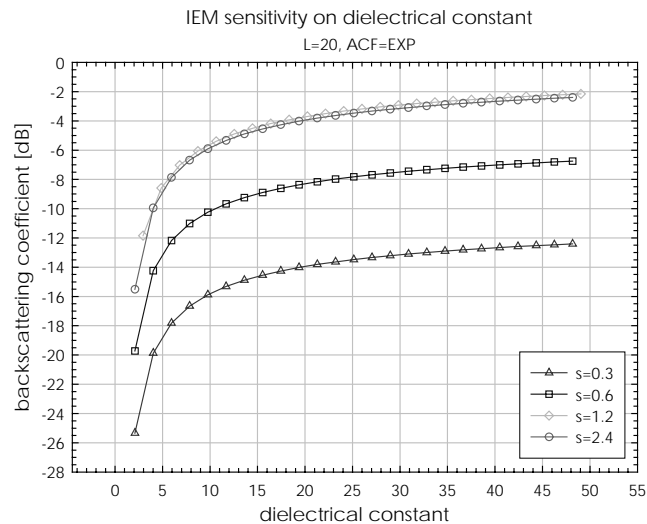
Figure 6.3:   IEM sensitivity on dielectric constant depending on rms height s; autocorrelation length: 20cm, exponential ACF

6.1.3.2   Surface roughness

The surface roughness has a strong influence on the IEM results. The incidence angle dependency of the backscattering coefficient is shown in Figure 6.4 for two different rms heights and diverse autocorrelation lengths. In the case of the smooth surface $(s = 0.65)$, the backscattering coefficient decreases with increasing incidence angle. A larger autocorrelation length results in a decrease of the backscattering coefficient.
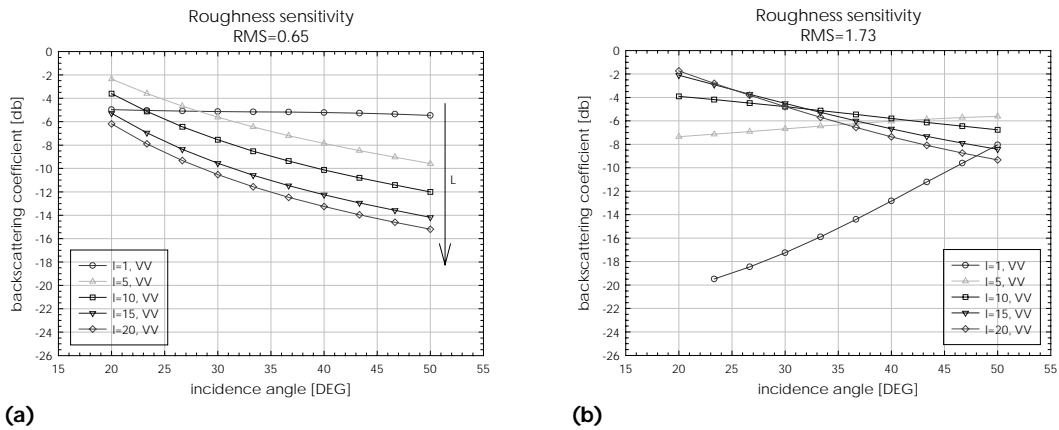
Figure 6.4: **Sensitivity of the IEM to surface roughness parameters for two rms heights and different autocorrelation lengths l; dielectric constant: 20, exponential autocorrelation function**

An increase of the vertical surface roughness ($s = 1.73$) decreases the angular sensitivity, as scattering towards the sensor increases (see also Figure 3.3). In the case of short autocorrelation lengths, the angular behaviour of the backscattering coefficient is even inverted to that of a smoother surface. The rougher surface is not satisfying the Rayleigh criteria, i.g. the surface is not smooth compared to the wavelength.

The surface roughness is the key parameter, having the strongest effect on the model results. The sensitivity analysis revealed that a reliable estimate of the autocorrelation length is critical, due to the high sensitivity of the model to that input parameter. Different combinations of rms height and autocorrelation length are capable to produce the same backscattering values, which is contradictory to a physically surface. To overcome this equifinality problem (BEVEN, 2001), it is desirable to find a physically based surface description, which is capable to predict a backscattering value as a function of surface properties in an unambiguous manner. This is discussed in the next section.

6.2 Empirical calibration of the IEM

Recent advances in using electromagnetic models for describing the surface scattering problem show that differences between modelled and measured backscattering values mainly result in an inaccurate surface roughness parameterisation of the model and not in a failure of the model itself (e.g. LOUIS *et al.*, 2003; LE HÉGARAT-MASCALE *et al.*, 2003; BAGHDADI *et al.*, 2002; ZRIBI and DECHAMBRE, 2002). The accurate estimation of the ACF is crucial in this context.

Experimental results, using different measurement techniques for the surface roughness, show clearly, that the estimated autocorrelation length depends strongly on the spatial scales which are considered in the ground measurements (DAVIDSON *et al.*, 2000; BAGHDADI *et al.*, 2000; MATTIA *et al.*, 2003). OH and KAY (1998) have shown in a theoretical study, that for short roughness profiles, the rms height can be estimated with an accuracy better than 15 %, meanwhile the error of the autocorrelation length exceeds 50 %.

Recently two approaches exist to overcome this drawback. Theoretical methodologies are dealing with a multiscale description of complex soil surfaces, decomposing them into higher and lower frequency terms (LOUIS *et al.*, 2003; CHANZY, MOLINEAUX and ZRIBI, 2003; LETOAN and DAVIDSON, 1998).

An empirical approach was proposed by BAGHDADI *et al.* (2002). Assuming that the autocorrelation length is the main source of modelling error, they propose an empirical calibration of the IEM. It is based on the idea, that an optimal autocorrelation length L_{opt} exists, which minimizes the difference between the simulated and measured backscattering coefficients. Based on ERS and RADARSAT datasets with different incidence angles, BAGHDADI *et al.* (2002) showed strong correlations between the rms height and L_{opt}, which are dependant on the incidence angle (Figure 6.5).
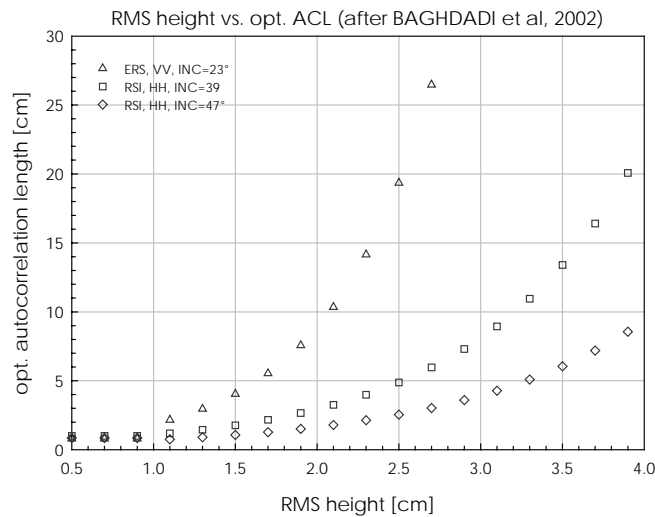
Figure 6.5: **Optimal autocorrelation length as a function of rms surface height, estimated by BAGHDADI *et al.* (2002) for the ERS and Radarsat (RSI) satellites and different incidence angles (INC)**

6.2.1 Application to ENVISAT ASAR observations

A similar approach is used for ENVISAT ASAR data to verify, whether the model proposed by BAGHDADI *et al.* (2002) is transferable on ASAR datasets.

6.2.1.1   Approach

Based on the available ground and SAR measurements the analysis using ENVISAT ASAR alternating polarisation data, is carried out as follows (Figure 6.6):

1. simulation of backscattering values by theoretical electromagnetic models

2. comparison of observed and simulated backscattering values

3. exclusion of simulations with a simulation error above a defined threshold

4. analysis of the remaining datasets
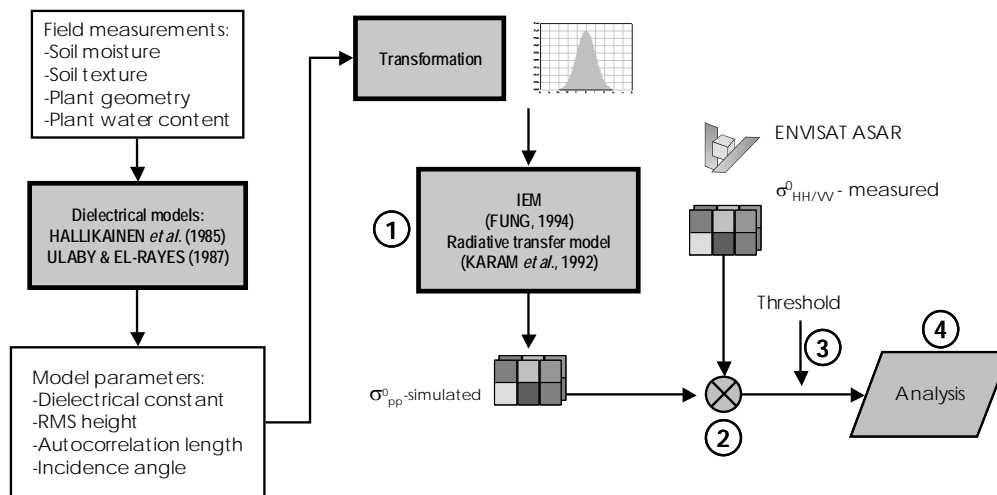
Figure 6.6:   **IEM empirical calibration procedure for ENVISAT alternating polarisation data based on theoretical backscatter simulations**

6.2.1.2   Simulation of theoretical backscattering values

The investigation is made for a winter wheat field (#2/03) for four dates in spring 2003, when the vegetation cover of the field was still sparse. Photographs of the field on DOY 101 and DOY 127 are shown in Figure 6.7. The sensor respective overflights used are listed in Table 6.1. It is emphasized that the images have significant different imaging geometries.
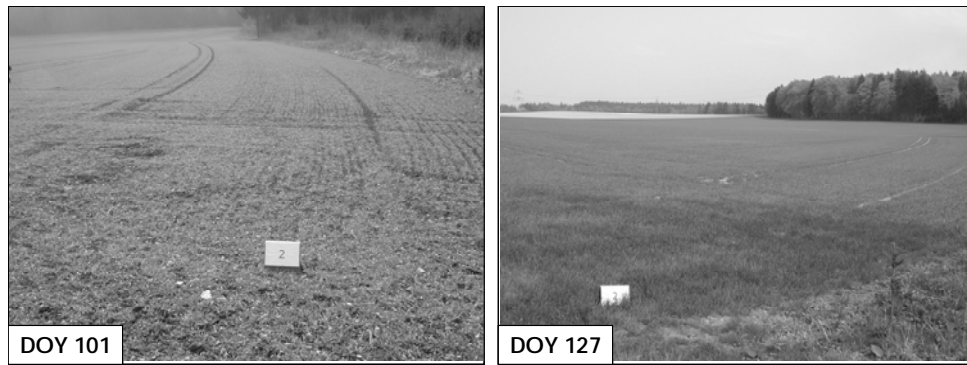
Figure 6.7: Photograph of Stürzer wheat (field #02) on DOY 101 and DOY 127

To take into account a possible vegetation effect on the backscattering coefficient, the IEM was coupled with the radiative transfer model of KARAM *et al.* (1992)[1], which can be used in this context because the leaves are rather small at this phenological stage and no vertical oriented stalk has to be taken into account.

The plant geometrical and dielectrical properties and the soil moisture values are derived directly from the field measurements. The dielectric constant of the plant is calculated using the Dual-Dispersion model from ULABY and EL-RAYES (1987). The soil dielectric constant is derived from the soil moisture measurements and soil texture information using the model of HALLIKAINEN *et al.* (1985).

It is assumed that the measured plant and soil parameters are a good approximation for the expected value. To care for the variability of these parameters within the SAR systems resolution cell, numerous parameterisations are realized, by adding noise to each input variable. The noise is added by means of a predefined probability density function (PDF). The PDFs used for the transformation of each parameter are also listed in Table 6.1.

The parameter space of the unknown surface roughness parameters s and l is sampled within a wide range of possible input values based on literature data (DAVIDSON *et al.*, 2000; MATTIA *et al.*, 2003; DAVIDSON *et al.*, 2003).

---

[1] The model was provided by Dr. Karam which is gratefully acknowledged

<p align="center">TABLE 6.1:   IEM SIMULATION DATASETS</p>

	PARAMETER	DOY 101	DOY 114	DOY 121	DOY 127	TRANS-FORM
SAR	θ	39.0	29.8	44.0	32.7	-
	σ^0_{VV}	-11.3	-8.0	-13.7	-14.2	-
	σ^0_{HH}	-11.8	-8.0	-12.8	-13.1	-
Soil	$\in_r$	14.0±4.0	12.2±2.5	13.3±4.0	6.7±1.5	G
	rms height [cm]	0.3 ... 5.0	0.3 ... 5.0	0.3 ... 5.0	0.3 ... 5.0	LU
	ACL [cm]	2.0 ... 20.0	2.0 ... 20.0	2.0 ... 20.0	2.0 ... 20.0	LU
plant	#-plants	233±10	233±10	233±10	233±10	G
	Height [cm]	7.3±1.0	12.4±1.0	15.5±1.0	31.3. ± 1.0	G
	#-leaf	4 ... 10	4 ... 10	4 ... 10	4 ... 10	LU
	Leaf Length [mm]	120±10	125±10	130±10	200±10	G
	Stalk Dia. [mm]	4.0±1.0	4.0±1.0	4.0±1.0	4.0±1.0	G
	$\in'^x_{Leaf}$	30.0±1.0	30.0±1.0	30.0±1.0	30.0±1.0	G
	$\in'_{Stalk}$	30.0±1.0	30.0±1.0	30.0±1.0	30.0±1.0	G

Transformations: G=Gaussian, LU=Log Uniform

The data range is given for each parameter. For gaussian distributed parameters, the values of the mean and standard deviation of the distribution are given

[x] The imaginary part of the DC can be numerically related to the real part. Therefore, only the real part is sufficient to parameterise the complex dielectric constant

6.2.1.3 Comparison of observed and simulated backscattering values

For each observation date, a number of 20.000 random model simulation parameter sets are generated. Using the coupled bare soil and radiative transfer (RT) model, the same number of simulated backscattering coefficients $\hat{\sigma}^0_{pp}$ are obtained, where the subscript *pp* stands for one of the two copolarisations. The simulation results are then compared to the observed backscattering values σ^0_{pp}.

The RMSE between observed and modelled SAR backscatter is computed for each date separately using the different polarisations by

$$RMSE = \sqrt{\frac{\left(\sigma^0_{vv} - \hat{\sigma}^0_{vv}\right)^2 + \left(\sigma^0_{hh} - \hat{\sigma}^0_{hh}\right)^2}{2}} \qquad (6.10)$$

A threshold is applied to the RMSE to exclude all data above the threshold from further investigations. The threshold is set to 1 dB to account for inaccuracies caused by calibration and model errors. Thus, the remaining datasets all result in nearly the same backscattering coefficient.

6.2.1.4 Analysis

Relationships between the rms height and autocorrelation length exist for these remaining datasets. An example for DOY 101 is shown in Figure 6.8. It can clearly be seen, that the samples form two populations, which correspond to very smooth (A) and rough surfaces (B).
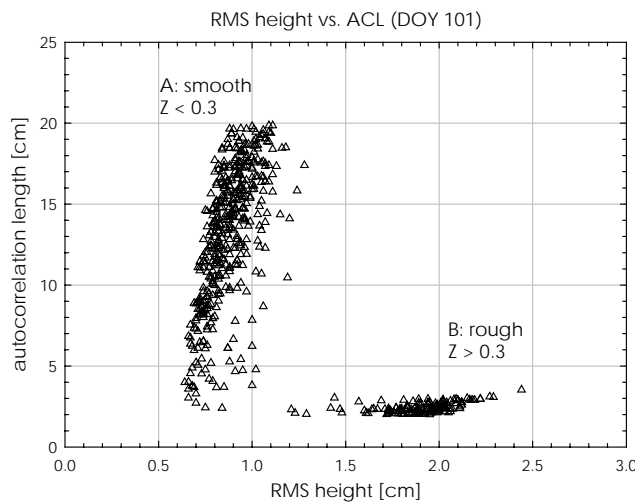
Figure 6.8: **Relationship between rms height s and optimal autocorrelation length l for backscattering values with RMSE < 1 dB (DOY 101)**

The autocorrelation length can be described as a function of the rms height, which is consistent with the observations of BAGHDADI *et al.* (2002). Thus there exists an optimal autocorrelation length L_{opt}, which results in reliable backscattering coefficients.

Roughness measurements of the test field showed, that the rms height is below 1 cm, which would correspond to the smooth surface samples (A). Nevertheless, the rougher samples (B), are within the same range as the data used by BAGHDADI *et al.* (2002). To be comparable with this the work, the following analysis is made for this roughness region. To separate both groups, a roughness parameter Z, is defined as (ZRIBI and DECHAMBRE, 2002)

$$z = \frac{s^2}{l} \tag{6.11}$$
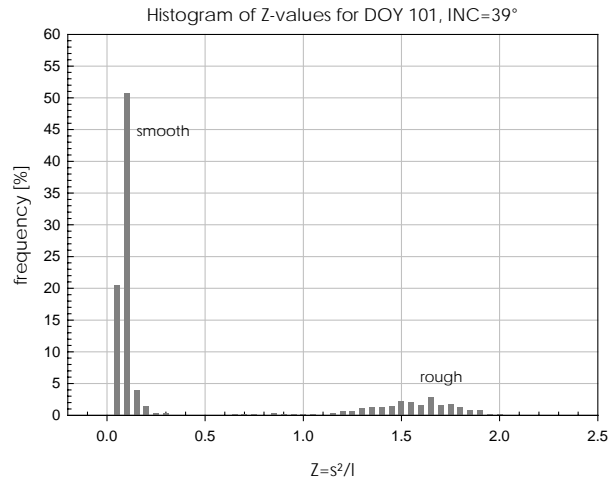
Figure 6.9: **Frequency distribution of Z-values for DOY 101**

The frequency distribution of the Z-value, shown in Figure 6.9, signifies that the smooth and rough surfaces can be separated easily using a threshold of Z=0.3.

At all observation dates, this bimodal behaviour is observed. Numerical solutions for smooth and rough surface characterizations are found by comparison with the measured backscattering coefficients and can be separated using the threshold for the Z-value. The Z-value frequency distributions of all observation dates are listed in Appendix D.

For each date, the relationship between s and l is estimated, by fitting an exponential least square line to the datasets with Z>0.3 by

$$l = y_0 + a\,e^{bs} \qquad\qquad (6.12)$$

Figure 6.10 shows the obtained relationships together with the estimates of BAGHDADI *et al.* (2002). It can be seen, that the results show a good concurrence with the ERS and RADARSAT observations. The relationships have a similar shape and show a dependency on the incidence angle. For low incidence angles, the sensitivity of the optimised autocorrelation length L_{opt} on rms height variations is high. With increasing incidence angle, this sensitivity decreases significantly. The estimated model parameters and diagrams for each date are given in Appendix D.
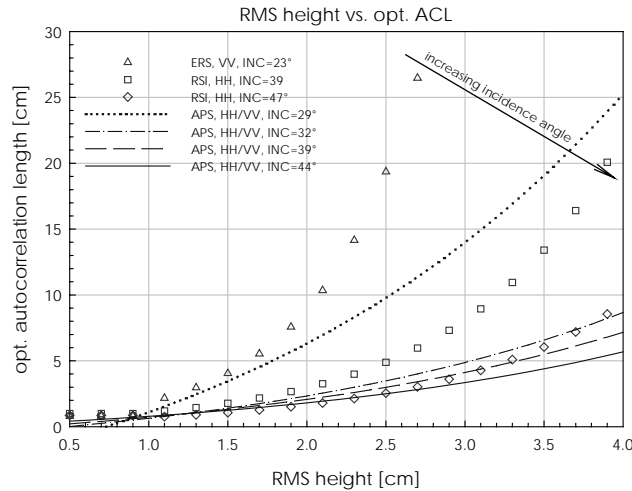
Figure 6.10: **rms height, L_{opt} relationships derived from** Baghdadi *et al.* **(2002), (*symbols*) and ENVISAT ASAR (APS) observations (*lines*)**

6.2.2 Results

Comparisons of simulated backscattering coefficients and SAR image datasets revealed strong relationships between the rms height and an optimised autocorrelation length. It denotes that the vertical and horizontal surface roughness components, affecting the backscattering coefficient, are strongly correlated for natural surfaces. This is contradictory to field measurements of surface roughness, where no, or only weak relationships were found between these two parameters. As already discussed, this can be caused by inadequate estimation of the autocorrelation length in the field measurements (see 3.2.1).

The estimated relationships are similar for different SAR systems and polarisations. An incidence angle dependency is observable. As a consequence, varying surface roughness parameterisations are required for different incidence angles, which is contradictory to a physically stationary surface. This leads to the central question whether there exists a "universal" surface roughness characterization with a physical meaning, capable to produce realistic backscattering values using the IEM. The model itself would then be reducible to a two parameter surface scattering model.

6.3 Derivation of a simplified bare soil model

A two parameter surface scattering model can be expressed by two functions. One is related to the surface roughness and the other to the dielectric properties. It can generally be formulated for the copolarised case as

$$\sigma_{pp}^{0} = A(\theta, sr) \cdot \Gamma_{0}^{\ b} \tag{6.13}$$

The surface roughness *sr* is represented by the function *A*, which depends on the incidence angle. The dielectric properties of the surface are represented by the surface reflectivity Γ_0 at normal incidence angle, which is scaled by an empirical parameter *b* (Hu *et al.*, 2003; RAMNATH *et al.*, 2003).

IEM simulation results over a wide parameter space are used in the following to calibrate a two parameter backscattering model, similar to (6.13) with a negligible error. It is then generalized to an incidence angle independent form to obtain a unique surface roughness parameterisation (Figure 6.11).

6.3.1 IEM simulation runs

The IEM simulations are conducted for HH and VV polarisation using the ENVISAT ASAR frequency of 5.33 GHz (C-band). The other simulation parameters are chosen to represent a realistic dynamic range. The parameter sets, used for the simulation runs are given in Table 6.2.
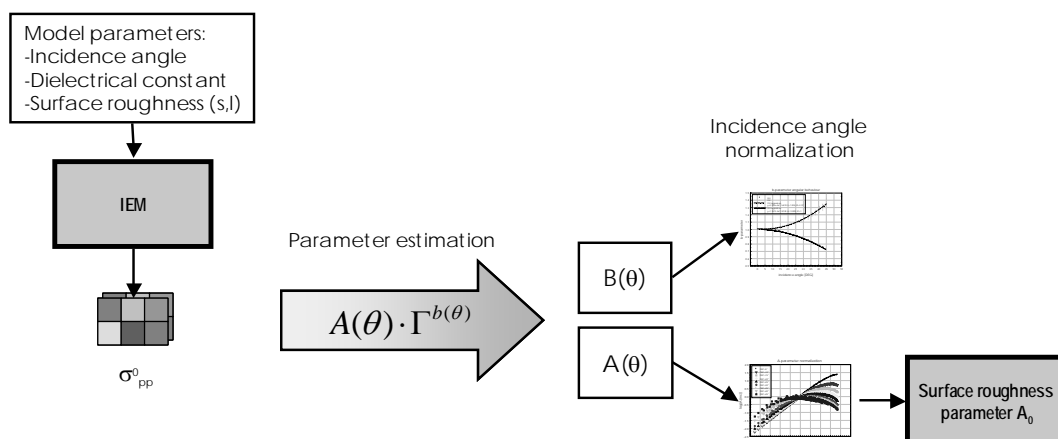
Figure 6.11: Derivation of a simplified bare soil backscattering model: Based on a wide parameter space, theoretical IEM simulations are reduced to a two parameter backscattering model, resulting in an incidence angle independent model parameterisation

<div align="center">

Table 6.2:   IEM simulation parameters

PARAMETER		UNIT	START	STOP	#-INTERVALS
Incidence angle:	θ	DEG	5.0	45.0	20
Frequency:	f	GHz	5.33	5.33	-
RMS height	s	cm	0.5	5.0	20
Autocorrelation length	l	cm	0.5	20.0	20
Dielectric constant	$\in_r$	-	5.0	50.0	20

</div>

A database of all possible parameter combinations is created, resulting in a total number of 160.000 combinations. For each parameter set, the backscattering coefficients σ_{pp}^0 are modelled using the IEM. Results, based on parameter values outside the validity range of the IEM, are not taken into account. In addition, the Fresnel reflectivities in nadir Γ_0 are calculated as (ULABY *et al.*, 1982; FUNG, 1994)

$$\Gamma_0 = \frac{1 - \sqrt{\in_r}}{1 + \sqrt{\in_r}} \qquad (6.14)$$

After a simple transformation, (6.13) can be linearized as

$$\sigma_{pp}^0(dB) = 10\log_{10}(A) + 10b\log_{10}(\Gamma_0) \qquad (6.15)$$

The empirical parameters $A(\theta,s,l)$ and $b(\theta)$ are determined using a simple linear regression approach. For each combination of roughness parameters and incidence angle, the A and B parameters are estimated. The backscattering coefficient is then recalculated, using the simplified scattering model (SSM), given by (6.13), which is parameterised with the obtained A and B values, and then compared with the results, achieved directly from the IEM simulations. Figure 6.12 shows the frequency distributions of the remaining modelling errors. The SSM results are nearly identical to the IEM simulations. The remaining error is negligible compared to the typical SAR calibration errors of approximately 0.5 dB.
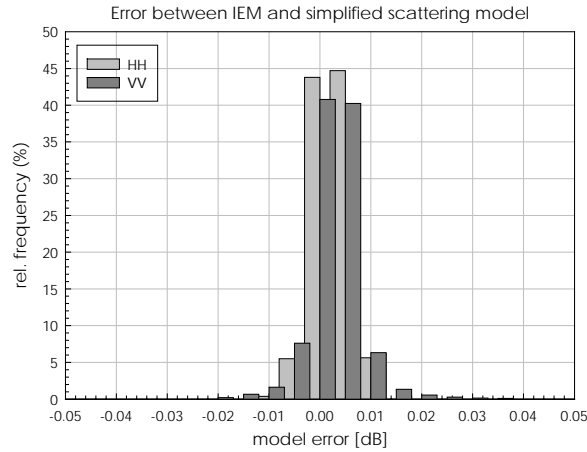
Figure 6.12: Frequency distribution of the modelling error between IEM and the simplified scattering model

6.3.2 Incidence angle normalization

The fitted A and B parameters show a strong incidence angle dependency. Both change rapidly with increasing incidence angle, which means, that different model parameter values are necessary for different angles. This is consistent with the observations in section 6.2. For a unique description of the surface roughness, a normalization procedure is necessary to consider influences of different imaging geometries.

6.3.2.1 b-parameter

As shown in Figure 6.13, the b-parameter strongly depends on the incidence angle, yet diametrically for the two polarisations. For VV, the b-parameter increases with increasing incidence angle, while it decreases for HH polarisation.
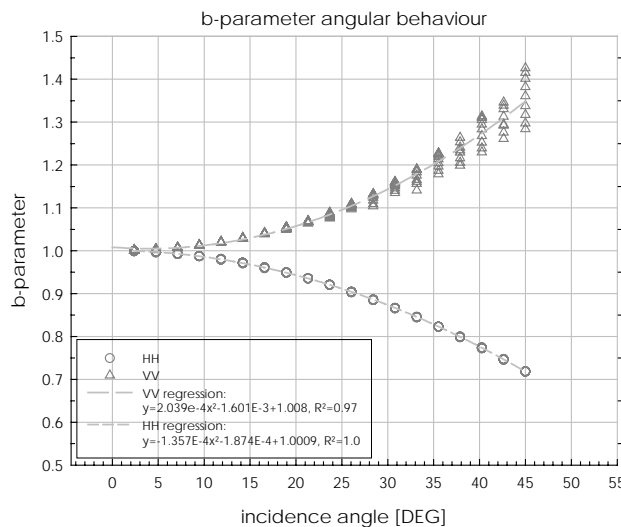
Figure 6.13: b-parameter angular behaviour for HH and VV polarisation

Table 6.3:   **B-parameter model coefficients**

POL	a_1	a_2	a_3	R^2
VV	2.039E-4	-1.601E-3	1.0080	0.97
HH	-1.357E-4	-1.874E-4	1.0009	1.0

The angular dependency can be described by a polynomial of the form

$$b = a_1\theta^2 + a_2\theta + a_3 \tag{6.16}$$

The estimated coefficients a_i and the coefficients of determination are listed in Table 6.3.

6.3.2.2   A-parameter

To normalize the incidence angle effect on the A-parameter, the relationship to a reference angle can be used as shown in Figure 6.14. Since it is the intention to create a model, being independent of the imaging geometry, the normalization is done for the nadir position (INC=0°).

A normalization can be achieved, by taking the decade logarithm of the A-parameters and then approximating the resulting relationship by a 2nd order polynomial for each incidence angle. Thus, the A-parameter for any given θ can be calculated as

$$A(\theta) = 10^{c_1 + c_2 \log(A(0)) + c_3 [\log(A(0))]^2} \tag{6.17}$$
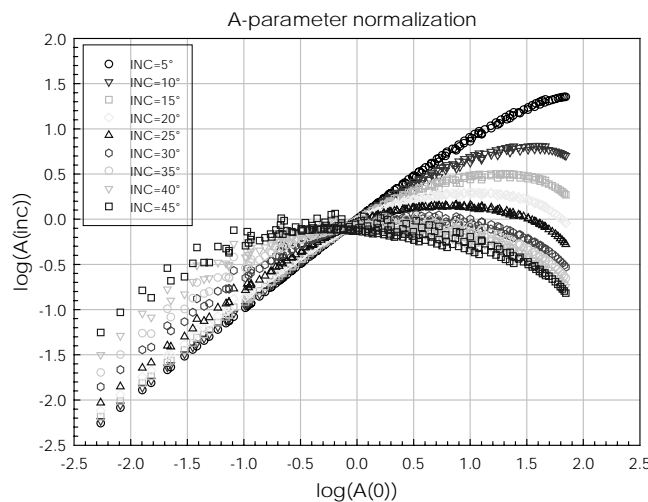
Figure 6.14:   **A-parameter normalization: The roughness parameter A is normalized for each incidence angle to A_0, corresponding to the nadir position**

The coefficients $c_i(\theta)$ for each polarisation, as well as the coefficients of determination are listed in Appendix D. The coefficient of determination for the polynomial fit always exceeds 0.9. For steep incidence angles, which are closer to the nadir, the normalization by the 2nd order polynomial is better than for larger angles.

The remaining surface roughness parameter $A_0=A(0)$ is independent from the imaging geometry. It can thus be used to describe a constant surface roughness property in a way, that the simulated backscattering coefficients using (6.13) are consistent with IEM results.

6.3.3 Forward model

It has been shown, that IEM results can be approximated with a simplified surface scattering model by separating the surface roughness influence from the dielectrical properties. The estimated model parameters have shown a strong angular dependency. By normalizing the model parameters to the nadir geometry, an incidence angle independent parameterisation can be derived.

Using (6.13) - (6.17), the final backscattering model is given as

$$\sigma_{pp}^0 = 10^{c_1(\theta)+c_2(\theta)\log(A_0)+c_3(\theta)[\log(A_0)]^2} \cdot \left[\frac{1-\sqrt{\in_r}}{1+\sqrt{\in_r}}\right]^{\left(a_1\theta^2+a_2\theta+a_3\right)} \tag{6.18}$$

The backscattering coefficient can then be calculated for a given incidence angle, using the surface roughness term A_0 and the dielectric constant $\in_r$ of the media.

6.3.3.1 Model accuracy

To assess the influence of uncertainty induced by the normalization procedure, an error analysis is conducted. For discrete combinations of rms height and autocorrelation length the A_0 parameters are taken from a look up table (Figure 6.15). The backscattering coefficients are then calculated by the IEM and SSM for a given combination of incidence angle, dielectric constant and surface roughness, using the simulation parameters given in Table 6.4.

Table 6.4: Validation parameter set

PARAMETER			START	STOP	INCREMENT
Incidence angle	[DEG]	θ	5.0	45.0	5.0
RMS height	[cm]	s	0.75	2.75	0.25
Autocorrelation length	[cm]	l	1.5	20.5	1.0
Dielectric constant		$\in_r$	5.0	50.0	5.0
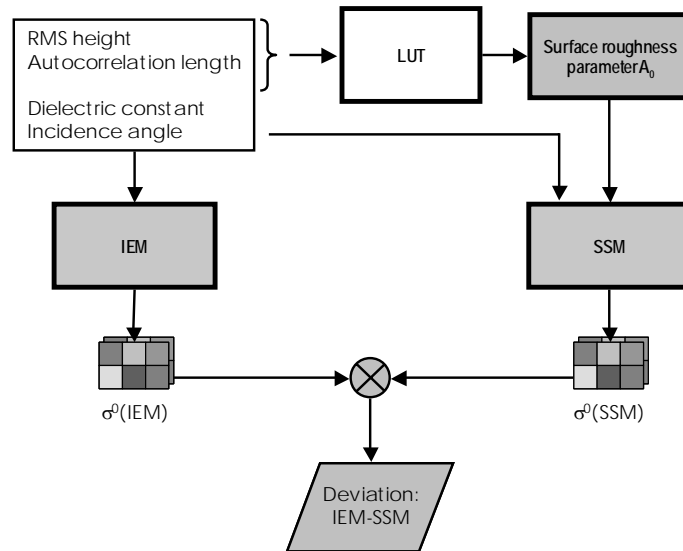
Figure 6.15:   Procedure for the analysis of deviations between IEM and SSM surface backscattering models, based on common input datasets

The residuals between both model results are then calculated and analysed. Figure 6.16 shows the frequency distribution of the deviation between IEM and SSM results. The mean deviation for both polarisations is less than 0.1 dB. Comparing both polarisations, it can be seen, that the difference between IEM and SSM is slightly higher for HH polarisation. The distributions doesn't reveal systematic deviations. An amount of 95 % of the values are within the interval of ±1 dB for VV polarisation and 90 % for HH respectively. For 85 % and 60 % of the simulations, the deviations are smaller than 0.5 dB for VV and HH polarisation respectively. Thus it can be stated that the backscattering coefficients of the IEM are reproduced by the SSM with an accuracy comparable to the image calibration accuracy (see 4.2.2).
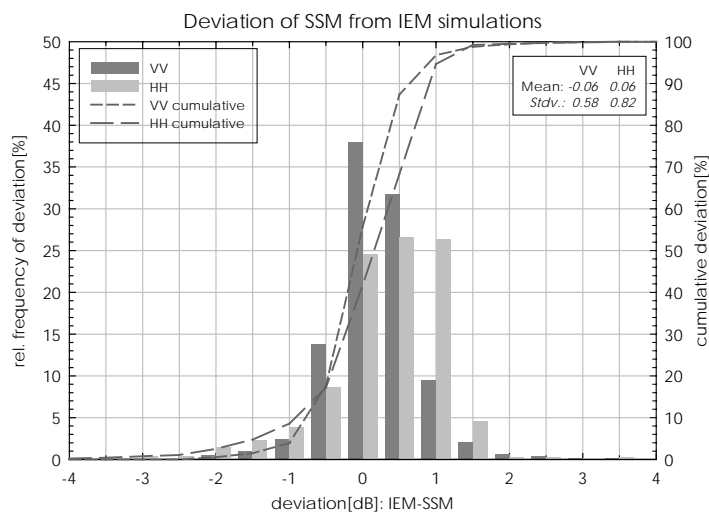
Figure 6.16:   Frequency distributions of the deviations between SSM and IEM modelling results
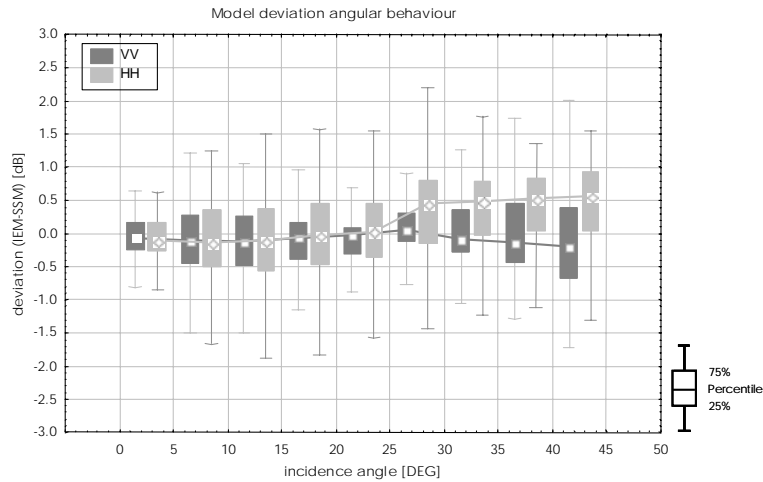
Figure 6.17: **Incidence angle dependency of the residuals between IEM and SSM**

To verify whether the deviations have an angular dependency, their frequency distributions are calculated for various incidence angle classes. The influence of the incidence angle on the model accuracy is not significant for VV polarisation, as shown in Figure 6.17. The mean and variance of the model deviation is stable over the whole incidence angle range. For HH polarisation an error progression of approximately 0.25 dB can be observed for larger incidence angles. Nevertheless, these deviations are within the confidence interval of the image calibration range.

6.3.4 Sensitivity analysis

A sensitivity analysis of the SSM is conducted to estimate the models sensitivity to the surface roughness parameter A_0, the dielectric constant and incidence angle.

6.3.4.1   Surface roughness and incidence angle

With increasing incidence angle, the backscattering coefficient decreases. For low values of A_0 the relationship is nearly linear. With increasing A_0 – corresponding to smoother surfaces - it develops an exponential shape and becomes steeper, as shown in Figure 6.18. The given example was calculated for different roughness parameterisations and a dielectric constant $\epsilon_r = 20$. It can be seen, that the sensitivity to surface roughness increases with increasing incidence angle which is consistent with the literature (e.g. LEWIS and HENDERSON, 1998; ULABY *et al.*, 1982)
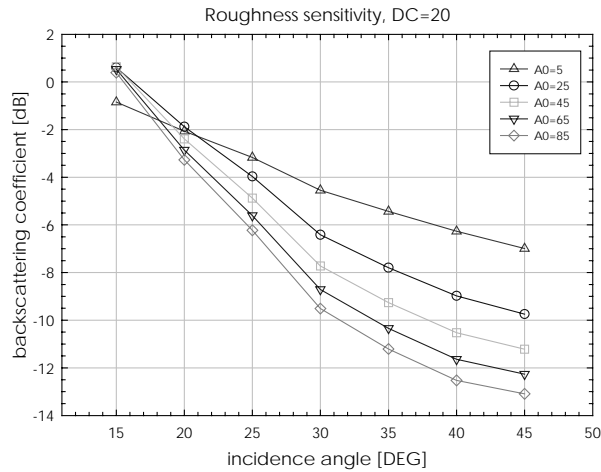
Figure 6.18: SSM incidence angle and surface roughness (A$_0$) sensitivity (dielectric constant=20)

6.3.4.2 Model sensitivity on soil moisture

Figure 6.19 shows the backscattering coefficient as a function of the moisture content for different surface roughnesses, It gives an impression of the dynamic range of σ^0.

For dry soils, the sensitivity of the model to changes of the moisture content is very high. With increasing moisture content, the sensitivity diminishes and reaches saturation above approximately 40 Vol.%.

The incidence angle dependency of the model sensitivity on soil moisture depends only on the b-parameter, which ranges from 0.8 to 1.0 for HH and from 1.0 to 1.5 for VV polarisation (Figure 6.13). Thus only a small influence of the incidence angle on the soil moisture sensitivity can be observed (Figure 6.20)
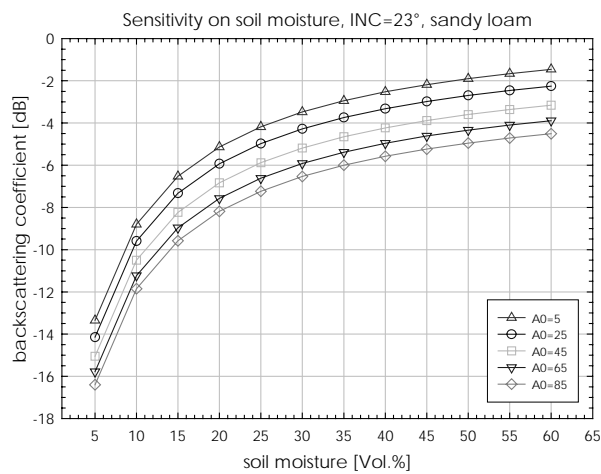
Figure 6.19: SSM model sensitivity on soil moisture for different surface roughness parameters A$_0$ (incidence angle: 23°)
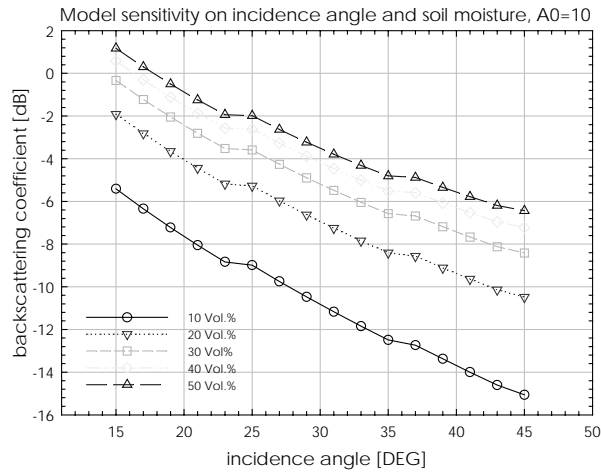
Figure 6.20: **Incidence angle dependency of SSM soil moisture sensitivity (constant surface roughness)**

6.3.5 Relating A_0 to classical roughness parameters

As a result of the model derivation and incidence angle normalization process a look up table can be generated, relating the roughness parameter A_0 to the classical surface roughness descriptors, rms height and autocorrelation length. As can be seen in Figure 6.21, there exists a strong relationship between the rms height and autocorrelation length for the same A_0 parameter. This is consistent with the results of section 6.2, where different combinations of rms height and autocorrelation length were also found to result in same backscattering coefficients.
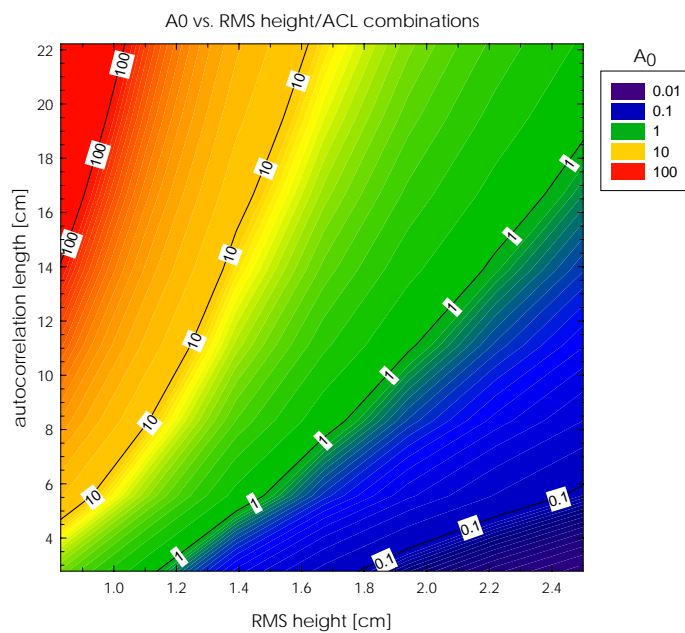
Figure 6.21: **Relationship between A_0 and classical surface roughness parameters rms height and autocorrelation length**
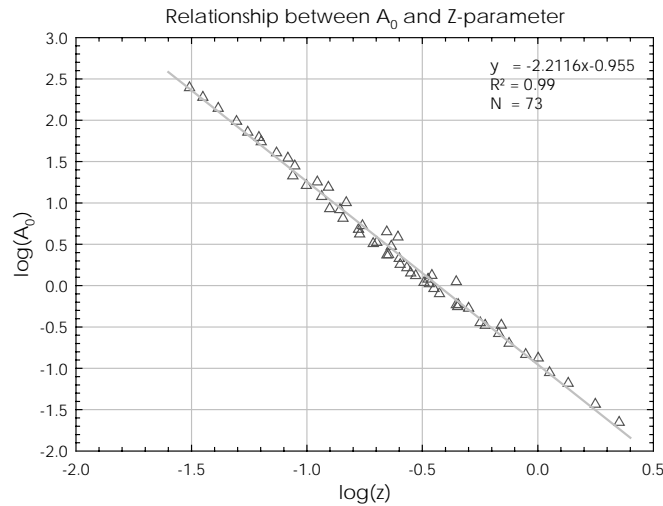
Figure 6.22: Relationship between the roughness parameters A_0 and z

The exponential relationship between rms height and autocorrelation length, addresses the question, whether a unique parameter can be derived from both, which is related to the estimated A_0 value.

Using the Z-parameter, suggested by ZRIBI and DECHAMBRE (2002) as given in (6.11) a strong relationship ($R^2=0.99$) between the Z-parameter and A_0 can be shown by

$$\log(A_0) = a \, \log(z) + b \tag{6.19}$$

where $a = -2.2116$ and $b = -0.955$ (Figure 6.22).

Thus, the empirically estimated A_0 can be related to the classical surface roughness parameters using the Z-parameter, which corresponds to the variance of the surface, normalized by the autocorrelation length.

6.4 Fractal surface parameters for backscatter modelling

The adequate description of randomly rough surfaces is crucial to obtain reliable backscattering model results. As shown in the previous section, the classical parameters rms height and autocorrelation length can be reduced to a normalized roughness parameter A_0. This parameter can be treated as an effective model parameter which integrates different surface roughness properties. To relate A_0 to surface characteristics an understanding of its physical meaning is needed.

Fractal geometry has become an efficient method for the mathematical description of complex irregular and fragmented objects as they often occur in nature (MANDELBROT, 1983). It has been used successfully for numerous different applications on a wide range of scales.

It has been shown that it is also well suited for the description of rough surfaces (BROWN, 1995; ZRIBI *et al.*, 2000; DAVIDSON *et al.*, 2000) and that fractal surface parameters can be used for theoretical backscattering models (FRANCESCHETTI *et al.*, 2000).

A theoretical approach is presented in the following to relate the surface roughness parameter A_0 to fractal properties of the surface. It is based on synthetically modelled fractal like surfaces.

6.4.1 Fractals

Literature provides several good introductions to the nature of fractal geometry and the derivation of the fractal dimension D as well as the synthetic generation of fractal objects and landscapes (e.g. PEITGEN and SAUPE, 1988; MANDELBROT, 1983; FALCONER, 1990; BARTON and LA POINTE, 1995). Therefore only some definitions, necessary for the understanding of the following are given here, which are mainly compiled from PEITGEN and SAUPE (1988).

One of the central concepts of fractal geometry is the property of *self-similarity* and scaling invariance of an object.

A D-dimensional self similar object can be divided into N smaller copies of itself using the downscaling factor

$$r = \frac{1}{\sqrt[D]{N}} \quad or \quad N = \frac{1}{r^D} \tag{6.20}$$

as shown in Figure 6.23. Conversely, given a self similar object of N parts scaled by a ratio r, its fractal or similarity dimension is given by

$$D = \frac{\log(N)}{\log(\frac{1}{r})} \tag{6.21}$$

	1-D	N parts scaled by ratio r=1/N
	2-D	N parts scaled by ratio r=1/N$^{1/2}$
	3-D	N parts scaled by ratio r=1/N$^{1/3}$
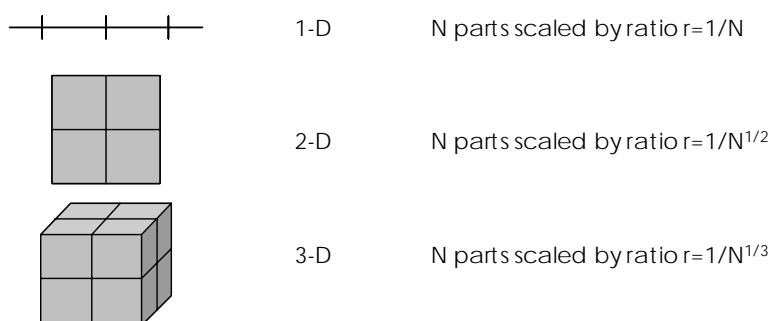
Figure 6.23: **Definition of the fractal dimension D for exact self-similar objects and different Euclidian dimensions (after PEITGEN and SAUPE, 1988)**

Figure 6.24: Recursive replacement procedure for generating the von Koch snowflake curve (left) and the snowflake for one, two and five iteration steps.

The fractal dimension, unlike the more familiar Euclidian dimension, doesn't need to be an integer value. An illustrative example of self similar objects is the *von Koch snowflake* curve, which can be generated using a simple recursive procedure. It is shown in Figure 6.24. As *D* increases, the resulting curves progress from being line-like to filling much of the plane. The fractal dimension, thus, provides a quantitative measure of the wiggliness of the curves.

6.4.2 Randomly rough self-affine fractal surfaces

Natural rough surfaces show a different scaling behaviour than self-similar objects. The variance of a single valued function *z(x)*, representing e.g. a roughness profile, is typically related to the scale the function is sampled at. It normally follows the scaling law

$$\Delta z \propto \Delta x^H \qquad with \quad \begin{aligned} \Delta z &= z_2 - z_1 \\ \Delta x &= x_2 - x_1 \end{aligned} \qquad (6.22)$$

where the parameter *H* in the range *0 < H < 1* is a scaling parameter, also known as the *Hurst* exponent. It relates the variance of a function to its scale. Objects satisfying (6.22) are not exactly self-similar, but they remain statistically *self-affine*. Self-affine functions can be described using *fractional Brownian motion* models (fBm). In addition to (6.22) it is required, that the phase spectra of the function is random (PEITGEN and SAUPE, 1988).

It can be shown that the Hurst exponent of one dimensional functions is related to the fractal dimension by

$$D = 2 - H \qquad (6.23)$$
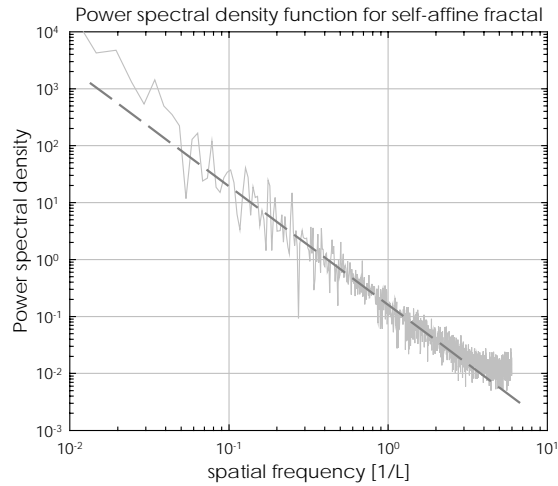
Figure 6.25: **Power spectral density function of a self-affine fractal surface**

Randomly rough natural surfaces, e.g. soils, can be commonly characterized by self-affine fractals, since they obey to the scaling law given by (6.22). Comparisons of natural roughness spectra have shown, that the power spectral density function $P(f)$ of natural surfaces follows the scaling law

$$P(f) = c\frac{1}{f^{\beta}} \tag{6.24}$$

where c is a proportionality constant, f denotes the spatial frequency and β is the spectral exponent. Figure 6.25 shows an example of the power spectral density for a rough surface. The spectral exponent β is defined by the gain of the linear least square fit.

The relationship between β and the fractal dimension D is given by (SAUPE, 1988)

$$D = \frac{5 - \beta}{2} \tag{6.25}$$

6.4.2.1 Generation of randomly rough surfaces

A number of algorithms have been described, which permit the generation of random fractal like surfaces. These include the *midpoint displacement technique* and simulations based on the *Weierstrass function* or *spectral synthesis* methods (SAUPE, 1988). The spectral synthesis method is suitable for the fast generation of long surface profiles as needed to be comparable with SAR system resolution cells.

As the power spectral density is defined as the square of the absolute value of the Fourier coefficients a_k, it follows from (6.24) that a self-affine random like fractal surface simply has to satisfy the condition

$$\left\langle \left| a_k \right|^2 \right\rangle \infty \frac{1}{f^{\beta}} \tag{6.26}$$

where $\left\langle \cdots \right\rangle$ denotes the ensemble average. The surface generation then simply comprises of randomly chosen coefficients satisfying (6.26) and the computing of the inverse Fourier transform to obtain the surface function $z(x)$.

Under the assumption of random, gaussian distributed height values, an algorithm for the surface generation by spectral synthesis has the following form (TURCOTTE and HUANG, 1995; SAUPE, 1988):

1. Generation of gaussian distributed random values for each frequency component, resulting in a white noise gaussian sequence

2. Taking the Fourier transform of the sequence

3. The resulting Fourier coefficients are filtered by multiplying with a factor of $f^{-\beta/2}$

4. A random phase value with unique distribution (white noise) is assigned to the filtered coefficients

5. The inverse Fourier transform of the sequence is taken, giving the surface $z(x)$

6. To remove edge effects (periodicities), due to the sampling theorem, only the central portion of the series is retained.
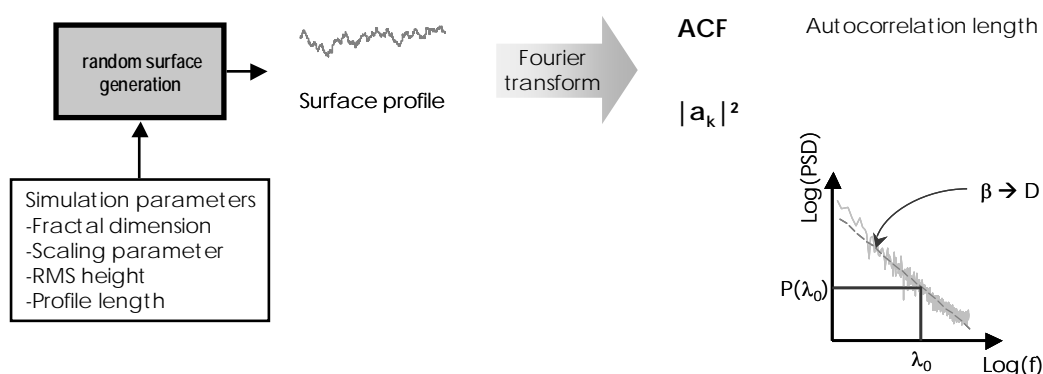
Figure 6.26: **Generation of random fractal surfaces for surface roughness characterization**

6.4.3 Modelling roughness characteristics by simulated surfaces

Randomly rough fractal surfaces are generated using the algorithm introduced above (Figure 6.26) in the following. The fractal surface properties are derived from the synthetically generated profiles and are empirically related to the surface roughness parameter A_0.

Different roughness states of the surface are realized, by using different values for the fractal dimension D which is directly related to the spectral exponent β by (6.25), and by using different values for the proportionality constant c in (6.24). The vertical variances are parameterised using the rms height s. The simulation input parameters are given in Table 6.5. Surfaces are generated for different profile length. Due to the addition of random noise during the surface generation process, the fractal dimension of the resulting surface profile is slightly different from the input fractal dimension. The fractal dimension of the simulated profile is therefore estimated by fitting a regression line, similar to Figure 6.25, to the power spectrum of the surface. Thus, the fractal dimension, as well as the power spectrum of the lower cut off frequency λ_0, given by the intersect between the regression line and the ordinate, can be estimated. The lower cut off frequency corresponds to the spatial frequency, where the wavelength of the surface is equal to the profile length. The surface autocorrelation function is calculated using the *correlation theorem,* which enables the fast calculation of autocorrelation functions based on Fourier coefficients (PRESS *et al.*, 1992). To be comparable with the surface backscattering model, only surfaces in the validity range of the IEM are used for further analysis.

Table 6.5:   Fractal surface simulation parameters

PARAMETER		START	STOP	INCREMENT
Fractal Dimension	D	1.0	2.0	0.1
Proportionality constant	C	0.1	100.0	5.0
RMS height	s [cm]	0.1	3.0	0.25
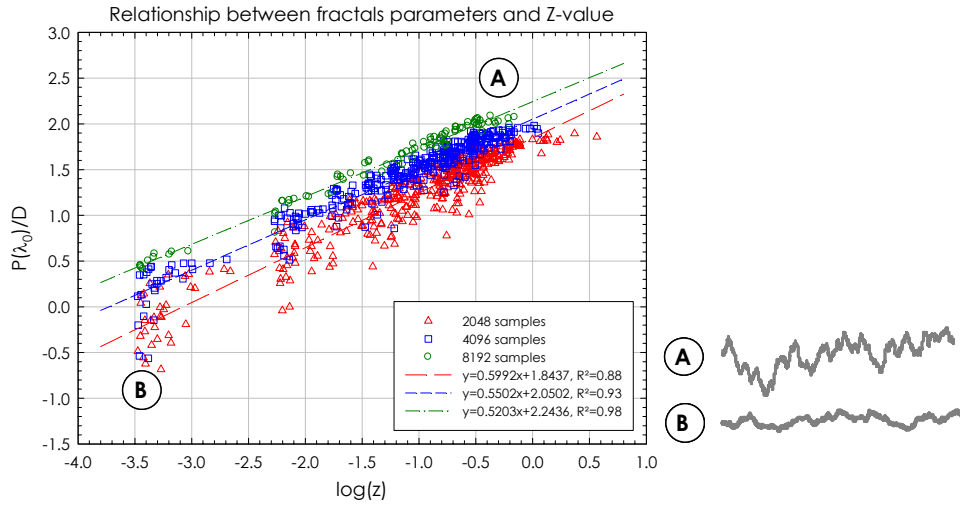
Figure 6.27: Relationship between fractal surface parameters and Z-values: A) rough, B) smooth surfaces

6.4.3.1   Relating fractal parameters to backscattering model variables

The analysis of the simulation results show a strong relationship (R^2=0.98) between the ratio of the power spectrum of the lower cut off frequency $P(\lambda_0)$, divided by the fractal Dimension D, and the Z-parameter (6.11), with d and e being regression coefficients, as

$$\frac{P(\lambda_0)}{D} = d \, \log(z) + e \qquad (6.27)$$

The relationship is found to be dependant on the profile length which is used to simulate the surface profile (Figure 6.27). High values of $P(\lambda_0)/D$ correspond to rather rough surfaces with high vertical variances and vice versa.

The regression coefficients and coefficients of determination for different sample sizes are summarized in Table 6.6. To be comparable with the resolution cell size of a SAR system, longer profiles are preferable.

Using (6.27), the surface roughness parameter A_0 can be related to the fractal parameters by

$$\log(A_0) = A \frac{P(\lambda_0)}{D} + B \qquad (6.28)$$

where A and B can easily be derived from (6.19) and (6.27) as $A = a/d$ and $B = b - (ae)/d$.

Table 6.6: Model parameters for Eq. (6.27)

# SAMPLES	COEFFICIENTS		R²
	d	e	
2048	0.5992	1.8437	0.88
4096	0.5502	2.0502	0.93
8192	0.5203	2.2436	0.98

With (6.28), the surface roughness parameter A_0, needed for the backscatter modelling using the SSM, can be directly derived from field measurements using high resolution sampled surface profiles. By calculating the power spectral density of the profile, $P(\lambda_0)$ and D can be determined. Longer surface profiles (several meters), sampled with a high horizontal sampling frequency would be desirable for this issue. Using existing laser profile measurement databases (e.g. DAVIDSON *et al.*, 2000) it should be possible to investigate the accuracies of the approach proposed above, to derive A_0 values directly from field measurements.

The theoretical results denote that the suggested surface roughness parameter A_0 has a physical meaning. The relationship to fractal surface characteristics enables the derivation of A_0 from field measurements without any need of describing the surface roughness by means of theoretical functions, as it is the case for the autocorrelation length (see 3.2.1.1). Surface roughness can therefore be described by a single parameter, incorporating the vertical and horizontal variances. The A_0 parameter is an applicable variable, integrating the influences of the entire roughness spectrum.

6.5 Derivation of surface roughness from ASAR data

The roughness of each resolution cell has to be known for spatially distributed modelling of the backscattering coefficient. This can be achieved by inversion of roughness information from image data itself. In the following, an algorithm is suggested to invert the roughness parameter A_0 from multitemporal ENVISAT ASAR imagery.

6.5.1 Approach

The SSM only needs the two input parameters A_0 and ϵ_r for modelling the HH and VV backscattering coefficient. The two polarisations are not independent variables. Especially for bare soils, they are very similar as shown in Figure 6.28 where the backscattering coefficients of an image subset are plotted for both copolarisations.
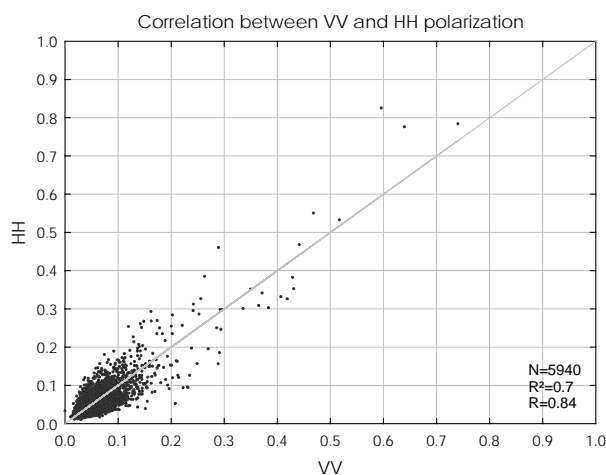
Figure 6.28:   Example for the correlation between HH and VV polarisation

Thus, an unambiguous estimate of the surface roughness cannot be retrieved from monotemporal datasets due to the need of at least two independent variables.

As shown in Figure 6.18, the models sensitivity to roughness increases with increasing incidence angles. Using multitemporal images with different imaging geometries, an estimation of the surface roughness state should be possible under the assumption that it remains constant between the different image acquisitions.

6.5.2 Soil roughness inversion

The different imaging capabilities of ENVISAT ASAR can be used to develop a surface roughness inversion strategy by means of multitemporal datasets, under the following limiting assumptions:

- the surface roughness remains constant for the whole set of images, used for the roughness inversion. Land use practice, as well as weathering effects on the roughness have to be taken into account.

- the dielectric constant of each acquisition is *unknown*, yet within a defined validity range

- the multitemporal images are acquired under different imaging geometries

- vegetation effects on the signal are negligible or can be parameterised

- calibration errors and model uncertainties are considered when comparing modelled and measured backscattering coefficients.

Under these restrictions one can derive the most *probable* surface roughness state from multitemporal image interpretation. Figure 6.29 sketches the proposed inversion scheme.
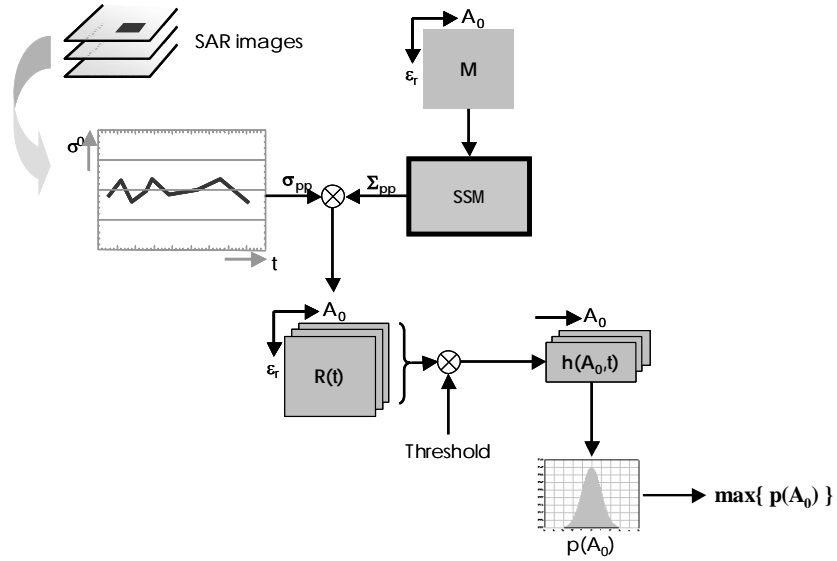
Figure 6.29: **Multitemporal soil roughness inversion scheme, based on image data and theoretical backscatter modelling**

For n available SAR images, the imaging parameters of a pixel are given by the vectors $\vec{\sigma}_{vv}$, $\vec{\sigma}_{HH}$ and $\vec{\theta}$. The matrix of all possible combinations of the roughness parameter A_0 and the dielectric constant $\in_r$ is denoted as $\mathbf{M}$. The surface scattering solutions Σ_{VV} and Σ_{HH} are found, using the SSM model given by (6.18), as

$$\Sigma_{pp} = SSM(\vec{\theta}, \mathbf{M}) \tag{6.29}$$

The residuals matrix between simulated and measured backscattering values is calculated independently for each acquisition date t as

$$\mathbf{R}(t) = \sqrt{\frac{\left(\Sigma_{VV}(t) - \vec{\sigma}_{vv}(t)\right)^2 + \left(\Sigma_{HH}(t) - \vec{\sigma}_{HH}(t)\right)^2}{2}} \tag{6.30}$$

The subset of probable solutions r is found, by applying a threshold T on the residuals matrix.

$$r \in R : R \leq T \tag{6.31}$$

A threshold of 1 dB was found suitable in this context to take model and calibration uncertainties into account. It corresponds to the SSM model and image data uncertainties.

By summarizing all valid solutions $\mathbf{r}(t)$, consisting of different roughness and dielectric properties for each acquisition date, the frequency distribution $h(A_0, t)$ of each roughness parameter set can be tabulated. It encloses all valid solutions for the same roughness state.

Under the assumption that each solution has the same *a priori* probability, the probability for a certain roughness A_0 is given by

$$p(A_0) = \frac{\sum_{k=1}^{n} h(A_0, t)}{m} \tag{6.32}$$

where m is the total number of valid solutions. The roughness parameter A_0, for a given surface, can then simply be estimated as the most *probable* solution of $p(A_0)$.

6.5.2.1 Model Validation

A validation of the roughness inversion scheme for bare soils can only be achieved, where the roughness is not changing during the acquisition period. To prove the model performance for a large number of images and image combinations, the soil has to be bare over the entire period. Therefore a reference target was chosen which meets this condition. It is situated in the northern part of the test site, close to Munich's suburbs, near *Freiham* (Figure 6.31). It is an open gravel covered remediation site, where the soil layer has been removed due to contamination. The surface is characterized by high roughness variability, which is caused by the gravel cover and a larger scale periodical surface structure which is oriented northwards. The dielectric constant is expected to be stable on a low level, due to lacking water storage capacity.

The roughness state of the area is constant and vegetation cover can be neglected as can be seen from Figure 6.30. Thus an inversion algorithm of surface roughness is expected to provide constant roughness values over the year.

Figure 6.30: Overview (left) and detailed view (right) of the roughness reference field near *Freiham*
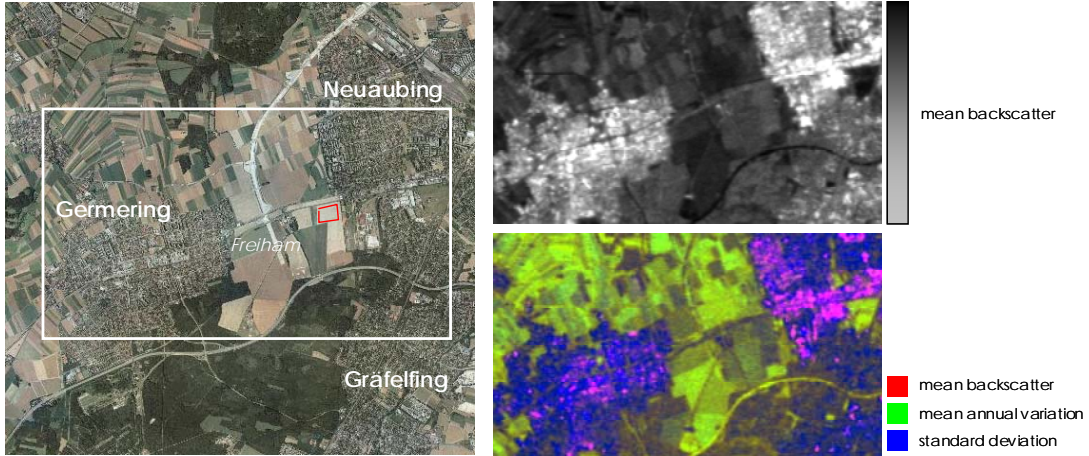
Figure 6.31: **Location of the roughness reference target near Freiham (red), mean backscatter image (upper) and composite image of mean backscatter, mean annual variation and standard deviation (below). Reproduction of orthophoto with courtesy of the Bavarian Geodetic Survey (#1700/04)**

The area is surrounded by agricultural areas and lies adjacent to the towns of *Neuaubing* and *Gräfelfing* (see Figure 6.31). An analysis of the available ENVISAT ASAR datasets confirms the significantly lower backscattering variation of the test field as compared to the surrounding agricultural fields. This analysis is done without any compensation of incidence angle effects. The mean backscattering coefficient, the standard deviation and the mean annual variation (mva), according to QUEGAN *et al.* (2000), defined for N images with intensities I, are calculated for the whole image stack given in Table 6.7 using (6.33).

$$mva = 10\log\left[\frac{2}{N(N-1)}\sum_{i=1}^{N-1}\sum_{j>i}R_{ij}\right] \quad with \quad R_{ij} = \max\left\{\frac{I_i}{I_j};\frac{I_j}{I_i}\right\} \tag{6.33}$$

The results are shown in Figure 6.31. Expectedly, the test field is characterized by a lower annual backscatter variation than the surrounding agricultural fields.

To prove the hypothesis that the roughness of the test field remains constant over different acquisitions and to prove the reproducibility of the roughness inversion scheme, a multitemporal validation strategy is applied. The inversion model is assumed to perform well, if it is capable to invert the same surface roughness state from different SAR images and image combinations. A total number of six different image combinations, as given in Table 6.7, is used to confirm this assumption. The different image combinations are used to invert the roughness parameter A_0 using the model proposed above.

Table 6.7: SAR image combinations used for roughness validation (x=used images)

DATE	DOY	INCIDENCE ANGLE [°]	COMBINATION #					
			#1	#2	#3	#4	#5	#6
10.03.2003	69	44.9	x			x		x
27.03.2003	86	44.0	x			x		x
02.04.2003	92	19.5	x			x		x
07.05.2003	127	32.4		x		x		x
05.06.2003	156	44.1		x		x		x
11.06.2003	162	32.5		x			x	x
17.06.2003	168	33.7			x		x	x
30.06.2003	181	23.4			x		x	x
20.08.2003	232	19.5			x		x	x
24.09.2003	267	19.5					x	x

The most probable surface roughness is calculated for each image combination using the surface roughness inversion scheme introduced above. The results, shown in Figure 6.32, indicate that the surface roughness is reproduced well and in a constant manner by the inversion model. For all image combinations considered, covering a wide range of imaging geometries, the surface parameter A_0 converges to a rather low value of approximately 11.0, which corresponds to a rough surface.
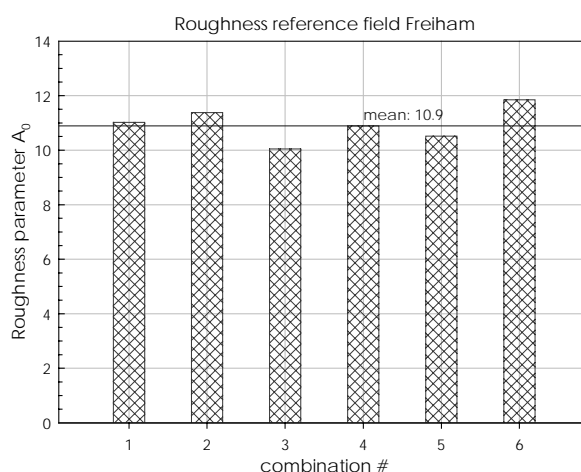
Figure 6.32: Surface roughness inversion results for the Freiham reference field, using different image combinations

Thus the roughness inversion model has proven its applicability to perform consistently for a constant rough surface over a wide range of imaging geometries and their combinations.

The surface roughness of the whole test site was estimated, using a multitemporal image datasets from spring 2003, where the soils were still bare. The roughness state for each image pixel was determined in that manner. The mean A_0 value was calculated for each investigated test field to obtain a single roughness value per field (see Appendix E). It should be noted, that the A_0 of the test fields are higher than that for the reference target in *Freiham*, which corresponds to a smoother surface. This is consistent with the field measurements. The calculated A_0 values, therefore seem to be good descriptors for the roughness state of the test fields.

6.5.3 Bare soil backscatter modelling

To validate the SSM bare soil backscattering model, the backscattering coefficient of the test fields is simulated, based on the roughness information derived from the image data and the *in situ* measured soil moisture values, while it is still bare. A total number of four alternating polarisation images are considered for wheat and triticale. The maize field is not analysed due to lack of field measurements within this period.

The model predictions of the SSM are promising. The backscattering coefficients are simulated well for both polarisations as can be seen from Figure 6.33. The RMSE between the modelled and measured values is 1.6 and 1.7 dB for HH and VV polarisation respectively and the coefficients of determination exceed 0.85 (Table 6.8). Detailed simulation results are given in Appendix D.
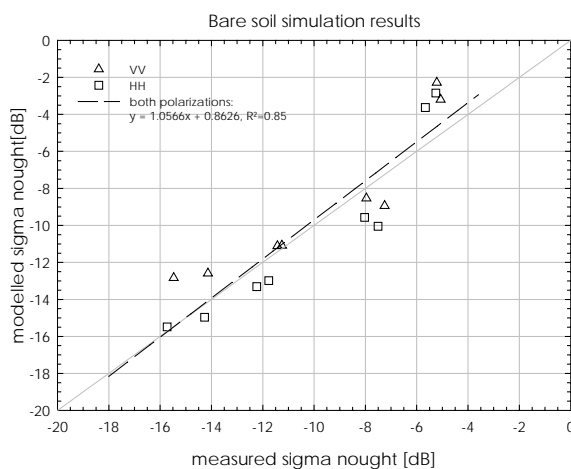
Figure 6.33:   Bare soil backscatter simulation results

Table 6.8:   Bare soil prediction accuracies

POLARISATION	LINEAR REGRESSION[(x)]		R²	RMSE [dB]	MEAN ERROR [dB]
	GAIN	OFFSET			
HH	1.1525	1.2390	0.89	1.6	1.4
VV	0.9449	0.3639	0.85	1.7	1.4
HH & VV	1.0566	0.8626	0.85	1.7	1.4

(x) the dependant variable is the modelled backscattering coefficient

6.6 Achievements

A new bare soil backscatter model was developed and calibrated based on IEM simulations. It has been shown, that classical model parameterisations, using the rms height and autocorrelation length lead to ambiguous surface roughness characterizations when comparing simulated data with measured backscattering coefficients of various imaging geometries.

Starting from that point, a simplified bare soil backscattering model was derived, which allows for the normalization of the surface roughness to the effective roughness parameter A_0, integrating the roughness components affecting the backscattering coefficient. It has been shown on a theoretical basis, that this parameter can be related to fractal surface properties. The parameter allows for the unique and unambiguous description of surface roughness of a physically stationary surface.

An algorithm was proposed to retrieve A_0, by means of multitemporal SAR imagery. The applicability of the roughness inversion approach was proven, using a reference field with constant surface roughness. It enables the derivation of spatially distributed roughness information as needed for backscatter modelling. Due to the option to derive the necessary A_0 parameter directly from the image data, uncertainties of the models and image data can be reduced.

Using the spatially distributed roughness information and the available *in situ* soil moisture measurements, the backscatter of bare soil fields was predicted by means of the developed backscattering model. The comparison with image data shows promising prediction results.

The presented model assists to overcome the problem of parameterisation ambiguities and allows for the derivation of surface properties. It reduces the number of necessary model parameters, which might simplify inversion strategies. It is valid for the entire validity range of the IEM and is the basis for a sophisticated analysis and description of microwave interactions with the land surface.

Chapter 7
Vegetation backscattering model

An adequate parameterisation of the vegetation influence on the backscattering signal is mandatory for the modelling of the backscattering coefficient over the vegetation period. Different imaging geometries have to be taken into account in this context, to make use of the multiple imaging capabilities of ENVISAT ASAR.

A semi empirical vegetation backscattering model for cereals and maize, valid for a wide range of incidence angles, is proposed in this chapter, using a dual polarisation approach. It is shown, that the model parameters are directly related to plant biophysical variables.

As discussed in Chapter 3, the backscattering coefficient of a vegetated area can be decomposed in soil and vegetation, as well as soil-vegetation interaction terms as

$$\sigma^0 = \sigma_S^0 \cdot e^{-2\tau} + \sigma_V^0 + \sigma_{V/S}^0 \qquad (7.1)$$

The bare soil backscatter contribution σ_S^0 can be modelled using the simplified bare soil scattering model (SSM), derived in Chapter 6. The remaining residuals between a measured backscattering value and a predicted bare soil backscattering coefficient, will be a function of the vegetation's influence on the signal. This vegetation contribution, given by the direct vegetation scattering term σ_V^0, the attenuation of the ground as a function of the optical depth τ and the soil ground interactions $\sigma_{V/S}^0$, varies for different imaging and plant geometries.

The changing imaging geometry has a major influence on the signal as can be seen in Figure 7.1, where the temporal development of the backscattering coefficient of a wheat field is shown exemplary. Over the entire vegetation period, the backscatter is inversely proportional to the incidence angle (e.g. DOY 156-181). This main mechanism is superposed by the plant development and changing surface soil moisture contents.
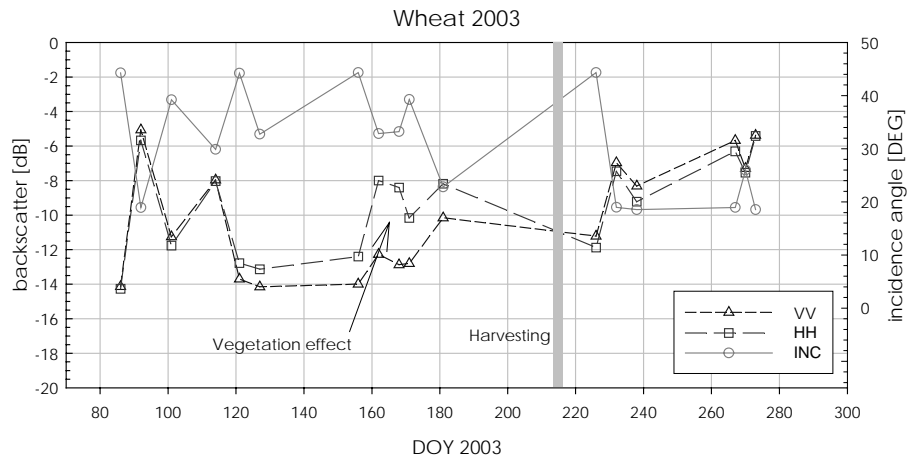
Figure 7.1: **Temporal dynamics of the measured backscattering coefficient of a wheat field**

It can also be observed, that the temporal development of the backscattering coefficient differs for different polarisations. VV is lower than the HH backscattering coefficient, which is caused by the stronger attenuation effects of the canopy, due to the vertically oriented stalks of the wheat plants.

The incidence angle effect is stronger for HH than for VV polarisation during the vegetation period, as can be observed on DOY 155-181. A similar incidence angle dependency is also observable for bare soils (e.g. before DOY 120) indicating that soil contributions have a major influence on the HH backscattering coefficient of vegetated areas.

First attempts to parameterise the canopy backscatter using the theoretical radiative transfer model of KARAM *et al.* (1992) failed due to a strong overestimation of the canopy attenuation (see 3.3.2). The large number of dielectric cylinders, necessary for the description of a wheat stand in the RT-model, and their independent treatment by the scattering model, lead to an highly overestimated attenuation value, resulting in unrealistically low backscattering coefficients.

Therefore a semi empirical approach is developed to describe the vegetation's influence on the signal. The method is based on the theoretical modelling of the bare soil backscatter contribution σ_S^0 using the SSM, given by (6.18). The necessary soil moisture information is taken from ground measurements. The roughness of each test field is derived from the spatially distributed roughness map, derived in Chapter 6. The remaining residuals $\Delta\sigma$ between the measured backscattering coefficient σ^0 and the simulated bare soil backscatter σ_S^0 are analysed and empirically related to the imaging geometry and vegetation parameters. This enables the derivation and calibration of species specific vegetation backscattering models (Figure 7.2).
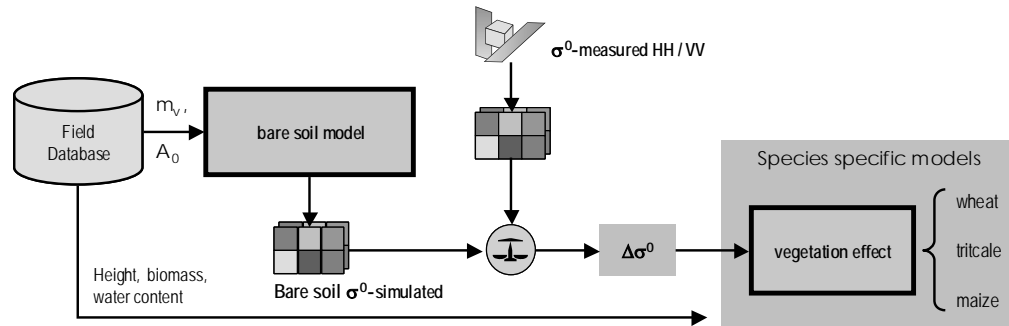
Figure 7.2: Estimation of the vegetation effect on the SAR backscattering coefficient and development of specific canopy scattering models

Two different approaches are chosen for cereals (wheat and triticale) and maize stands. The distinction in these two groups is founded on the completely different shapes and sizes of the plants with respect to the radar wavelength. Different interactions of the electromagnetic wave with the canopy are therefore expected. Due to the similar shape of the wheat and triticale plants these two species are analysed together.

All available image datasets until harvesting are used for the investigations. The datasets show high dynamics of the backscattering coefficient and were acquired under different imaging geometries (Figure 7.1). The range of incidence angles covers nearly the whole ENVISAT ASAR swath width from 15 to 45°. Surface roughness is assumed to be constant over the vegetation period. The backscattering coefficients were derived from the image data by averaging all image pixels within a test field.

An overview about the available database for the analysis is given in Figure 4.15. Detailed information about the images and measured soil and plant parameters can be found in Appendix E.

7.1 Cereals

Empirical models have been successfully applied to compensate the vegetation contributions to the backscattering coefficient of vegetated areas (e.g. ROMBACH and MAUSER, 1997; ATTEMA and ULABY, 1978) without the need to decompose the direct scattering and attenuation terms in (7.1).

The distinct, polarisation dependant vegetation interactions can be expressed in terms of the copolarisation ratio *CP*, defined as

$$CP = \frac{\sigma_{HH}^{0}}{\sigma_{VV}^{0}} \qquad (7.2)$$

This ratio is mainly influenced by the different attenuation and scattering properties of the canopy for different polarisations. The attenuation of the electromagnetic field by the vertically oriented stalks has a major influence for wheat. High values of the *CP* therefore indicate a strong attenuation of the signal in VV polarisation and vice versa. Thus, the copol ratio may be treated as a measure of the extinction properties of the plants which can be directly derived from the image data. As reported by MATTIA *et al*. (2003), a strong relationship exists between the copol ratio and the vegetation biomass.

7.1.1 Copol normalization

The interactions of the electromagnetic wave with the plant compartments are also dependant on the path of radiation through the canopy. The length of the path *p* is a function of the canopy height *h* and the incidence angle θ as

$$p = \frac{h}{\cos(\theta)} \qquad (7.3)$$

The copol ratio *CP* is an ambiguous variable. The same copol ratio can be observed under different conditions, as shown in Figure 7.3. If a low vegetation cover is illuminated by a shallow electromagnetic incident field, the radiation path through the canopy is quite large, resulting in strong interactions with the canopy. The power of the returned signal is indicated by the size of the arrows in Figure 7.3. The same value of *CP* can also be observed, if the vegetation cover is higher and the incident ray has a smaller incidence angle.
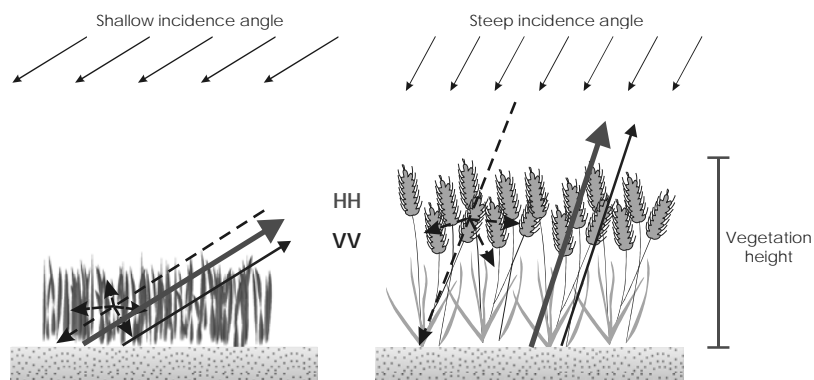
Figure 7.3: Effect of vegetation height and local imaging geometry on the COPOL ratio (thickness of arrows indicate scattered power)

Thus the path through the vegetation remains the same. Under the assumption of the same extinction and scattering properties, the copol ratio can therefore not be used to characterize the extinction properties of a vegetation cover in an unambiguous, incidence angle independent, manner.

If the vegetation height h and the incidence angle are known, CP can be normalized to get a normalized copol ratio CP_N defined as

$$CP_N = \frac{CP}{p} = \frac{CP \cdot \cos(\theta)}{h}$$ (7.4)

This parameter contains information about the intrinsic scattering and attenuation properties of the canopy, as observed by the SAR system. It is independent of the imaging geometry and therefore allows for the multitemporal analysis and comparison of different ENVISAT ASAR images.

7.1.2 Relating plant properties to CP_N

It should be possible to relate this parameter to plant specific variables which affect the microwave interactions. Figure 7.4 shows the relationship of the CP_N to the dry biomass and absolute water content of the plants. For both species, wheat and triticale, a strong relationship exists for both variables, following an exponential decline.

High values of CP_N indicate low interaction and low CP_N values occur when the biomass is large and interaction terms are strong. The relationship saturates at a dry biomass of approximately 1000 g/m².

Various models are tested to describe the relationship between the plant variables and the CP_N. Best results are obtained by taking the decade logarithm of both, the CP_N as well as the biomass or water content values, and fitting a straight line to these datasets. Thus the CP_N value is related to the plant parameters as

$$\log(CP_N) = a \, \log(P) + b$$ (7.5)

where P [g/m²] is the dry biomass or absolute water content. Models for each species (wheat and triticale), as well as for the combined dataset are calibrated. The combined model predictions are shown in Figure 7.4 together with the measured values. The regression parameters and coefficients of determination for the various models are given in Table 7.1.
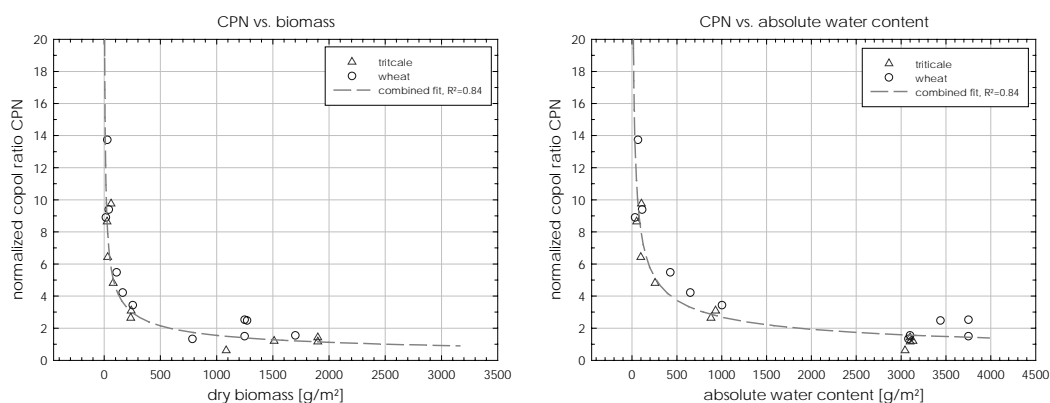
Figure 7.4: Relationship between normalized copol ratio and vegetation parameters dry biomass (left) and absolute water content (right)

Table 7.1: Coefficients determining the relationship between CP_N and plant biophysical variables using Eq. (7.5)

MODEL		LINEAR REGRESSION[†]		R²
		a	b	
Dry biomass	wheat	-0.4344	1.6048	0.88
	triticale	-0.5125	1.6758	0.86
	combined	-0.4722	1.6397	0.84
Water content	wheat	-0.4301	1.7997	0.88
	triticale	-0.5511	1.9842	0.91
	combined	-0.4780	1.8622	0.84

[†]Linear regression of the form $\log10(CPN) = a \log10(x) + b$,
where x is the plant water content [g/m²] or the dry biomass [g/m²]

As expected, the different species interact very similar with the electromagnetic waves. The relationships between the observed CP_N values and the plant parameters are therefore comparable. The use of both datasets results in a model with a coefficient of determination of 0.84, the coefficients of determination of the species specific models are slightly higher.

The fact, that the copol ratio can be directly related to plant biophysical variables indicates, that it can be used to parameterise the vegetation influence on the signal, using this information from the image data itself. It might also be used to invert vegetation biomass or water content with help of dual polarised image datasets. A priori information about the vegetation height is needed in this context to estimate the normalized copol ratio.

7.1.3 Vegetation model calibration

To predict the influence of the vegetation on the backscattering coefficient, expressed in terms of CP_N, the residuals between modelled bare soil backscatter and observed backscattering coefficients can be used.

Making use of the available field measurements, the bare soil backscatter can be calculated using the SSM. The remaining $\Delta\sigma$ between the measured values σ_M^0 and the bare soil predictions σ_S^0 is defined as

$$\Delta\sigma_{pp}(dB) = \sigma_S(A_0, \in_r) - \sigma_M \tag{7.6}$$

where pp denotes the polarisation. The residuals are calculated for each dataset from available ground measurements (see 5.2) and SAR imagery. The derived relationships between $\Delta\sigma_{pp}$ and the normalized copol ratio CP_{N_t} are shown in Figure 7.5.
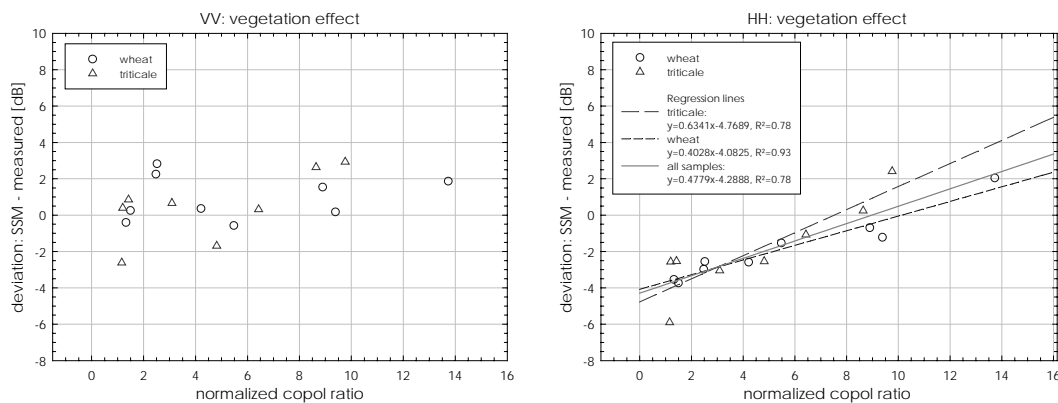
Figure 7.5: **Bare soil model residuals for VV (left) and HH (right) polarisation, related to the normalized copol ratio**

The backscatter residuals have no significant relationship to the normalized copol ratio for VV polarisation. Strong relationships exist for HH polarisation on the other hand. This denotes, that strong interactions and attenuations occur in VV polarisation, resulting in a signal, where no significant information about the vegetations influence can be extracted from the backscatter residuals.

In HH polarisation, the backscattering coefficient is underestimated for most cases. The negative residuals, correspond to samples with high vegetation biomass, signifying that the canopy adds an additional scattering term to the total signal.

The residuals $\Delta\sigma_{HH}$ can be described as a function of CP_N as

$$\Delta\sigma_{HH} = 0.6341\,CP_N - 4.7689 \quad R^2 = 0.78 \quad \textit{Triticale}$$
$$\Delta\sigma_{HH} = 0.4028\,CP_N - 4.0825 \quad R^2 = 0.93 \quad \textit{Wheat} \qquad (7.7)$$
$$\Delta\sigma_{HH} = 0.4779\,CP_N - 4.2888 \quad R^2 = 0.78 \quad \textit{Wheat \& Triticale}$$

The results denote that cereals can be modelled as a volume filled with random scatterers with predefined scattering and attenuation properties. Exact information about the geometrical shape of the individual scatterers is not needed. The empirical relationship between the CP_N and the backscatter residuals, enables the quantitative description of the vegetation influence on the signal. Additional *a priori* information about the vegetation height is needed in this context. The information about the intrinsic scattering and extinction properties of the canopy is contained in the image datasets and can be parameterised with help of the normalized copol ratio. This can be used to predict the vegetation backscatter contributions.

The strong relationship of the CP_N to plant biophysical variables enables the derivation of plant information from image data, as well as the synthetic modelling of the vegetation backscatter, based on biophysical datasets.

7.1.4 Modelling cereal vegetation backscatter

The backscattering coefficient of cereals can be estimated with help of the bare soil model results and the vegetation scattering submodel. This forward scattering model, given by (6.18) and (7.2) – (7.7), can be used to predict the backscattering coefficient of cereals in HH and VV polarisation, based on available ground measurements. To validate the model performance and accuracy, the backscatter of the test fields is simulated during the vegetation period. To asses the quality of the model for practical applications, two different scenarios are used for the simulations (Figure 7.6). Both approaches use the same image data and ground measurements, but differ in the estimation of the vegetation influence on the signal.

A.) It is assumed that land surface parameters should be derived from available dual-polarisation SAR imagery. Thus the vegetation influence on the signal can be estimated directly from the *image data itself* with help of the normalized copol ratio CP_N. A priori vegetation height information is required for this approach. The bare soil backscatter is simulated, based on the available roughness and soil moisture information. The *a priori* informations are obtained from ground measurements. In practice, one would be interested in the derivation of these parameters.
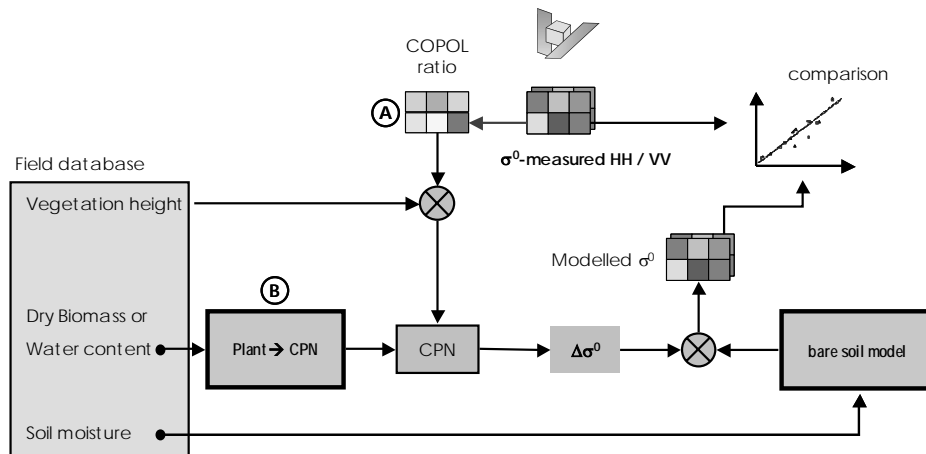
Figure 7.6: **Final combined SAR backscattering model and accuracy assessment scheme**

A method for the inversion of soil moisture values by means of the suggested scattering model, will be given later in Chapter 8. A comparison of the plant specific models for wheat and triticale, as well as the combined vegetation model, given by (7.7), is made in this analysis.

B.) The second scenario is the simulation of a SAR image, based on available bio- and geophysical input parameters. Thus, *no image data* is used to parameterise the vegetation influence on the signal, which is estimated using the relationships between the plant variables and the CP_N, given by (7.5). The vegetation contribution to the signal is calculated, using the specific formulas, given in (7.7). Together with the results of scenario A, these backscatter predictions can be used to assess the backscatter model accuracy and the additional uncertainties introduced by the conversion of plant parameters to the CP_N.

The backscattering coefficient is simulated for each available dataset using this coupled bare soil and vegetation model. The simulation results for both scenarios are shown in Figure 7.7 and Figure 7.8. The modelling error is assessed by calculating the mean and root mean square error of the datasets and by fitting a linear regression line to the samples, for which the modelled backscatter is treated as the dependant variable. This is done for each model, polarisation and plant species. The obtained parameters and accuracies are given in Table 7.2 and Table 7.3.
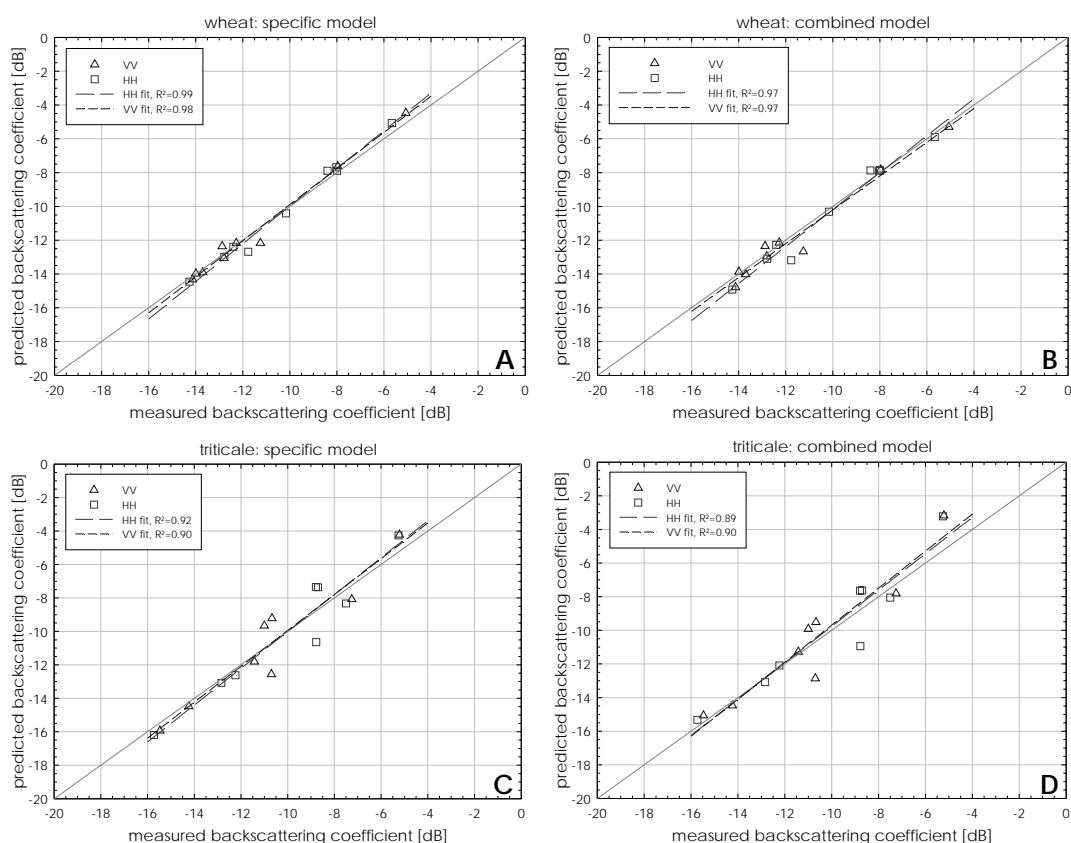
Figure 7.7: Modelled vs. measured backscattering coefficients for cereals, using species specific and combined models for wheat and triticale, *using copol information from image data (scenario A)*

Table 7.2: Model prediction accuracies for plant specific and combined models (*scenario A*)

TYPE	POLARISATION	MODEL	LINEAR FIT[†]		R²	RMSE [dB]	⟨Δσ⟩[††] [dB]
			GAIN	OFFSET			
Wheat	HH	Specific	1.1142	1.161	0.99	0.4	0.3
		Combined	1.0934	0.7427	0.97	0.6	0.4
	VV	Specific	1.069	0.7976	0.98	0.4	0.3
		Combined	1.0001	-0.2054	0.97	0.6	0.4
Triticale	HH	Specific	1.1015	1.0125	0.92	1.1	0.9
		Combined	1.081	1.0409	0.89	1.2	1.0
	VV	Specific	1.0717	0.7708	0.91	1.1	0.9
		Combined	1.1011	1.3188	0.90	1.2	1.0

[†] Linear regression: the modelled backscattering coefficient is the dependant variable

[††] mean absolute error
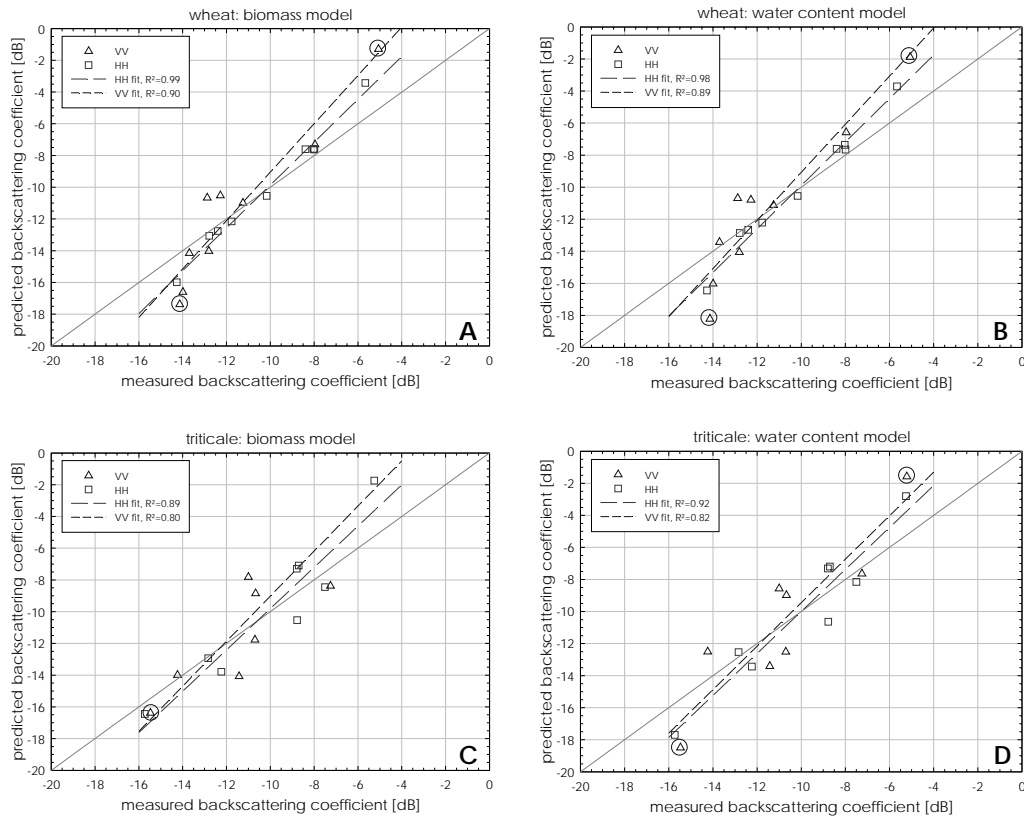
Figure 7.8: Modelled vs. measured backscatter for cereals, *using the biomass and water content model for the parameterisation of the CP_N (scenario B)*; circles denote datasets with low vegetation heights

Table 7.3: Model prediction accuracies using only plant biophysical parameters as input variables (*scenario B*)

TYPE	POLARISATION	MODEL	LINEAR FIT[†]		R²	RMSE [dB]	$\langle \Delta \sigma \rangle$[††] [dB]
			GAIN	OFFSET			
Wheat	HH	Biomass	1.3506	3.6467	0.99	1.0	0.8
		Wat. Cont.	1.3563	3.6683	0.98	1.1	0.8
	VV	Biomass	1.5251	6.1987	0.90	2.2	1.80
		Wat. Cont.	1.5015	5.9381	0.89	2.2	1.78
Triticale	HH	Biomass	1.3016	3.2039	0.89	1.5	1.74
		Wat. Cont.	1.3106	3.1109	0.92	1.4	1.57
	VV	Biomass	1.4199	5.1725	0.8	2.1	2.68
		Wat. Cont.	1.3569	4.1206	0.82	2.1	2.28

[†] Linear regression: the modelled backscattering coefficient is the dependant variable; [††] mean absolute error

The species specific models provide slightly better results than the combined model for wheat and triticale. The triticale model is generally less accurate than the wheat model. Especially the RMSE is higher for triticale than for wheat. The major reason is the weaker correlation between the normalized copol ratio and the vegetation influence on the signal given by (7.7).

It is obvious, when comparing both simulation scenarios, that the relationship between measured and modelled backscatter has a higher gain when no image data is used to parameterise the vegetation extinction and scattering properties. Responsible for this overestimation are mainly two image datasets recorded in early spring (DOY 86 & 92) when vegetation cover is still sparse. This leads to an overestimation of the vegetation effect on the signal. If these two samples are excluded from the analysis, the gain of the relationship between measured and modelled backscatter reduces significantly.

All simulation results show a strong correlation between measured and predicted backscattering coefficients. The root mean square errors range from 0.4 up to 2.2 dB. The corresponding coefficients of determination range from 0.8 up to 0.99. The HH backscattering coefficient is generally better reproduced than the VV polarised one. This is obviously related to the calibration of the model for the HH polarisation. The VV backscatter is derived from the HH simulation results, using (7.2). Additional uncertainties are introduced in this processing step, resulting in a less accurate estimate of the VV polarisation. This is particularly evident when the copol ratio is calculated from plant biophysical variables, instead of using the available copol information from the image datasets.

The proposed cereal backscattering model shows promising simulation results. Using dual polarisation image datasets, the vegetation influence on the signal can be directly estimated from the image data, resulting in excellent prediction accuracies. The modelling error increases, when vegetation influence on the signal is only parameterised by plant biophysical variables. For low vegetation heights, the vegetation effect on the signal can be overestimated. Nevertheless, this approach also results in reliable backscatter estimates.

The suggested model is valid for a wide range of incidence angles. The separation of the vegetation and ground scattering terms simplifies the transferability of the model to agricultural fields with different soil moisture or roughness conditions. The similarity of the wheat and triticale samples indicates, that the backscattering behaviour of these species is similar due to their similar physiological shape. It is therefore expected, that the model can be transferred to other cereals with an appropriate shape, as e.g. barley.

7.2 Maize

Maize plants have a significantly different size and shape than other crops. The stalk of a maize plant is much larger than that of e.g. wheat. This affects the interactions with the electromagnetic wave. In case of a C-band SAR system, the stalk diameter is comparable to the wavelength. Therefore strong interactions of the electromagnetic wave with the different parts of the maize canopy and especially with the stalk are expected. A further difference between maize and other crops is the smaller number of plants, typically varying between 8 and 12 per square meter.

In the following, a maize backscattering model for multiple imaging geometries is recommended. Two maize fields were investigated in the year 2003 during the field campaign. Unfortunately, it turned out during image analysis, that the maize field in Argelsried (#05/2003) was too small to be clearly detectable in the image dataset. The maize backscattering model is therefore calibrated, using only the maize test field in Tiefenbrunn (#04/2003), where pure pixels are available for the analysis. A total of six image datasets, ranging from June to August are used for the investigation (see Appendix E). This limited database complicates the derivation of a maize backscattering model. The construction of such a model is limited to the existing measurements. A semiempirical model calibration is therefore presented and validated for only one test field. It will be shown later on in Chapter 8, that the suggested procedure is transferable to other maize fields.

Based on the analysis of the residuals between bare soil backscatter predictions and the measured maize backscatter (A), the major vegetation scattering mechanism is identified (Figure 7.9). To allow for the transferability of the model to various imaging geometries and plant conditions the effect of this scattering mechanism is analysed using a theoretical radiative transfer model (B).
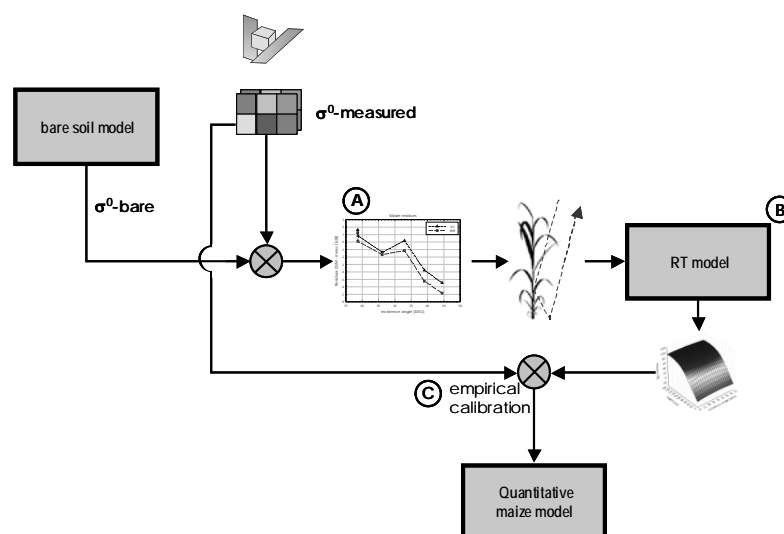
Figure 7.9: Development and calibration of a maize backscattering model

The RT-model results are used for the qualitative description of the backscattering mechanisms as a function of incidence angle and vegetation height. An overestimation of the attenuation effect on the simulated signal prohibits the quantitative interpretation of the theoretical model results (see 3.3). The maize backscattering model is therefore calibrated empirically, based on the existing image datasets (C) and ground measurements, resulting in a quantitative maize backscattering model.

Maize signatures
The temporal development of the backscattering coefficient of maize (Figure 7.10) is rather different from that of cereals (see Figure 7.1). A strong, inversely proportional, angular dependency can also be observed here. Except for DOY 226, where a small difference between HH and VV polarisation can be detected, no significant polarisation dependency of the backscattering coefficient can be found. This contradicts to the wheat case. The backscatter of maize has a lower dynamic range than that of a wheat field. The backscatter varies typically between –10 and -8 dB during the development of the maize canopy.

Therefore, no information about the vegetations influence on the signal can be extracted from the copol ratio, as it was done for the cereal model. Hence, a different vegetation backscattering model is needed for maize.
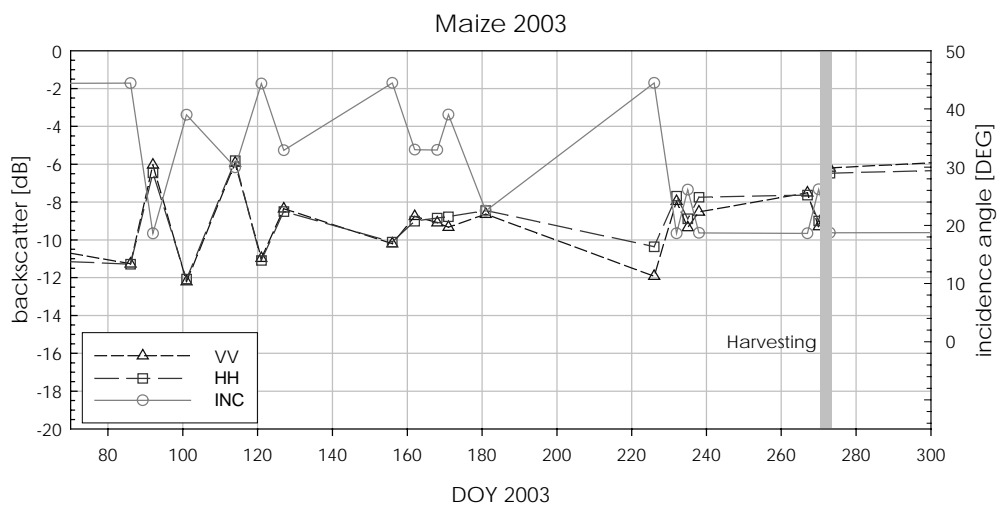
Figure 7.10: Temporal dynamics of the backscattering coefficient of maize

Residuals analysis

Using the bare soil backscattering model and available ground measurements, the residuals between the measured and modelled maize backscatter can be calculated similar to that for cereals, using (7.6).

As can be seen from Figure 7.11, the residuals are not dependant on plant parameters, while a strong angular dependency can be observed for both polarisations. The influence of the canopy properties on the recorded signal therefore have to depend on an incidence angle influenced scattering mechanism.
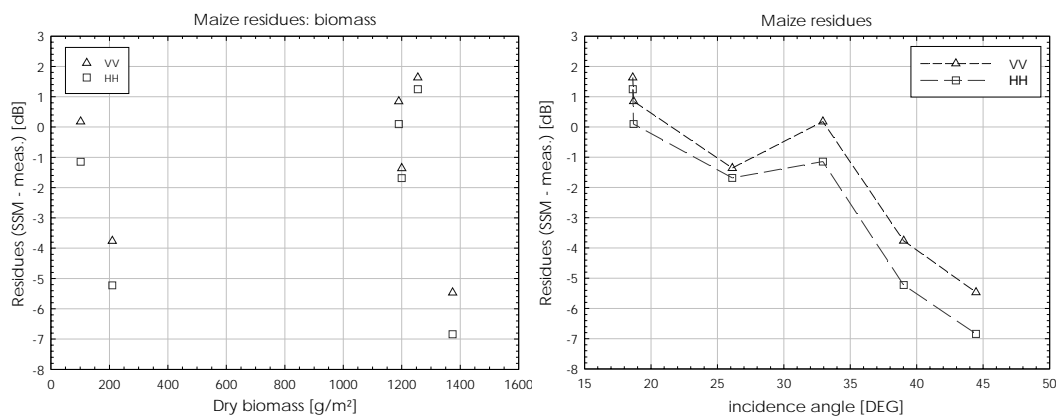
Figure 7.11: **Maize residuals as a function of dry biomass (left) and incidence angle (right) for both polarisations**

7.2.1 Theoretical modelling of maize-ground interactions

The observed negative residuals denote that the canopy mainly contributes to the signal by a strong angular dependant scattering term. A maize stand can be characterized by a two layer medium, where the upper layer mainly consists of leaves and the lower one of stalks (Figure 7.12).
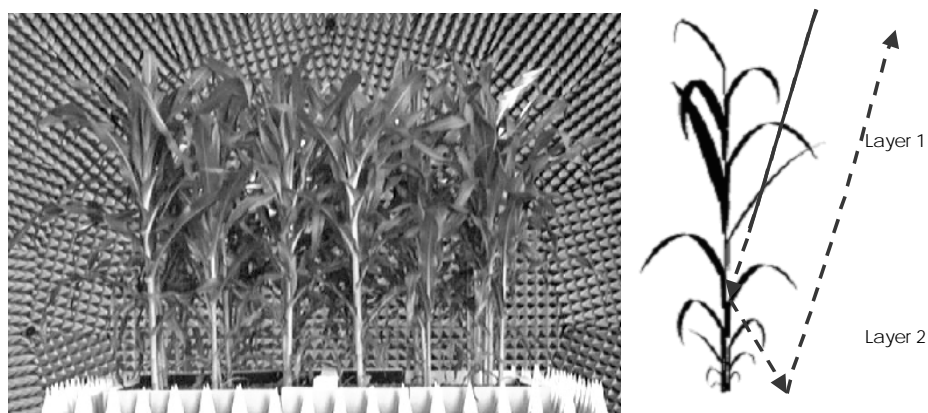
Figure 7.12: **Maize stand geometry and dihedral scattering at the stalk (modified after** BALLESTER-BERMAN, LOPEZ-SANCHEZ **and** GUASCH, **2004)**

Measurements of the backscatter of a maize stand in the laboratory show, that the main vegetation influences are an attenuation of the signal in the upper layer and a dihedral type corner reflection at the lower canopy layer (BALLESTER-BERMAN, LOPEZ-SANCHEZ and GUASCH, 2004). This interaction between ground and stalk has a strong angular component and results in strong backscattering intensities, because the electromagnetic wave is reflected directly to the sensor. The observed backscatter residuals, which also show a strong angular dependency, may result from this dihedral corner reflection mechanism.

To verify this hypothesis, the angular dependency of the stalk-ground backscattering coefficient is examined, using a theoretical backscattering model. To investigate only the vegetation ground interactions of the stalk, the maize stand is simulated by vertically oriented cylinders, representing the stalks (Figure 7.13). Leaves are completely neglected in this representation. The dielectric constant of the stalk is kept constant at a typical plant water content of 0.8.
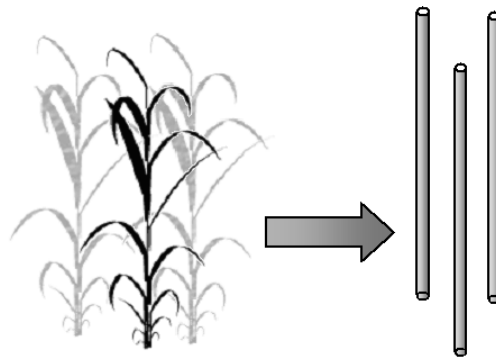
Figure 7.13:   **Representation of a maize stand by dielectric cylinders for the theoretical radiative transfer model**

The lower plant density of the maize canopy results in fewer dielectric cylinders, required for the description of the canopy, as it is the case for e.g. wheat. As discussed in section 3.3, the radiative transfer model (RT) of KARAM *et al.* (1992) uses the independent scatterer assumption, which results in an overestimated vegetation attenuation by the model. Especially for VV polarisation, the vertically oriented stalks result in strong simulated attenuation values. As the vegetation-ground interactions are less influenced by this attenuation, the model can be used to analyse the angular dependency of the scattering term. It is expected, that the model gives reliable qualitative results for the scattering mechanism and its relationship to different model input parameters. It is not expected to provide correct quantitative backscattering values.

Using the radiative transfer model of KARAM *et al.* (1992), the backscattering contributions of soil, vegetation and vegetation-ground interactions are simulated for different soil roughness values, soil moistures, vegetation heights and incidence angles as given in Table 7.4.

Table 7.4:   Maize radiative transfer model input parameters

VARIABLE	UNIT	START	STOP	INCREMENT
Roughness parameter A_0	$\log(A_0)$	0.1	2.0	0.1
Soil dielectric constant	-	5.0	30.0	2.0
Vegetation height	cm	10.0	200.0	20.0
Vegetation dielectric constant	-	31.0-j10.0		
Incidence angle	DEG	15.0	45.0	5.0

A total number of 46625 simulation results are obtained from this parameter set. The contribution of each backscattering term (soil, vegetation-ground and vegetation), is then calculated for each result.

Expectedly the major source of backscattering results from the interaction of the electromagnetic wave with the stalk and the ground. Figure 7.14 shows the frequency distribution of the stalk-ground interaction portions. For 70 % of the simulations, the fraction of the stalk-ground interaction term exceeds 50 % of the total signal.
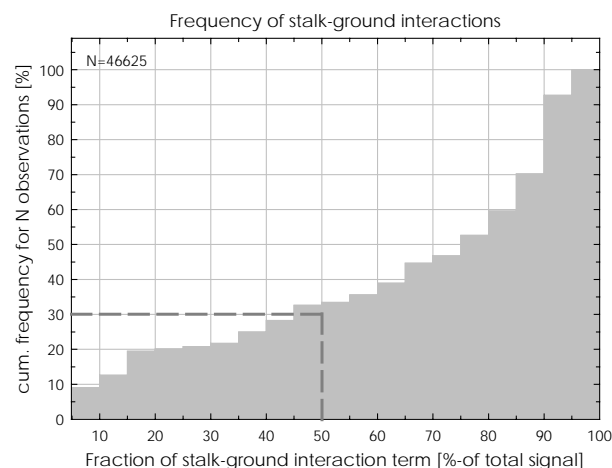
Figure 7.14:   Cumulative frequency distribution of the stalk-ground interaction term contributions to the total signal

The simulated angular behaviour of the dihedral like stalk-ground scattering mechanism is shown in Figure 7.15 for different vegetation heights. It can be seen, that an increasing vegetation height results in an higher angular sensitivity of the signal. It can also be seen, that the modelled stalk-ground interactions show a similar angular behaviour as the calculated residuals from the image data, which is an indication, that this mechanism can be used to characterize the residuals.
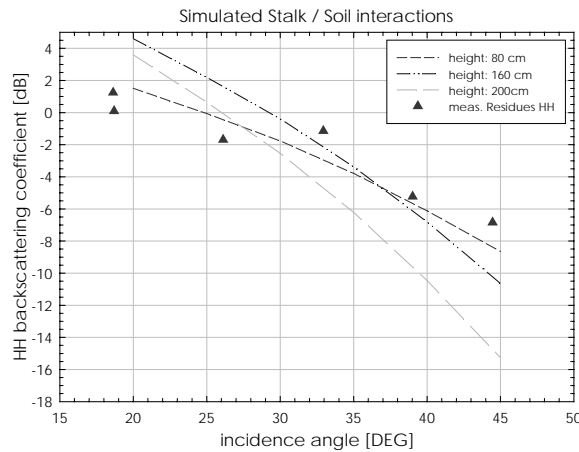
Figure 7.15: **Simulated stalk/ground interactions for different vegetation heights (lines) and measured backscatter residuals (symbol)**

Due to the sparse vegetation density of maize canopies, bare soil contributions have a large influence on the signal at low canopy heights. As the plants grow, the fraction of bare soil contribution decreases, while the stalk-ground interaction term becomes relatively more important as shown in Figure 7.16. The contribution of the interaction term to the total signal increases with increasing vegetation height. The fraction α of the vegetation ground interaction is calculated as

$$\alpha = \frac{\sigma_{V/G}^0}{\sigma^0} \tag{7.8}$$

The radiative transfer model results show a difference between both copolarisations. For the VV polarised case, the fraction α is dependant on the vegetation height as well as on the incidence angle. For HH polarisation, only the vegetation height has a major influence. The reason is, that the attenuation of the vertically oriented stalks, being dependant on the incidence angle, is predicted to be large for VV polarisation. Therefore, the soil contribution is strongly attenuated, resulting in a higher fraction of the interaction term, which is not the case for HH polarisation. As shown in Figure 7.11, no significant differences can be observed between both polarisations.

Fraction of vegetation-ground interactions

VV   HH
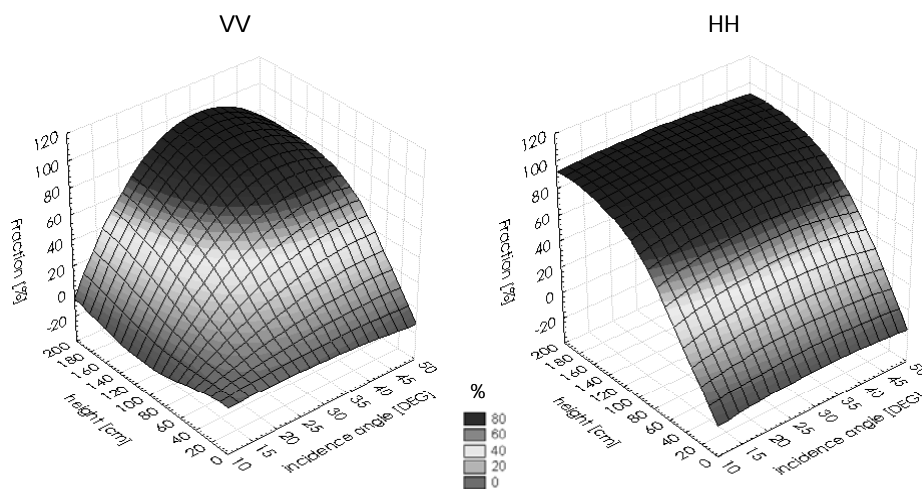
Figure 7.16: **Fraction of stalk/ground interactions, dependant on vegetation height and incidence angle for both copolarisations**

The fact, that the simulated VV backscatter behaviour differs from the observed denotes that the VV estimates are not very trustworthy. This is emphasized by the fact, that the VV backscattering coefficients show unrealistically low backscattering values below –20 dB. The simulated soil and total backscattering coefficients of the HH polarisation are found to be more reliable instead. The influence of the overestimated attenuation have a lower effect on these simulation results. The following analysis will therefore focus only on the HH polarisation case.

7.2.2 A backscattering model for maize canopies

The simulation results indicate, that the major influence on backscattering from a maize stand results from a dihedral type corner reflection between the stalk of the maize plant and the ground. The contribution of this scattering term is dependant on the vegetation height.

Thus, the backscattering coefficient of a maize stand can be described as a function of a direct bare soil component σ_S^0, the stalk-ground interaction $\sigma_{V/G}^0$ and by the attenuation and scattering properties of the plant itself. It is assumed that these can be expressed in terms of the optical depth τ and that interactions between leaves and the ground are negligible.
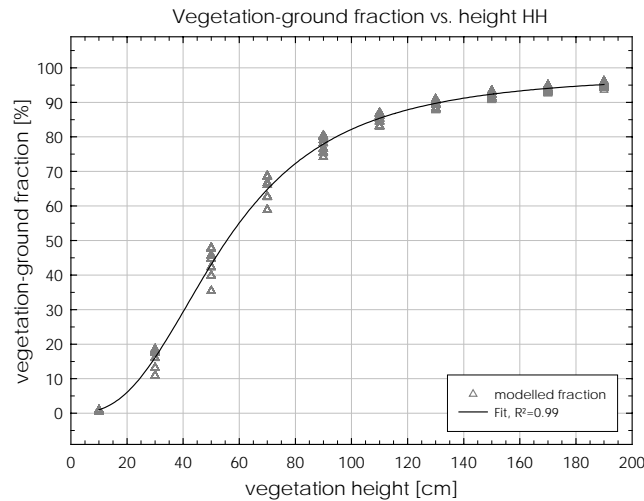
Figure 7.17: Fraction of stalk-ground interaction backscatter as a function of vegetation height

The theoretical model results denote, that the fraction of the stalk-ground interaction term α increases with increasing vegetation height. The backscattering coefficient of a maize stand can thus be described as

$$\sigma^0 = (1-\alpha)\sigma_S^0 + \alpha\,\sigma_{V/G}^0 + \varepsilon \tag{7.9}$$

where ε is a negligible residual term incorporating the leaf-ground interactions.

The fraction of the vegetation-ground interaction can be expressed as a function of the plant height h [cm] as (Figure 7.17)

$$\alpha = a \cdot \left(1 + \left[\frac{h}{h_0}\right]^b\right)^{-1} \tag{7.10}$$

The model coefficients are a=98.5269, h_0=54.9611 and b=-2.6976. The coefficient of determination for the fit is R²=0.99.

If the soil moisture and soil surface roughness is known, the bare soil backscattering coefficient σ_S^0 can be obtained from SSM results. The vegetation ground interaction term $\sigma_{V/G}^0$ can be derived from the theoretical radiative transfer model results. These show a strong relationship between $\sigma_{V/G}^0$ and the attenuated bare soil backscattering coefficient, which can be described as

$$\sigma_{V/G}^0[dB] = m\,10\log\left(\sigma_S^0\,e^{-2\tau}\right) + y_0 \tag{7.11}$$
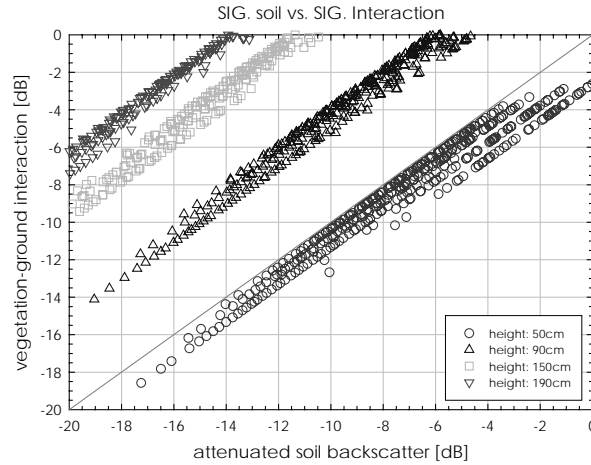
Figure 7.18: **Relationship between attenuated bare soil backscatter and vegetation ground interactions for different vegetation heights**

As shown in Figure 7.18, the gain m remains constant for different vegetation heights, while the offset y_0 shows a dependency on the vegetation height. The reason is an increased modelled optical depth τ with increasing vegetation height. As stated before, the radiative transfer model is expected to produce reliable results about the scattering mechanisms, but not about the correct magnitude of the signal. Therefore m and y_0 can not be taken from the theoretical model results. They have to be calibrated empirically, using available field measurements and image datasets.

The extinction properties of the plants are mainly a function of their water content. The optical depth τ can be described as (JACKSON and SCHMUGGE, 1991)

$$\tau = \frac{h\,K_e}{\cos(\theta)}, \quad where \; K_e = VWC \cdot b \tag{7.12}$$

where h is the vegetation height and K_e is the extinction coefficient, which can be expressed in terms of the vegetation water content (VWC) and an empirical parameter b. For maize, the b-parameter varies between 0.13 and 0.2 (JACKSON and SCHMUGGE, 1991). Using (7.9) and (7.11), the total backscattering coefficient can be written as

$$\sigma^0 = (1-\alpha)\,\sigma_S^0 + \alpha \left(\sigma_S^0 e^{-2\tau}\right)^m y_o \tag{7.13}$$

The parameters m and y_0 can be calibrated, based on available ground measurements. To relate the VWC to the optical depth, a b-parameter of 0.2 was found to be suitable. Using the in situ measured soil moisture and roughness information as well as the vegetation height and plant water content, the backscattering coefficient is simulated using (7.13) for all available image datasets.

A calibration of m and y_0 is possible by comparing the retrieved backscattering coefficients to the corresponding measured values. After a nonlinear minimization of the deviations between measured and modelled backscattering coefficients, the model parameters are determined as m=0.23 and y_0= -5.5 dB. Figure 7.19 shows the final simulation results compared to the measured values.

As can be seen, the model predicts the measured backscattering values very well. The RMSE is 0.46 dB and the coefficient of determination is 0.81.
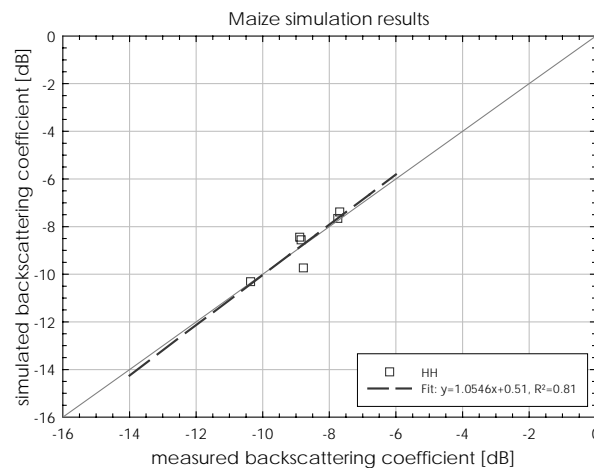
Figure 7.19:   Maize model backscatter simulation results compared to measured backscattering values

Validity range

The validity range of the proposed model is restricted to the used simulation parameter sets given by Table 7.4. These cover most of the possible natural roughness and dielectric conditions. The model was calibrated only for HH polarisation, because the radiative transfer model results were contradictory to the observed VV polarisation signatures.

The primary assumption of the model is the dominance of the stalk-ground interaction. It is dependant on the fraction of bare soil and can be described as a function of vegetation height. The effect of the leaves on the signal can be reduced to an attenuation within the upper layer of the canopy. Recently published measurements of maize stands in the laboratory underline the dominance of this scattering mechanism (BALLESTER-BERMAN, LOPEZ-SANCHEZ and GUASCH, 2004).

7.3 Results

Two different canopy backscattering models were suggested for agricultural crops. Due to the different geometrical shapes and stand densities, the backscattering

mechanisms within maize stands are different from those of cereals. The backscatter differences for the polarisations can be used to parameterise the extinction and scattering influences of the canopy for wheat and triticale. The derived normalized copol ratio is strongly correlated to plant biophysical variables.

A dihedral corner reflection was identified as the major source of backscattering for maize. This is consistent with recently published polarimetric measurements of a maize stand in the laboratory. A model was proposed, weighting the different backscatter contributions as a function of the vegetation height. The model was calibrated using available ground measurements.

Both vegetation backscattering models make use of the bare soil backscatter simulation results of the simplified scattering model, suggested in Chapter 6. The vegetation and soil contributions were separated successfully by means of this model. Due to the reduced number of only two necessary input parameters, the bare soil model allows for an unambiguous estimate of the backscattering coefficient, which can not be achieved with classical approaches. This enables the accurate simulation of the backscattering coefficients of vegetated areas. Contrary to existing vegetation scattering models, the recommended approach is valid for a wide range of imaging geometries and takes into account the changing vegetation influence on the signal over the vegetation period.

Like all calibrated models, the proposed combined vegetation and bare soil backscattering model is formally restricted to the range of the calibration datasets, used for the calibration. The year 2003 was dominated by a hot summer. The measured soil moisture values are therefore mainly from the lower part of the potential soil moisture range. Due to the successful separation of the bare soil and vegetation contributions, the backscattering model is expected to be valid also over a wider range of input parameters. Contrary to empirical models, the use of a theoretical bare soil model enables the transferability of the procedure to higher soil moisture values.

Both vegetation models need *a priori* information about the vegetation height. The maize model needs additional information about the plant vegetation water content.

For spatially distributed modelling, these initial variables have to be available for each resolution cell, which is a sophisticated task. Land surface process models can be used in this context to provide the necessary input parameters as spatial datasets for the backscattering model. The coupling of such a land surface process model to the presented microwave backscattering model is the subject of the following chapter.

Chapter 8
Coupled modelling of land surface microwave backscattering

Land surface process models are widely used to describe energy and mass fluxes at the Earth surface at various scales. They play a decisive role in regional and global aspects of climate change research and are used in manifold manner to simulate and predict processes at the land surface.

An adequate spatially distributed parameterisation of those models is crucial to obtain reliable simulation results, but yet is often difficult to achieve due to lack of appropriate input datasets. Remote sensing data is used in this context to describe static and dynamic land surface variables, as e.g. land use, soil moisture, snow cover, leaf area index (LAI) or topography (e.g. STOLZ, 1998; LÖW, LUDWIG and MAUSER, 2003; RABUS *et al.*, 2003). It is therefore a useful tool to provide necessary input parameters to land surface process models and to validate their simulation results.

Coupling of a land surface process model with remote sensing models, as e.g. those introduced in the previous chapters, enables the generation of synthetic remote sensing images. By comparison with real image data, this approach allows for the adjustment and spatially distributed recalibration of the land surface process model parameterisation, until best coincidence between simulated and real image data is achieved. The image data therefore enables to reduce the uncertainties within the land surface process model parameterisation and leads to an improved description of the land surface state.

It has been shown, that such a combined modelling can be used to enhance process model results and to improve the environmental monitoring and management capabilities (BACH, VERHOEF and SCHNEIDER, 2000; BACH and MAUSER, 2003; BACH, MAUSER and SCHNEIDER, 2003).

The development of an appropriate interface between land surface and remote sensing models is needed in this context. The land surface process model has the function to provide quantitative spatio-temporal series of land surface parameters as e.g. vegetation height, biomass and soil moisture for heterogeneous areas, which

can not be achieved by ground measurements. These are used to parameterise a remote sensing model to obtain synthetic images.

Such a coupled approach might also be useful for an improved derivation of land surface parameters from remote sensing datasets. Due to the direct linkage between remote sensing and land surface models, the image data is assimilated to the process model without any need of inversion models. The current state of land surface variables is simply given by the process model results, using this additional information.

The chapter deals with the spatially distributed modelling of the SAR backscattering coefficient and the derivation of land surface parameters from SAR imagery. Based on the backscattering models, developed in the previous chapters, a linkage between those and a physically based land surface process model is established. After a brief description and validation of the land surface process model, the SAR backscattering coefficients are simulated on the point scale, based on parameter sets provided by the process model. The adequacy of the coupling approach and the accuracy of the results are assessed and the method is transferred to spatially distributed predictions of the backscattering coefficient. The resulting spatially distributed backscatter values are compared to real ENVISAT ASAR image datasets. A quantitative analysis of the deviations between the simulation results and measured values is carried out and discussed.

The coupled modelling approach is used to derive spatially distributed land surface parameters from SAR imagery. The parameter inversion capabilities are demonstrated and validated for the example of soil moisture.

8.1 Promet-V

8.1.1 Model description

The process-oriented land surface model PROMET-V (PROcess-oriented Multiscale Environmental and Vegetation model) was developed to simulate plant growth, water and nitrogen fluxes. It was developed on the basis of PROMET (MAUSER and SCHÄDLICH, 1998) by SCHNEIDER (1999). A brief introduction and examples for assimilation of remote sensing data in PROMET-V can be found in SCHNEIDER (2003).
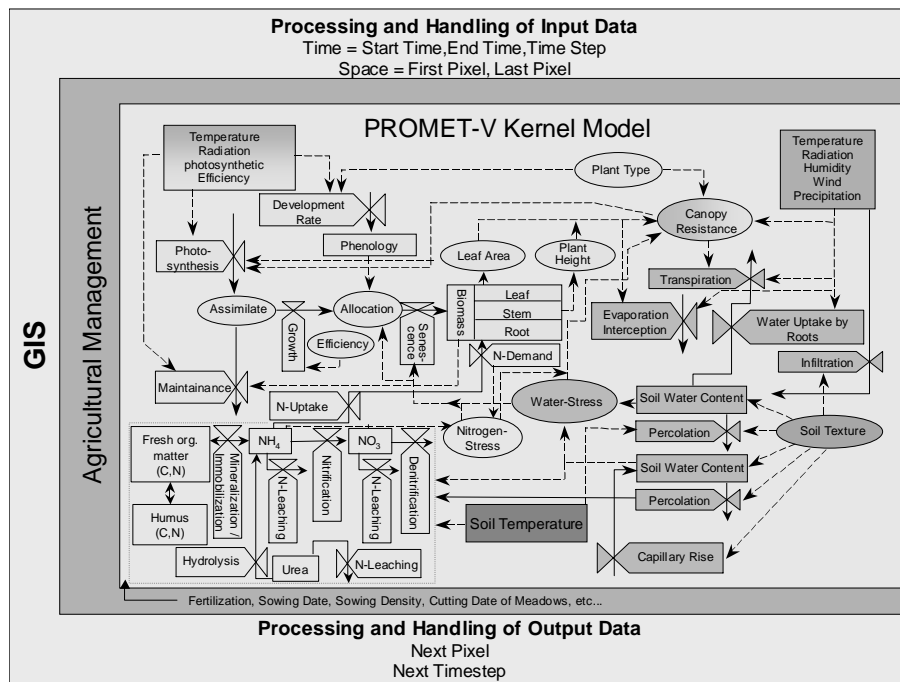
Figure 8.1: Coupling of land surface processes in PROMET-V (SCHNEIDER, 2003)

PROMET-V consists of five coupled sub-models, shown in different colours in Figure 8.1, which describe the flow of water in the soil-plant-atmosphere system, plant growth, nitrogen formation and transport, soil temperature and agricultural management practice. The various submodels are described in detail in the referred literature and are therefore not discussed here.

Currently, PROMET-V supports the plant growth simulation of cereals, corn, meadows and forest canopies. The different plant growth models are described in the literature (JONES and KINIRY, 1986; MOHREN, 1987; SHEEHY and JOHNSON, 1988; HODGES and RITCHIE, 1991; TOPP and DOYLE, 1996; MENZEL, 2000). The hydrological model calculates the evapotranspiration, using the Penman-Monteith equation (MAUSER and SCHÄDLICH, 1998; LUDWIG, 2000) and the soil water balance by using a multilayered soil water model, based on the Philips infiltration model (PHILIP, 1960), combined with a cascade approach (SCHNEIDER, 1999).

The nitrogen model considers all major nitrogen transformations and the nitrogen transport in the soil (GODWIN and SINGH, 1998) and plant matter (LEMAIRE and GASTAL, 1997). The soil temperature model is mainly based on WILLIAMS *et al.* (1989) and plays an essential role for the parameterisation of the soil microbial activity and the infiltration capacity in case of frozen soils.

PROMET-V was designed to allow for the spatially distributed modelling of land surface processes. Based on spatially distributed input datasets, it calculates time series of land surface parameters as shown in Figure 8.2. Its raster structure makes it suitable for comparison and coupling with remote sensing data products.

It has been shown, that the model can provide reliable input data series for remote sensing models, and that it can be used for assimilation strategies (SCHNEIDER, 2003; BACH, VERHOEF and SCHNEIDER, 2000; BACH and MAUSER, 2003; BACH, MAUSER and SCHNEIDER, 2003).
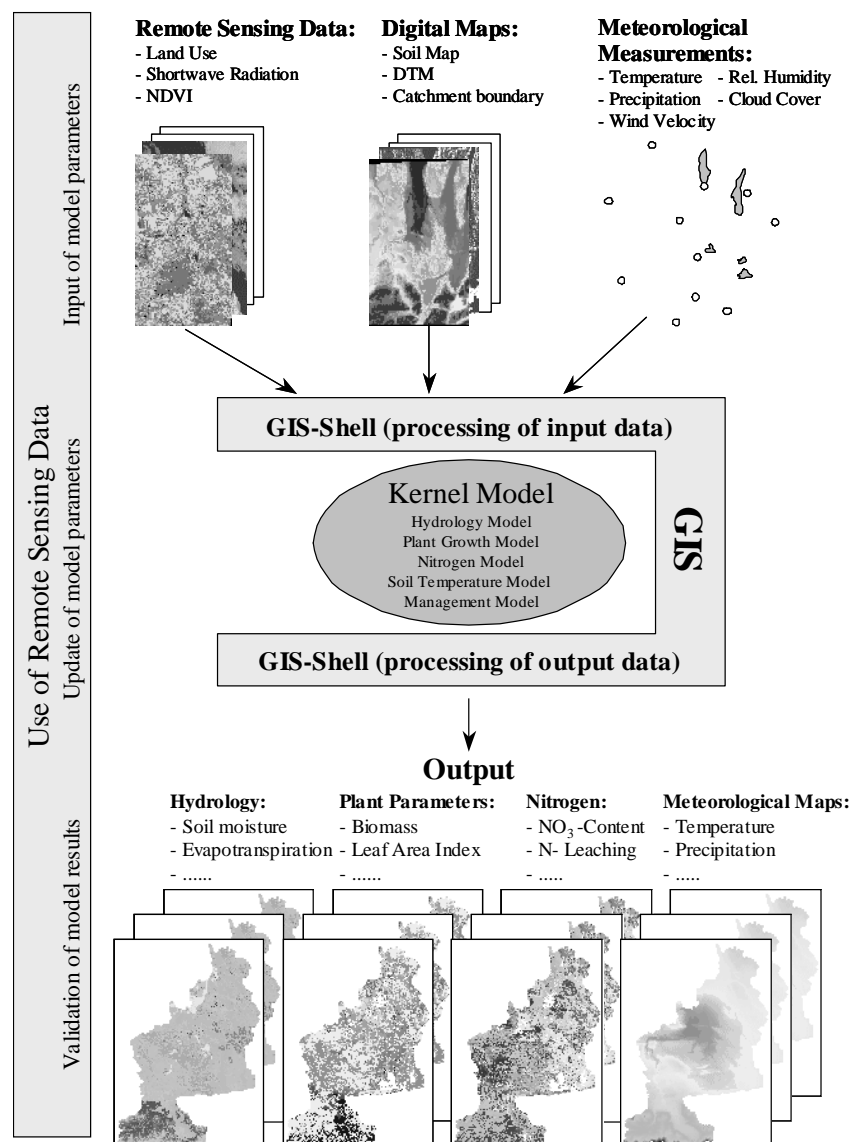
Figure 8.2: PROMET-V model structure: Time series of spatially distributed land surface variables are generated based on spatial and punctual input datasets (SCHNEIDER, 2003)

8.1.2 Model interfaces

The land surface process model output variables as e.g. soil moisture are not necessarily applicable as such for the backscattering model where the dielectric constant is needed instead of the volumetric soil moisture. Therefore a functional interface has to be defined which derives appropriate input parameters for the backscattering model from regular PROMET-V outputs. Figure 8.3 shows the process model output variables and the relationship to the backscattering model input parameters.

While the vegetation height and dry biomass can be used directly, the dielectric constant and plant water content have to be estimated by means of specific submodels.

The dielectric constant is derived from the volumetric soil moisture content, using soil texture information and the dielectric model of HALLIKAINEN *et al*. (1985), given by (3.10). Only the soil moisture of the upper soil layer (5 cm) is taken into account, corresponding approximately to the maximum penetration depth of the electromagnetic waves in C-band.

Plant water content and Wet biomass
The amount of vegetation bound water is essential for the determination of the normalized copol ratio, using the water content model for cereals and an estimation of the extinction properties of the maize stands.
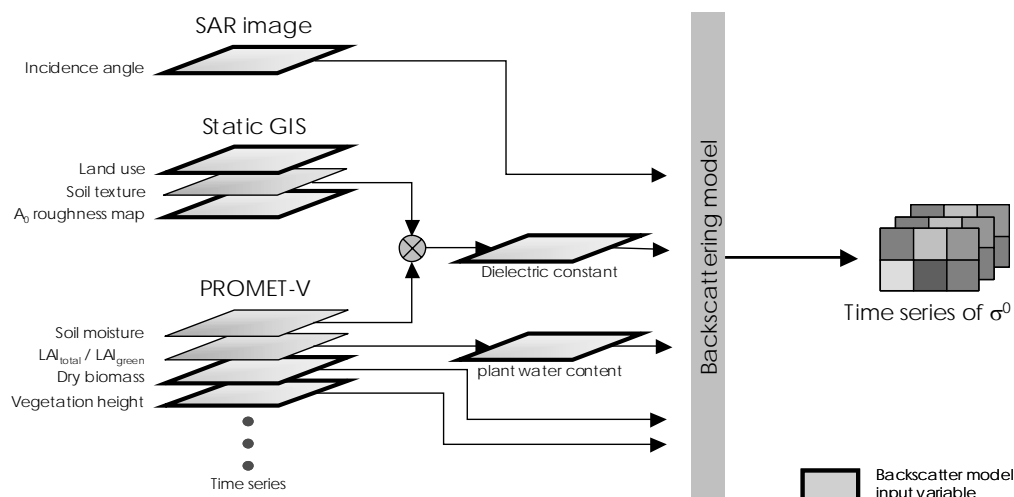
Figure 8.3: **Definition of an interface between the land surface and backscattering models to generate spatio-temporal series of simulated backscattering coefficients**

TABLE 8.1:   PLANT WATER MODEL PARAMETERS

LAND USE	a	b	c	R²
Cereals	0.6606	0.079	0.30	0.67
Maize	1.261	-0.5437	0.48	0.86

Plant water content can be derived from PROMET-V output variables using the total and green LAI. BACH *et al.* (2000a) derived the vegetation water content VWC as a function of a LAI-index as

$$LAI_{index} = LAI_{green} + c \cdot \left(LAI_{green} - LAI_{total}\right)$$ (8.1)

where the parameter *c* is species specific. The plant water content can then be derived using a simple linear regression of the form

$$VWC \ [kg / m^2] = a \, LAI_{index} + b$$ (8.2)

The gain *a* and offset *b* as well as the estimated coefficients of determination are given in Table 8.1. The wet biomass Bio_{Wet} of the stand can easily be calculated using the dry matter biomass Bio_{Dry}, which is provided by the process model, and VWC as

$$Bio_{Wet} = Bio_{Dry} + VWC$$ (8.3)

The simulated wet biomass values are further compared to ground measurements in the next section to assess the accuracy of the estimated absolute water content.

8.2 Plant growth model results for the year 2003

The land surface process model is used to simulate the hydrological and plant growth processes for the vegetation period in 2003, where ENVISAT ASAR images are available. During the research for this work the meteorological records of the DWD network (see 5.2.4.1), needed as model input to PROMET-V, were only available until DOY 181 (30.06.2003). Therefore PROMET-V simulation results are only calculated until this date and the comparisons with image data are made for this period. Wheat and triticale were harvested in the mid of July. Thus almost the entire vegetation period is covered for cereals. Maize was harvested at the end of September but the first field measurements are available at DOY 168 (17.06.2003). Thus, only the first part of the growing period is taken into account for the coupled modelling (Figure 8.4).
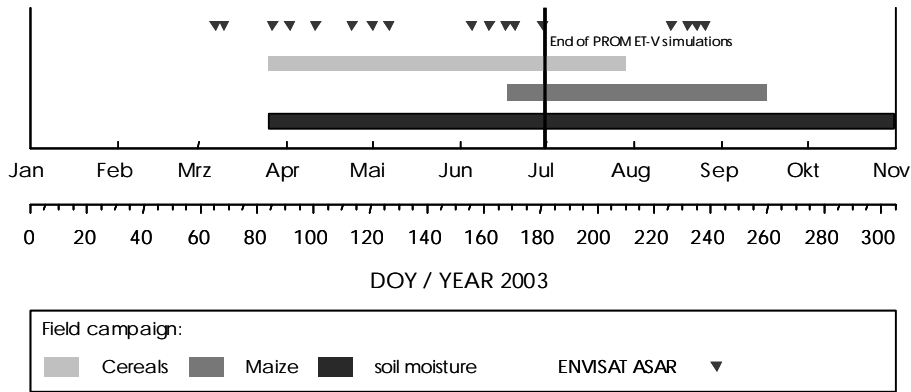
Figure 8.4: Available image datasets and ground measurements of the Gilching testsite usable for coupled modelling

8.2.1 Model parameterisation

To parameterise the process model for each land use, different model parameterisations are necessary. The soil is parameterised using five soil layers with different depths (5,15,40,90,200 cm) and equal soil texture. The static parameters as e.g. elevation, aspect, slope and soil texture are taken from the geographical information system (see 5.1.2). The agricultural management data are mainly taken from the literature (HYDRO AGRI, 1993; BAYERISCHE LANDESANSTALT FÜR BODENKUNDE UND PFLANZENBAU, 1997).

As yet, simulations can only be made for the supported land use types as cereals, corn, meadows and forests. Other crop types, as rape or legumes, are not yet supported due to a lack of a sufficiently accurate plant parameterisation. The model simulations started in autumn 2002 and ended with the availability of the meteorological input data (DOY 181). To assess the quality of the PROMET-V outputs, point scale comparisons to field measurements are conducted and discussed in the following.

8.2.2 Wheat results

The PROMET-V results of vegetation height, biomass, LAI and soil moisture are shown in Figure 8.5 for wheat. The plant development is well reproduced by the process model. The calculated wet and dry biomass are realistic. This indicates, that the derivation of vegetation water content based on LAI simulations, as given by (8.2), performs well. The soil moisture dynamics as well as the ground measurements, with their respective standard deviations, are given in Figure 8.5d. The modelled soil moisture of the upper soil layer (5 cm) is comparable to the field measurements after DOY 130. Before that date, a systematic underestimation of the volumetric water content can be detected. The reason is a delayed modelling of snow melt, indicated by the soil moisture peak at DOY 70.
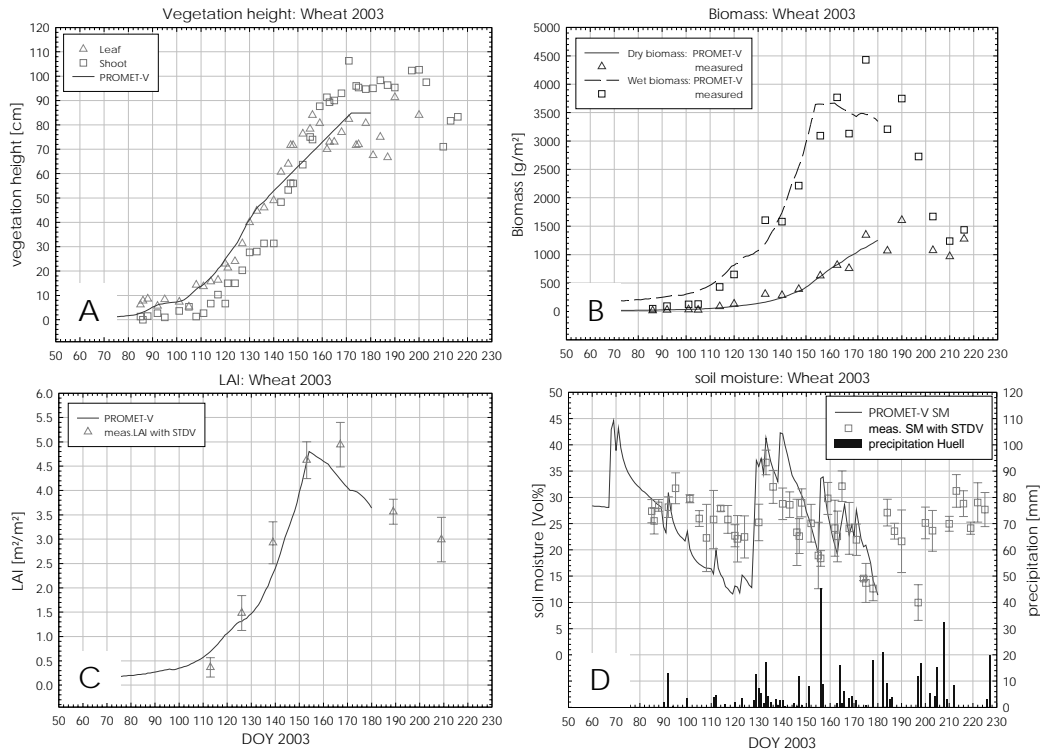
Figure 8.5: Comparisons between measured and simulated soil moisture and plant variables for Wheat 2003

The snow melt is modelled with a delay of around 10 days, compared to synoptic snow observations, producing significant modelled runoff. This water is no longer available in the soil layers. The measured soil moisture values indicate, that more water was bound in the soil column after the snow melt event, than is predicted by the model. The generally good description of the soil and plant parameters by PROMET-V (Figure 8.5) makes it a valuable tool for the spatially distributed prediction of wheat growth and soil conditions, as needed for the suggested backscatter model.

8.2.3 Triticale results

The model results for the triticale field (#01/2003) are comparable to those of the wheat field (Figure 8.6). The vegetation height and biomass development is well reproduced. The LAI is overestimated at higher values. A reason might be the fact, that the plant specific growth parameters for triticale, which control the assimilation of the leaves, have to be adjusted for the triticale test field. As can be seen in Figure 8.6b this doesn't affect the calculated wet biomass values. An underestimation of the soil moisture values can also be observed before DOY 130. The reasons have already been described for the case of wheat. After that date, the modelled soil moisture values fit even better to the field measurements than in the case of the wheat field.
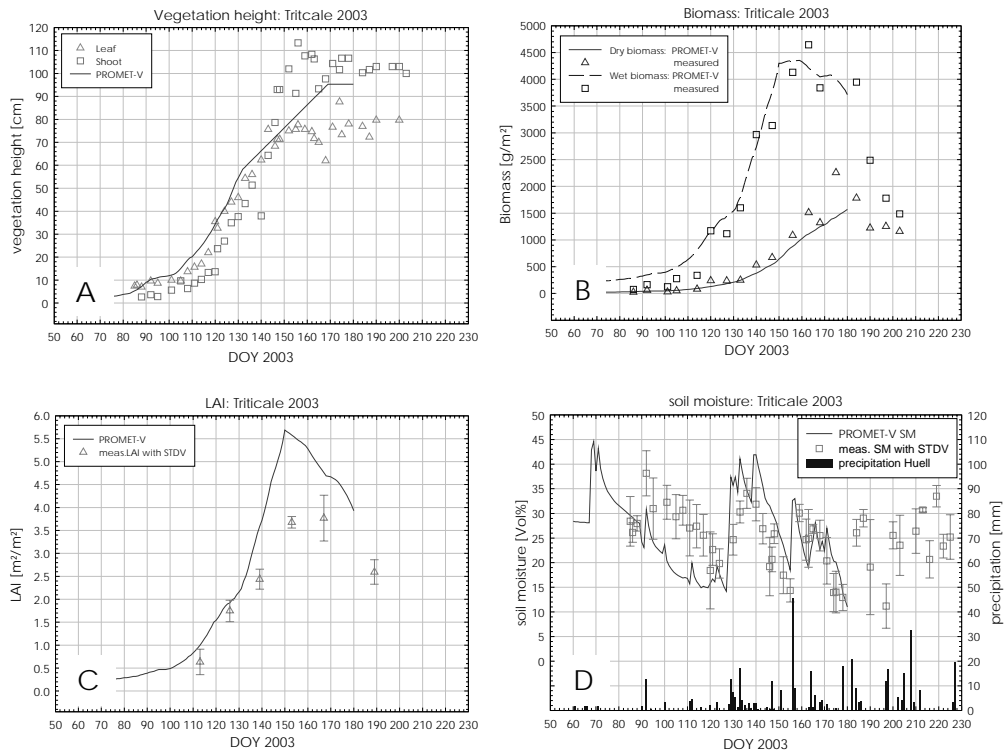
Figure 8.6: Comparisons between measured and simulated soil moisture and plant variables for Triticale 2003

8.2.4 Maize results

The ground measurements of the maize field started at DOY 170. This means, that there is only a short overlap between the field campaign data and the PROMET-V simulations, shown in Figure 8.7. It can be seen, that the modelled vegetation height is higher than the measured one, indicating a significantly faster simulated growth than in reality. Different model parameterisations were not capable to minimize this effect. Only a later seeding date in the model would lead to simulated vegetation heights being comparable with the in situ measurements. Due to the fact that the simulated seeding at DOY 135 is already to late compared to the actual seeding date in mid April (DOY 107, personal communication by the farmer), the model was not forced to fit with the ground measurements.

The biomass development however agrees well with the measured values. The simulation of the wet biomass provides good estimates of this parameter, using the approach given in section 8.1.2. The soil moisture measurements also show a good agreement with the simulations. The results of the short overlapping period between ground measurements and model predictions indicate, that PROMET-V is capable to generate applicable input datasets for the maize backscattering model. The effect of the overestimated vegetation height will have to be taken into account when analysing the backscattering model results.
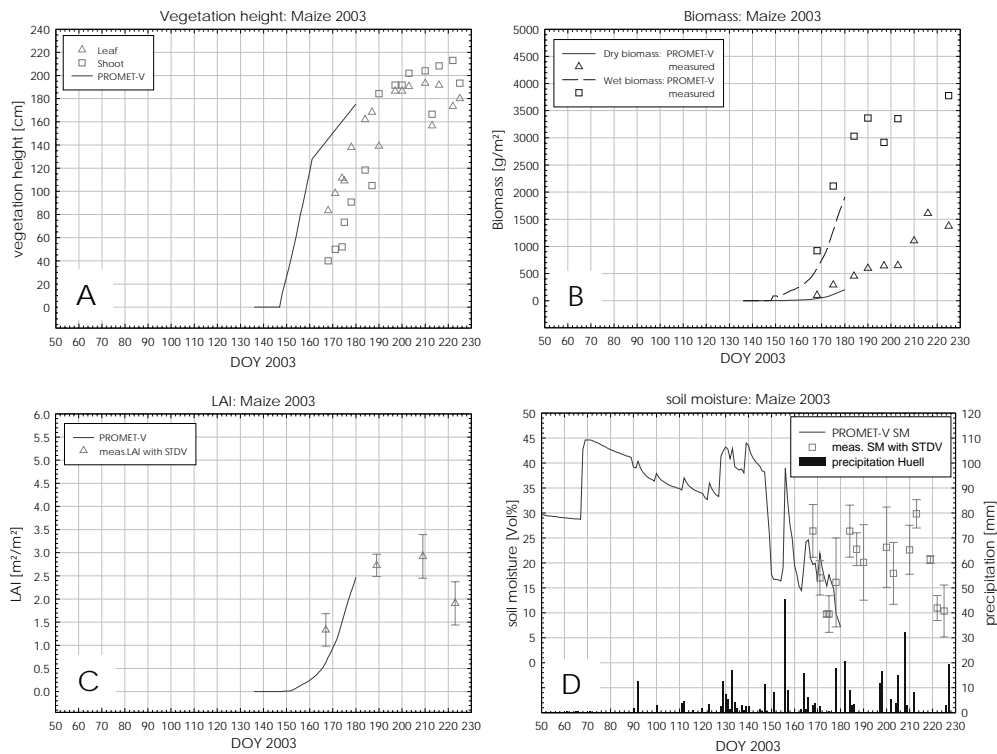
Figure 8.7: Measured and modelled plant and soil parameters for Maize Tiefenbrunn 2003

8.3 Field based coupled backscatter modelling

It has been shown, that the land surface process model can be used to provide reliable estimates of the soil and plant conditions. These can be used to derive spatially distributed input parameter sets for the backscattering model. Using these parameter sets the backscattering coefficient can be simulated for the entire vegetation period, based on PROMET-V results.

In the following section, coupled simulations of the backscattering coefficients are conducted. The results are first compared with measured SAR backscattering coefficients on the point scale, which means that field averaged values are used. The approach is then transferred to spatially distributed predictions of the backscattering coefficient within fields. The results are compared to real image datasets.

8.3.1 Cereals

Based on the modelled plant biophysical parameters and soil moisture values provided by PROMET-V, the HH and VV backscattering coefficients of the wheat and triticale fields are simulated using the biomass and the water content model, given by (7.5). The VV polarised backscatter is obtained using (7.2) and (7.4).

A comparison between simulated and measured backscattering coefficients is shown for both modelling approaches in Figure 8.8. The relationships between the measured and simulated backscattering coefficients are calculated for each test field and modelling approach. The respective linear regression coefficients and coefficients of determination are given in Table 8.2.

The predicted backscattering coefficients show good agreement with the measured ENVISAT ASAR measurements for the biomass and water content model in both polarisations. The gain of the linear fit between measured and modelled backscatter ranges from 0.9 to 1.1 with an offset between –1.0 and 3.0 dB. The coefficients of determination range from 0.6 to 0.9. Worst results are obtained for the test fields, using the water content model for the VV polarised case, which is the result of two overestimated extreme values, indicated by the blue circles in Figure 8.8 (DOY 86 & 92). At the same time the modelled HH backscatter shows good agreement with the measurements, the backscattering coefficient for VV is overestimated. The reason is the low vegetation height, resulting in a low value for the copol ratio and therefore an overestimated calculation of the VV backscatter, using (7.2) and (7.4).

The model accuracies are of the same order as those, obtained from the parameterisation based on ground measurements (see Figure 7.8 and Table 7.3). Due to the sensitivity of the modelled VV polarised backscatter on the canopy height, the application of the water content model is restricted to larger vegetation heights.

No significant differences between the biomass and the water content approach can be observed for HH polarisation. Nevertheless, the biomass model is expected to be less sensitive to errors in the input datasets. While the water content approach uses two LAI simulations (green and total, see 8.1.2) and the dry biomass as input variables, the biomass model is only based on the simulated dry matter content. Uncertainties in the biomass estimates will therefore have an influence on both backscattering model variants, while errors in the LAI predictions will only have an effect on the water content model. The biomass model is therefore expected to be more robust to input parameter uncertainties.
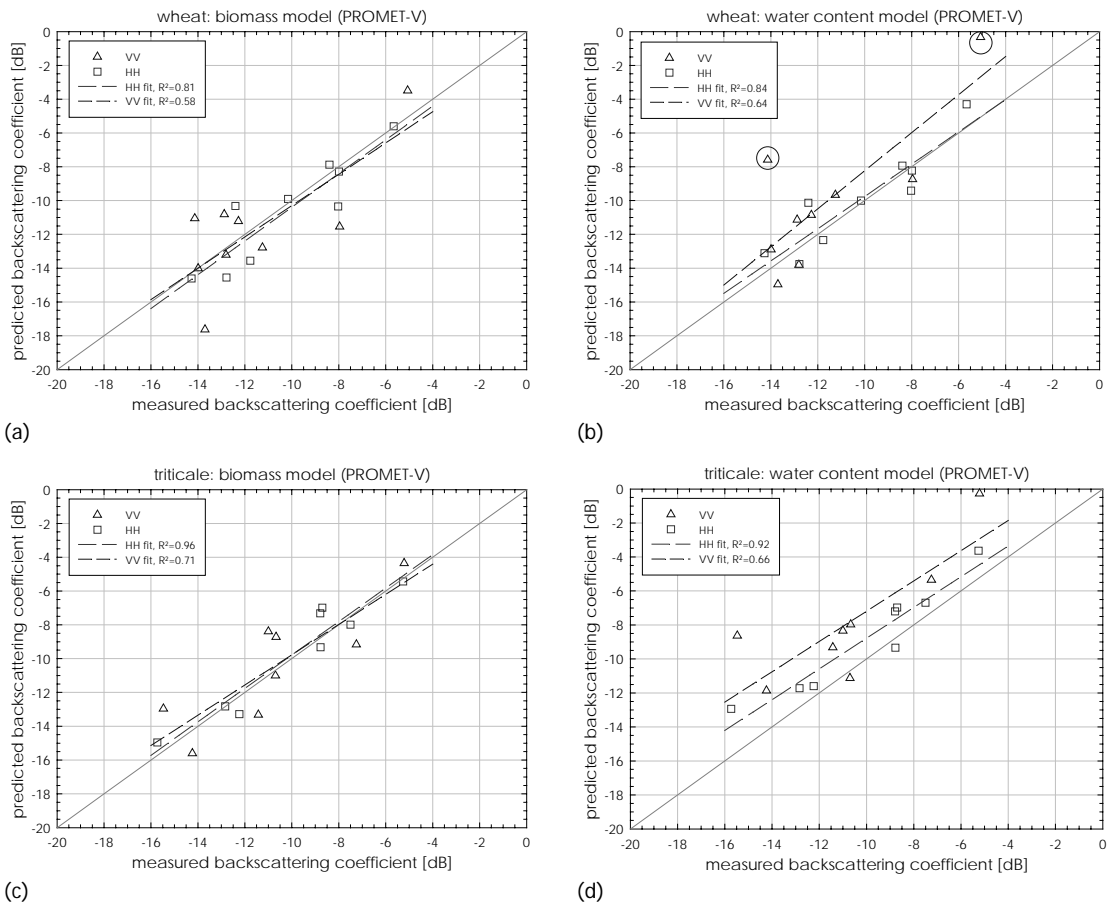
Figure 8.8: Coupled backscatter simulation results for wheat and triticale, based on PROMET-V data, using the biomass and water content model (blue circles: DOY 86 and 92)

Table 8.2: Relationship between modelled and measured backscattering coefficients using PROMET-V

TYPE	POLARIS.	MODEL	LINEAR FIT[†]		R²	RMSE [dB]	⟨Δσ⟩[††] [dB]
			GAIN	OFFSET			
Wheat	HH	Biomass	0.9980	-0.4178	0.81	1.4	1.0
		Wat. Cont.	0.9555	0.1997	0.84	1.1	1.0
	VV	Biomass	0.9269	-1.0302	0.58	2.3	1.9
		Wat. Cont.	1.1265	3.0304	0.64	2.9	2.2
Triticale	HH	Biomass	0.9897	0.1138	0.96	0.9	0.8
		Wat. Cont.	0.9044	0.2639	0.92	1.5	1.4
	VV	Biomass	0.8941	-0.8307	0.71	1.8	1.7
		Wat. Cont.	0.8909	1.7161	0.66	3.5	3.0

[†]predicted backscattering coefficient is the dependant variable

[††]mean deviation

8.3.2 Maize

For the verification of the maize model, only those image datasets can be used, for which PROMET-V simulation results are available. The simulation ended at DOY 181. Thus a total of four image datasets can be used for the analysis.

The field based output of PROMET-V is used to simulate the SAR backscattering coefficient, using the maize backscattering model suggested in the previous chapter. The results are shown in Figure 8.9.
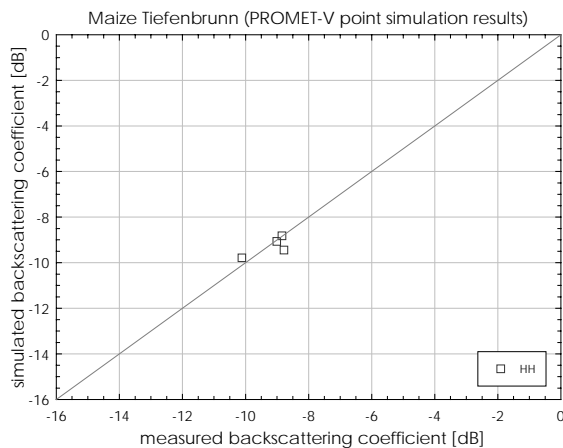
DOY	σ_{meas}	σ_{mod}	$\Delta\sigma$
156	-10.1	-9.8	-0.3
162	-9.0	-9.1	0.1
168	-8.8	-8.8	-0.0
171	-8.8	-9.4	0.6

Figure 8.9:   Coupled maize model prediction results

For this limited dataset the simulation results show good agreement with the measured values. The root mean square error is 0.37 dB. Care has to be taken, when interpretating these results. As has been shown in the previous section, the vegetation height is significantly overestimated by PROMET-V, which must result in an overestimated fraction of the stalk ground interaction term α using (7.10) and should therefore lead to an overestimated backscattering coefficient. The higher vegetation height also results in a higher optical depth τ using (7.12) which partially compensates this effect. Thus the simulated backscattering values show good agreement with the measured values, but are based on an inaccurate model parameterisation. The consequences for spatially distributed backscatter modelling have therefore to be assessed using different test fields. This will be done in section 8.4.

8.3.3 Results

The results on the point scale indicate, that the PROMET-V model can be used in combination with the defined interface as input data source for the backscattering model, to produce reliable estimates of the SAR backscattering coefficients. The vegetation models for cereals and maize were calibrated for the HH polarisation (see 7.1.3 and 7.2.2). Best results are therefore expected for this polarisation type. By using the relationships between the imaging geometry, vegetation height and normalized copol ratio, the VV backscattering coefficient can be estimated for cereals. For low vegetation heights, the VV backscatter is overestimated as has been discussed in section 7.1.4.

Based on the results of this section, the coupled approach is applied for spatially distributed modelling of the backscattering coefficient in the next section.

8.4 Spatially distributed backscatter modelling

Using the spatially distributed time series of land surface variables provided by PROMET-V, a synthetic SAR image can be generated for each model time step. The needed static input variables are a land use and soil texture map and the distributed surface roughness information derived in Chapter 6.

Using the coupled backscattering model, the backscattering coefficient can be simulated for wheat, triticale and maize for any imaging geometry. For each available ENVISAT ASAR image, covering the testsite, a corresponding synthetic SAR image is simulated. This allows to

- assess the accuracies of the modelling approach

- transfer the suggested backscattering models to other fields,

- assess the reliability of the spatially distributed PROMET-V predictions.

Comparisons between the observed and predicted backscattering coefficients can be analysed on a field scale or by direct comparison of each resolution cell. The deviations between modelled and measured backscattering coefficients and their temporal development may be used to derive land surface parameters from SAR images and help to assimilate this information directly to the land surface process model. Different sources of uncertainty, influencing the final coupled model accuracy, can be identified in this context.

8.4.1 Sources of uncertainty

It is obvious that each modelling process has a remaining level of uncertainties, resulting in residuals between predicted and observed variables. In the case of the coupled backscattering model, proposed in this chapter, the sources of uncertainty can be allocated as follows:

Spatial datasets

The basis to all spatial modelling approaches is an accurate geographical information system. It is needed for the land surface process model as well as for the backscatter simulations. Until now, it is difficult to obtain reliable information about the spatial distribution of *soil texture*. Nevertheless, soil texture is a key parameter in the modelling process. It is used to estimate the volumetric water content of the top soil layer and is also necessary for the conversion of soil moisture to the dielectric constant.

The *roughness map*, derived in Chapter 6 was calculated with the best available datasets, under the assumption, that no change in surface roughness and vegetation cover occurred between the observations. The promising results, obtained with the derived A_0 values (see 6.5), indicate that this dataset is a reliable estimate of the surface roughness components affecting the backscatter. Nevertheless, an uncertainty remains about the correct roughness estimate for each pixel.

The *climatic data* is known to have measurements errors. Especially the measurement of precipitation is difficult and the error can exceed 20 % if significant wind drift occurs. It has to be interpolated from point measurements to precipitation fields, which is a source of additional error.

Land surface process model (PROMET-V)

Each model is a simplification of the real physical processes. It has been shown, that PROMET-V is capable to provide reliable results for the description of plant growth when comparing it to ground measurements. Nevertheless some major simplifications need to be addressed. The model output variables are aggregated to daily values[1]. This can lead to deviations between the SAR observed soil moisture values and those simulated by PROMET-V, especially in case of rainfall after the sensor pass on the same day.

---

[1] Generally, the model allows for the generation of output variables for any given temporal resolution (e.g. each hour). This leads to huge datasets which are difficult to handle. As a compromise, daily model output was chosen for the investigations.

Model Interface

The interface, used for the translation of PROMET-V variables to the backscattering model is also a source of uncertainty. Soil moisture has to be converted to the dielectric constant using an empirical *dielectric model* (see 3.2.2).

The *vegetation water content* is derived using an empirical relationship between the VWC and the LAI. This relationship, given by (8.2), determines 86 % and 67 % of the variance for maize and cereals respectively. Thus the rest of the variance remains unexplained by the model.

Backscattering model

The *bare soil backscattering model* suggested in Chapter 6 is based on theoretical simulation results, using the Integral Equation Model (IEM). It is therefore limited to the validity range and accuracy of the IEM. Additional uncertainties result from the incidence angle normalization procedure. As discussed in section 6.3.3, these deviations are below 1 dB.

The calibration of the *vegetation backscattering models* is based on ground measurements taken from the test fields, which also have a limited accuracy. The sampling concept, using three sample points per field, is an approximation to the true variability within a test field. The heterogeneities within the field, as observed by the SAR sensor can not be measured appropriately. The backscattering coefficient of a test field is obtained by averaging various image pixels. Thus, the backscattering value, used for the model calibration is an averaged value with a related backscatter variance.

SAR image data

The SAR image datasets must also be considered a possible source of uncertainty. All used image datasets were preprocessed using the best available geometric and radiometric correction methods. Datasets, which didn't seem to be trustworthy, were not used for the investigations (e.g. IS1 calibration problem, see 4.2.3). The geometric distortion of the data is expected to be below one resolution cell. Nevertheless, misalignments can occur, resulting in deviations – especially, when comparing modelled and simulated data on a pixel by pixel basis. The radiometric accuracy of the sensor is reported in the literature (see 4.2.2) and lies between 0.5 and 1.0 dB.

Beyond these uncertainties, the coupling approach has already proven its applicability on the point scale and is applied for the generation of spatio-temporal series of the backscattering coefficient next.

8.4.2 Modelling approach

For all available SAR images, a corresponding simulated backscatter image is generated. As discussed in section 8.2, the soil moisture simulations of PROMET-V didn't correspond well with the field measurements until DOY 130. To investigate the effect on the SAR simulation results, the first image, considered for the simulations was recorded on DOY 92 (2.4.2003). A total of nine images, given in Table 8.3, are used for the analysis.

The backscattering coefficient is calculated for all supported field crops, namely wheat, triticale and maize, using daily aggregated output data of PROMET-V. To reduce the uncertainties introduced by the backscattering model, the simulations are carried out using the dry biomass for the parameterisation of the vegetation scattering properties of cereals. Since the maize model is only valid for HH polarisation and the cereal vegetation scattering model also provided more reliable results for the HH polarisation, all simulations are done for this polarisation.

Table 8.3:   ENVISAT ASAR images used for coupled backscatter modelling

DATE	DOY	DIRECTION	INCIDENCE ANGLE [°]
02.04.2003	92	ASC	18.9
11.04.2003	101	ASC	39.2
24.04.2003	114	ASC	29.9
01.05.2003	121	DESC	43.0
07.05.2003	127	DESC	32.7
05.06.2003	156	DESC	43.0
11.06.2003	162	DESC	32.8
17.06.2003	168	ASC	33.2
20.06.2003	171	ASC	39.3

8.4.3 Simulation results

The simulated SAR images can be directly compared to real SAR imagery. Only those pixels containing information in the SAR image and at the same time information on the land surface simulation results, are used for the comparison. An example of a simulated SAR scene is given in Figure 8.10. The complete detailed simulations results are given in Appendix F. The fields with available simulation results, corresponding to wheat, triticale and maize, are extracted from the original image dataset for better comparability. It can be seen, that the backscattering coefficients have the same magnitude and even similar features can be observed in both datasets.
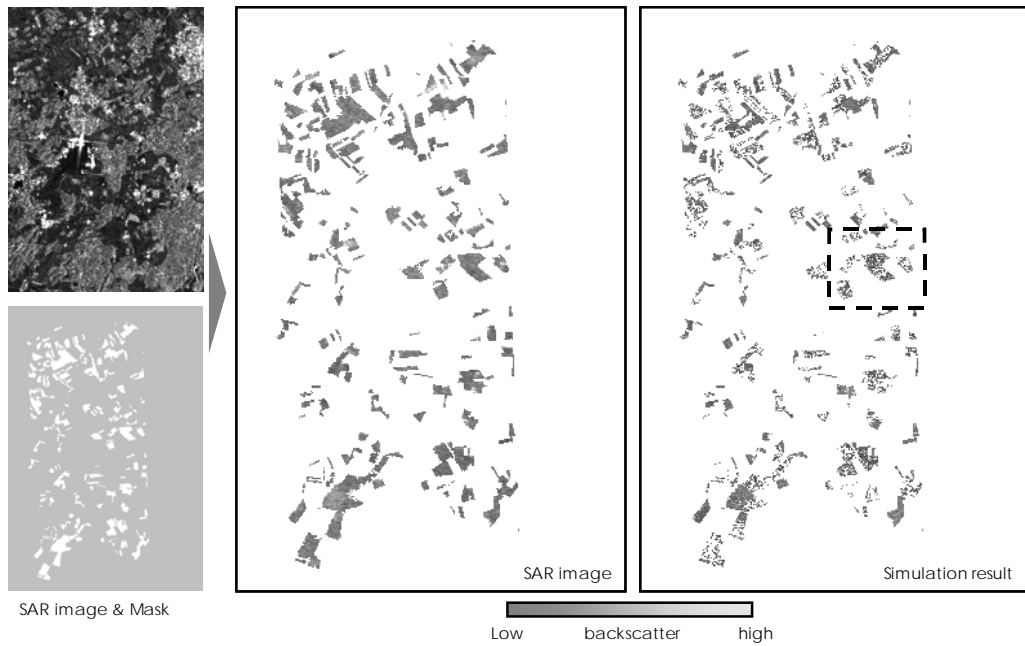
Figure 8.10: Simulated and observed SAR image (05.06.2003, DOY156); the original image is masked to simplify comparisons with the modelling results (an enlarged Figure can be found in Appendix F)
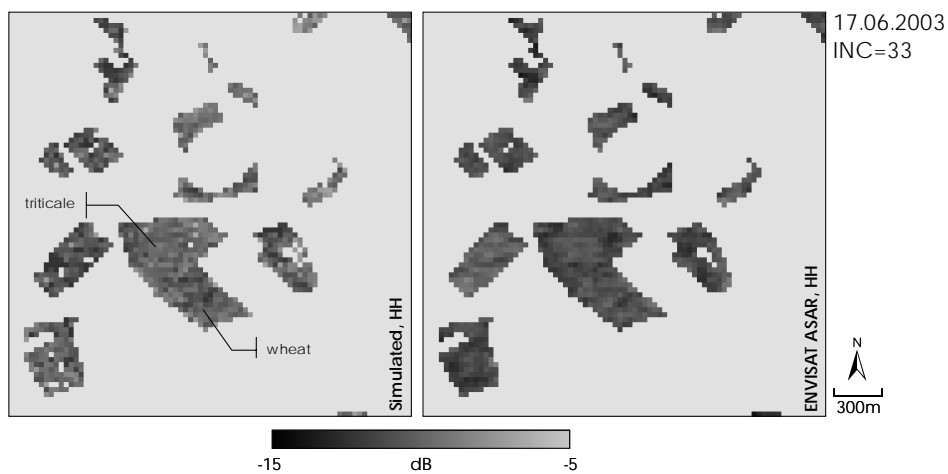
Figure 8.11: Example of simulated (left) and real (right) SAR image at Gut Huell

A more detailed example, covering the area around the test fields at *Gut Huell* is given in Figure 8.11. The simulation results show several voids, which result from invalid simulation parameters or backscattering model results. These occur when no vegetation height is provided by PROMET-V or a VWC value is calculated using (8.1), which is less than zero.

The accuracy of the simulated backscattering coefficients is assed by correlating simulated and measured backscattering coefficients and by analysing the residuals. This is done for all dates on a pixel by pixel basis without any filtering applied to the datasets, which is the most sophisticated approach. Figure 8.12 shows the pixelwise correlation of the simulated and measured backscattering values and the frequency distribution of the residuals for all images used for the investigation. Positive residuals indicate an overestimation of the backscattering coefficient by the model and vice versa.
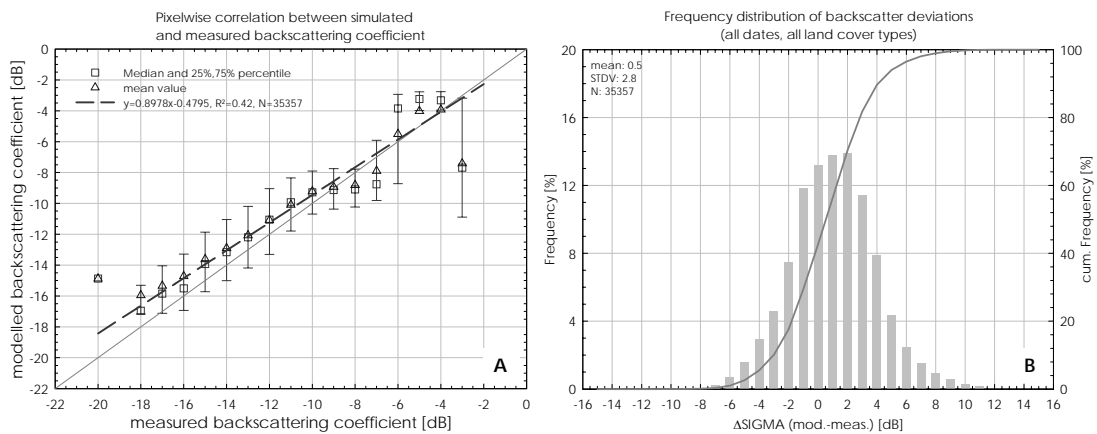
Figure 8.12:   Pixelwise analysis of the simulation accuracy for all dates and land cover types: (A) correlation between simulated and measured backscattering coefficient (bars indicate the 25% and 75% percentiles); (B) Frequency distribution of backscatter residuals

It can be seen, that the backscattering coefficients are generally well predicted by the backscatter model. The gain of the regression line is almost unity. The residuals are normally distributed with an average of 0.5 dB. The residuals have a standard deviation of 2.8 dB. Around 70% of all values are within the interval of ± 2 dB. It can be seen from Figure 8.12a, that the variances are rather similar for the backscatter range, corresponding typically to agricultural fields (-18 ... -6 dB, see also e.g. Figure 7.1)

This indicates, that the model generally provides good estimates of the backscattering coefficient. The simulated input parameters, provided by PROMET-V, have lower dynamics within an agricultural field than in reality. The reason is that the land surface model input parameters as e.g. soil texture are rather homogeneous over larger areas. In reality, the microscale variations of soil hydrological properties are more heterogeneous. Due to similar other input variables, as e.g. temperature and precipitation fields, the land surface model predictions have a lower spatial variance than in reality.

This can lead to deviations of the simulated backscattering coefficient. The typical standard deviation of the observed backscatter, within agricultural fields, ranges between one and two decibels, dependant on the size of the field, which is comparable to the standard deviations of the observed residuals. The deviations between simulated and observed backscattering coefficients might be used to enhance land surface model parameterisation. This will be discussed later in section 8.4.4.

The frequency distributions of the residuals of individual observation dates are given in Appendix F. All show a similar gaussian frequency distribution with standard deviations between 1.5 and 2.9 decibels. Figure 8.13 gives an overview of the temporal characteristics of the residuals for each simulated scene.
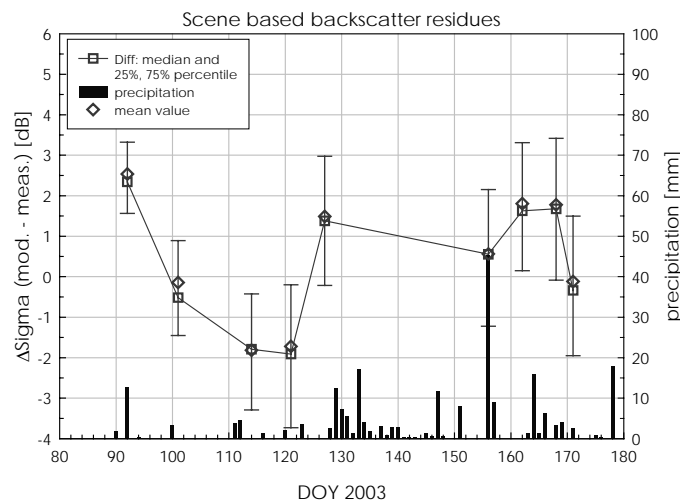
Figure 8.13: Scene based backscatter residuals (pixelwise comparison): median (squares), mean values (diamonds), 25 %, 75 % percentiles (bars)

The figure shows for each image date the median value and corresponding 25 % and 75 % percentiles of the backscatter residuals. These are calculated on a pixel by pixel basis. Each sample corresponds to more than 3000 image pixels from heterogeneous fields and soils. It can be seen, that the variance of the residuals is almost equal for all dates. A temporal development of the residuals can be observed. These can be partly interpretated as the result of an imprecise soil moisture prediction of PROMET-V. It is underestimated on DOY 114 and DOY 121, as was already mentioned in section 8.2, resulting in an underestimation in the simulated backscattering coefficient (see e.g. Figure 8.5). The high positive residual on DOY 92 can be explained by rain during and after the sensor pass.

Field based analysis

To investigate the transferability of the method to other fields and to discriminate the sources of deviation between modelled and measured backscattering coefficients, a more detailed, field based analysis is carried out. To get a general impression about the possible deviations, the average backscattering coefficient is calculated for all wheat, triticale and maize fields larger than 1.5 ha (more than 20 image pixels). The results are shown in Figure 8.14 for each date. It can be seen, that the backscattering model predictions generally show good agreement with the measured values. The gain of the regression line is almost unity. The mean deviation is 0.9 dB with a corresponding standard deviation of 2.0 dB and a rms error of 2.2 dB. The deviations are not systematic, but show differences between the observation dates. Low deviations can e.g. be observed at DOY 101, while there are larger residuals at e.g. DOY 168. This may be explained by a temporally changing model input parameter which affects the variability between different fields of the same land use.
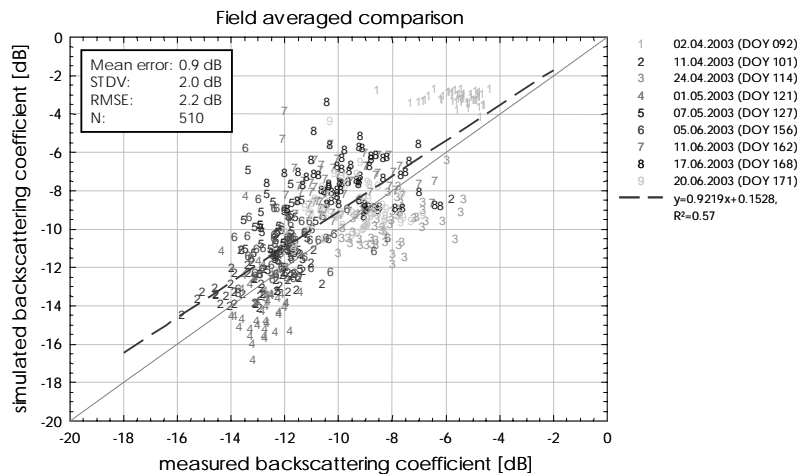
Figure 8.14:   Comparison between modelled and measured field averages

To examine this effect, the backscattering behaviour of different fields of the same crop type are analysed. Four test fields are therefore selected within the test area for cereals and maize respectively. Additionally the backscattering variability of the investigated test fields, used for the model calibration, namely the wheat and triticale fields at *Gut Huell* and the maize field at *Tiefenbrunn*, are analysed. The locations of the fields are shown in Figure 8.15 together with the corresponding soil texture map. Each field has a unique identification number.
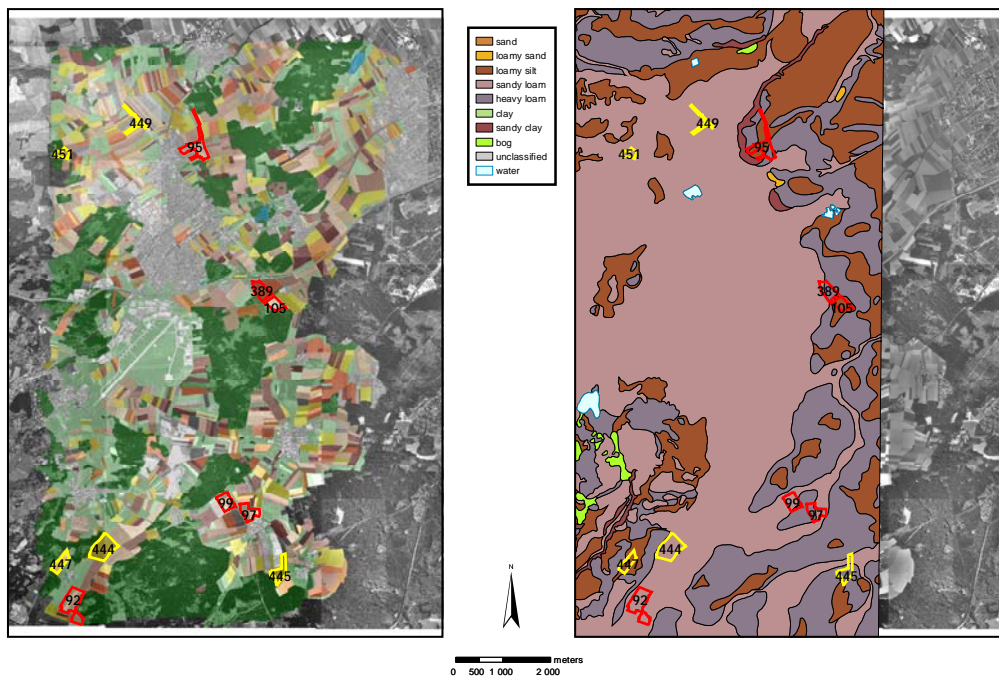
Figure 8.15. **Location of the test fields, used for detailed investigations and corresponding soil texture map; red: cereals, yellow: maize; see also Figure 5.2**

Cereals

The statistics of the backscattering coefficients are extracted from the modelled and measured image datasets for each field. A comparison between the modelling result and measured values for the cereal test fields at *Gut Huell* is given in Figure 8.16. To account for the intra field variability, the median value, as well as the 25% and 75% percentiles are calculated, which are represented by the boxes. The total data range is represented by the whiskers in the diagram.
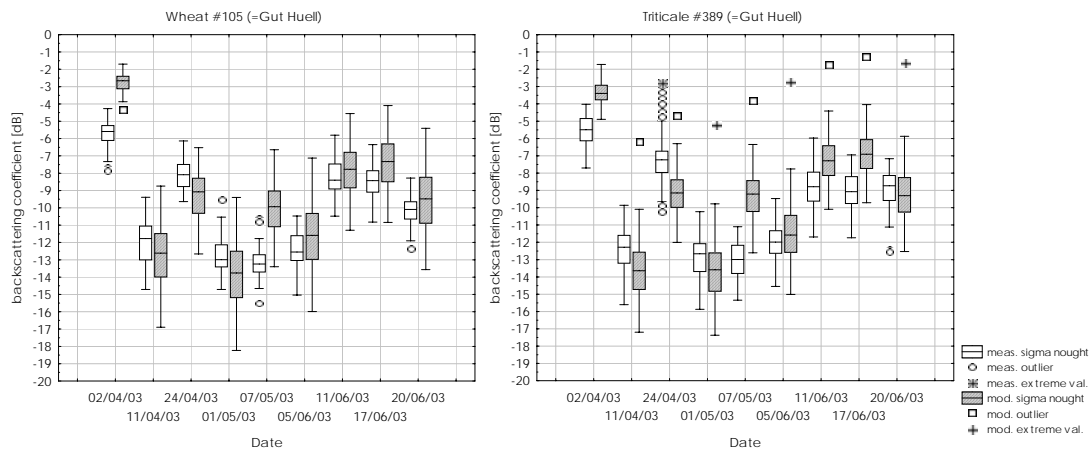
Figure 8.16: **Modelled and measured backscatter variability for wheat and triticale test fields at Gut Huell (investigation fields)**

The intra field variability and magnitude of the data is well reproduced by the backscattering model. Higher deviations can be observed on the 2nd of April and the 7th of May. The triticale field shows slightly higher deviations of the modelled backscattering coefficient than it can be observed for the wheat field (e.g. on 11.06.2003).

The extracted statistic for the other cereal test fields is shown in Figure 8.17 in the same way. The dynamic range of the measured backscatter is also well reproduced for these fields. Field #92 shows best agreement between measured values and modelling results. All test fields show an underestimated modelling result on 1st of May. The fields #95, #97 and #99 all show an overestimated modelled backscattering coefficient on 11th and 17th of June, while field #92 also agrees well with the measured values on these dates.
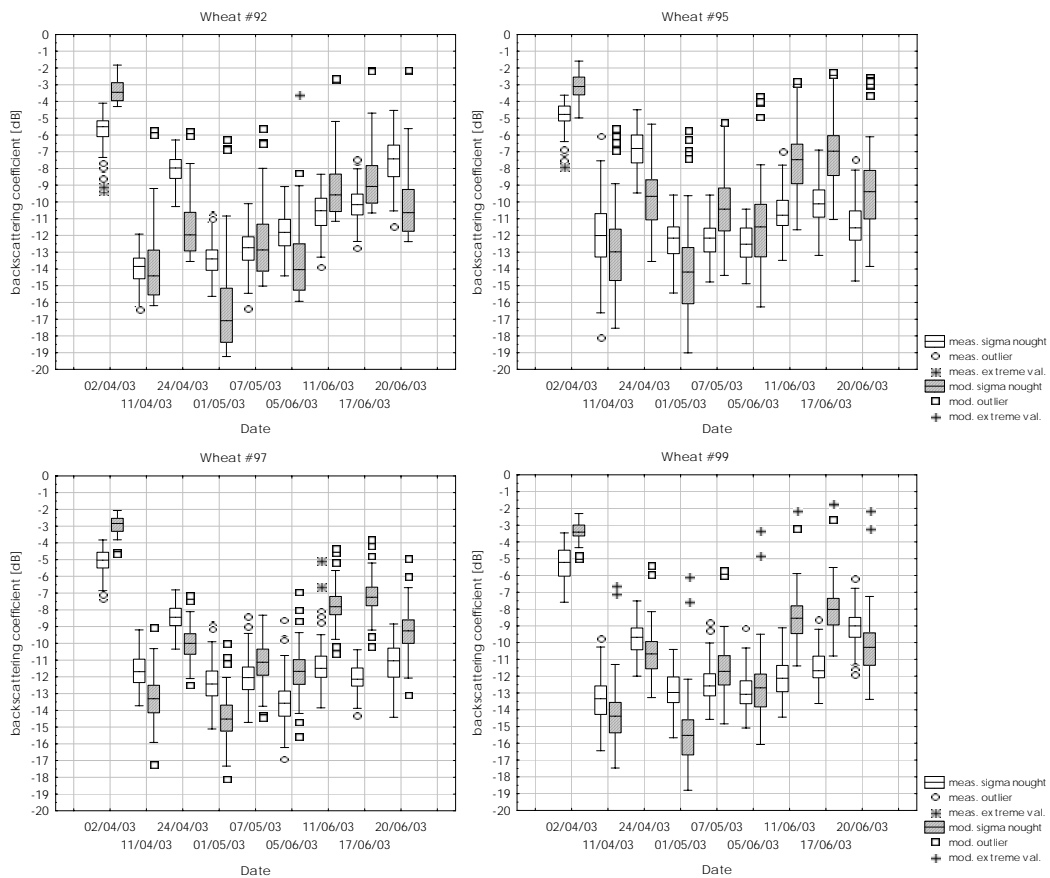
Figure 8.17: **Intra field backscatter variability for selected cereal test fields**

Maize

The reference maize field in Tiefenbrunn, used for the calibration of the maize backscattering model, has shown good agreement of the backscattering coefficients on the point scale (see 8.2.4). It is therefore expected to have similar accuracies when spatially distributed modelling is performed. This is confirmed by the field statistics shown in Figure 8.18.
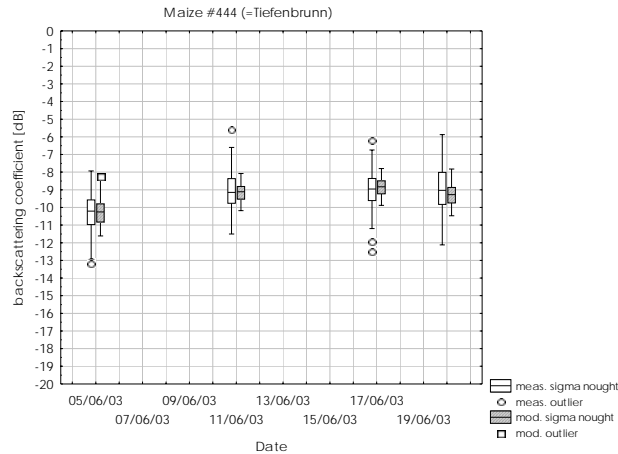
Figure 8.18:   Backscatter comparisons for maize field Tiefenbrunn

Compared to the wheat and triticale field, the measured backscattering coefficients have a lower dynamic range. The variability between the different observation dates, as well as the intra field variability is lower than in nature which is the result of a higher optical depth, simulated by the model. The generally good correspondence of the expected values is an indication for the functionality of the defined PROMET-V interface, despite the problem of overestimated height values.

The maize model was calibrated, using only a single test field. Therefore, it is of special interest, whether the maize backscattering model also provides reliable results on other maize fields. The backscattering statistics of the four other selected maize fields, shown in Figure 8.15, is given in Figure 8.19.

A good agreement between modelled and measured SAR backscatter can be stated. The simulated backscatter values show a lower variability than the measured ones, which is in agreement with the observations made on the calibration test field at Tiefenbrunn. A systematic deviation can be observed for field #445, where the modelled backscattering coefficients are overestimated on all dates. No significant differences can be found for the fields #447 and #449. For field #451, an underestimation of the backscattering coefficient can be observed for the 17th and 20th of June.
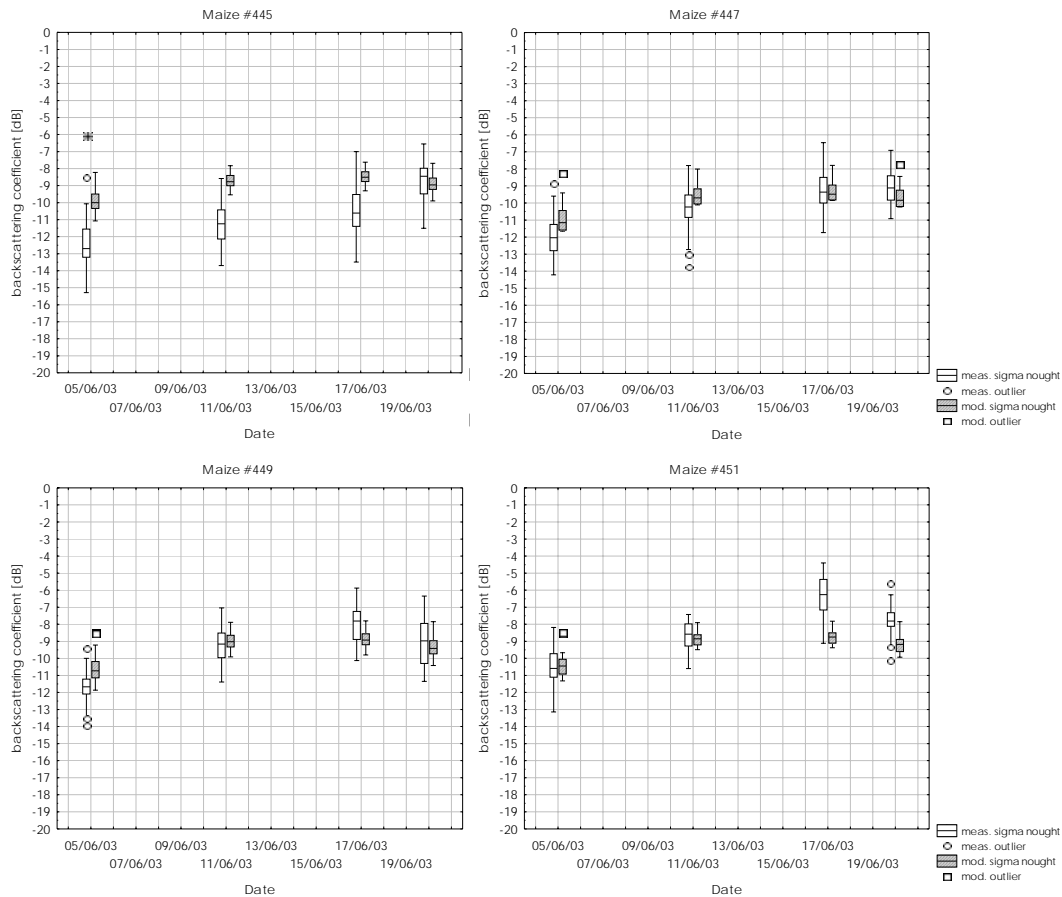
Figure 8.19:   Backscattering statistics of selected maize fields

8.4.4 Discussion

It has been shown, that the coupled modelling approach provides reliable results in most cases. The analyses were made on a pixel-by-pixel basis, which is the most sophisticated approach, because even small geometric distortions have an influence on the results.

The good performance of the model for most of the pixels and also most of the test fields is an indication, that the used surface roughness map (see 6.5) is of high quality. The backscattering model and model interfaces are well suited to provide reliable results. It has been shown, that certain systematic deviations of the backscattering coefficient can be observed on the field scale for cereals, as well as for maize.

These may be the result of imprecise input parameters to the backscattering model. The fact, that a systematic over- or underestimation of the backscattering coefficient can only be observed on certain dates, leads to the assumption that a temporally variable input parameter might be the major source of uncertainty.

A seasonal parameter, with a sustainable effect on the simulation results is soil moisture. Soil moisture values of the upper soil layer (5 cm), provided by the land surface model, are used for the backscatter simulations. Soil texture has a strong influence on the simulated volumetric moisture content in this context. As a result the soil texture map is clearly visible in the simulated soil moisture values, as shown in Figure 8.20.
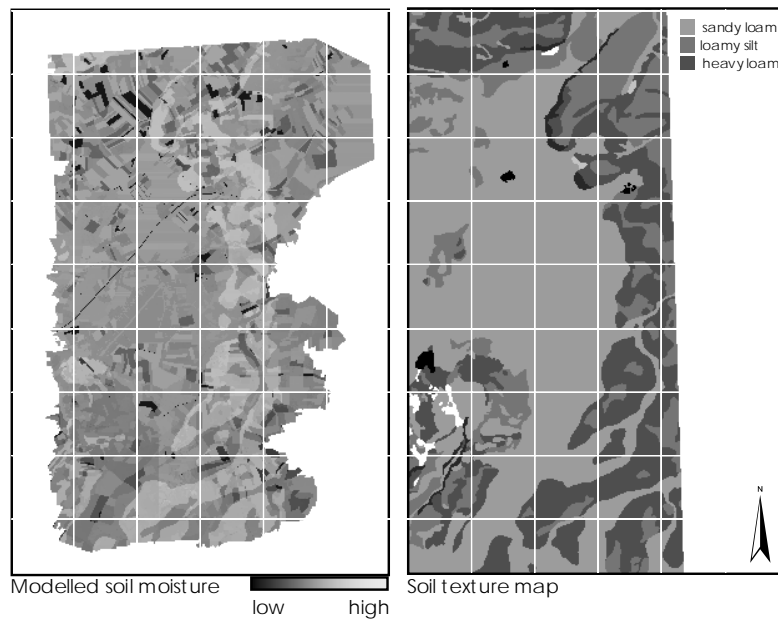
Figure 8.20:   Dependency of simulated soil moisture (left) on soil texture (right)

Beyond this direct effect on the simulation results of the land surface model, the soil texture is also used to relate the volumetric moisture content of the soil to its dielectric properties (see 3.2.2), which can result in significantly different simulated backscattering coefficients for the same soil moisture value.

It is remarkable, that the test fields with higher model deviations (e.g., #95, #97, #445), have soils with a higher clay content, while those with only slight differences are situated on more porous soils. The fact, that the wheat fields #95, #97 and #99 all show overestimated simulation results after a short rain period (see Figure 8.13) denotes that the soil moisture dynamics is not well reproduced by the land surface model. The soil moisture dynamics of the upper soil layer, corresponding to the sensitivity range of the SAR system, seems to have higher dynamics than that simulated by the land surface model. Currently, all soil layers in the land surface model are parameterised in the same way with the same soil texture. Due to missing additional soil information this is a main drawback.

Some deviations as e.g. for maize field #451 on 17th and 20th of June can not be explained by means of imprecise soil moisture predictions (see Figure 8.19). These deviations remain unexplained. No precipitation event or other model uncertainties could be identified for this field. The fact, that the backscattering coefficient is simulated accurately for the first two dates and then shows a systematic deviation which can not be explained by model uncertainties, reveals that other influences might also have to be considered as e.g. land use practice by the farmer.

The fact, that the soil moisture dynamic is observable with SAR imagery and that it can be detected by the modelled backscatter residuals, may help to provide information about the soil hydrological properties and soil moisture content. Latter is shown in the following section.

8.5 Soil moisture inversion using coupled modelling

It has been shown, that the proposed forward backscattering model provides good results for point as well as for spatially distributed modelling. The differences between the simulation results and observed SAR backscatter might be used to derive land surface parameters directly from the SAR images. In the following, the derivation of soil moisture from ENVISAT ASAR data is investigated, using the coupled modelling approach. The results are compared to *in situ* soil moisture measurements of the field campaign.

8.5.1 Approach

To derive soil moisture from ENVISAT ASAR alternating polarisation datasets, a simple iterative inversion strategy can be used. The backscattering models need informations about the soil moisture state and vegetation parameters. If vegetation parameters are provided by a land surface process model, the soil moisture is the only remaining unknown variable. Using the coupled modelling approach, discussed in the previous sections, the such generated synthetic SAR images can be compared with ENVISAT ASAR observations. By changing the soil moisture value, until best coincidence between measured and simulated backscattering coefficients is achieved, the soil moisture of the upper soil layer can be determined.

The amount of soil water is unknown for each image acquisition, while the extinction properties of the canopy can be determined for cereals from the image data, using the copol ratio $\sigma_{HH}^0 : \sigma_{VV}^0$ (see 7.1). In the case of maize, additional information about the vegetation water content is needed.

The investigated soil moisture value m_v is restricted to a certain predefined soil moisture range Δm_v. Theoretically it can range between the wilting point and

saturation. If *a priori* information about an initial soil moisture value m_{init} is available, as e.g. from PROMET-V simulation results, this can be used to restrict the range of possible valid solutions to improve the inversion accuracy.

The backscattering coefficient is simulated for distinct soil moisture values within the predefined validity range, with and without initial soil moisture information. By minimizing the error E between the simulated and measured backscattering coefficients $\hat{\sigma}_{HH}^{0}$ and σ_{HH}^{0}, an estimate of m_v becomes possible. The best solution is found if it satisfies the condition

$$E(m_v) = \min\left\{\left|\hat{\sigma}_{HH}^{0} - \sigma_{HH.}^{0}\right|\right\} \quad with \quad \left|m_v - m_{init}\right| \leq \Delta m_v = f(\Delta \in_r) \qquad (8.4)$$

where $\Delta \in_r$ is the possible range of the dielectric constant. The result of this inversion strategy is the soil moisture value which corresponds to the smallest backscatter deviation.

8.5.2 Derivation of soil moisture from ENVISAT ASAR alternating polarisation data

To derive soil moisture from the image data, PROMET-V results are used to parameterise the vegetation height and water content. The soil moisture is then derived twice from the image datasets. Once, no *a priori* information about the actual soil moisture conditions is provided to the algorithm. All possible soil moisture solutions between the wilting point and saturation are possible (*simple approach*). The second inversion uses the soil moisture information of PROMET-V as an initial estimate of the true value which is then converted to the dielectric constant. A predefined validity range of $\in_r \pm 30\%$ is allowed for possible inversion solutions (*a priori approach*)[1]. The possible range of ±30% is chosen to allow for a validity range, which guarantees, that the initial soil moisture value has an effect on the inversion results, without being too restrictive.

The soil moisture, calculated for each image pixel, is then derived by minimizing the error between simulated and measured backscattering coefficient. Only the soil moisture values within the predefined validity range are considered. The inversion approach is validated using the same image datasets as in the previous section. Table 8.4 gives an overview about the image datasets and availability of soil moisture ground measurements.

---

[1] example: if the dielectric constant of the initial soil moisture value is 20.0, the dielectric constant of the solution can range from 14.0 to 26.0

TABLE 8.4:   SAR IMAGES USED FOR SOIL MOISTURE INVERSION

DATE	DOY	REFERENCE SOIL MOISTURE AVAILABLE		
		Tritcale	Wheat	Maize
02.04.2003	92	✓	✓	
11.04.2003	101	✓	✓	
24.04.2003	114	✓	✓	
01.05.2003	121	✓	✓	
07.05.2003	127			
05.06.2003	156		✓	
11.06.2003	162	✓	✓	
17.06.2003	168	✓	✓	✓
20.06.2003	171	✓	✓	✓

8.5.3 Results

An example of the derived soil moisture maps is shown in Figure 8.21 for both approaches. It can be seen, that the two maps differ significantly. The *simple* inversion approach leads to highly variable inversion results, corresponding to the solution with the smallest simulation error. The SM values cover the whole possible soil moisture range. Using the *a priori* information of the land surface model, the spatial distribution of the soil moisture values is less variable. Neighbouring image pixels show similar inversion results.

A detailed view of the area around *Gut Huell*, where the test fields are situated, is given in Figure 8.22. It shows a truecolor representation of an aerial hyperspectral image of the area, acquired by the AVIS sensor (MAUSER and OPPELT, 2001) with a spatial resolution of four meters and the soil moisture inversion results of the same area. The AVIS image shows a bright structure in the investigated triticale field, corresponding to an area with coarser grain size distribution of the soil particles. The same structure can also be observed in the inverted soil moisture image, where lower soil moisture values are detected from the SAR image. Thus, information about the underlying soil is visible in the inverted soil moisture maps.
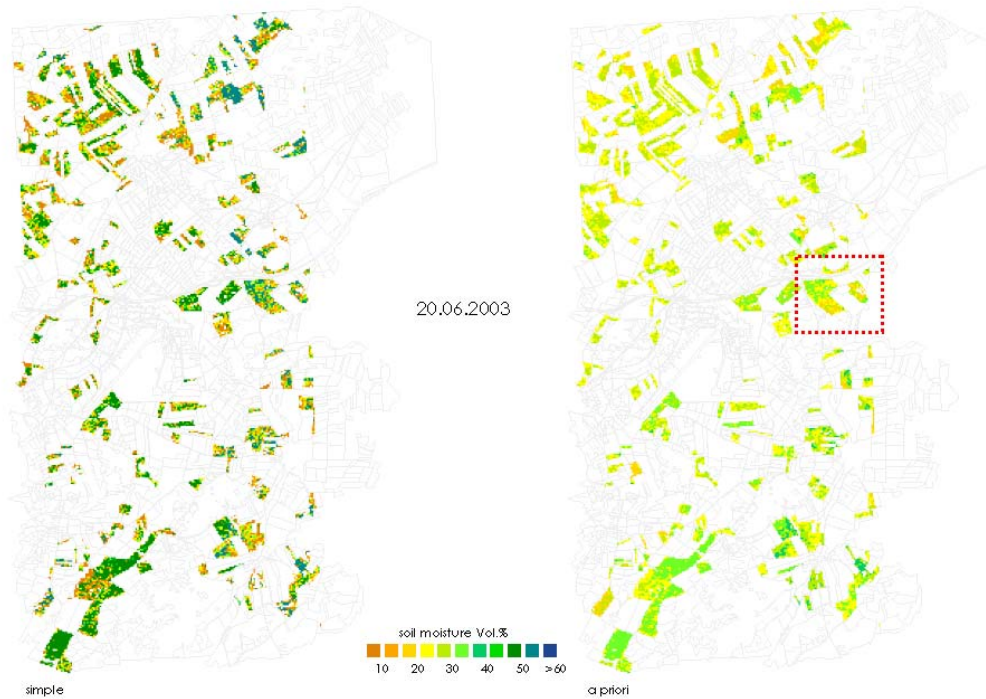
Figure 8.21: **Soil moisture map (20.06.2003):** *simple* **approach (left) and** *a priori* **approach, using inital soil moisture values (right)**; **enlarged version can be found in Appendix F**
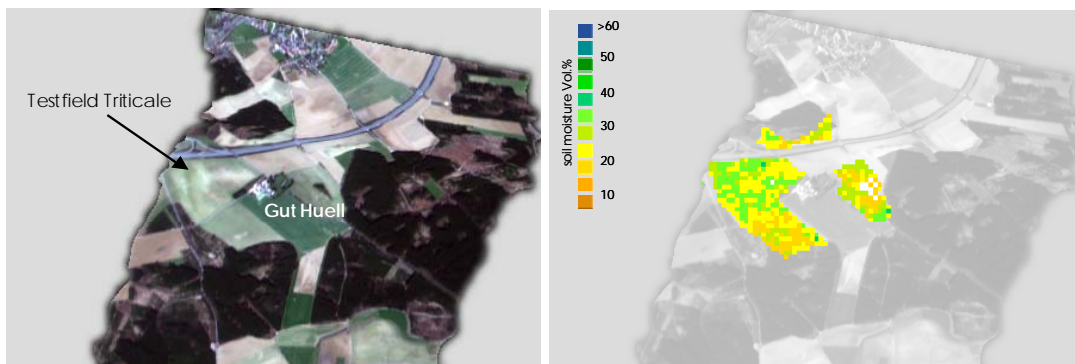
Figure 8.22: **Detailed soil moisture result of 20th of June 2003 (right), compared to an aerial AVIS image (left) around Gut Huell (16th of April 2003)**

To assess the accuracy of the soil moisture inversion results using the *simple* and the *a priori* approach, comparisons with in situ measured soil moisture values are conducted. To take into account the intra field variability of the soil moisture values, the histograms of their distributions are calculated for each field. Figure 8.23 shows an example of the soil moisture frequency distribution for both inversion strategies. Additional information about the initial soil moisture value, as well as the results of the TDR field measurements are shown. The width of the ground measured soil moisture value bars indicates the standard deviation of the samples, resulting from the three sampling points within each test field.
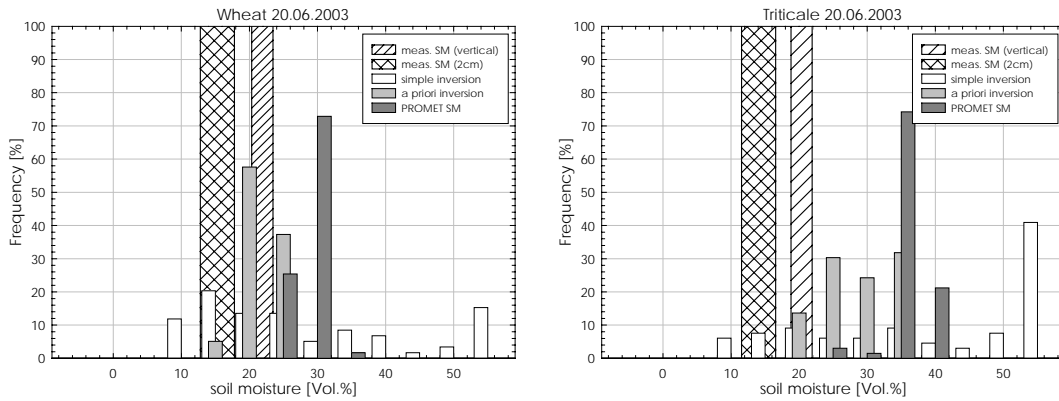
Figure 8.23: **Soil moisture frequency distributions for cereal fields on DOY 171. white:** *simple*, **light grey:** *a priori* **inversion approach; dark grey: initial soil moisture value, width of the in situ measured soil moisture value indicate the measured standard deviation**

It can be seen, that the results of the *simple* inversion approach have a frequency distribution, which covers the entire possible soil moisture range. The distribution of the *a priori* approach has an unimodal shape with a more accentuated modal value.

The *a priori* approach shows good agreement with the measured soil moisture values for the wheat field. The inversion results for the triticale field show larger deviations from the measured soil moisture values. It can be seen, that the inverted soil moisture of the *a priori* approach is overestimated by the algorithm. The reason is the highly overestimated initial soil moisture value provided by PROMET-V. Due to the restricted possible soil moisture range, used within the *a priori* method, the inversion procedure wasn't able to invert the soil moisture correctly. It converged to the lower boundary of the possible soil moisture data range. The overestimated soil moisture prediction by PROMET-V may again be a result of the imprecise parameterisation of the soil hydrologic conductivity of the upper soil layer (see 8.4.4 and Figure 8.15).

The histograms of the other fields and dates are given in Appendix F. They all show a similar behaviour. The modal value of the *a priori* approach generally agrees better with the measured soil moisture values of the upper soil layer. On some dates, higher deviations, similar to the example shown in Figure 8.23, are observable, which are the result of an overestimated initial soil moisture value.

To quantify the obtained soil moisture inversion accuracy, a direct comparison between the observed and measured soil moisture values is made. Due to the asymmetrical frequency distributions of the soil moisture values, the median value is expected to be the best discriminator for the expected value (LOZÁN and KAUSCH, 1998). Figure 8.24 shows the median value of the inverted soil moisture for all test fields and observation dates, compared to the in situ measured soil moisture values.

Comparisons are made for the vertical TDR samples, as well as for the horizontal measurements, made in 2 cm depth[1]. The detailed values are tabulated in Appendix F.

Distinct difference between both inversion approaches have been observed by comparison of the soil moisture histograms. The *a priori* approach provided more accurate inversion results. This difference is reduced, when the median value is used for the expected value of the whole field.
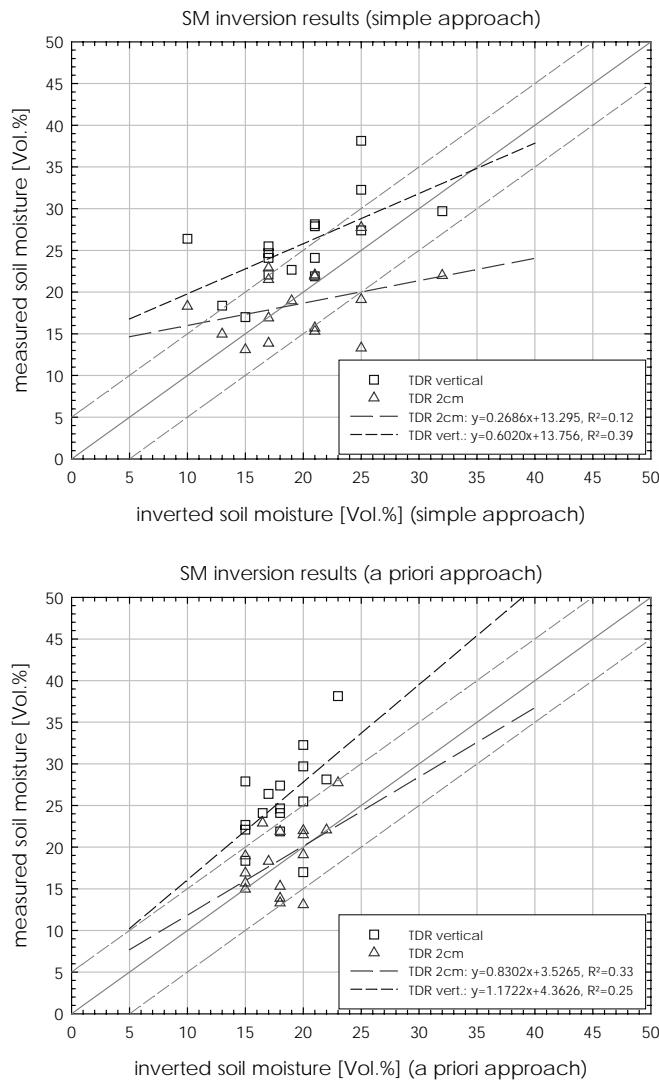
Figure 8.24: **Soil moisture inversion results; a)** *simple* **approach b)** *a priori* **approach**

---

[1] Note, that the inverted soil moisture values are shown on the abscissae for better readability of the diagram.

Table 8.5:   Relationship between inverted and in situ measured soil moisture values

METHOD	TDR VERTICAL			TDR 2cm		
	Gain / offset	R²	RMSE [Vol.%]	Gain / offset	R²	RMSE [Vol.%]
simple	0.6020 / 13.756	0.39	7.4	0.2686 / 13.295	0.12	5.5
a priori	1.1722 / 4.362	0.25	8.5	0.8302 / 3.526	0.33	3.5

A positive correlation between measured and derived soil moisture values can be observed for both approaches. The vertical *in situ* soil moisture measurements have higher values than the inversion results. This indicates, that the SAR sensors penetration depth is smaller than the sampling depth of the vertical TDR probe (~120 mm). Thus for the examples shown, the underlying soil has a higher moisture content than the uppermost centimetres, which is confirmed by the comparison of the measured 2 cm and vertical TDR probes.

The coefficients of determination are rather small for the linear regressions between inverted and measured soil moisture values (Table 8.5). Nevertheless, the inversion results are almost all within ±5 Vol.% of the expected value, and therefore within the intra field variability of the *in situ* soil moisture measurements. Best results, with an RMSE of 3.5 Vol.% are obtained for the inversions of the *a priori* approach, compared to the soil moisture measurements of the upper 2 cm. This accuracy is comparable to results reported in the literature (see 3.4.1).

Due to the dry period in 2003, most of the soil moisture values are within the lower part of the possible soil moisture spectrum. The model can therefore not be validated for higher soil moisture values. Due to the separate soil and vegetation backscattering models, it is expected, that the method is transferable also to higher soil moisture values, which would not have been possible with a simple empirical model.

The results show, that spatially distributed soil moisture maps can be generated by applying the proposed inversion scheme. Additional information about the initial soil moisture content of the upper soil layer can help to improve the inversion results. This becomes more obvious when the histograms of the derived soil moisture results are directly compared to the *in situ* soil moisture measurements. The spatial patterns of the *a priori* results are more reliable. Adjacent image pixels have similar soil moisture values, while extremely different solutions can be observed, if no initial information is used. Deviations between observed and inverted values result not only from the uncertainties of the inversion model, but also from the intra field

variability and the difficulty to transfer the point measurements of a TDR probe to the resolution cell size of a SAR system. Thus, the validation of the inversion accuracy becomes difficult, if the soil moisture shows low dynamics, as it is the case in 2003, and if the inversion results scatter within the natural variability of the investigated parameter.

A drawback of the recommended *a priori* inversion algorithm is the dependency on the quality of the initial soil moisture value. Due to the fact, that the inverted soil moisture is restricted to a predefined range, a false initial value can lead to unsatisfactory inversion results even if the SAR image contains the correct information about the soil moisture condition.

The current algorithm only minimizes the deviation between the modelled and measured backscattering coefficient by changing the soil moisture value within a predefined range. The result is the *best* estimate within the interval. By taking into account additional information about uncertainties of the model input variables, such as vegetation height, biomass and soil moisture, and also by adequate weighting of the resulting backscattering residuals, the possible range of valid soil moisture solutions might be dynamically adjusted for each image pixel during the inversion procedure. The outcome of such an approach would be the probability density function for the soil moisture values of each pixel. Thus, not the *best*, but the most *probable* soil moisture value would be inverted by such an approach, which might help to minimize the errors introduced by an inaccurate initial soil moisture value.

Chapter 9
Conclusions - Towards an improved synergistic spatio-temporal characterization of land surface variables from remote sensing data

The preceeding chapters have shown, that valuable information about the state of the land surface can be derived from microwave remote sensing data. Sensors with multiple imaging capabilities, as e.g. ENVISAT ASAR, are the basis for frequent and accurate monitoring of the environment. It was the intent of this thesis to develop suitable procedures for the understanding of these complex multiple image datasets and their practical utilization.

Therefore sophisticated methods have been developed to investigate the different challenging microwave land surface interactions, caused by the multiple imaging geometries and polarisations.

A modelling approach, linking a microwave backscattering model with a process oriented land surface model was found to be suited for this undertaking. It makes use of the spatio-temporal parameter simulation capabilities of the land surface model, and uses the backscattering model for the simulation of synthetic SAR images which can then directly be compared to measured image data.

A careful preprocessing of the image datasets is mandatory for the quantitative analysis of SAR imagery. A sophisticated image processing and geocoding procedure was therefore developed for ENVISAT ASAR images. It corrects the terrain induced geometric and radiometric distortions of the image data on a high level of accuracy. It is therefore a main building block for any further quantitative analysis steps.

The understanding and separation of the different scattering terms is crucial for an accurate modelling of the backscattering coefficient, and finally also for the stable derivation of land surface parameters from SAR imagery with multiple imaging geometries. One of the major achievements is the successful implementation of a generalized microwave backscattering model of the land surface. It combines the bare soil and vegetation contributions and is valid over the vegetation period and for a wide range of imaging geometries, including all swathes of the ENVISAT ASAR sensor.

A new bare soil backscattering model was proposed in this context. Based on the results of a theoretical electromagnetic scattering model, it has been shown, that the bare soil backscatter can be predicted, using a simple two parameter approach, which only needs information about the dielectric and roughness properties of the surface. It has been useful to overcome the drawback of an ambiguous surface roughness characterization of classical theoretical bare soil backscattering models. A new surface roughness parameter was developed for this purpose which integrates the surface roughness components affecting the backscattering coefficient into a single variable. It has been shown on a theoretical basis, that it can be directly related to the intrinsic fractal properties of the surface which enables its derivation from field measurements.

Starting from that point, a model for the spatially distributed derivation of surface roughness was proposed and successfully applied. It makes use of the different scattering behaviours of natural surfaces under different imaging geometries. The roughness inversion model was validated for a reference target of constant roughness. It was then used, to derive a spatially distributed surface roughness map for the testsite.

The accuracy of the bare soil backscattering model was assessed, using field measurements of surface soil moisture and the automatically derived roughness information. The RMSE was 1.6 and 1.7 dB for HH and VV polarisation respectively.

The residuals between the bare soil backscattering coefficient and measured SAR observations were analysed to assess the vegetation influences on the signal by using available ground truth datasets. It has been found, that the intrinsic scattering mechanisms of cereals (wheat, triticale) and maize are different. Therefore two different vegetation backscattering models were developed. For stands with small, but dense plants (e.g. a wheat field), the effect of the canopy on the signal can be parameterised by a random volume with a predefined height. It has been shown, that the vegetation influence on the signal can be directly derived from

multipolarised image datasets, using the ratio of the two copolarisations, which can be related to plant biophysical variables as the dry biomass or water content. Two scenarios were compared in this context. For once, the image data was directly used to parameterise the vegetation influence on the signal. The second approach used plant biophysical variables for the compensation of this effect. Best results were obtained, using the information from the image data itself.

The different shape of maize plants results in a different scattering mechanism. A dihedral corner reflection at the stalk of the maize plants was identified as the major factor influencing the vegetation contribution to the signal. The angular behaviour of this scattering mechanism could be parameterised by means of a theoretical radiative transfer model. The amount of bare soil and stalk ground interaction contributions to the signal can be described as a function of the vegetation height. The maize scattering model was calibrated using available ground measurements.

The necessary backscattering model input parameters, as e.g. vegetation height, can be provided by a process oriented land surface model, which simulates plant biophysical variables as well as the soil moisture conditions from given environmental and meteorological data. To be comparable with spatial remote sensing datasets, time series of spatially distributed land surface variables are needed in this context. The used land surface model PROMET-V was suited for this undertaking.

An interface was implemented in order to couple the land surface process and the combined backscattering model. The coupled land surface backscattering model was used to predict the signal return of the land surface, based on the simulation results of the plant and soil conditions.

The promising results, obtained at the point scale with this coupled approach, enabled the transfer of the approach to a spatially distributed simulation of SAR images. The comparison of these synthetic backscattering images with ENVISAT ASAR observations revealed an overall good performance of the modelling approach for the different ENVISAT ASAR swathes. Nevertheless, deviations exist between the measured and observed backscattering coefficients. A detailed field based analysis indicated, that a major source of uncertainty results from imprecise soil moisture predictions by the land surface model, which is mainly due to inadequate soil parameterisations.

The interface between the land surface model and microwave backscattering model allows for an easy iterative inversion of surface parameters from SAR imagery. A simple approach for the derivations of the soil moisture of the upper soil layer has been proposed.

It turned out, that the use of initial soil moisture values, provided by the land surface model, lead to more consistent inversion results, than a simpler approach, which does not make use of *a priori* information. Problems can occur, if the initial soil moisture value is significantly different from the expected one. Then the *a priori* approach could fail, due to a restricted possible parameter range.

9.1 Outlook

The correct parameterisation of the soil hydrological properties is crucial in this context. Accurate and detailed information about the soil texture and conductivity is normally not available for larger areas. Therefore large soil moisture modelling uncertainties are introduced by inaccurate soil texture maps. At present no better maps are available. A correct parameterisation of the soil texture, especially for the uppermost centimetres, is crucial to obtain reliable backscattering results. Thus, time series of the residuals between the modelled and measured backscattering values contain valuable information about the hydrological properties of the soils. A multitemporal analysis of these backscattering residuals would enable the derivation of spatially distributed soil property maps by means of SAR imagery. The coupled modelling approach could therefore help to characterize the spatio-temporal dynamics of the soil hydrological processes. By adapting the land surface model parameters within a predefined validity range, they could be adjusted until best agreement between modelled and simulated values is achieved.

It is remarkable, that subsurface soil conditions seem to influence the image data. Figure 9.1 shows a times series of SAR images around *Gut Huell*. One field (#101) is situated at flat terrain, while the other two fields (#105, 389) are situated at the glacial moraine (see 5.1). It can be seen that the marked fields have similar backscattering coefficients on the 27th of March. The images of the 2nd and the 11th of April were acquired during and shortly after a precipitation event. The image, acquired on April 2nd, *during* the raining event, shows very similar backscattering coefficients of the fields. This changes on the image acquired *after* the precipitation event (11th April). The fields, which have a similar vegetation cover on all dates, now show different backscattering behaviours. The fields on the moraine (#105, 389) appear brighter than the other one. From field measurements it is known, that the soils on the moraine are influenced by damming wetness, while the soils on the flat glacial spillway dry out faster. Thus, the damming of the underlying soil layer has a significant influence on the soil moisture of the uppermost few centimetres, which can be seen in the image data. This might be used to enhance the soil parameterisation for soil layers below the penetration depth of the microwaves, by applying an adequate soil process model.
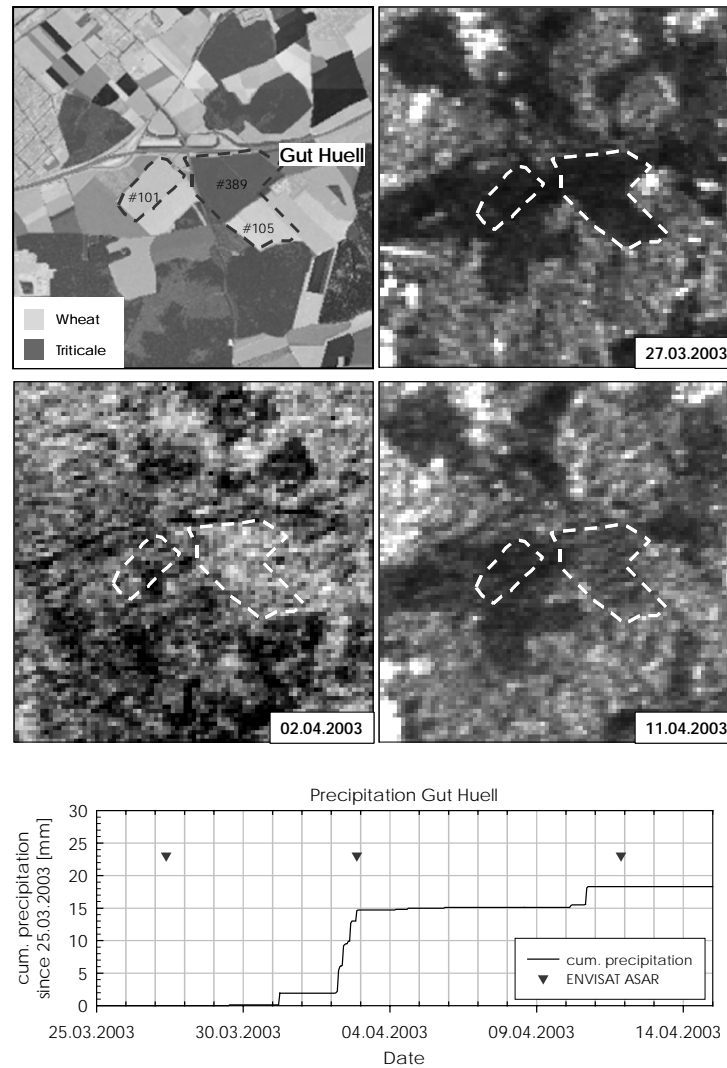
Figure 9.1: Temporal development of the SAR backscattering coefficient during two precipitation events

The suggested modelling approach and developed procedures therefore provide a suitable tool for a process model supported analysis of remote sensing data. Much information is contained within the image data and especially in the residuals between measured and modelled backscattering values. The spatial variability of the plant conditions, as e.g. plant density, variable heights and biomass, has not yet been incorporated in the analysis. The land surface model uses fixed plant densities for the simulations. These can be inverted from optical remote sensing data, using a similar coupled approach with a radiative transfer model for the optical domain (e.g. BACH, VERHOEF and SCHNEIDER, 2000; BACH and MAUSER, 2003). By synergistic use of optical and microwave remote sensing data, the backscattering model parameterisation might still be improved.

The developed models enable the derivation of surface roughness and surface moisture information from the image data. By means of multitemporal analysis, they might be used to enhance the spatially distributed description of static soil parameters. Informations about the vegetation biomass and water content can be derived for cereals by means of the copol ratio.

The direct linkage to a land surface process model enables the assimilation of the remote sensing information into that model and helps to improve the description of the highly dynamic nature of the processes at the land surface. Due to the validity of the developed models for a wide range of incidence angles, they allow for a systematic and frequent monitoring. This might help to improve our knowledge and understanding, as well as our management capabilities of the limited natural resources.

The presented thesis is therefore a contribution towards a sophisticated operational use of remote sensing data. The author hopes, that this work will have a meaningful contribution to this topic.

References

Attema, E. P. W., Ulaby, F.T. (1978): Vegetation modelled as a water cloud. *Radio Science*. Vol. 13 (2). pp. 357-364.

Autret, M., Bernard, R., Vidal-Madjar, D. (1989): Theoretical study of the sensitivity of the microwave backscattering coefficent to the soil surface parameters. *Int. J. Remote Sensing*. Vol. 10 (1). pp. 171-179.

Bach, H., Boreaud, M., Häme, T., van Leeuwen, H., Manninen, T., Mauser, W., Schneider, K., Schouten, L., Stolz, R., Verhoef, W. (2000): Retrieval of Geo- and Biophysical Information from Remote Sensing data – Overview of the GeoBIRD study, *Proc. ERS-ENVISAT Symp. Gothenburg, Sweden, 16.-20. October 2000*. pp. 125-134.

Bach, H., Schneider, K., Mauser, W., Stolz, R., Manninen, T., Häme, T., van Leeuwen, H., Schouten, L., Verhoef, W. (2000a): GeoBird: The retrieval of geo- and biophysical information from remote sensing data. Final report. ESA Contract Ref.: 12950/98/NL/GD.

Bach, H., Verhoef, W., Schneider, K. (2000): Coupling remote sensing observation models and a growth model for improved retrieval of (geo)biophysical information from optical remote sensing data. *Remote Sensing for Agriculture, Ecosystems and Hydrology*, SPIE Vol. 4171. pp. 1-11.

Bach, H., Mauser, W. (2003): Methods and Examples of Remote Sensing Data Assimilation in Land Surface Process Modelling. *IEEE Trans. Geosci. Remote Sensing*. Vol. 41 (7). pp. 1629-1637.

Bach, H., Mauser, W., Schneider, K. (2003): The use of radiative transfer models for remote sensing data assimilation in crop growth models. In: J. Stafford, A. Werner (ed.): Precision Agriculture. pp. 35-40.

Baghdadi, N., Paillou, P., Davidson, M., Grandjean, G., Dubois, P. (2000): Relationship between profile length and roughness parameters for natural surfaces. *Int. J. Remote Sensing*. Vol. 21 (17). pp. 3375-3381.

Baghdadi, N., King, C., Chanzy, A., Wigneron, J.P. (2002): An empirical calibration of the integral equation model based on SAR data, soil moisture and surface roughness measurements over bare soil. *Int. J. Remote Sensing*. Vol. 23 (20). pp. 4325-4340.

Ballester-Berman, J.D., Lopez-Sanchez, J.M., Guasch, J.F. (2004): Estimation of Extinction coefficients and its implications in crop monitoring with polarimetric SAR interferometry. *Proc. EUSAR 2004, 25-27 May 2004, Ulm, Germany*. pp. 737-740.

Bamler, R., Schättler, B. (1993): SAR Data Acquisition and Image Formation. In: Schreier, G. (Ed.): SAR Geocoding – Data and Systems. pp. 53-102. Wichmann: Karlsruhe.

Barton, C.C., La Pointe, P.R. (1995): Fractals in the Earth Sciences. Plenum Press: New York.

Bayerische Landesanstalt für Bodenkunde und Pflanzenbau (1997): Leitfaden für die Düngung von Acker- und Grünland. LBP, Freising-München.

Bayerischer Klimaforschungsverbund (BAYFORKLIM) (1996): Klimaatlas von Bayern. Meteorol. Institut, Universität München (Ed.).

Beaudoin, A., Troufleau, D., Desbois, N., Piet, L., Deshayes, M. (1995): On the use of ERS-1 SAR data over hilly terrain: Necessity of radiometric corrections for thematic applications. *Proc. IEEE Int. Geos. RS Symposium*, *10-14 July 1995, Florence, Italy.* Vol. 3. pp. 2179-2182.

Beckmann, P., Spizzichino, A. (1987): The scattering of electromagnetic waves from rough surfaces. Artech House: Norwood.

Benallegue, M., Taconet, O., Vidal-Madjar, D., Normand, M. (1995): The use of radar backscattering signal for measuring soil moisture and surface roughness. *Remote Sens. Environ.* Vol. 53. pp. 61-68.

Benzing, A.G., Kimmig, M. (1987): Geographische Koordinaten und Gitterkoordinaten. Geographisches Taschenbuch. pp. 100-109.

Beven, K. J. (2001): Calibration, Validation and Equifinality in Hydrological Modelling. In: Anderson, M.G. and Bates, P.D. (Ed.): Model Validation: Perspectives in Hydrological Science. Wiley: Chichester. pp. 43-55.

Bicheron, P., Leroy, M. (1999): A method of biophysical parameter retrieval at global scale by inversion of a vegetation reflectance model. *Remote Sens. Environ.* Vol. 67. pp. 251-266.

Bindlish, R., Barros, A.P. (2000): Multifrequency soil moisture inversion from SAR measurements with the use of IEM. *Remote Sens. Environ.* Vol. 71. pp. 67-88.

Bindlish, R., Barros, A.P. (2001): Parameterization of vegetation backscatter in radar-based soil moisture estimation. *Remote Sens. Environ.* Vol. 76. pp. 130-137.

Boerner, W.M., Mott, H., Lüneburg, E., Livingstone, C., Brisco, B., Brown, R.J., Paterson, J.S. (1998): Polarimetry in Radar Remote Sensing: Basic and applied concepts. In: Henderson and Lewis (Ed.): Principles and applications of imaging radar. Manual of Rem. Sensing. Vol. 2. pp.271-357.

Brandelik, A., Hübner, C. (1996): Soil moisture determination – accurate, large and deep. *Phys. Chem. Earth*. Vol. 21 (3). pp. 157-160.

Brisco, B., Brown, R.J. (1998): Agricultural applications with radar. In: Henderson and Lewis (Ed.): Principles and applications of imaging radar. Manual of Rem. Sensing. Vol. 2, pp. 381-434.

Brown, S.R. (1995): Measuring the Dimension of Self-Affine Fractals: Example of rough surfaces. In: Barton, C. and La Pointe, P.R. (Ed.): Fractals in the earth sciences, Plenum Press: New York.

Brown, S.C.M., Quegan, S., Morrison, K., Bennett, J.C., Cookmartin, G. (2003): High-Resolution measurements of scattering in wheat canopies – implications for crop parameter retrieval. *IEEE Trans. Geosci. Remote Sensing*. Vol. 41 (7). pp. 1603-1610.

Bugayevskiy, L.M., Snyder, J.P. (1995): Map projections – a reference manual, Taylor & Francis: London.

Bundesanstalt für Geowissenschaften und Rohstoffe und Geologische Landesämter (BGR) (Ed.) (1995): Bodenkundliche Kartieranleitung. Schweiz'bartsche Verlagsbuchhandlung: Stuttgart.

Chanzy, A., Molineaux, B., Zribi, M. (2003): Influence of surface roughness frequency components on radar backscattering: Consequences on roughness sampling. *Proc. IEEE Int. Geos. RS Symposium, 21-25 July 2003, Toulouse.*, Vol. 2, pp. 1414- 1416.

Combal, B., Baret, F., Weiss, M., Trubuil, A., Macé, D., Pragnere, A., Myneni, R., Knyazikhin, Y., Wang, L. (2002): Retrieval of canopy biophysical variables from bi-directional reflectance using prior information to solve the ill-posed inverse problem. *Remote Sens. Environ.* Vol. 84. pp. 1-15.

Cookmartin, G., Saich, P. Quegan, S., Cordey, R., Burgess-Allen, P., Sowter, A. (2000): Modeling microwave interactions with crops and comparison with ERS-2 SAR observations. *IEEE Trans. Geosci. Remote Sensing*. Vol. 38 (2). pp. 658-670.

Crosson, W.L., Laymon, C.A., Inguva, R., Schamschula, M.P. (2002): Assimilating remote sensing data in a surface flux-soil moisture model. *Hydrological Processes*. Vol. 16. pp. 1645-1662.

Curlander, J.C., McDonough, R.N. (1991): Synthetic aperture radar : systems and signal processing. Wiley Series in Remote Sensing.

Dammert, P.B.G., Askne, J. (1998): Interferometric tree height observations in boreal forests with SAR interferometry. *Proc. IEEE Int. Geos. RS Symposium, Seattle.* Vol. 3, pp. 1363- 1366.

Davidson, M., LeToan, T., Mattia, F., Satalino, G., Manninen, T., Borgeaud, M. (2000): On the characterization of agricultural soil roughness for radar remote sensing studies. *IEEE Trans. Geosci. Remote Sensing.* Vol. 38 (2). pp. 630-640.

Davidson, M., Le Toan, T., Mattia, F., Satalino, G. Borgeaud, M. (2001): Perspectives on the use of SAR data for bare soil moisture mapping. *Proc. 8th international sympos. Phys. Meas. And Signatures in Rem. Sens., ISPRS, 8-12 January 2001, Ausois, France.*

Davidson, M., Mattia, F., Satalino, G., Verhoest, N.E.C., LeToan, T., Borgeaud, M., Louis, J.M.B., Attema, E. (2003): Joint statistical properties of RMS height and correlation length derived from multisite 1-m roughness measurements. *IEEE Trans. Geosci. Remote Sensing.* Vol. 41 (7). pp. 1651-1658.

Dedieu, J.P., Gauthier, Y., Bernier, M. Hardy, S. Vincent, P. Durand, Y. (2003): Radiometric and geometric correction of RADARSAT-1 images acquired in alpine regions for mapping the Snow Water Equivalent (SWE). *Proc. IEEE Int.Geos. RS Symposium, 21-25 July 2003, Toulouse.*, Vol. 2, pp. 851- 853.

Dermircan, A. (1995): Die Nutzung fernerkundlich bestimmter Pflanzenparameter zur flächenhaften Modellierung der Ertragsbildung und Verdunstung. = Münchener Geographische Abhandlungen, Reihe B, Bd. 20.

Disney, M.I., Saich, P. and Lewis, P. (2003): Modelling the radiometric response of a dynamic, 3D structural model of Scots Pine in the optical and microwave domains. *Proc. IEEE Int. Geos. RS Symposium, 21-25 July 2003, Toulouse.*, Vol. 6, pp. 3537- 3539.

Dobson, M.C., Ulaby, F.T., Hallikainen, M.T., El-Rayes, M. (1985): Microwave Dielectric behaviour of wet soil – Part II: Dielectric Mixing Models. *IEEE Trans. Geosci. Remote Sensing.* Vol. GE-23 (1). pp. 35-46.

Dobson, M.C., Ulaby, F.T., LeToan, T., Beaudoin, A., Kasischke, E.S., Christiansen, A. (1992): Dependance of radar backscatter on conifer forest biomass. *IEEE Trans. Geosci. Remote Sensing.* Vol. 30 (2). pp. 403-411.

Dobson, M.C., Ulaby, F.T., Pierce, L.E., Shark, T.L., Bergen. K.M., Kellndorfer, J., Kendra, J.R., Li, E., Lin, Y.C., Nashashibi, A., Sarabandi, K., Siqueira, P. (1995): Estimation of Forest Biophysical Characteristics in Northern Michigan with SIR-C/X SAR. *IEEE Trans. Geosci. Remote Sensing*. Vol. 33 (4). pp. 877-893.

Dobson, M.C., Ulaby, F.T. (1998): Mapping soil moisture distribution with imaging radar. In: Henderson and Lewis (Ed.): Principles and applications of imaging radar. Manual of Rem. Sensing. Vol. 2, pp. 407-430.

Doleschel, P. (1998): Triticale. In: Die Landwirtschaft. Bd. 1: Pflanzliche Erzeugung. BLV Verlagsanstalt. pp. 281-286.

Dubois, P.C. , van Zyl, J.J., Engman, T. (1995): Measuring soil moisture with imaging radar. *IEEE Trans. Geosci. Remote Sensing*. Vol. 33 (4). pp. 915-926.

DWD (2004): Die klimatische Wasserbilanz im Jahr 2003 im Vergleich zu den vieljährigen Werten. *URL: http://www.agrowetter.de/news/ klim_wasserbilanz_2003.ht*ml (1.4.2004)

Eder, J. (1998): Mais. In: Die Landwirtschaft. Bd. 1: Pflanzliche Erzeugung. BLV Verlagsanstalt. pp. 322-348.

Engelen, G. (ed.) (2000): MODULUS: A Spatial Modelling Tool for Integrated Environmental Decision-Making, Final Report, Contract ENV4-CT97-0685, Directorate General XII, Environment IV Framework, Brussels, Belgium.

Engman, E.T., Chauhan, N. (1995): Status of Microwave soil moisture measurements with remote sensing. *Remote Sens. Environ.* Vol. 51. pp. 189-198.

ESA (2002): EnviSAT ASAR product handbook. Issue 1.1, 1st December, 2002.

ESA (2004): European Space Operation Centre – ENVISAT Orbits: URL: http://nng.esoc.esa.de/envisat/index.html (01.06.2004).

Ewe, H.T., Chuah, H.T. (2000): A multilayer scattering model for a dense vegetation medium. *Proc. of Progress in Electromagnetics Research Symposium, 5.-14. July, 2000, Cambridge, MA, USA*.

Falconer, K. (1990): Fractal Geometry. Wiley: Chichester.

Ferré, P.A., Rudolph, D.L., Kachanoski, R.G. (1996): Spatial averaging of water content by time domain reflectrometry: Implications for twin rod probes with and without dielectrical coatings. *Wat. Resour. Research*. Vol. 32. pp. 271-279.

Floury, N. (1999): Modélisation radars des couverts forestiers : Application à la télédétection. *PhD thesis. University of Paris VII.*

Frei, U., Graf, K.C., Meier, E. (1993): Cartographic Reference Systems. In: Schreier, G. (Ed.): SAR Geocoding – Data and Systems. pp. 213-234. Wichmann: Karlsruhe.

Fournier, C., Andrieu, B. (1999): ADEL-maize: an L-system based model for the integration of growth processes from the organ to the canopy. Application to regulation of morphogenesis by light availability. *Agronomie.* Vol. 19. pp. 313-327.

Francheschetti, G., Iodice, A., Maddaluno, S., Riccio, D. (2000): A fractal based theoretical framework for retrieval of surface parameters from electromagnetic backscattering data. *IEEE Trans. Geosci. Remote Sensing.* Vol. 38 (2). pp. 641-650.

Frost, V.S., Stiles, J.A., Shanmugan, K.S., Holtzman, J.C. (1982): A Model for Radar Images and its Application to Adaptive Digital Filtering of Multiplicative Noise. *IEEE Trans. Patt. Analy. Mach. Intell.* Vol. 4 (2). pp. 157-166.

Fundinger, R., Köhler, K. (1992): Messung der Material- und Bodenfeuchte mit der TRIME-Methode. Technical document, Fa. IMKO, Ettlingen.

Fung, A., Li, Z., Chen, K.S. (1992): Backscattering from a Randomly Rough Dielectric Surface. *IEEE Trans. Geosci. Remote Sensing.* Vol. 30 (2). pp. 356-369.

Fung, A. (1994): Microwave scattering and emission models and their applications. Artech House: London.

Gabriel, J., Schmullius, C. Papathanassiou, K., Darizhapov, D., Tathkov, G., Tsybjitov, T., Boerner, W. (1999): Tree height extraction using polarimetric SAR interferometry. *Proc. IEEE Int. Geos. RS Symposium, 28 June – 2 July 1999, Hamburg.* pp. 2131-2133.

Geomatics (1998): Radarsat Distance Learning Program. Geomatics International Inc.

Gietl, G. (2004): Das Trockenjahr 2003 – (k)ein Jahrhundertereignis. *LWF aktuell,* Bayerische Landesanstalt für Wald- und Forstwirtschaft (Ed.). 43(1), pp. 1-3.

Godwin, D.C., Singh, U. (1998): Nitrogen balance and crop response to nitrogen in upland and lowland cropping systems. In: Tsuji, G.Y., Hoogenboom, G., Thornton, P. (Ed.): Understanding Options for Agricultural Production. pp. 55-79. Kluwer Academic Publishers: Dordrecht.

Graul, H. (1962): Die naturräumlichen Einheiten auf Blatt 180 Augsburg. Geographische Landesaufnahme 1:200000. = Naturräumliche Gliederung Deutschlands, Bad Godesberg.

Hallikainen, M.T., Ulaby, F.T., Dobson, M.C., El-Rayes, M.A., Wu, L. (1985): Microwave dielectric behaviour of wet soil – Part I: Empirical models and experimental observations. *IEEE Trans. Geosci. Remote Sensing*. Vol. GE-23 (1). pp. 25-34.

Hanssen, R.F., Weckwerth, T.M., Zebeker, H.A., Klees, R. (1999): High-Resolution Water Vapor Mapping from Interferometric Radar Measurements. *Science*. Vol. 283 (5406). pp. 1297-1299.

Le Hégarat-Mascle, S., Alem, F., Quesney, A., Normand, M., Loumagne, C., Weisse, A. (2001) : Surface soil moisture monitoring from ERS/SAR data : method and validation over three different watersheds. *Proc. 8th international sympos. Phys. Meas. And Signatures in Rem. Sens., ISPRS, 8-12 January 2001, Ausois, France.*

Le Hégarat-Mascle, S., Zribi, M., Alem, F., Weisse, A., Loumagne, C. (2002): Soil moisture estimation from ERS/SAR data: Toward an operational methodology. *IEEE Trans. Geosci. Remote Sensing*. Vol. 40 (12). pp. 2647-2658.

Le Hégarat-Mascle, S., Zribi, M., Marticorena, B., Bergametti, G., Kardous, M., Callot, Y., Chazette, P., Rajot, J.L. (2003). Use of ERS/SAR measurements for soil geometric and aerodynamic roughness estimation in semiarid and arid areas. *Proc. IEEE Int. Geos. RS Symposium, 21-25 July 2003, Toulouse.*, Vol. 4, pp. 2272-2274.

Hellwich, O., Ebner, H. (2000): Geocoding SAR interferograms by least squares adjustment*. J. of Photogramm. and Remote Sensing*. Vol. 55. pp. 277-288.

Henderson, F.M., Lewis, A.J. (1998): Principles and Applications of Imaging Radar, = Manual of Rem. Sensing. Vol. 2.

Hodges, T., Ritchie, J.T. (1991): The CERES-WHEAT phenology model. In: Hodges, T. (Ed.) Predicting Crop Phenology. pp. 133-141. CRC Press: Boca Raton.

Holecz, F. (1993): Postprocessing von SAR Satellitenbilddaten. = *Remote Sensing Series*. Vol. 23.

Holzhauser, J. (2002): Möglichkeiten und Grenzen bei der Bestimmung des Blattflächenindex mit dem Li-COR LAI2000 am Beispiel von Weizen und Mais. *unpublished master thesis. University of Munich, Geography*.

Huisman, S. (2002): Mesasuring Soil Water Content with Time Domain Reflectrometry and Ground Penetrating Radar – Accuracy, Reproducibility and Feasibility. *PhD Thesis University of Amsterdam*. ISBN: 90-76894-23-X.

Huisman, J.A., Hubbard, S.S., Redman, J.D, Annan, A.P. (2003): Measuring Soil water Content with Ground Penetrating Radar: A Review. *Vadose Zone Journal*. *In press*.

Hu, Y., Shi, J., Zhen, L., Guo, H., Zhang, Z. (2003): Temporal and Spatial soil moisture change pattern detection using multi-temporal Radarsat ScanSAR images. *Proc. IEEE Int. Geos. RS Symposium*, *21-25 July 2003, Toulouse.*, Vol. 2, pp. 1420-1422.

Hygro Agri Dülmen GmbH (1993): Faustzahlen für Landwirtschaft und Gartenbau. BLV: München.

Jackson, T.J., Schmugge, T.J. (1991): Vegetation effects on the microwave emission of soils. *Remote Sens. Environ.* Vol. 36. pp. 203-212.

Jones, C.A., Kiniry, J.R. (1986): CERES-Maize – Simulation model of maize growth and development. Texas University Press.

Jones, S.B., Wraight, J.M., Or, D. (2002): Time domain reflectrometry measurement principles and applications. *Hydrological processes*. Vol. 16. pp. 141-153.

Karam, M.A., Fung, A.K. (1988): Electromagnetic scattering from a layer of finite length, randomly oriented, dielectric, circular cylinders over a rough interface with application to vegetation. *Int. J. Remote Sensing*. Vol. 9 (6). pp. 1109-1134.

Karam, M.A., Fung, A.K., Lang, R.H., Chauhan, N.S. (1992): A microwave scattering model for layered vegetation. *IEEE Trans. Geosci. Remote Sensing*. Vol. 30 (4). pp. 767-784.

Karam, M.A., Amar, F., Fung, A.K., Mougin, E., Lopes, A., LeVine, D.M., Beaudoin, A. (1995): A microwave polarimetric scattering model for forest canopies based on vector radiative transfer theory. *Remote Sens. Environ.* Vol. 53. pp. 16-30.

Klausing, H., Holpp, W. (2000): Radar mit realer und synthetischer Apertur. Verlag Oldenburg: Oldenburg.

Köppen, W., Geiger, R. (1961): Die Klimate der Erde. Darmstadt.

Koskinen, J.T., Pulliainen, J.T., Hallikainen, M.T. (1997): The use of ERS-1 SAR data in snow melt monitoring. *IEEE Trans. Geosci. Remote Sensing*. Vol. 35 (3). pp. 601-610.

Kurvonen, L., Pulliainen, J., Hallikainen, M. (1999): Retrieval of biomass from multi-temporal ERS-1 and JERS-1 SAR images. *IEEE Trans. Geosci. Remote Sensing*. Vol. 37 (1). pp. 198-205.

Laur, H., Meadows, P., Sanchez, J.I., Dwyer, E. (1993): ERS-1 SAR Radiometric calibration, *Proceedings of the CEOS SAR Calibration Workshop, (ESA WPP-048) Sept. 1993.*

Laur, H., Bally, P., Meadows, P., Sanchez, J., Schättler, B., Lopinto, E., Esteban, D. (1998): Derivation of the backscattering coefficient σ^0 in ERS SAR PRI products. ESA Technical Document. ES-TN-RS-PM-HL09. Iss. 2.5b, 7. September. 1998.

Laws, K.I. (1980): Rapid texture identification. *Proc. SPIE Image process. missile guide.* Vol. 238. pp. 376-380.

Lee, J.S. (1981): Refined filtering of image noise using local statistics. *Computer Graphics and image processing*. Vol. 15. pp. 380-389.

Lee, J.S. (1986): Speckle suppression and analysis for SAR images. *Optical Engineering*. Vol. 25(5). pp. 636-643.

Lemaire, G., Gastal, F. (1997): N uptake and distribution in plant canopies. In: Lemaire, G. (Ed.): Diagnosis of Nitrogen Status in Crops. pp. 1-43. Springer: Berlin.

Lewis, A., Henderson, F.M. (1998): Radar fundamentals: The geoscience perspective. In: Henderson and Lewis (Ed.): Principles and applications of imaging radar. Manual of Rem. Sensing. Vol. 2, pp. 131-181.

Lewis, P., Saich, P., Disney, M., Andrieu, B., Fournier, C., Ljutovac, S. (2003): Modelling the radiometric response of a dynamic, 3D model of wheat in the optical and microwave domains. *Proc. IEEE Int. Geos. RS Symposium*, *21-25 July 2003, Toulouse.*, Vol. 6, pp. 3543-3545.

Li, Q., Shi, J., Chen, K.S. (2002): A generalized power law spectrum and its applications to the backscattering of soil surfaces based on the integral equation model. *IEEE Trans. Geosci. Remote Sensing*. Vol. 40 (2). pp. 271-280.

LI-COR, INC (1991): LAI-2000 Plant Canopy Analyser, Operating Manual. Technical document. Lincoln (Nebraska/USA).

Lin, Y.C., Sarabandi, K. (1999): A Monte Carlo coherent scattering model for forest canopies using fractal generated trees. *IEEE Trans. Geosci. Remote Sensing*. Vol. 37 (1). pp. 440-451.

Lindenmayer, A. (1975): Developmental algorithms for multicellular organizms: A survey of L-systems. *J. Theoretical Biol.* Vol. 54. pp. 3-22.

Löw, A. (2000): Ableitung forstlicher Parameter aus AeS-1 SAR Daten für ein Untersuchungsgebiet im Schweizer Mittelland. *Unpublished master thesis, University of Munich, Geography.*

Löw, A., Mauser, W. (2003): Generation of geometrically and radiometrically terrain corrected ScanSAR images. *Proc. IEEE Int. Geos. RS Symposium, 21-25 July 2003, Toulouse.*, Vol. 6, pp. 3995-3997.

Löw A., Ludwig, R., Mauser, W. (2003): Land use dependant snow cover retrieval using multitemporal, multisensoral SAR images to drive operational flood forecasting models. *Proc. 3rd workshop on remote Sensing of Land Ice and Snow, 11-13 March 2002, Bern.* EARSel eProceedings. Vol. 2 (1/2003).

Löw, A., Ludwig, R., Mauser, W. (2003a): Mesoscale soil moisture estimation from SAR data using subscale landuse information. *Proc. IEEE Int. Geos. RS Symposium, 21-25 July 2003, Toulouse.*, Vol. 2, pp. 1396-1398.

Louis, J., Floury, N., Davidson, M., Attema, E., Borgeaud, M. (2003): Surface Roughness characterization for SAR applications. *Proc. IEEE Int. Geos. RS Symposium, 21-25 July 2003, Toulouse.* Vol. 2, pp. 1408-1410.

Lozan, J.L., Kausch, H. (1998): Angewandte Statistik für Naturwissenschaftler. =Pareys Studientexte 74. Parey Buchverlag: Berlin.

Ludwig, R. (2000): Die flächenverteilte Modellierung von Wasserhaushalt und Abflußbildung im Einzugsgebiet der Ammer. = Münchener Geographische Abhandlungen, Reihe B. Band B32.

Ludwig, R., Mauser, W., Niemeyer, S., Colgan, A., Stolz, R., Escher-Vetter, H., Kuhn, M., Reichstein, M., Tenhunen, J., Kraus, A., Ludwig, M., Barth,M., Hennicker, R. (2003): Web-based modelling of energy, water and matter fluxes to support decision making in mesoscale catchments - the integrative perspective of GLOWA-Danube. *Physics and Chemistry of the Earth.* Vol. 28. pp. 621-634.

Magagi, R.D., Kerr, Y.H. (2001): Estimating surface soil moisture and soil roughness over semiarid areas from the use of the copolarization ratio. *Remote Sens. Environ.* Vol. 75. pp. 432-445.

Mandelbrot, B.B. (1983): The fractal Geometry of Nature. Freeman: New York.

Marliani, F., Paloscia, S., Pampaloni, P., Kong, J.A. (2002): Simulating coherent backscattering from crops during the growth cycle. *IEEE Trans. Geosci. Remote Sensing.* Vol. 40 (1). pp. 162-177.

Martinez, J.M., Floury, N., LeToan, T., Beaudoin, A., Hallikainen, M., Makynen, M. (2000): Measurements and modelling of vertical backscatter distribution in forest canopy. *IEEE Trans. Geosci. Remote Sensing*. Vol. 38 (2). pp. 710-719.

Mattia, F., Davidson, M., LeToan, T., D'Haese, C.M.F., Verhoest, N.E.C., Gatti, A.M., Borgeaud, M. (2003): A Comparison between soil roughness statistics used in surface scattering models derived from mechanical and laser profiles. *IEEE Trans. Geosci. Remote Sensing*. Vol. 41 (7). pp. 1659-1671.

Mattia, F., LeToan, T. Picard, G., Posa, F., Alessio, A., Notarnicola, C., Gatti, A.M., Rinaldi, M., Statalino, G., Pasquariello, G. (2003a): Multitemporal C-Band radar measurements on wheat fields. *IEEE Trans. Geosci. Remote Sensing*. Vol. 41 (7). pp. 1551-1559.

Mätzler, C. (1987): Applications of the interaction of microwaves with the natural snow cover. *Remote Sensing Reviews*. Vol. 2. pp. 259-387.

Mauser, W., Schädlich, S. (1998): Modelling the spatial distribution of evapotranspiration on different scales using remote sensing data. *Journal of Hydrology*. Vol. 212-213. pp. 250-267.

Mauser, W., Stolz, R., Schneider, K., Bach, H. (2000): Comparison of ERS SAR data derived soil moisture distributions with SVAT-model results, *Proceedings of ERS-ENVISAT-Symposium 2000*, Gothenburg 2000, Looking down to Earth in the New Millennium, ESA SP-461.

Mauser, W., Oppelt N. (2001): AVIS – A New Sensor for Environmental Monitoring and Precision Farming. *Proceedings International Workshop on Spectroscopy Application in Precision Farming IWSAPF, 16 – 18 January, Freising Germany* , pp. 41-44.

Mauser, W., Ludwig, R. (2002): A research concept to develop integrative techniques, scenarios and strategies regarding global changes of the water cycle. In: M. Beniston (Ed.): Climatic Change: Implications for the hydrological cycle and for water management. - Advances in Global Change Research 10. pp. 171-188.

Mauser, W. (2003): Integrative hydrologische Modellentwicklung zur Entscheidungsunterstützung beim Einzugsgebietsmanagement. *Petermanns Geographische Mitteilungen.* Vol. 147 (6). pp. 68-75.

Meadows, P., Wright, P. (2002): ASAR APP and APM image quality. *Proc. ENVISAT Validation Workshop, 9-13. December 2002, Frascati, Italy.*

Meadows, P., Rosich, B. (2003): The ERS-2 SAR performance: another further update. *Proc. Of CEOS Working Group on Calibration / Validation SAR Workshop, London, United Kingdom, 24-26 September 2002 (ESA SP-526, March 2003).*

Meier, E., Frei, U., Nüesch, D. (1993): Precise terrain corrected geocoded images. In: Schreier, G. (Ed.): SAR Geocoding – Data and Systems. pp. 173-186. Wichmann: Karlsruhe.

Menzel, A. (2000): Trends in phenological phases in Europe between 1951 and 1996. *International Journal of Biometeorology*. Vol. 44. pp. 76-81.

Meynen, E., Schmithüsen, J. (1962): Handbuch der naturräumlichen Gliederung Deutschlands. Band I (1953-1962), Bundesanstalt für Landeskunde und Raumforschung. Bad Godesberg.

Michler, G. (1994): Die naturräumlichen Einheiten auf Blatt 181 München. Geographische Landesaufnahme 1:200000. = Naturräumliche Gliederung Deutschlands, Bad Godesberg.

Moeremans, B., Dautrebande, S. (2000): Soil moisture evaluation by means of multi-temporal ERS SAR PRI images and interferometric coherence. *Journal of Hydrology*. Vol. 234. pp. 162-169.

Mohren, G.M.J. (1987): Simulation of forest growth, applied to Douglas fir stands in the Netherlands. *PhD Thesis, Landbouwuniversiteit Wageningen, The Netherlands.*

Mojid, M.A., Wyseure, G.C.L., Rose, D.A. (1997): Extension of the measurement range of electrical conductivity by time-domain reflectometry (TDR). *Hydrology and Earth System Sciences*. Vol. 1. pp. 175-183.

Montenbruck, O., Gill, E. (2000): Satellite Orbits – Models, Methods and Applications. Springer: Berlin.

Moran, M.S., Vidal, A., Troufleau, D., Inoue, Y., Mitchell, T.A. (1998): Ku- and C-band SAR for discriminating agricultural crop and soil conditions. *IEEE Trans. Geosci. Remote Sensing*. Vol. 36 (1). pp. 265-272.

Moreira, J.R. (1992): Bewegungsextraktionsverfahren für Radar mit synthetischer Apertur. = DLR Forschungsberichte. DLR-FB-92-31.

Moremans, B., Dautrebande, S. (2000): Soil moisture evaluation by means of multi-temporal ERS SAR PRI images and interferometric coherence. *Journal of Hydrology*. 234. 162-169.

Nagler, T., Rott, H. (2000): Retrieval of wet snow by means of multitemporal SAR data. *IEEE Trans. Geosci*. Remote Sensing. Vol. 38 (2). pp. 754-765.

NIMA (2000): Department of Defence World Geodetic System 1984 – Its definition and relationships with local geodetic systems. Technical report. NIMA 8350.2, 3rd edition, 3 January 2000, NIMA Stock No. DMATR83502WGS84.

Oh, Y., Sarabandi, K., Ulaby, F.T. (1992): An empirical model and an inversion technique for radar scattering from bare soil surfaces. *IEEE Trans. Geosci. Remote Sensing*. Vol. 30 (2). pp. 370-381.

Oh, Y., Kay, Y.C. (1998): Condition for precise measurement of soil surface roughness. *IEEE Trans. Geosci. Remote Sensing*. Vol. 36 (2). pp. 691-695.

Olmsted, C. (1993): Scientific SAR User's guide. Alaska SAR facility. *Technical Document. ASF-SD-003.*

Oppelt, N. (2002): Monitoring of Plant Chlorophyll and Nitrogen Status Using the Airborne Imaging Spectrometer AVIS. *PhD. Thesis. University of Munich, Geography.*

Oppelt, N. and Mauser, W. (2004): Hyperspectral Monitoring of Physiological Parameters of Wheat during a Vegetation Period Using AVIS Data. *Int. J. Remote Sensing*. Vol. 25 (1). pp. 145-159.

Peitgen, H.O., Saupe, D. (1988): The science of fractal images. Springer Verlag: New York.

Peplinski, N.R., Ulaby, F.T., Dobson, M.C. (1995): Dielectric properties of soils in the 0.3-1.3 GHz range. *IEEE Trans. Geosci. Remote Sensing*. Vol. 33 (3). pp. 803-807.

Philip, J.R. (1960): General method of exact solution of the concentration-dependent diffusion equation. *Australian J. Physics*. Vol. 13. pp. 1-12.

Picard, G., LeToan, T. (2002): A multiple scattering model for C-band backscatter of wheat canopies. *J. Electromagn. Waves. Applicat.* Vol. 16 (10). pp. 1447-1466.

Picard, G., LeToan, T., Mattia, M. (2003): Understanding C-Band Radar Backscatter from Wheat canopy using a multiple-scattering coherent model. *IEEE Trans. Geosci. Remote Sensing*. Vol. 41 (7). pp. 1583-1591.

Power, W.L., Tullis, T.E. (1995): Review of the fractal character of natural fault surfaces with implications for friction and the evolution of fault zones. In: Barton, C. and La Pointe, P.R. (Ed.), Fractals in the Earth Sciences, Plenum Press. pp. 89-106.

Press, W.H., Teukolsky, S.A., Vetterling, W.T., Flannery, B.P. (1992): Numerical Recipes in FORTRAN. 2nd edition. Cambridge University Press.

Prusinkiewicz, P., Lindenmayer, A. (1990): The algorithmic beauty of plants. Springer Verlag: New York.

Pulliainen, J., Hallikainen, M. (2001): Retrieval of regional snow water equivalent from space-borne passive microwave observations. *Remote Sens. Environ.* Vol. 75. pp. 76-85.

Quegan, S., Le Toan, T., Yu, J.J., Ribbes, F., Floury, N. (2000): Multitemporal ERS SAR Analysis applied to forest mapping. *IEEE Trans. Geosci. Remote Sensing*. Vol. 38 (2). pp. 741-753.

Quesney, A., Le Hégarat-Mascle, S., Taconet, O., Vidal-Madjar, D., Wigneron, J.P., Loumagne, C., Normand, M. (2000): Estimation of Watershed soil moisture index from ERS/SAR data. *Remote Sens. Environ.* Vol. 72. pp. 290-303.

Rabus, B., Eineder, M., Roth, A., Bamler, R. (2003): The shuttle radar topography mission – a new class of digital elevation models acquired by spaceborne radar. *Journal of Photogrammetry and Remote Sensing*. Vol. 57. pp. 241-262.

Raney, K.R. (1998): Radar Fundamentals: Technical Perspective. In: Henderson and Lewis (Ed.): Principles and applications of imaging radar. Manual of Rem. Sensing. Vol. 2, pp. 9-124.

Ranson, K.J., Sun, G. (1994): Mapping biomass of northern forest using multifrequency SAR data. *IEEE Trans. Geosci. Remote Sensing*. Vol. 32 (2). pp. 388-396.

Raggam, J., Strobl, D., Hummelbrunner, W. (1993): Product Quality Enhancement and Quality Evaluation. In: Schreier, G. (Ed.): SAR Geocoding – Data and Systems. pp. 187-206. Wichmann: Karlsruhe.

Ramnath, V.K., King, R.L., Younan, L.H., Shi, J. (2003): Estimation of soil moisture using RADARSAT repeat-passes. *Proc. IEEE Int. Geos. RS Symposium, 21-25 July 2003, Toulouse.*, Vol. 1, pp. 327-329.

El-Rayes, A., Ulaby, F.T. (1987): Microwave Dielectric spectrum of Vegetation – Part I: Experimental observations. *IEEE Trans. Geosci. Remote Sensing*. Vol. GE-25 (5). pp. 541-549.

Rice, S.O. (1951): Reflection of electromagnetic waves from slightly rough surfaces, *Commun. Pure Appl. Math.*. Vol 4. p. 351.

Riegler G., Mauser W. (1998): Geometric and Radiometric Terrain Correction of ERS SAR Data for Applications in Hydrologic Modelling. *Proc. IEEE Int. Geos. RS Symposium, 6-10 July 1998, Seattle, USA.*

Riegler, G. (2000): Bestimmung von hydrologischen Modellparametern aus ERS.SAR Daten*. Phd Thesis, University of Munich, Geography*.

Rignot, E., Salas, W.A., Skole, D.L. (1997): Mapping deforestation and secondary growth in Rondonia, Brazil, using imaging radar and Thematic Mapper data. *Remote Sens. Environ.* Vol. 59. pp. 167-179.

Rombach M., Mauser W. (1997): Multi-anual analysis of ERS surface soil moisture measurements of different land uses. *Proc. of the Third ERS Symposium: Space at the Service of Our Environment, Florence 1997*, ESA-SP- 414. Vol. 1, May 1997. pp. 27-34.

Rombach, M. (2000): Bestimmung der räumlichen und zeitlichen Variation der Bodenoberflächenfeuchte von landwirtschaftlichen Nutzflächen mit Hilfe von Fernerkundungsdatensätzen. *PhD Thesis. University of Munich, Geography.*

Rosich, B. (2002a): ASAR image and wide swath mode optimisations and product quality update. *Proc. ENVISAT Validation Workshop*, 9-13. December 2002, Frascati, Italy.

Rosich, B. (2002b): IM and WS Mode Level 1 product quality update. *Presentation held at ENVISAT Validation Workshop, 9-13. December 2002, Frascati, Italy.*

Rosich, B., Zink, M., Torres, R., Closa, J., Buck, C. (2003): ASAR instrument performance and product quality status. *Proc. IEEE Int. Geos. RS Symposium, 21-25 July 2003, Toulouse.*, Vol. 2, pp. 1109-1111.

Rosich, B., Meadows, P. (2004): Absolute calibration of ASAR Level 1 products generated with PF-ASAR. ESA technical note. ENVI-CLVL-EOPG-TN-03-0010. version 1.4, 23.01.2004.

Rufenacht, H.R., Proulx, J., Cefola, P. (1997): Improvement of RADARSAT image localization. In: Geomatics in the Era of Radarsat. Directorate of Geographical Operations, Canadian National Defense. CD-ROM.

Saatchi, S., Soares, J.V., Alves, D.S. (1996): Mapping deforestation and land use in Amazon rainforest using SIR-C imagery. *Remote Sens. Environ.* Vol. 59. pp. 191-202.

Saatchi, S., Moghaddam, M. (1999): Estimation of Boreal forest biomass using spaceborne SAR systems. *Proc. IEEE Int. Geos. RS Symposium, 28 June – 2 July 1999, Hamburg.*

Saupe, D. (1988): Algorithms for random fractals. In: Peitgen, H.O. and Saupe, D. (Ed.): The science of fractal images. Springer Verlag: New York. pp. 71-136.

Schneider, K., Oppelt, N. (1998): The determination of mesoscale soil moisture patterns with ERS data. *Proc. IEEE Int. Geos. RS Symposium*, *6-10 July 1998, Seattle, USA*.

Schneider, K. (1999): Gekoppelte flächenverteilte Modellierung von Pflanzenwachstum und Verdunstung im Ammereinzugsgebiet mit dem prozessorientiertem Evapotranspirations- und Vegetationsmodell PROMET-V. *State doctorate thesis, University of Munich*.

Schneider, K. (2003): Assimilating remote sensing data into a land-surface process model. *Int. J. Remote Sensing*. Vol. 24 (14). pp. 2959-2980.

Schröder, R., Puls, J., Hajnsek, I., Jochim, F., Neff, T., Kono, J., Paradella, W.R., da Silva, M., Valeriano, D., Costa, M. (2004): Mapsar: A small L-band SAR mission for land observation. *4th IAA Symposium on small satellites for Earth Observation, 07-10.04.2003, Berlin*. Wissenschaft und Technik Verlag.

Schulz, W., Merkel, U., Bach, H., Appel, F., Ludwig R., Löw, A., Mauser, W. (2002): Inferno – Integration of remote sensing data in operational water balance and flood prediction modelling. *Proceedings of the International Conference on Flood Estimation. Berne 6-8 March 2002, Switzerland, CHR Report no. II-17*. pp. 659-668.

Schwäbisch, M. (1995): Die SAR-Interferometrie zur Erzeugung Digitaler Geländemodelle, = DLR Forschungsberichte. DLR-FB 95-25.

Seeber, G. (1989): Satellitengeodäsie - Grundlagen, Methoden u. Anwendungen. De Gruyter: Berlin.

Serbin, G., Or, D., Blumberg, D.G. (2001): Thermodielectric effects on radar backscattering from wet soils. *IEEE Trans. Geosci. Remote Sensing*. Vol. 39 (4). pp. 897-901.

Sheehy, J.E., Johnson, I.R. (1988): Physiological models of grass growth. In: Jones, M.B., Lazenby, A. (Ed.): The Grass Crop. pp. 243-275. Chapman and Hall: London.

Shepard, N. (2000): Extraction of Beta Nought and Sigma Nought from RADARSAT CDPF products. *Canadian Space Agency Technical Document. Rev. 4, 28. April 2000.*

Shi, J., Dozier, J. (2000a): Estimation of snow water equivalence using SIR-C/X SAR, Part I: Inferring snow density and subsurface properties. *IEEE Trans. Geosci. Remote Sensing*. Vol. 38 (6). pp. 2465-2474.

Shi, J., Dozier, J. (2000b): Estimation of snow water equivalence using SIR-C/X SAR, Part II: Inferring snow depth and particle size. *IEEE Trans. Geosci. Remote Sensing*. Vol. 38 (6). pp. 2475-2488.

Skriver, H., Svendsen, M.T., Thomsen, A.G. (1999): Multitemporal C- and L-band polarimetric signatures of crops. *IEEE Trans. Geosci. Remote Sensing*. Vol. 37 (5). pp. 2413-2429.

Smith, A.J.E. (2003): Near real-time geocoding of SAR imagery with orbit error removal. *Int. J. Remote Sensing*. Vol. 24 (24). pp. 5219-5228.

Soil Survey Staff (1975): Soil Taxonomy. A Basic System of Soil Classification for Making and Interpreting Soil Surveys - Soil Conservation Service, U.S. Department of Agriculture, Agriculture Handbook No. 436, U.S. Government Printing Office, Washington D.C.

Srivastava, S.K., Banik, B.T., Adamovic, M., Gray, R., Hawkins, R.K., Lukowski, T.I., Murnagham, K.P., Jefferies, W.C. (1999): RADARSAT-1 Image Quality – Update. *Proc. Of CEOS SAR Workshop, Toulouse, France, Oct. 26-29.*

STMLF (Bayerisches Staatsministerium für Landwirtschaft und Forsten. Landesanstalt für Landwirtschaft) (2004): Agrarmeteorologisches Messnetz Bayern. URL: http://www.landwirtschaft.bayern.de/alle/cgi-bin/go.pl?region=home&page=http://www.stmlf.bayern.de/lbp/agm/station/agm_start.html (10.05.2004).

Stolz, R. (1998): Die Verwendung der Fuzzy Logic Theorie zur wissensbasierten Klassifikation von Fernerkundungsdaten. = Münchener Geographische Abhandlungen, Reihe B. Band B26.

Stolz, R., Schneider, K., Schouten, L., Bach, H. (2000): Combining the microwave model CLOUD and the growth model PROMET-V for soil moisture retrieval from ERS-SAR data. *Proc. of ERS-ENVISAT-Symposium Gothenburg 2000, Looking down to Earth in the New Millennium*, ESA SP-461.

Strasser G., Schneider K., Mauser W. (1999): The Use of ERS SAR Data derived Soil Moisture Distributions for SVAT-Model Validation. *Proc. IEEE Int. Geos. RS Symposium, Hamburg, Germany.*, Vol. 4, pp. 1921-1923.

Strozzi, T., Dammert, P., Wegmüller, U., Martinez, J.M., Beaudoin, A., Askne, J., Hallikainen, M. (1998): European Forest Mapping with SAR interferometry. *Proc. 2nd Int. Workshop on Retrieval of Bio- and Geophys. Param. From SAR data for land applications. ESTEC, Nordwijk, 21-23 October 1998.*

Strozzi, T., Wegmüller, U. Mätzler, C. (1999): Mapping wet snowcovers with SAR interferometry. *Int. J. Remote Sensing*. Vol. 20 (12). pp. 2395-2403.

Taconet, O., Vidal-Madjar, D., Emblachn, C., Normand, M. (1996): Taking into account vegetation effects to estimate soil moisture from C-band radar measurements. *Remote Sens. Environ.* Vol. 56. pp. 52-56.

Tipler, P.A. (1994): Physik. Spektrum Akademischer Verlag: Heidelberg.

Le Toan, T., Davidson, M. (1998): Improved observation and modelling of bare soil surfaces for soil moisture retrieval. *Proc. 2nd Int. Workshop on Retrieval of Bio- and Geophys. Param. From SAR data for land applications. ESTEC, Nordwijk, 21-23 October 1998.*

Topp, C.F.E., Doyle, C.J. (1996): Simulating the impact of global warming on milk and forage production in Scotland: 1. The effects on dry-matter yield of grass and grass-white clover swards. *Agricultural Systems.* Vol. 52. pp. 213-242.

Topp, G.C., Davis, J.L., Annan, A.P. (1980): Electromagnetic Determination of Soil Water Content: Measurements in Coaxial Transmission Lines. *Water Resources Research.* Vol. 16 (3). pp. 574-582.

Tsang, L., Kong, J.A., Shin, R.T. (1985): Theory of Microwave Remote Sensing. New York: Wiley.

Turcotte, D.L., Huang, J. (1995): Fractal distributions in Geology. In: Barton, C. and LaPointe, P.R. (Ed.): Fractals in the Earth Sciences, Plenum Press: New York. pp. 1-40.

Ulaby, F.T., Moore, R., Fung, A.K. (1982): Microwave remote sensing: Active and Passive: Vol. 2 – Radar Remote Sensing and surface scattering and emission theory. Addison-Wesley.

Ulaby, F.T., El-Rayes, M.A. (1987): Microwave dielectric spectrum of vegetation - Part 2: Dual-dispersion model. *IEEE Trans. Geosci. Remote Sensing.* Vol. 25 (5). pp. 551-557.

Ulaby, F.T., Sarabandi, K., McDonald, K., Whitt, M., Dobson, M.C. (1990): Michigan microwave canopy scattering model (MIMICS). *Int. J. Remote Sensing.* Vol. 11 (7). pp. 1223-1253.

Ulander, L.M.H., Dammert, P.B.G., Hagberg, J.O. (1995): Measuring Tree Height using ERS-1 SAR interferometry. *Proc. IEEE Int. Geos. RS Symposium, 1995, Firenze, Italy.*, pp. 2189-2191.

Ulander, L.M.H. (1996): Radiometric Slope Correction of Synthetic-Aperture Radar Images. *IEEE Trans. Geosci. Remote Sensing.* Vol. 34 (5). pp. 1115-1122.

Walker, J.P., Willgoose, G.R., Kalma, J.D. (2001): One-dimensional soil moisture profile retrieval by assimilation of near-surface observations: a comparison of retrieval algorithms. *Advanc. Water Resources*. Vol. 24. pp. 631-650.

Wang, J.R. (1980): The dielectric properties of soil-water mixtures at microwave frequencies. *Radio Science*. Vol. 15 (5), pp. 977-985.

Wang, J.R., Hsu, A., Shi, J.C., O'Neill, P.E., Engman, E.T. (1997): A comparison of soil moisture retrieval models using SIR-C measurements over the little Washita River Watershed. *Remote Sens. Environ.* Vol. 59. pp. 308-320.

Weimann, A. (1996): Bestimmung der Bodenfeuchte mittels aktiver Mikrowellensensoren. = DLR Forschungsberichte. DLR-FB-96-38.

Weiss, M., Baret, F., Myneni, R.B., Pragnère, A., Knyazikhin, Y. (2000): Investigation of a model inversion technique to estimate canopy biophysical variables from spectral and directional reflectance data. *Agronomie.* Vol. 20. pp. 3–22.

Welles, J.M., Norman, J.M. (1991): Instrument for Indirect Measurement of Canopy Architecture. *Agronomy Journal*, Vol. 83, pp. 818-825.

Wigneron, J.P., Ferrazzoli, P., Olioso, A., Bertuzii, P., Chanzy, A. (1999): A simple approach to monitor crop biomass from C-band radar data. *Remote Sens. Environ.* Vol. 69. pp. 179-188.

Williams, J.A., Jines, C.A., Kiniry, J.R., Spanel, D.A. (1989): The EPIC crop growth model. *Transactions of the ASAE*. Vol. 32. pp. 497-511.

Xu, H., Steven, M.S., Jaggard, K.W. (1996): Monitoring leaf area of sugar beet using ERS-1 SAR data. *Int. J. Remote Sensing*. Vol. 17 (17). pp. 3401-3410.

Zadoks J.C., Chang T.T., Konzak C.F. (1974): A decimal code for the growth stages of cereals. *Weed Research*. Vol. 14. pp. 415-421.

Zebecker, H.A., van Zyl, J.J., Held, D.N. (1987): Imaging radar polarimetry from wave synthesis. *Journal of Geophysical Research*, Vol. 92. pp. 683-701.

Zimmermann, G. (1998): Weizen. In: Die Landwirtschaft. Bd. 1: Pflanzliche Erzeugung. BLV Verlagsanstalt. pp. 261-281.

Zribi, M., Ciarletti, V., Taconet, O., Paillé, J., Boissard, J. (2000) : Characterisation of the soil structure and microwave backscattering based on numerical three-dimensional surface representation: analysis with a fractional Brownian Model. *Remote Sens. Environ.* Vol. 72. pp. 159-169.

Zribi, M., Dechambre, M. (2002): A new empirical model to retrieve soil moisture and roughness from C-band radar data. *Remote Sens. Environ.* Vol. 84. pp. 42-52.

Zribi, M., Le Hégarat-Mascle, S., Ottlé, C., Kammoun, B., Guerin, C. (2003): Surface soil moisture estimation from the synergistic use of the (multi-incidence and multi-resolution) active microwave ERS Wind Scatterometer and SAR data. *Remote Sens. Environ.* Vol. 86. pp. 30-41.

van Zyl, J.J., Zebecker, H.A., Elachi, C. (1987): Imaging radar polarization signatures: theory and observations. *Radio Science.* Vol. 22 (4). pp. 529-543.

Maps

Bayerisches Landesvermessungsamt (Ed.): Topographische Karte 1 : 50.000, Blatt L 7932 Fürstenfeldbruck, 8. Auflage, 1999

Buechler, E., Grottentaler, W., Keller, X. (1986): Standortkundliche Bodenkarte 1 : 50.000, Blatt L 7932 Fürstenfeldbruck. Bayerisches Geologisches Landesamt (Ed.).

Grottentaler, W. (1980): Geologische Karte von Bayern 1 : 25.000, Blatt 7833 Fürstenfeldbruck. Bayerisches Geologisches Landesamt (Ed.).

APPENDIX

Table of Contents

Appendix A: SAR basics

A.1: The radar equation

Derivation of the Radar Equation

In the following the formula for the radar equation is derived. It is mainly based on the expositions of LEWIS and HENDERSON (1998) and KLAUSING and HOLPP (2000).

The power density in a distance R_T from an isotropical point energy source is proportional to the transmitted energy P_T and the surface of the surrounding sphere. It is given by

$$Power\ Density = \frac{P_T}{4\pi R_T^2}$$ (A.1)

However, a side looking SAR system has a directional antenna characteristic with a given antenna gain pattern for transmission G_T. The power density at a target is then given by

$$Power\ Density\ at\ Target = \frac{P_T G_T}{4\pi R_T^2}$$ (A.2)

The energy intercepted by the target is proportional to its receiving area A_S. A part of the energy is absorbed and the rest is scattered. A fraction of the scattered power has a directional component towards the receiver of the imaging system. Usually all these target characteristics are combined into a single parameter called the radar cross section (RCS) sigma (σ). The power reradiated towards the receiver is then

$$Power \rightarrow Receiver = \frac{P_T G_T}{4\pi R_T^2}\sigma$$ (A.3)

Only a part of the scattered power is reaching the sensor. It is also dependant on the distance R_R towards the sensor. The power at the receiver is then given as

$$Power\ at\ Receiver = \frac{P_T G_T}{4\pi R_T^2}\sigma\left(\frac{1}{4\pi R_R^2}\right)$$ (A.4)

The total received power P_R depends on the size of the antenna array A_R.

$$Total\ received\ Power = \frac{P_T G_T}{4\pi R_T^2} \sigma \left(\frac{1}{4\pi R_R^2} \right) A_R \tag{A.5}$$

Equation (A.5) is the radar equation. Assuming a monostatic radar with the same antenna size and transmit and receive characteristics as well as the same range distance, it can be simplified. It is introduced that

$$A_R = A_T = A = \frac{\lambda^2 G}{4\pi}, \tag{A.6}$$

$R_T = R_R = R$

$G_T = G_R = G$

This gives

$$P_R = \frac{P_T G^2 \lambda^2}{(4\pi)^3 R^4} \sigma \tag{A.7}$$

In order to maintain independence of the signal and target, the RCS is redefined as radar scattering per unit area (σ^0). The total cross section of an area A becomes

$$\sigma = \sigma^0 A \tag{A.8}$$

So the final and commonly used form of the radar equation is obtained as

$$P_R = \frac{P_T G^2 \lambda^2}{(4\pi)^3 R^4} \left(\sigma^0 A \right) \tag{A.9}$$

A.2 ENVISAT ASAR

ENVISAT ASAR offers different programmable swathes. Each swath has different imaging properties. They differ in the incidence angle range and therefore also in the spatial resolution and swath width. The following table summarizes the swath properties:

Table A.1:   ASAR image swathes (ESA, 2002)

ASAR SWATHES	SWATH WIDTH [KM]	NEAR RANGE INCIDENCE ANGLE	FAR RANGE INCIDENCE ANGLE
IS1	108.4 - 109.0	14.1 - 14.4	22.2 - 22.3
IS2	107.1 - 107.7	18.4 - 18.7	26.1 - 26.2
IS3	83.9 - 84.3	25.6 - 25.9	31.1 - 31.3
IS4	90.1 - 90.6	30.6 - 30.9	36.1 - 36.2
IS5	65.7 - 66.0	35.5 - 35.8	39.2 - 39.4
IS6	72.3 - 72.7	38.8 - 39.1	42.6 - 42.8
IS7	57.8 - 58.0	42.2 - 42.6	45.1 - 45.3

Appendix B: Remote Sensing data

B.1   SAR Geocoding

Table B.1:   **Positioning accuracy for an ENVISAT ASAR AP image (30m resolution)**

GCP #	IMAGE		MAP		ΔEAST [M]	ΔNORTH [M]
	EASTING [M]	NORTHING [M]	EASTING [M]	NORTHING [M]		
1	657661.24	5326365.64	657679.83	5326397.85	18.59	32.21
2	658649.53	5327119.67	658611.23	5327129.67	-38.30	10.00
3	656585.11	5323635.05	656596.36	5323641.67	11.25	6.63
4	656775.45	5319857.60	656767.44	5319868.56	-8.01	10.96
5	656768.13	5318115.29	656748.43	5318081.79	-19.70	-33.50
6	656804.73	5317185.57	656814.96	5317178.90	10.23	-6.67
7	657580.72	5314264.64	657594.29	5314289.66	13.58	25.03
8	659242.04	5312490.67	659235.23	5312495.10	-6.80	4.43
9	660727.67	5318718.92	660717.57	5318735.28	-10.10	16.36
10	659927.71	5319244.61	659912.65	5319237.37	-15.07	-7.24
11	662761.85	5320535.97	662733.88	5320544.38	-27.98	8.41
12	663081.84	5321907.33	663060.63	5321915.15	-21.21	7.82
13	670624.31	5306422.41	670599.85	5306438.22	-24.45	15.81
14	672327.08	5303388.28	672297.37	5303393.84	-29.70	5.56
15	671687.11	5302188.34	671675.75	5302166.52	-11.36	-21.82
16	674109.84	5299319.92	674114.44	5299337.32	4.60	17.40
17	671104.28	5309456.54	671093.97	5309466.66	-10.31	10.12
Mean					-9.69	5.97
STDV					16.64	16.05

Appendix C: Field campaign

| Table C.1:	Land cover code table 2003	
CODE	GROUP	LAND USE CLASS
100		undifferentiated
101		Winter wheat
102		Summer wheat
103		rye
104		Winter barley
105		Summer barley
106		oat
107		triticale
108	Arable land	Corn maize
109		Fodder maize
201		beans
202		rape
206		potatoes
300		Not cultivated
301		Fallow land
302		Legumes
303		Sun flowers
320		other horticulture
321	horticulture	flowers
322		strawberries
400	grassland	undifferentiated
401		grassland
402		pasture
403		pasture
407		Golf course
500		undifferentiated
501		deciduous
502	forest	coniferous
503		mixed
505		Logging area
601		Bog with trees
701		water
800		Gravel pit
900		Sealed area (undiff.)
910		Residental (undiff)
911		Compact residental area
912	others	Residental area
913		building
921		highway
922		Main street
923		street
924		path
1000		unclassified

A-6

Appendix D: Bare soil model

D.1 Empirical soil model calibration

Z-parameter frequency distributions

The following diagrams show the frequency distributions of the Z-values for different acquisition dates. The Z-parameter is given by

$$z = \frac{s^2}{l}$$

As can be seen, the threshold of 0.3 is applicable to all image datasets for the separation of smooth and rough surfaces. It can be seen, that the separability of the two classes reduces with steeper incidence angle (DOY 114), which can be interpretated as lower roughness sensitivity of the signal.
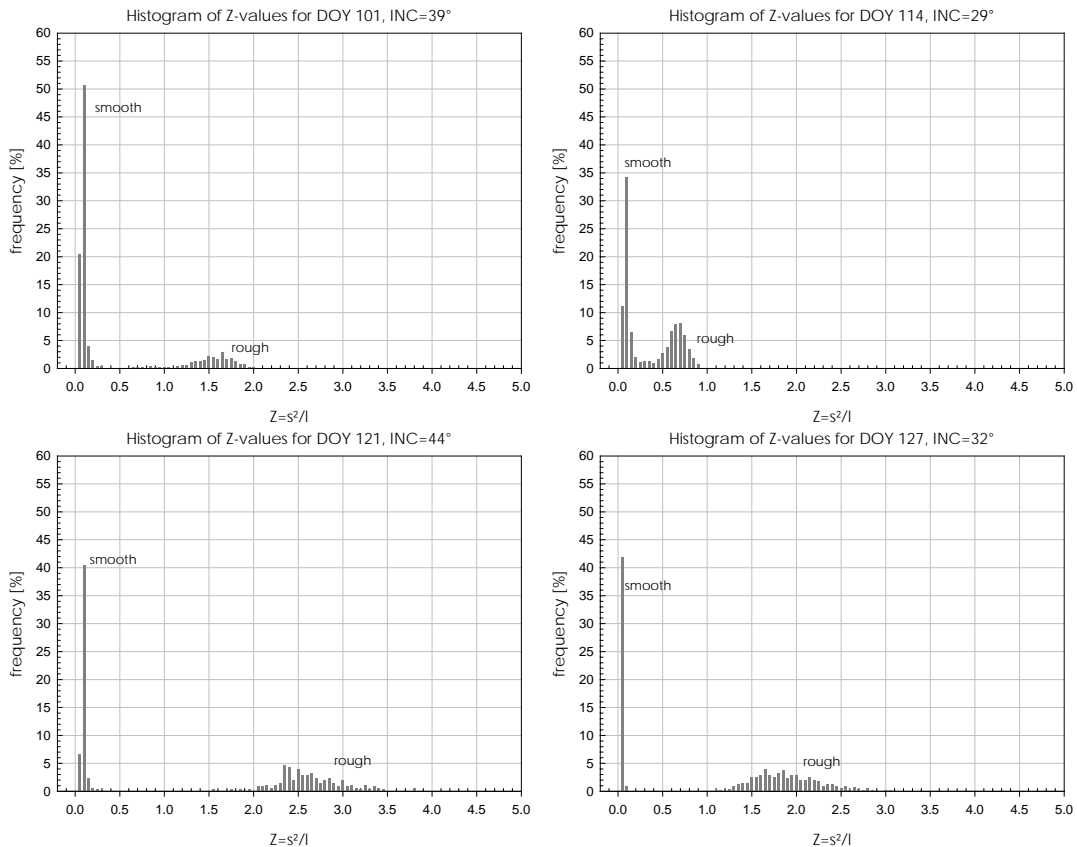
RMS height versus optimal autocorrelation length

The results of the fit between the RMS height and optimal autocorrelation length is shown in the following Figures. The model parameters for each data are given in Table D.1. Clearly can be seen, the different behaviour of the relationship as function of incidence angle.

Table D.1: **Regression parameters for the relationship between rms height and optimal autocorrelation length**

DOY	Y_0	A	B	R^2
101	2.1611	0.0003	3.5652	0.40
114	-10.0325	7.5721	0.3847	0.96
121	-1.1965	1.3119	0.4141	0.96
127	-2.7807	2.2854	0.4028	0.85
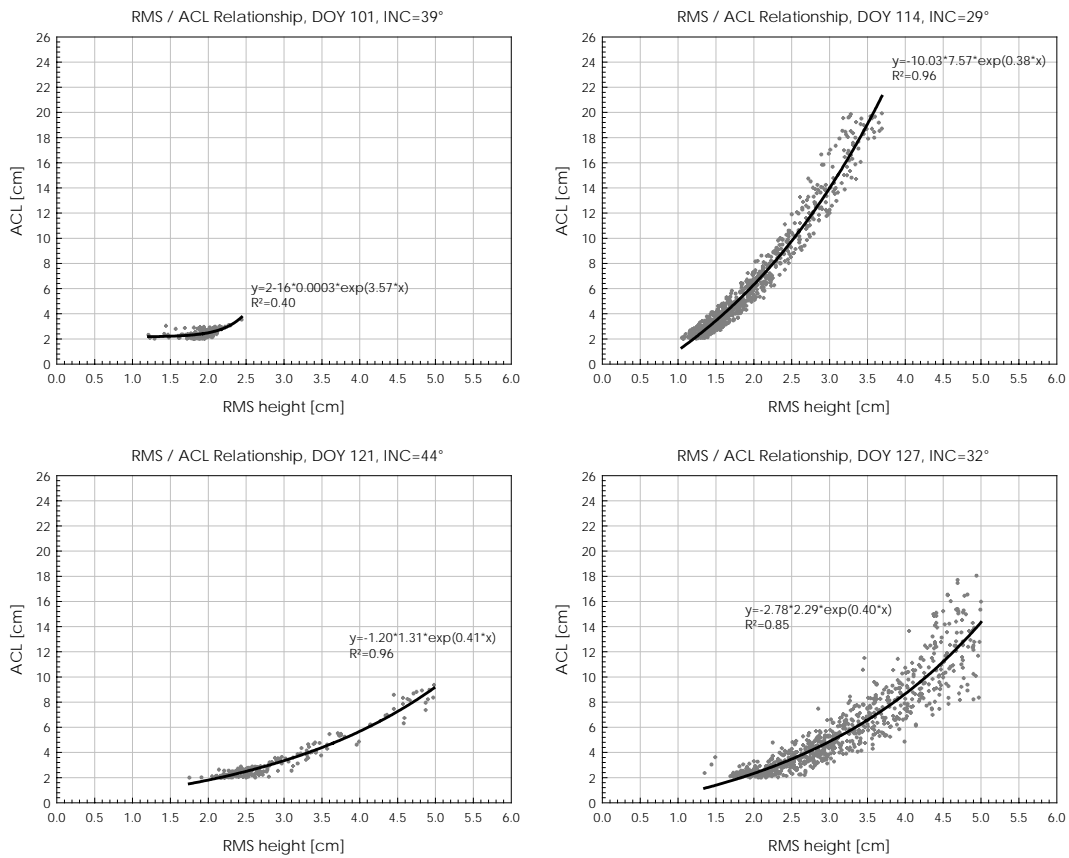
D.2 Bare soil backscattering model

A-parameter incidence angle normalization

The following tables list the estimated regression parameters for the A-parameter incidence angle normalization. The used model has the following form:

$$A(\theta) = 10^{c_1 + c_2 \log(A(0)) + c_3 \log(A(0)^2)}$$

Table D.2: **Regression coefficients for A-parameter normalization: VV polarization**

INC	RMSE	C1	C2	C3	R^2
5	0.03410	4.91337E-03	9.08956E-01	-6.42901E-02	1.00
7.5	0.05180	2.13543E-03	8.29693E-01	-1.11958E-01	1.00
10	0.06070	-4.07657E-03	7.58254E-01	-1.49072E-01	0.99
12.5	0.06400	-1.19141E-02	6.92473E-01	-1.78437E-01	0.99
15	0.06350	-2.02854E-02	6.31102E-01	-2.01826E-01	0.99
17.5	0.06060	-2.85634E-02	5.73231E-01	-2.20259E-01	0.99
20	0.05590	-3.65675E-02	5.18056E-01	-2.34378E-01	0.99
22.5	0.05030	-4.39773E-02	4.65269E-01	-2.44867E-01	0.99
25	0.04450	-5.06332E-02	4.14243E-01	-2.52014E-01	0.99
27.5	0.03930	-5.65005E-02	3.64779E-01	-2.56137E-01	0.99
30	0.03580	-6.16389E-02	3.16617E-01	-2.57447E-01	0.99
32.5	0.03480	-6.59133E-02	2.69363E-01	-2.56070E-01	0.99
35	0.03680	-6.94096E-02	2.22964E-01	-2.52186E-01	0.99
37.5	0.04110	-7.21300E-02	1.77332E-01	-2.45974E-01	0.98
40	0.04700	-7.40510E-02	1.32234E-01	-2.37453E-01	0.97
42.5	0.05330	-7.51741E-02	8.75872E-02	-2.26888E-01	0.95
45	0.05960	-7.53641E-02	4.34222E-02	-2.14537E-01	0.93

Table D.3:   Regression coefficients for A-parameter normalization: HH polarization

INC	RMSE	C1	C2	C3	R^2
5	0.03460	2.16644E-03	9.06563E-01	-6.47393E-02	1.00
7.5	0.05380	-4.17534E-03	8.24658E-01	-1.13008E-01	0.99
10	0.06480	-1.45378E-02	7.50173E-01	-1.50890E-01	0.99
12.5	0.07110	-2.67871E-02	6.81080E-01	-1.81424E-01	0.99
15	0.07440	-3.99824E-02	6.15962E-01	-2.06317E-01	0.98
17.5	0.07590	-5.36186E-02	5.53830E-01	-2.26639E-01	0.98
20	0.07620	-6.71747E-02	4.94039E-01	-2.43251E-01	0.98
22.5	0.07610	-8.06957E-02	4.35880E-01	-2.56645E-01	0.97
25	0.07590	-9.41513E-02	3.79017E-01	-2.67226E-01	0.97
27.5	0.07610	-1.07586E-01	3.23065E-01	-2.75293E-01	0.96
30	0.07660	-1.21134E-01	2.67785E-01	-2.81085E-01	0.95
32.5	0.07800	-1.35048E-01	2.12837E-01	-2.84744E-01	0.95
35	0.08010	-1.49531E-01	1.58236E-01	-2.86436E-01	0.94
37.5	0.08290	-1.64790E-01	1.03732E-01	-2.86221E-01	0.93
40	0.08640	-1.81224E-01	4.93340E-02	-2.84190E-01	0.92
42.5	0.09060	-1.99145E-01	-4.96904E-03	-2.80489E-01	0.92
45	0.09530	-2.18842E-01	-5.91810E-02	-2.75225E-01	0.91

Bare soil backscatter simulation results

The following table lists the bare soil backscattering coefficients of the test fields, as measured by the sensor and modelled by the SSM model.

Table D.4:   **Bare soil simulation results, compared to measured data**

FIELD	DOY	INCIDENCE ANGLE	MEASURED [dB]		SIMULATED [dB]		Δ [dB]	
			VV	HH	VV	HH	VV	HH
Triticale	86	44.3	-15.5	-15.7	-12.8	-15.5	2.6	0.2
Wheat	86	44.3	-14.1	-14.3	-12.6	-15.0	1.5	0.7
Wheat	92	18.9	-5.1	-5.7	-3.2	-3.6	1.9	2.0
Triticale	92	18.9	-5.2	-5.3	-2.3	-2.8	2.9	2.4
Triticale	101	39.2	-11.4	-12.2	-11.1	-13.3	0.3	1.1
Wheat	101	39.2	-11.3	-11.8	-11.1	-13.0	0.2	1.2
Wheat	114	29.9	-8.0	-8.0	-8.5	-9.6	0.6	1.5
Triticale	114	29.9	-7.3	-7.5	-8.9	-10.0	1.7	2.5

Appendix E: Vegetation model

E.1   Image data and Ground measurements
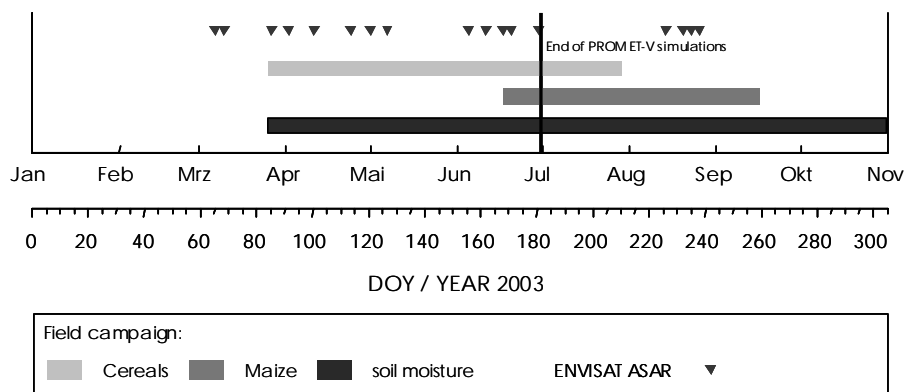
Ground measurements

The following diagrams give an overview about the measured plant and soil parameters of the field campaign for each test field. The land surface model results are included into the plots, until the availability of meteorological input data.
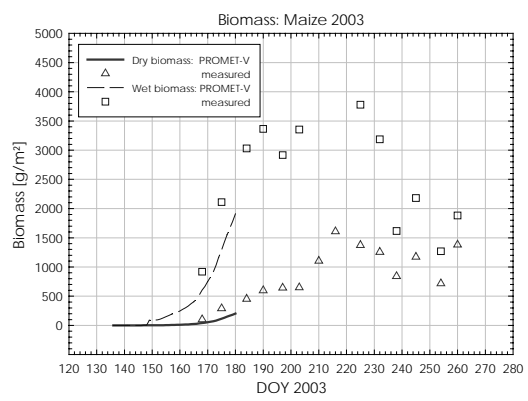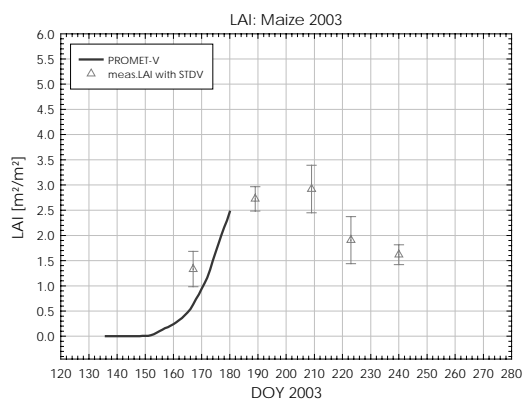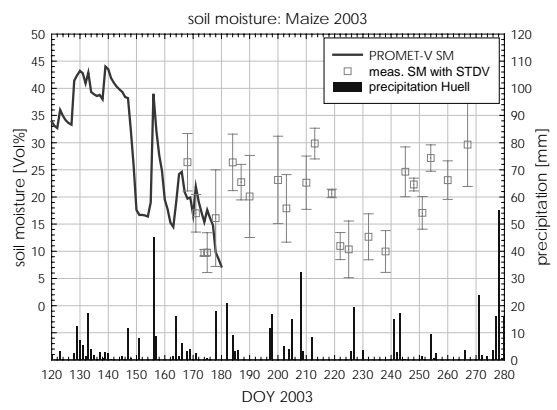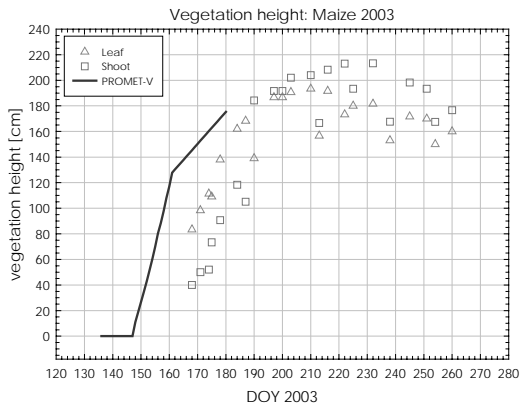
Triticale Stürzer (Field #1/2003)

Vegetation height: Tritcale 2003

soil moisture: Triticale 2003

LAI: Triticale 2003

Biomass: Triticale 2003
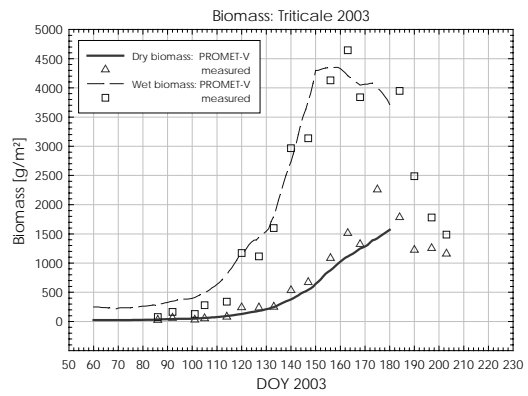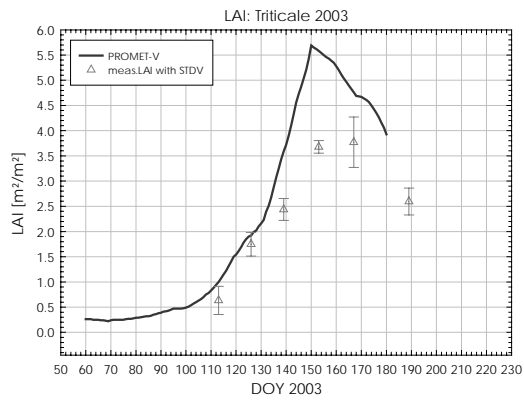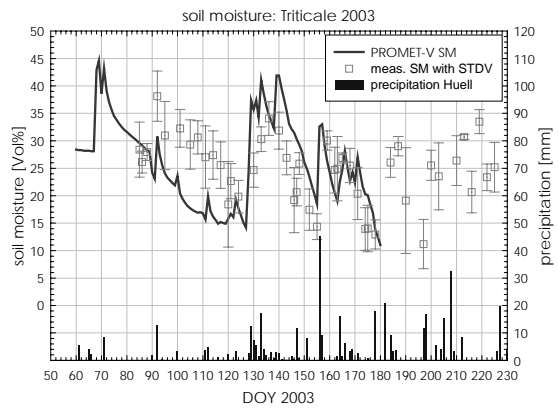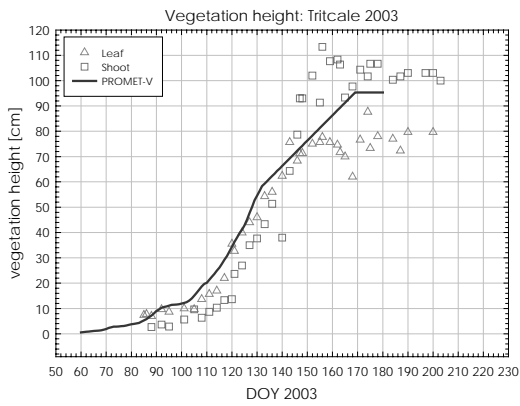
Wheat Stürzer (Field #2/2003)

Vegetation height: Wheat 2003

soil moisture: Wheat 2003

LAI: Wheat 2003

Biomass: Wheat 2003
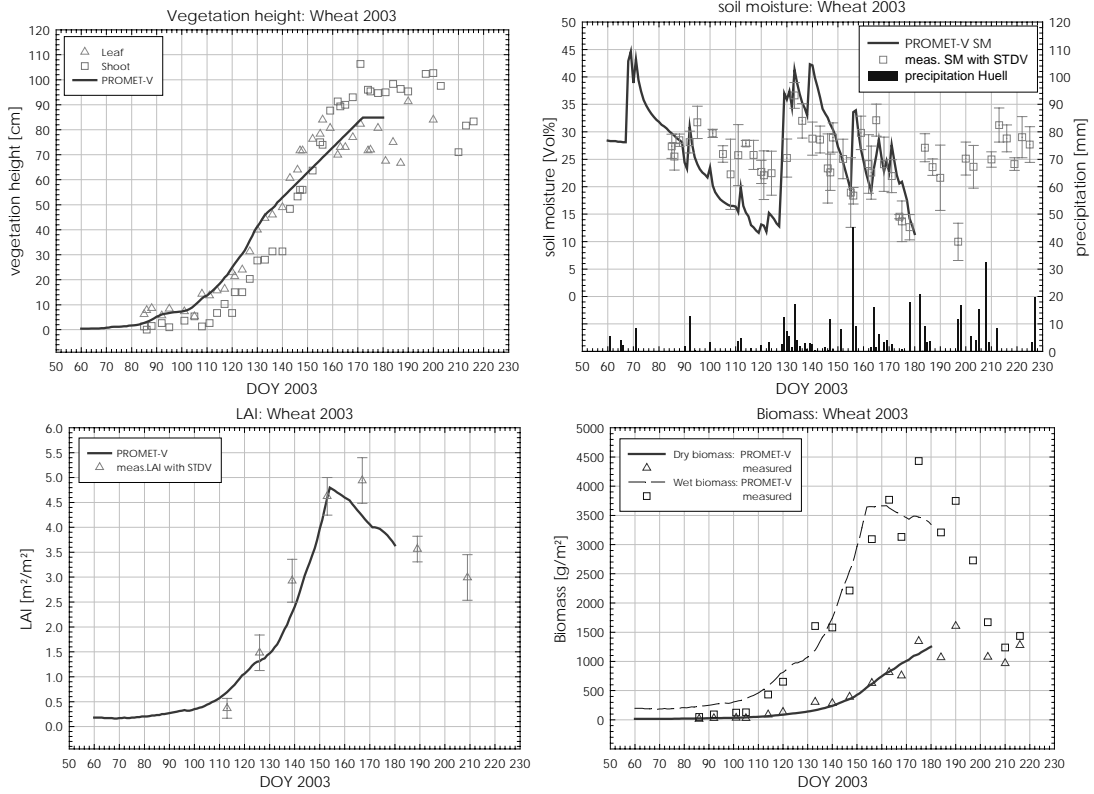
Maize Tiefenbrunn (Field #5/2003)

Vegetation model input datasets

The following tables summarize the datasets used for the calibration and validation of the vegetation backscattering model. The field specific measured and simulated backscattering coefficients and the additional ground truth informations are given. The datasets end with harvesting, due to the then changing surface roughness conditions.

The necessary surface roughness parameters for the testfields were derived, using the roughness inversion algorithm in Chapter 6.

The following roughness parameters A_0 were used for the simulations:

Tritcale: 46.5

Wheat: 40.6

Maize Tiefenbrunn: 36.0

All backscattering coefficients are given in decibels.

Table E.1   Vegetation model parameters and results: Maize

Maize Tiefenbrunn (#4/2003)

Date	DOY	SAR				Soil		Vegetation			Model results			
											Bare soil		Total	
		INC	VV	HH	CP-ratio	SM	DC	height [cm]	Wet Bio. [g/m²]	Dry Bio. [g/m²]	VV	HH	VV	HH
07.03.03	66	39.0	-10.3	-10.4	1.0	no SM	-	-	-	-	-	-	-	-
10.03.03	69	44.4	-10.7	-11.1	0.9	no SM	-	-	-	-	-	-	-	-
27.03.03	86	44.4	-11.3	-11.3	1.0	no SM	-	-	-	-	-	-	-	-
02.04.03	92	18.6	-6.0	-6.5	0.9	no SM	-	-	-	-	-	-	-	-
11.04.03	101	39.0	-12.2	-12.1	1.0	no SM	-	-	-	-	-	-	-	-
24.04.03	114	30.0	-5.9	-5.8	1.0	no SM	-	-	-	-	-	-	-	-
01.05.03	121	44.4	-11.0	-11.1	1.0	no SM	-	-	-	-	-	-	-	-
07.05.03	127	32.9	-8.4	-8.5	1.0	no SM	-	-	-	-	-	-	-	-
05.06.03	156	44.5	-10.2	-10.1	1.0	no SM	-	-	-	-	-	-	-	-
11.06.03	162	33.0	-8.8	-9.0	0.9	no SM	-	-	-	-	-	-	-	-
17.06.03	168	32.9	-9.1	-8.8	1.1	26.4	14.1	83.3	919.0	101.6	-8.9	-10.0	-	-8.6
20.06.03	171	39.0	-9.3	-8.8	1.1	17.0	7.7	98.0	1500.0	210.0	-13.1	-14.0	-	-9.7
30.06.03	181	22.5	-8.6	-8.4	1.0	no SM	-	150.0	2700.0	400.0	-	-	-	-
14.08.03	226	44.5	-11.9	-10.4	1.4	10.4	4.4	193.0	3778.0	1374.0	-17.4	-17.2	-	-10.3
17.08.03	229	-	-	-	-	11.0	4.7	200.0	3400.0	1300.0	-	-	-	-
20.08.03	232	18.6	-8.0	-7.7	1.1	12.7	5.4	181.0	3186.0	1255.0	-6.3	-6.4	-	-7.4
23.08.03	235	26.1	-9.4	-8.9	1.1	11.0	4.7	180.0	2500.0	1200.0	-10.7	-10.6	-	-8.4
26.08.03	238	18.7	-8.5	-7.7	1.2	10.0	4.2	180.0	2500.0	1190.0	-7.7	-7.7	-	-7.7

Table E.2   Vegetation model parameters and results: Cereals

TRITICALE (#1/2003)

Date	DOY	SAR				Soil		Vegetation			Model results			
											Bare soil		Total	
		INC	VV	HH	CP-ratio	SM	DC	height [cm]	Wet Bio. [g/m²]	Dry Bio. [g/m²]	VV	HH	VV	HH
07.03.03	66	39.2	-7.1	-8.1	0.8	no SM	-	-	-	-	-	-	-	-
10.03.03	69	44.6	-10.5	-11.8	0.7	no SM	-	-	-	-	-	-	-	-
27.03.03	86	44.3	-15.5	-15.7	0.9	26.1	12.1	7.8	76.6	25.3	-12.8	-15.5	-15.1	-15.3
02.04.03	92	18.9	-5.2	-5.3	1.0	38.1	21.1	9.6	165.1	60.7	-2.3	-2.8	-3.2	-3.2
11.04.03	101	39.2	-11.4	-12.2	0.8	32.3	16.4	10.0	128.0	30.1	-11.1	-13.3	-11.3	-12.1
24.04.03	114	29.9	-7.3	-7.5	0.9	27.4	13.0	17.0	337.0	80.3	-8.9	-10.0	-7.8	-8.1
01.05.03	121	44.2	-14.2	-12.8	1.4	22.7	10.0	32.0	1172.0	240.0	-13.6	-15.9	-14.5	-13.1
07.05.03	127	32.8	-14.2	-12.8	1.4	no SM	-	44.0	1116.0	236.0	-	-	-	-
05.06.03	156	43.0	-11.6	-11.9	0.9	no SM	-	110.0	4129.0	1085.0	-	-	-	-
11.06.03	162	32.9	-10.7	-8.8	1.5	24.7	11.2	108.0	4643.0	1511.0	-10.3	-11.4	-9.5	-7.6
17.06.03	168	33.2	-11.0	-8.7	1.7	25.5	11.7	100.0	5000.0	1900.0	-10.1	-11.2	-9.9	-7.6
20.06.03	171	39.2	-10.7	-8.8	1.6	20.4	8.7	104.0	5000.0	1900.0	-13.3	-14.7	-12.9	-10.9
30.06.03	181	22.8	-9.3	-7.8	1.4	no SM	-	105.0	-	-	-	-	-	-
						H A R V E S T I N G								

WHEAT (#2/2003)

Date	DOY	SAR				Soil		Vegetation			Model results			
											Bare soil		Total	
		INC	VV	HH	CP-ratio	SM	DC	height [cm]	Wet Bio. [g/m²]	Dry Bio. [g/m²]	VV	HH	VV	HH
07.03.03	66	39.2	-7.2	-7.6	0.9	no SM	-	-	-	-	-	-	-	-
10.03.03	69	44.6	-8.2	-9.5	0.7	no SM	-	-	-	-	-	-	-	-
27.03.03	86	44.3	-14.1	-14.3	1.0	25.5	11.7	7.8	48.4	14.3	-12.6	-15.0	-14.3	-14.5
02.04.03	92	18.9	-5.1	-5.7	0.9	28.1	13.5	6.0	93.7	26.8	-3.2	-3.6	-5.3	-5.9
11.04.03	101	39.2	-11.3	-11.8	0.9	29.7	14.6	7.3	154.4	40.4	-11.1	-13.0	-12.7	-13.2
24.04.03	114	29.9	-8.0	-8.0	1.0	27.9	13.3	15.6	538.4	110.4	-8.5	-9.6	-7.8	-7.9
01.05.03	121	44.2	-13.7	-12.8	1.2	22.1	9.7	21.0	814.9	164.6	-13.3	-15.4	-14.0	-13.1
07.05.03	127	32.7	-14.2	-13.1	1.3	no SM	-	31.0	1257.0	253.9	-	-	-	-
05.06.03	156	44.3	-14.0	-12.4	1.4	18.4	7.7	78.0	3867.0	785.0	-14.4	-15.9	-13.9	-12.3
11.06.03	162	32.8	-12.3	-8.0	2.7	24.1	10.9	91.0	4710.0	1271.7	-10.0	-11.0	-12.1	-7.9
17.06.03	168	33.2	-12.9	-8.4	2.8	24.1	10.9	93.0	5000.0	1250.0	-10.0	-11.0	-12.3	-7.9
20.06.03	171	39.3	-12.8	-10.2	1.8	21.9	9.6	95.0	5000.0	1250.0	-12.5	-13.9	-13.0	-10.3
30.06.03	181	22.8	-10.2	-8.2	1.6	no SM	-	94.0	4800.0	1700.0	-	-	-	-
						H A R V E S T I N G								

E.2 Vegetation model calibration

Relating plant biophysical parameters to image parameters

The following Figures show the estimated relationships between the plant biophysical variables and the normalized copol ratio.
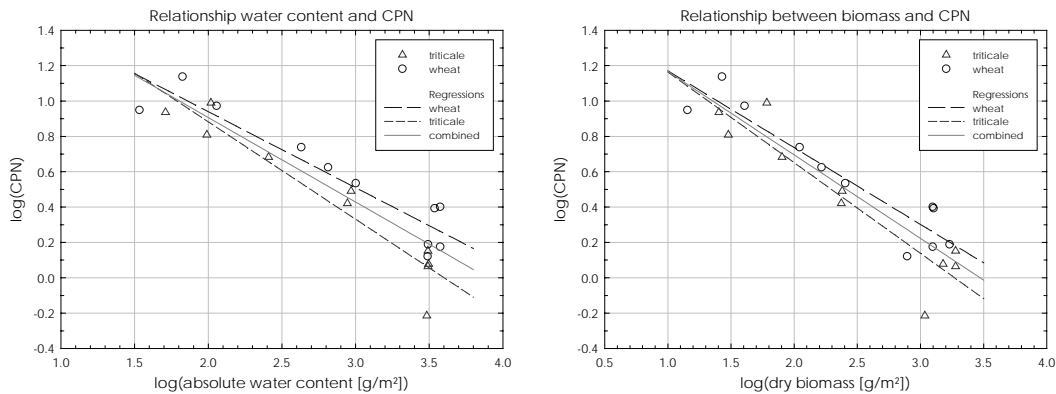

Table E.3:   **Coefficients determining the relationship between CPN and plant biophysical variables using Eq. (7.5)**

MODEL		LINEAR REGRESSION[†]		R²
		a	b	
Dry biomass	wheat	-0.4344	1.6048	0.88
	triticale	-0.5125	1.6758	0.86
	combined	-0.4722	1.6397	**0.84**
Water content	wheat	-0.4301	1.7997	0.88
	triticale	-0.5511	1.9842	**0.91**
	combined	-0.4780	1.8622	0.84

[†]Linear regression of the form $\log_{10}(CPN) = a \log_{10}(x) + b$,

where x is the plant water content [g/m²] or the dry biomass [g/m²]

Appendix F: Coupled modelling

F.1   Spatially distributed modelling results

Spatially distributed predictions of the SAR backscattering coefficients are the result of the coupled modelling approach. Time series of the backscattering coefficient can be simulated based on bio- and geophysical input variables. The following maps show the predicted backscattering coefficients, compared to the ENVISAT ASAR image datasets.

For better comparability, the ASAR images were masked. Only the relevant landuse classes, supported by the backscattering model (wheat, triticale and maize) are shown. Simulated data is only available for those pixels with a vegetation height greater than zero. Due to the later development of the maize, the backscatter for maize fields is not simulated for the images in spring.

An overview of the location and relevant land use classes (greyed) is given in the following figure:

Simulation result

SAR image

11.04.2003

Low backscatter high

simulation result

SAR image

24.04.2003

Low backscatter high

07.05.2003

simulation result

SAR image

Low   backscatter   high

05.06.2003

simulation result

SAR image

Low   backscatter   high

17.06.2003

simulation result

SAR image

Low   backscatter   high
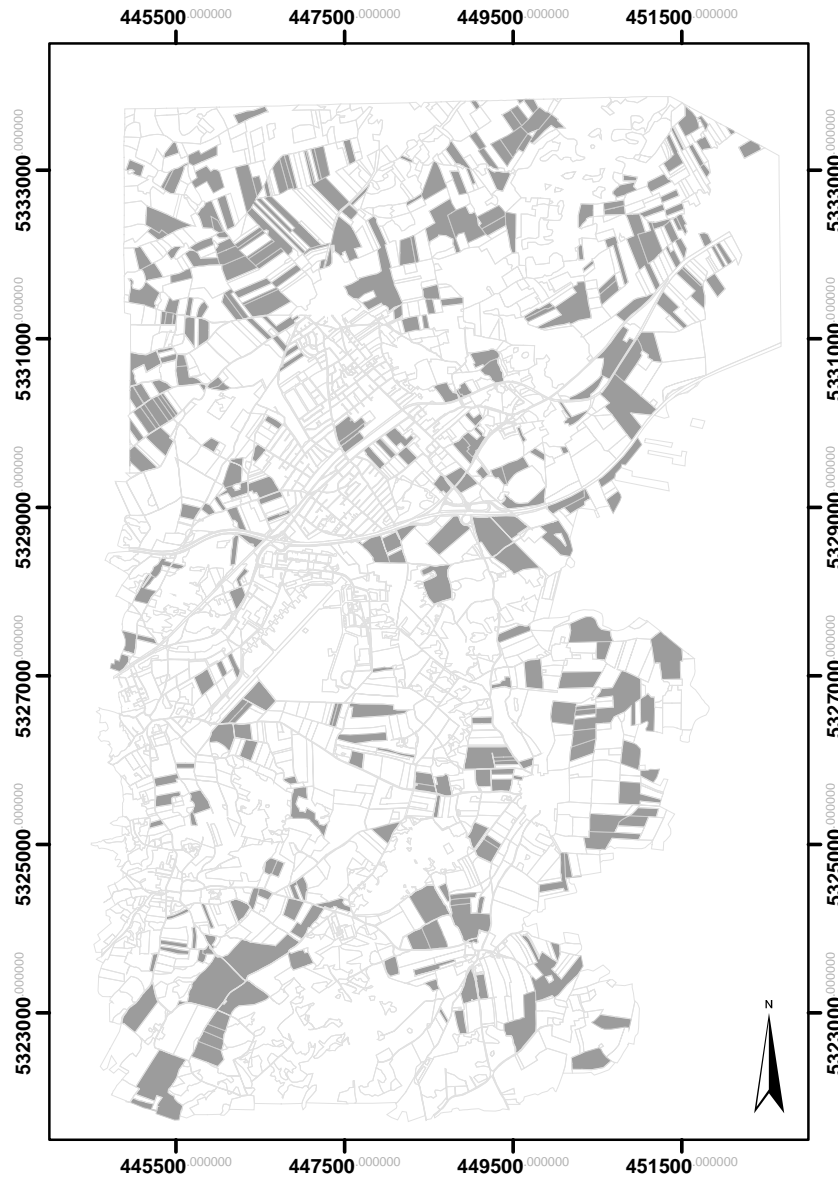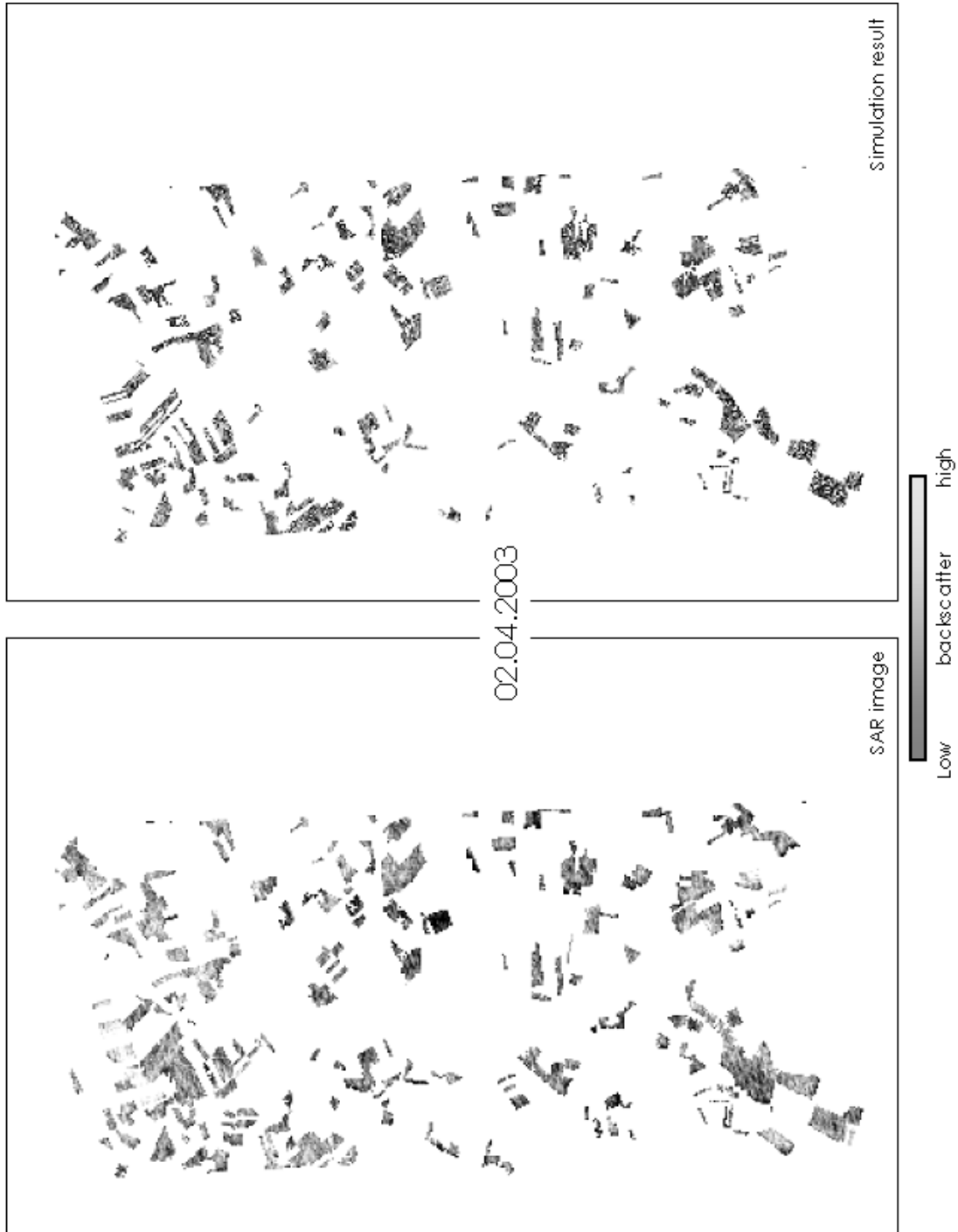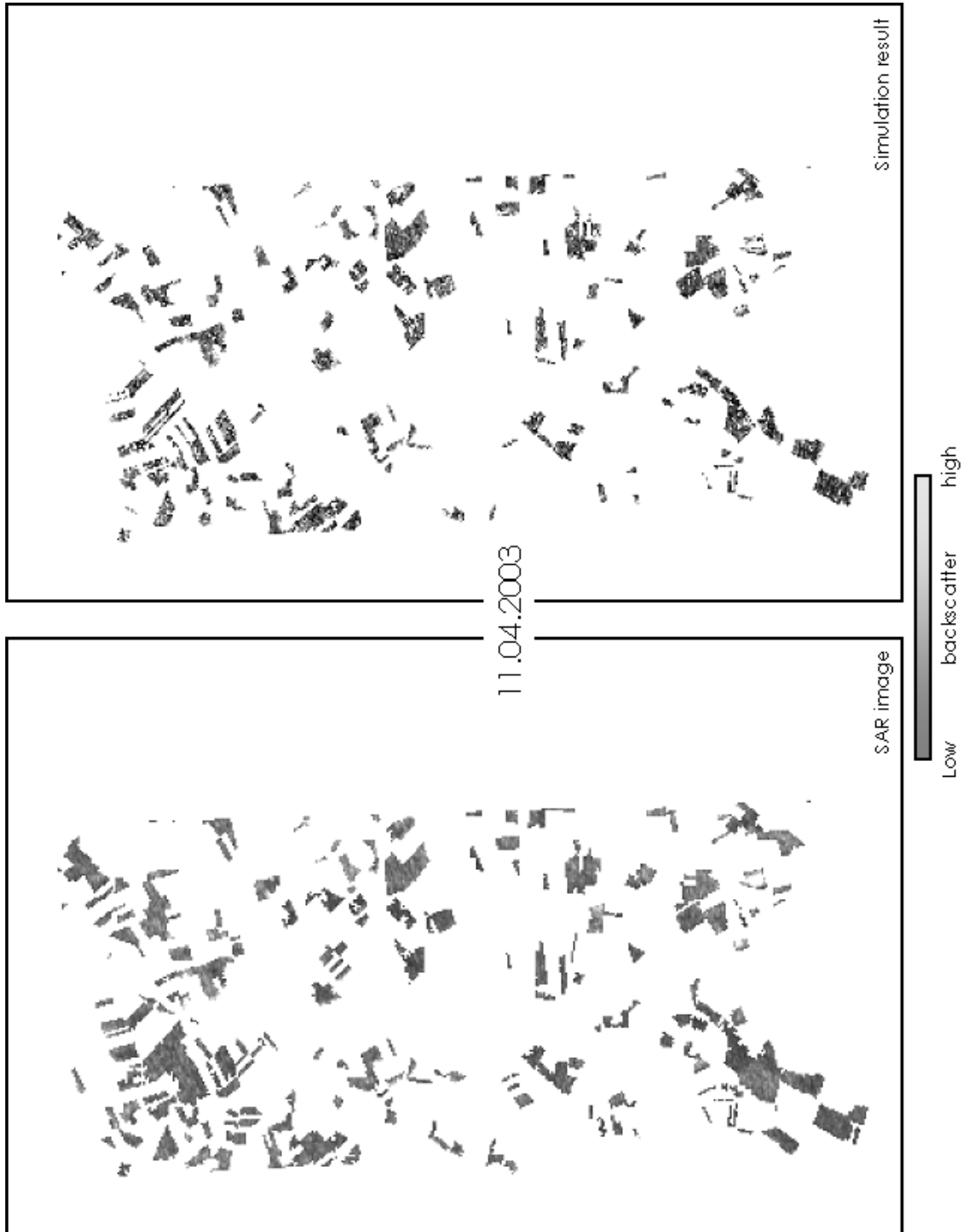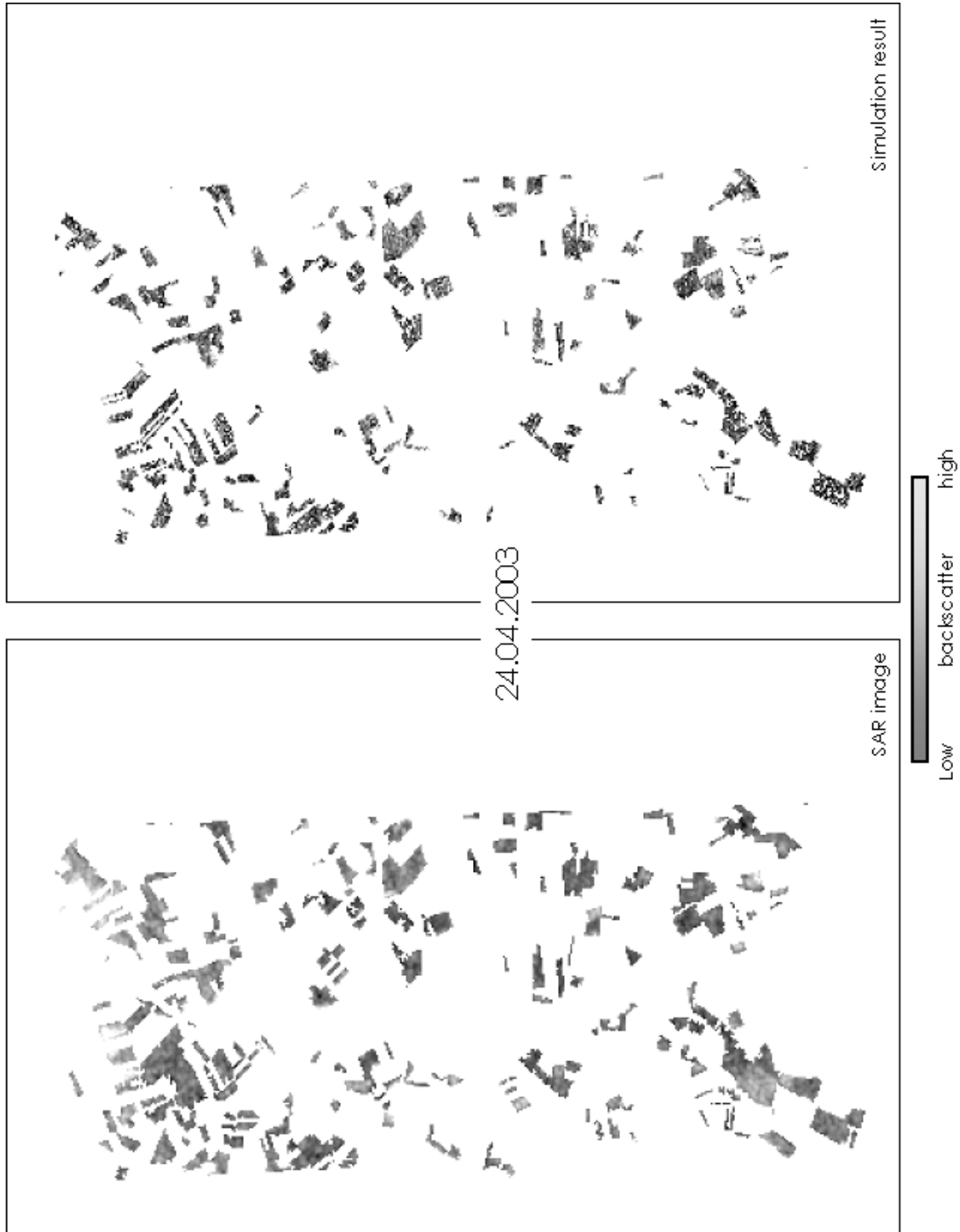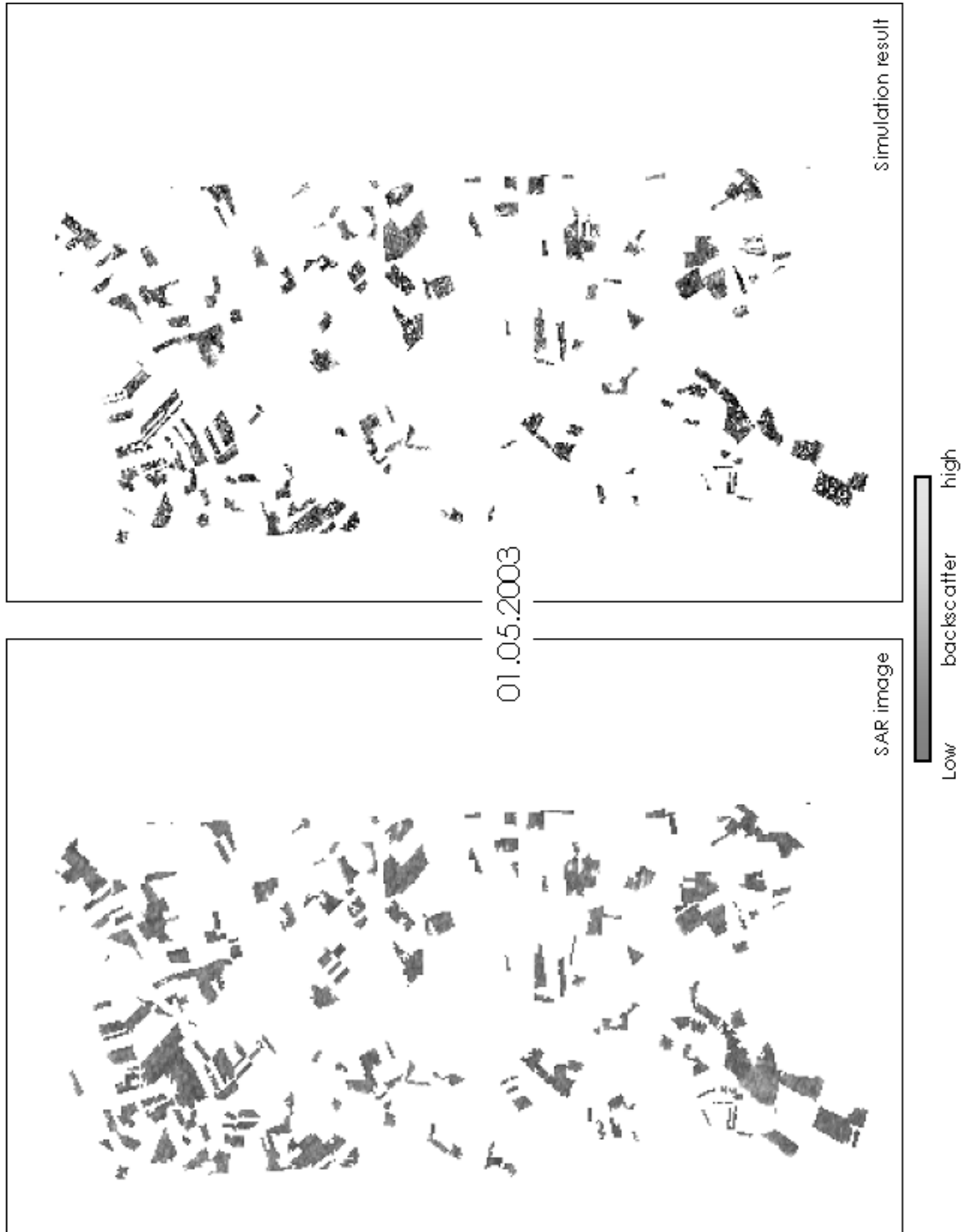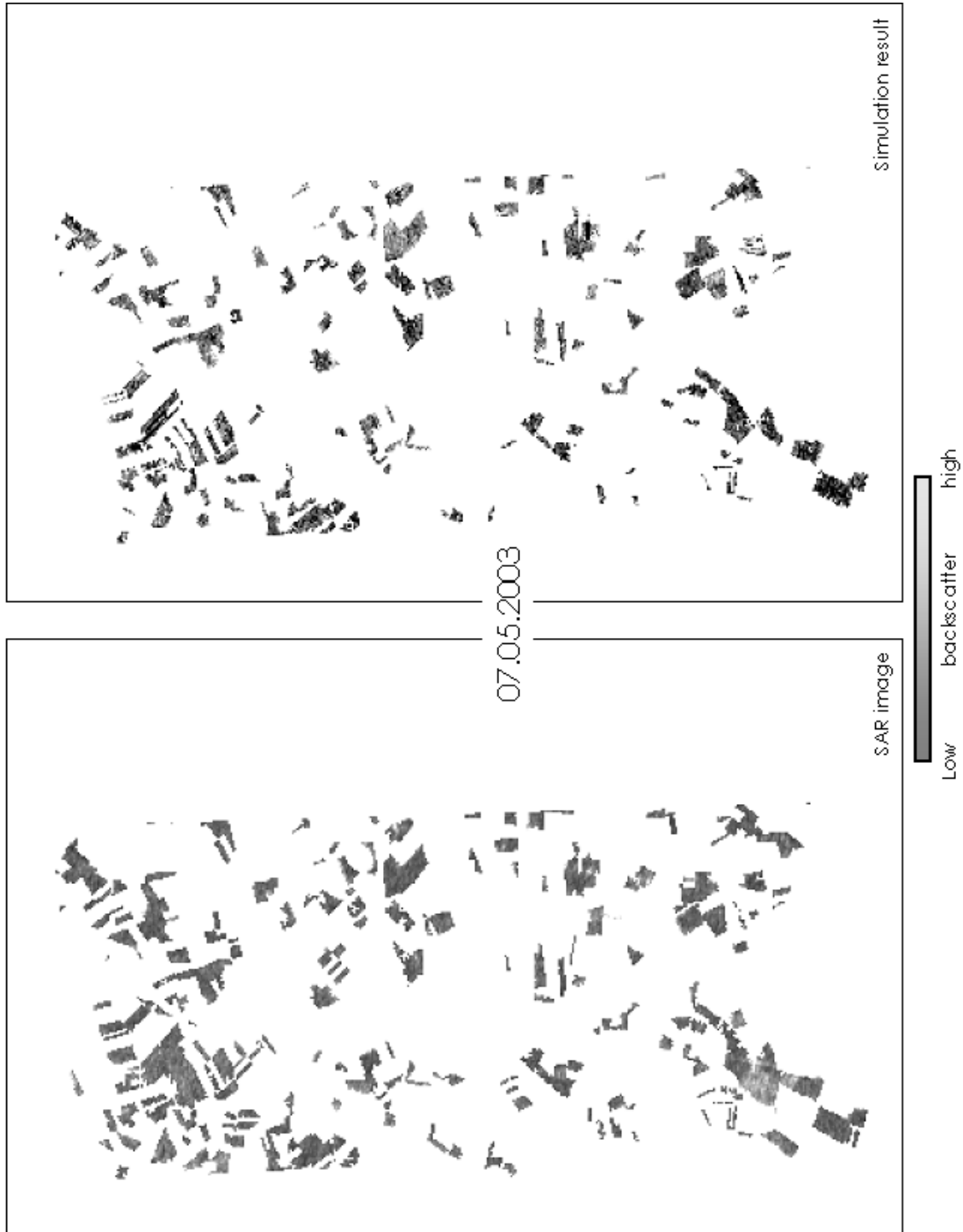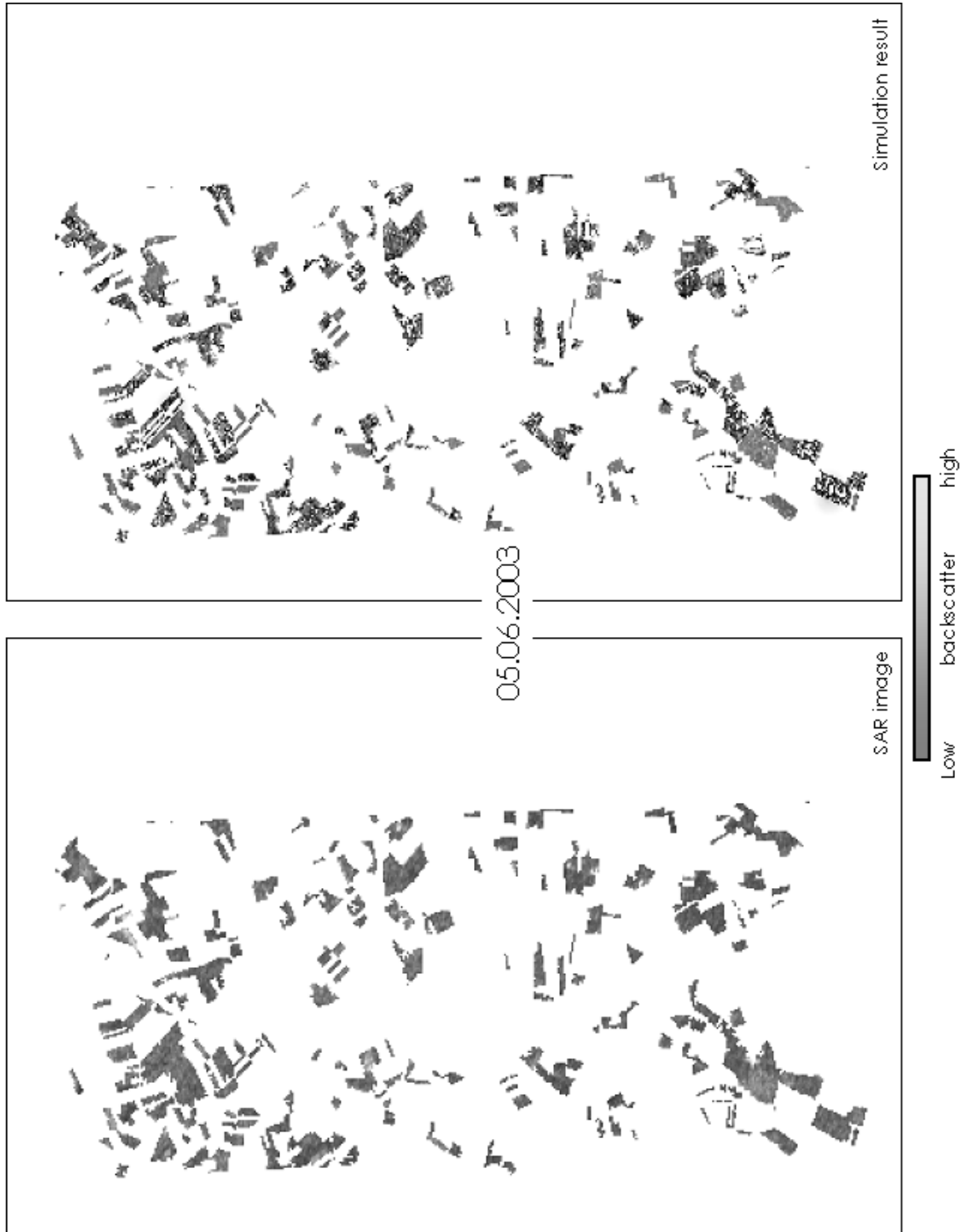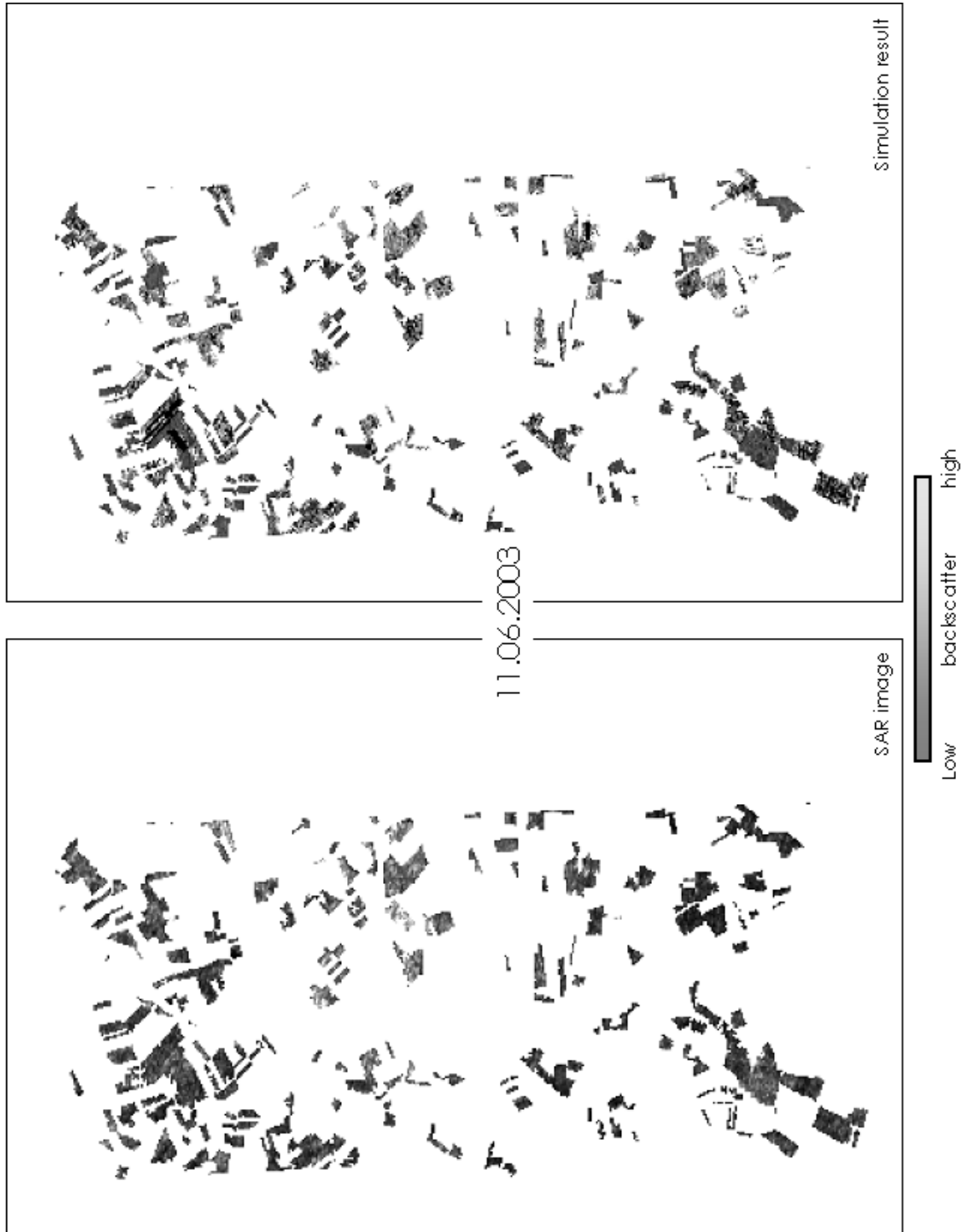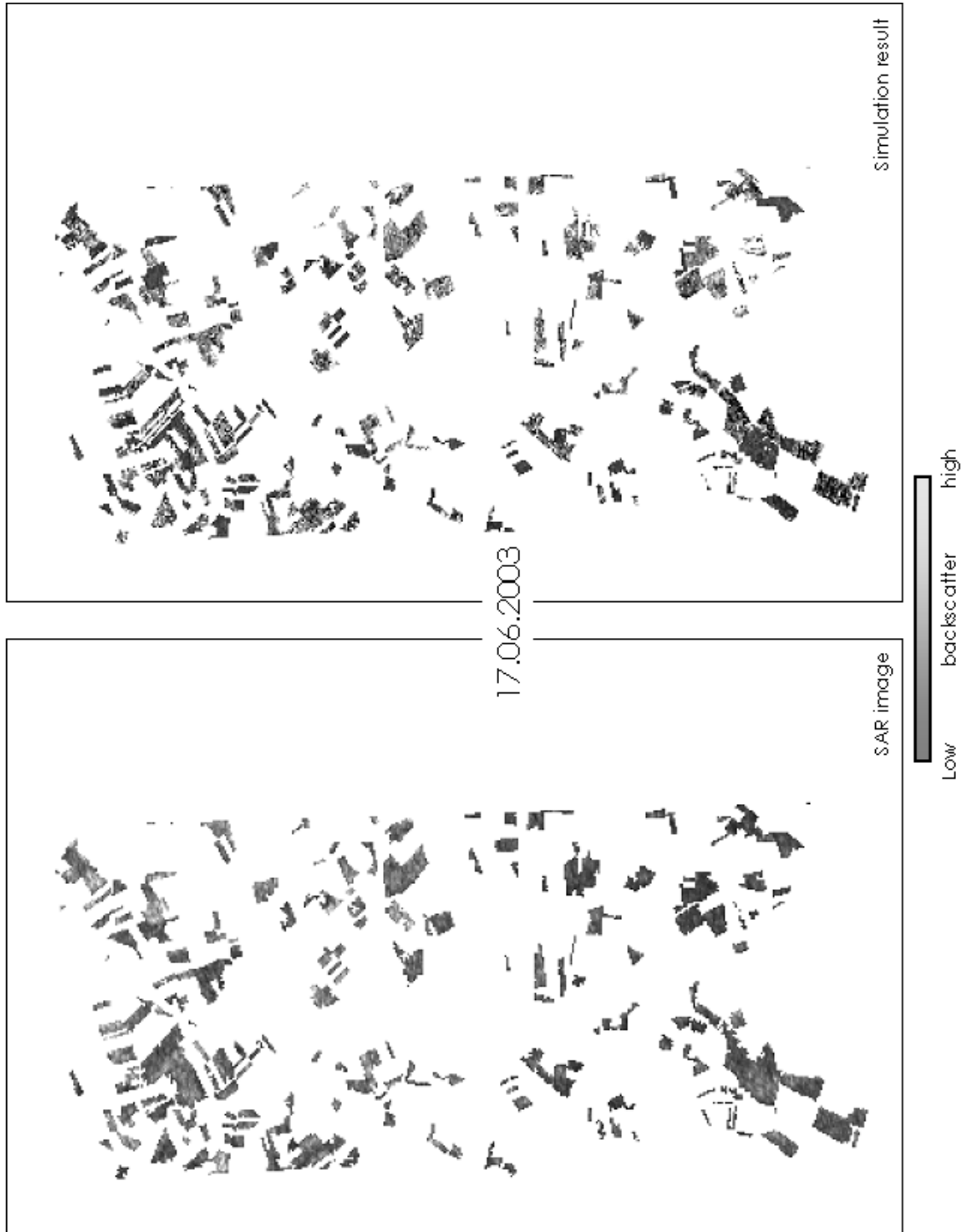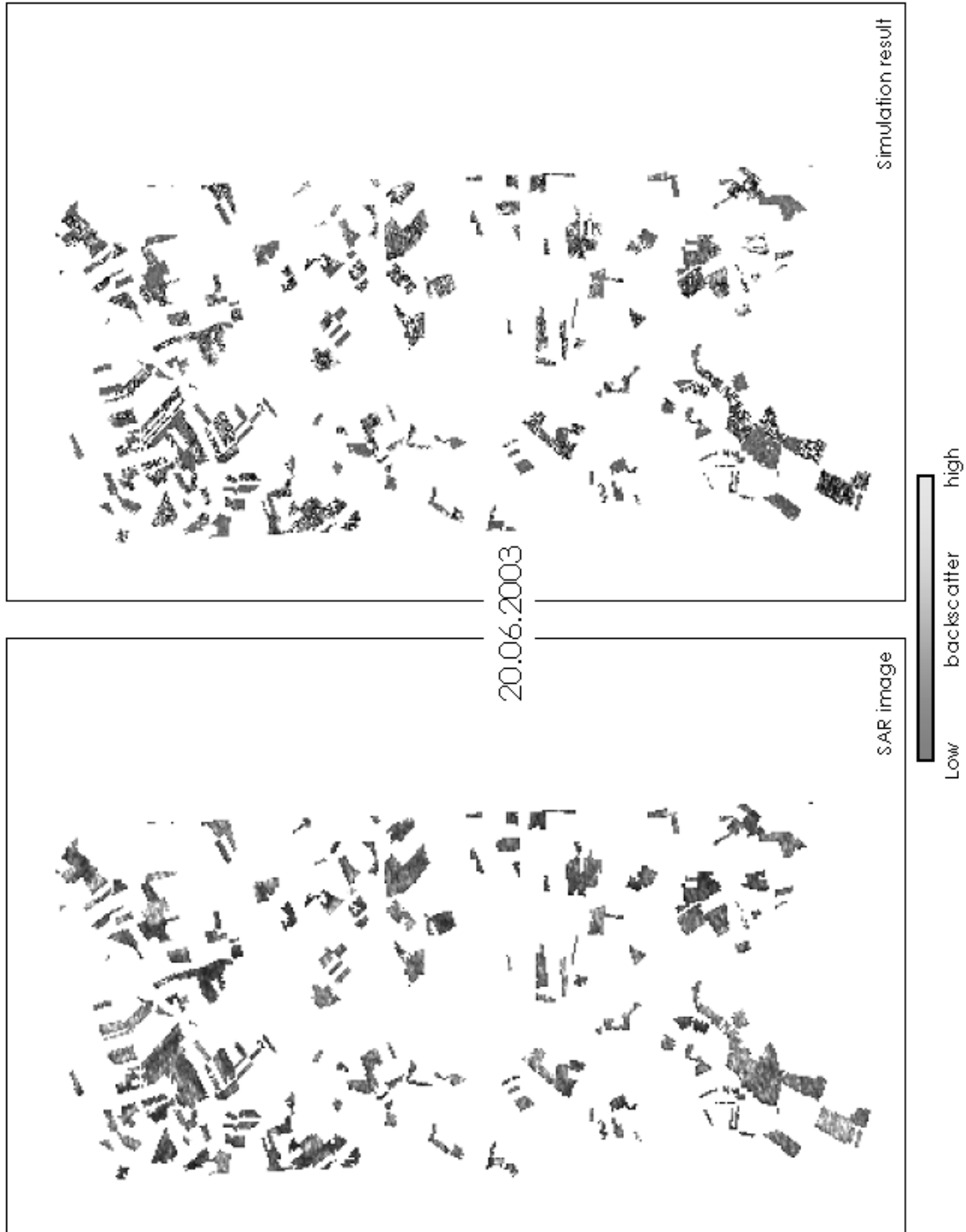
Histograms of the backscatter residuals

The following histograms show the deviations between measured and simulated backscattering coefficients for the land use classes wheat, triticale and maize for the *entire test area*. The backscatter residues were estimated on a pixel by pixel basis.

11.06.2003 (whole scene)

17.06.2003 (whole scene)

20.06.2003 (whole scene)
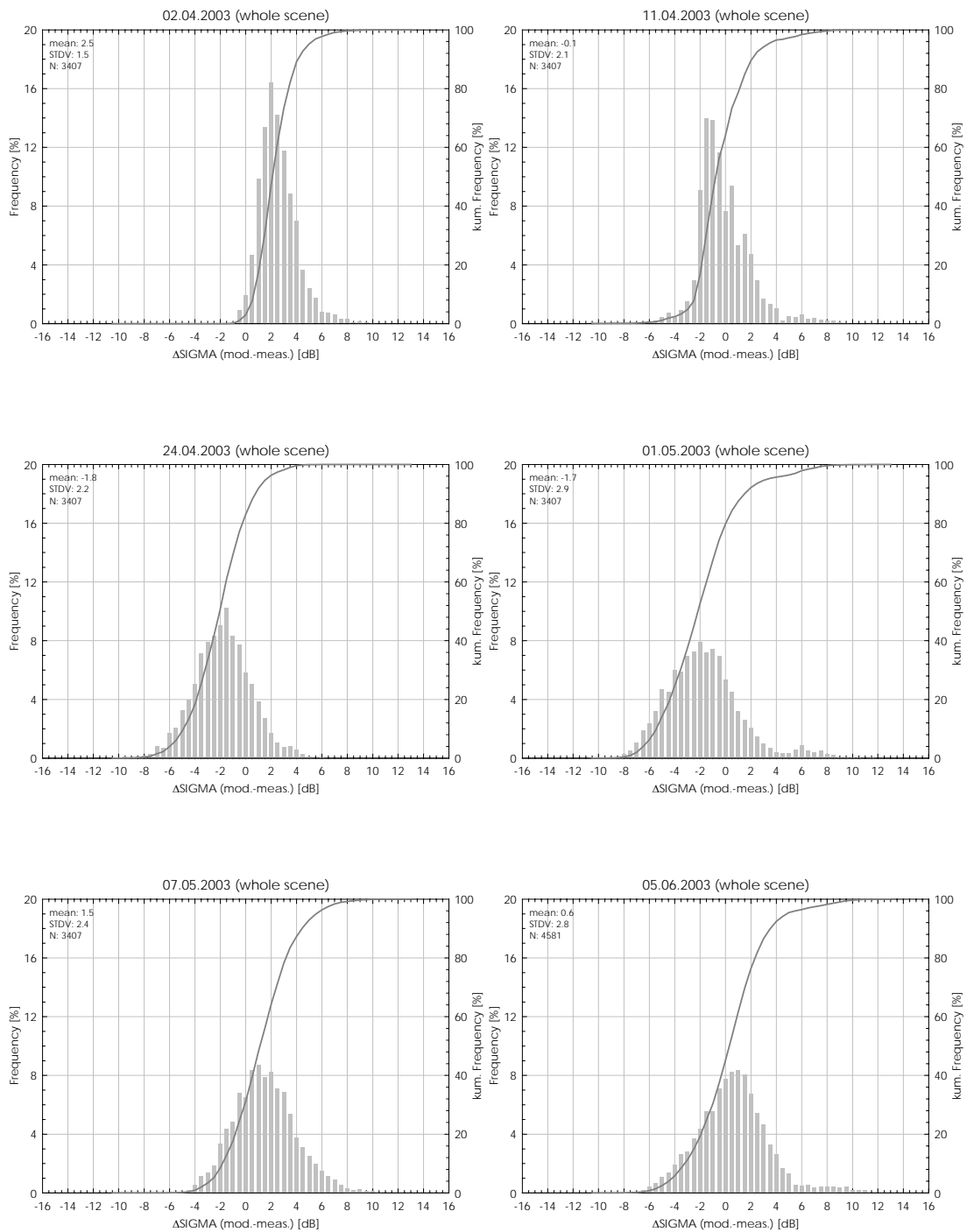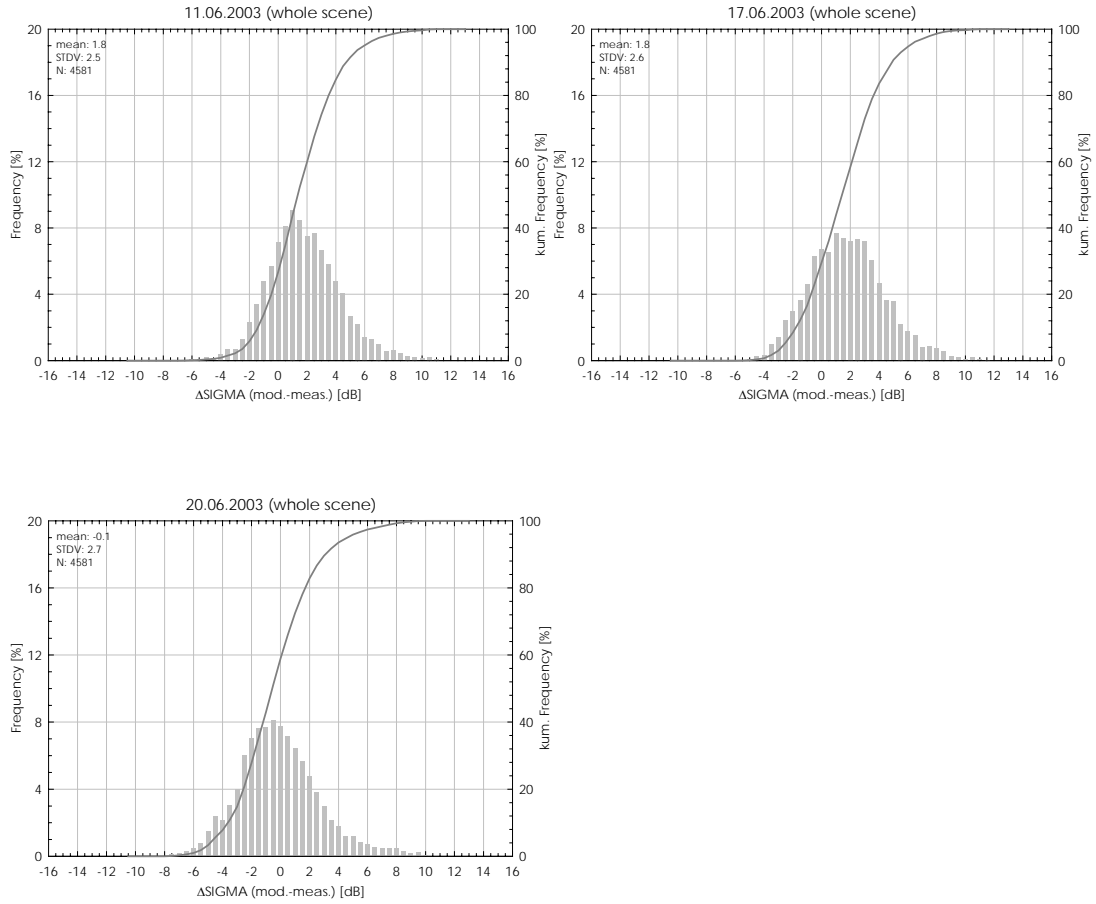
F.2   Soil moisture inversion

Inverted soil moisture maps

The following maps show the spatially distributed inversion results of the soil moisture of the upper soil layer. The maps were derived, using the *simple* and *a priori* inversion strategies.

The inversion results are only available for fields with the supported land uses, namely wheat, triticale and maize, where a vegetation height was existing.
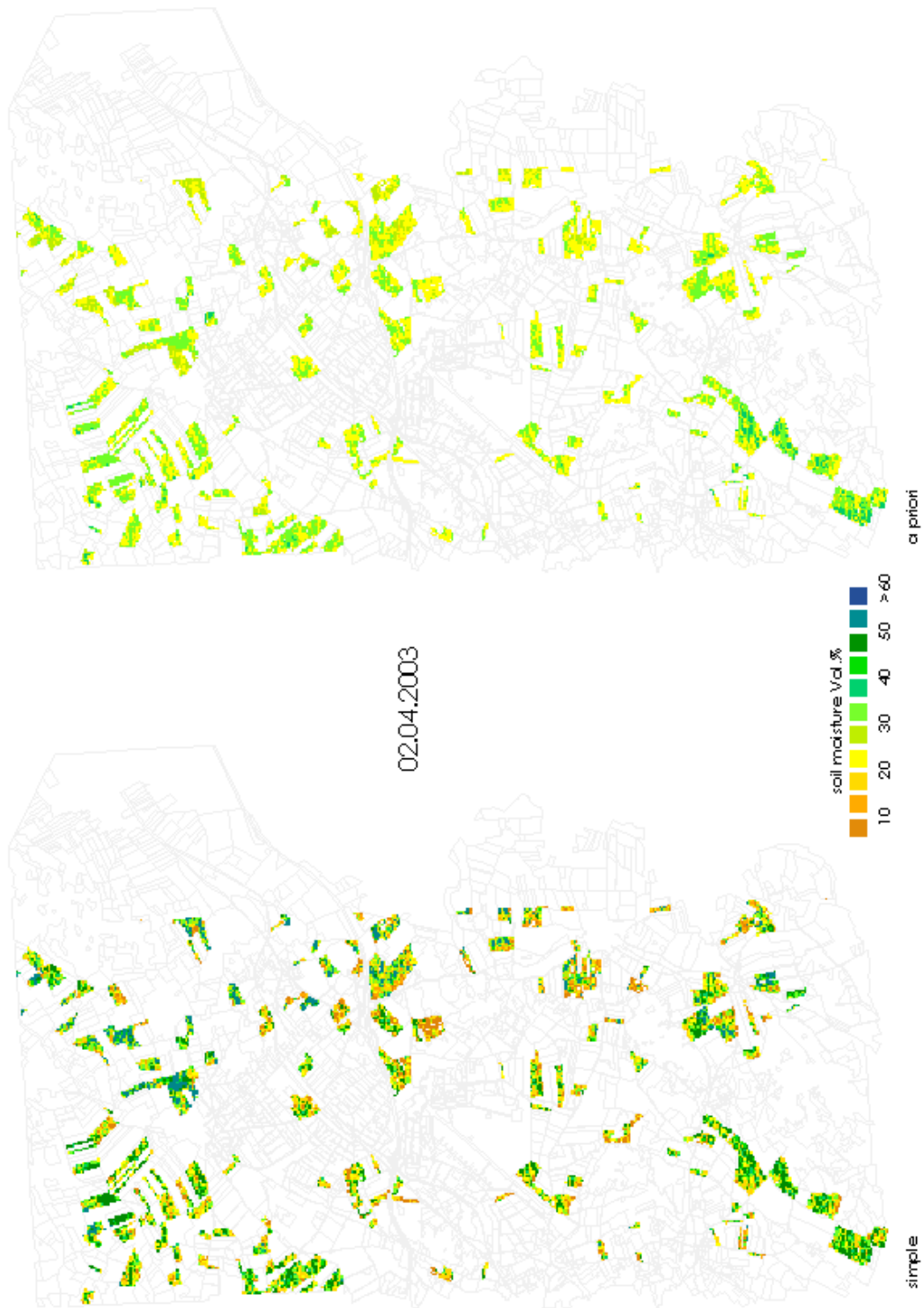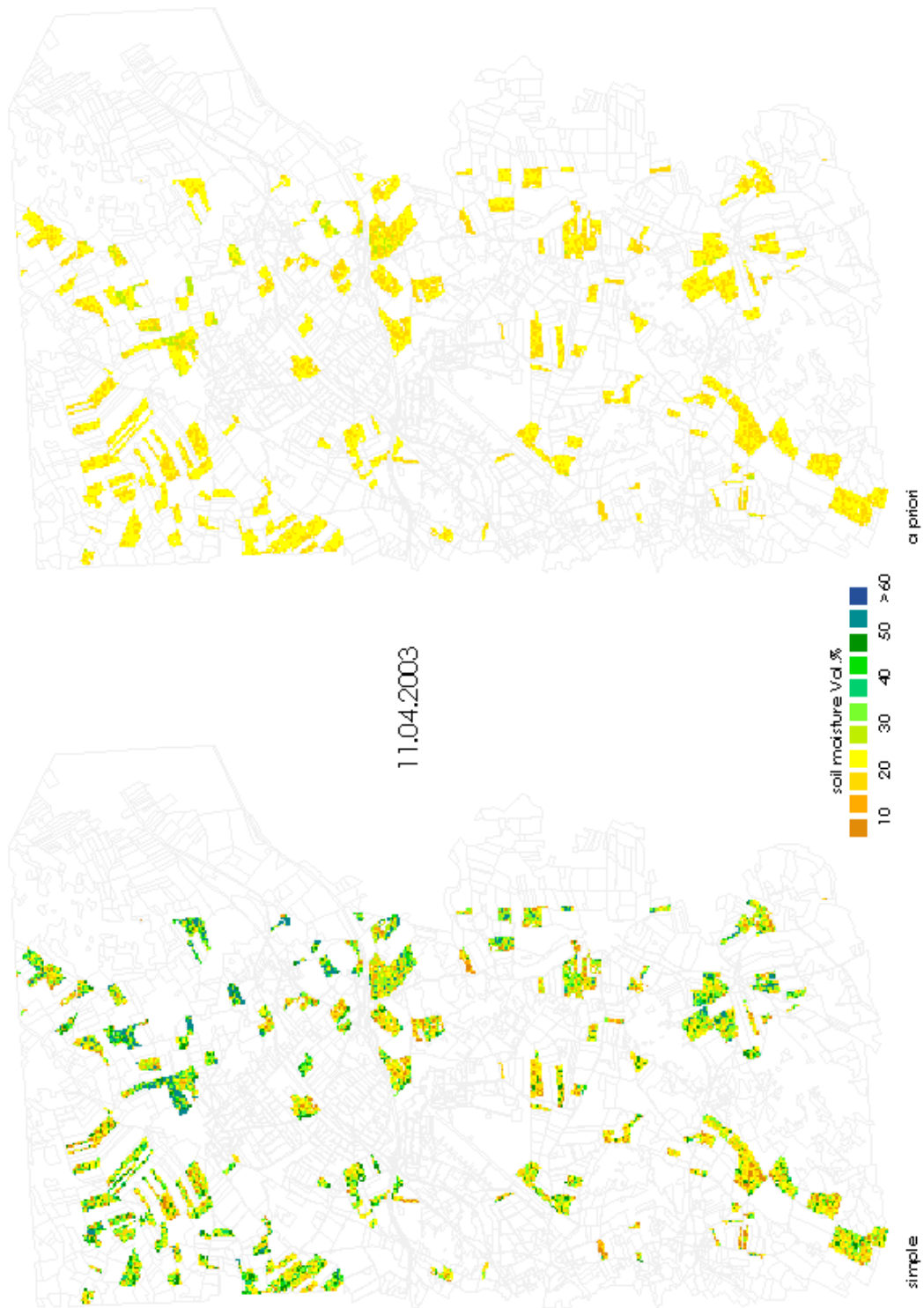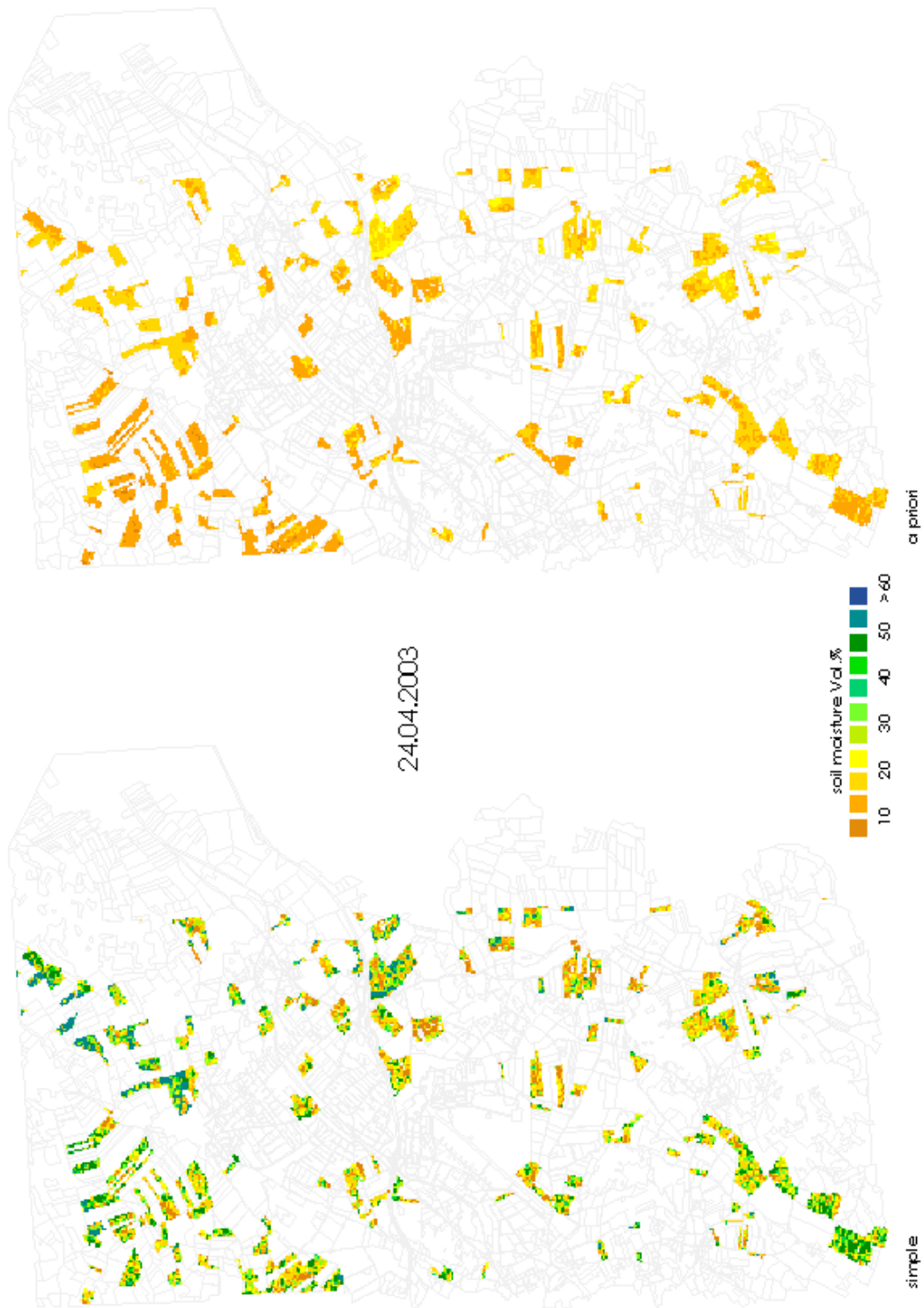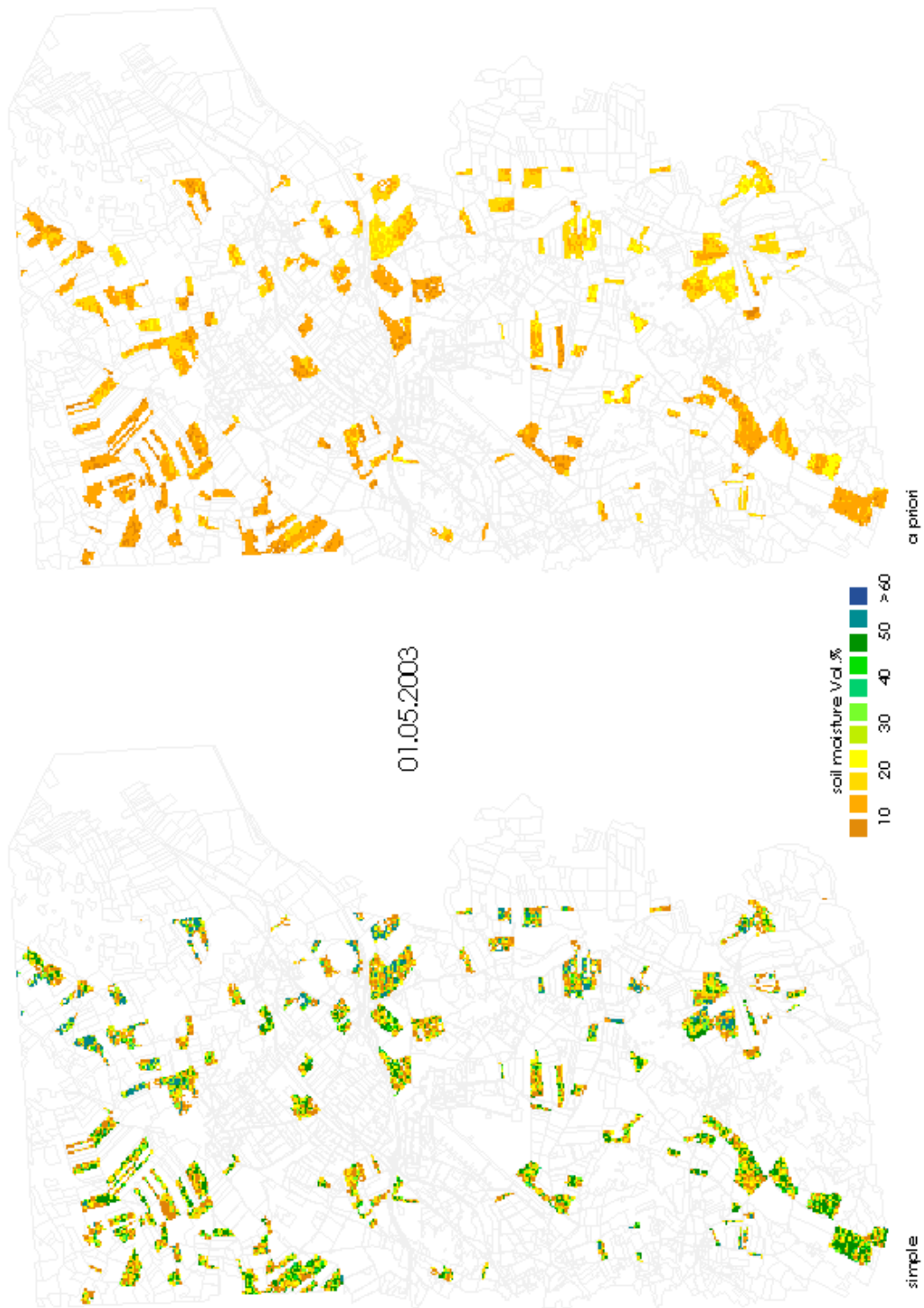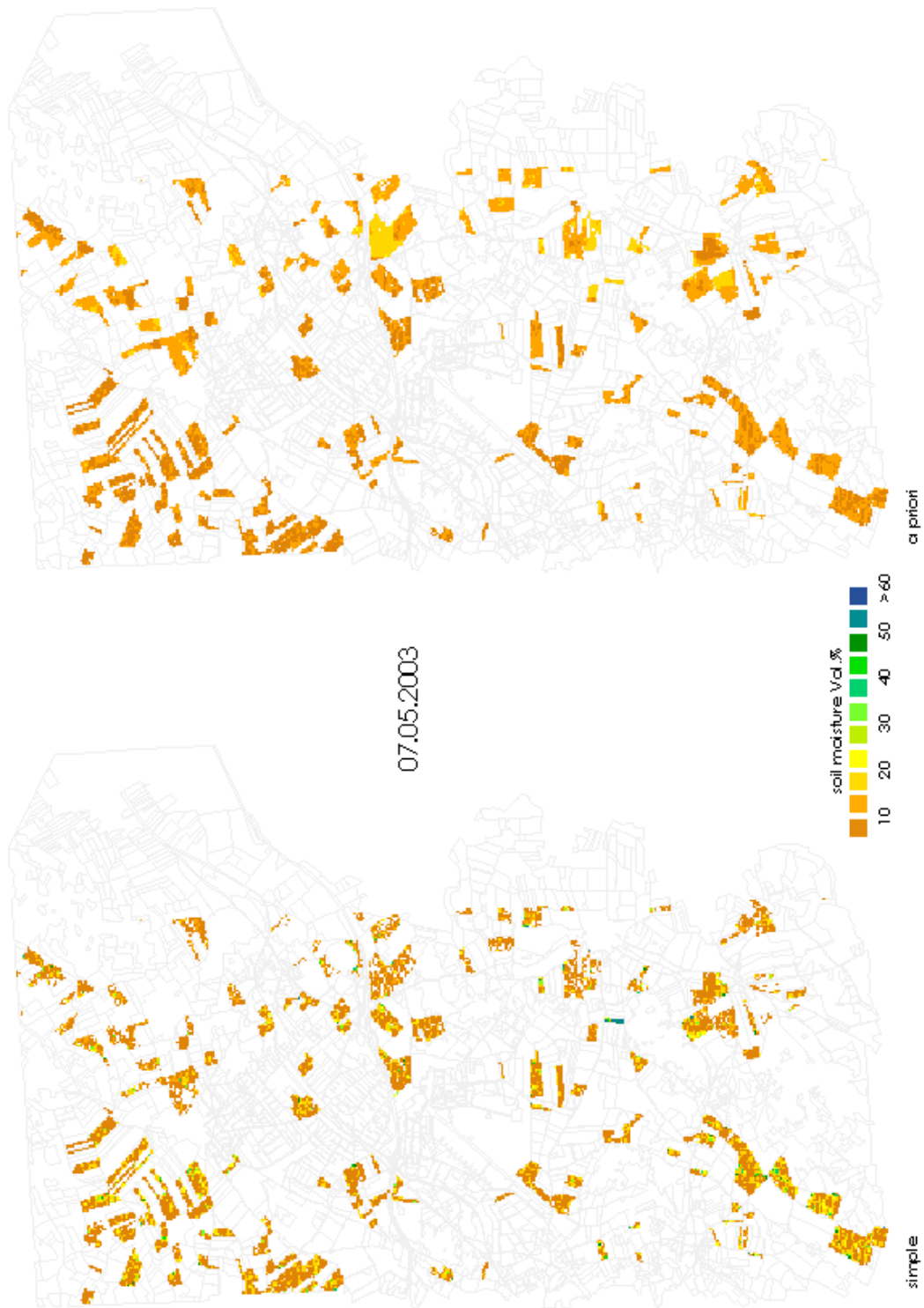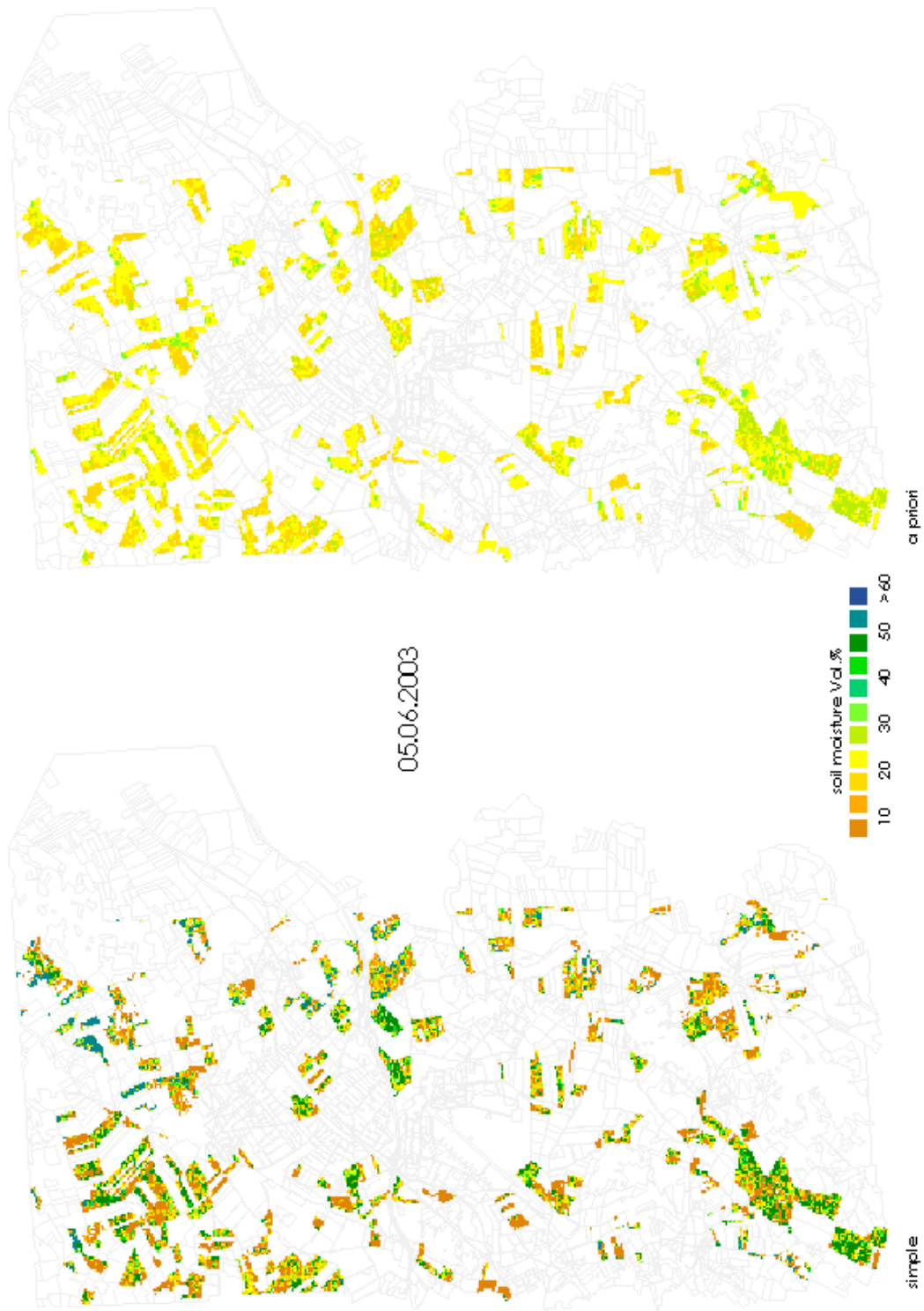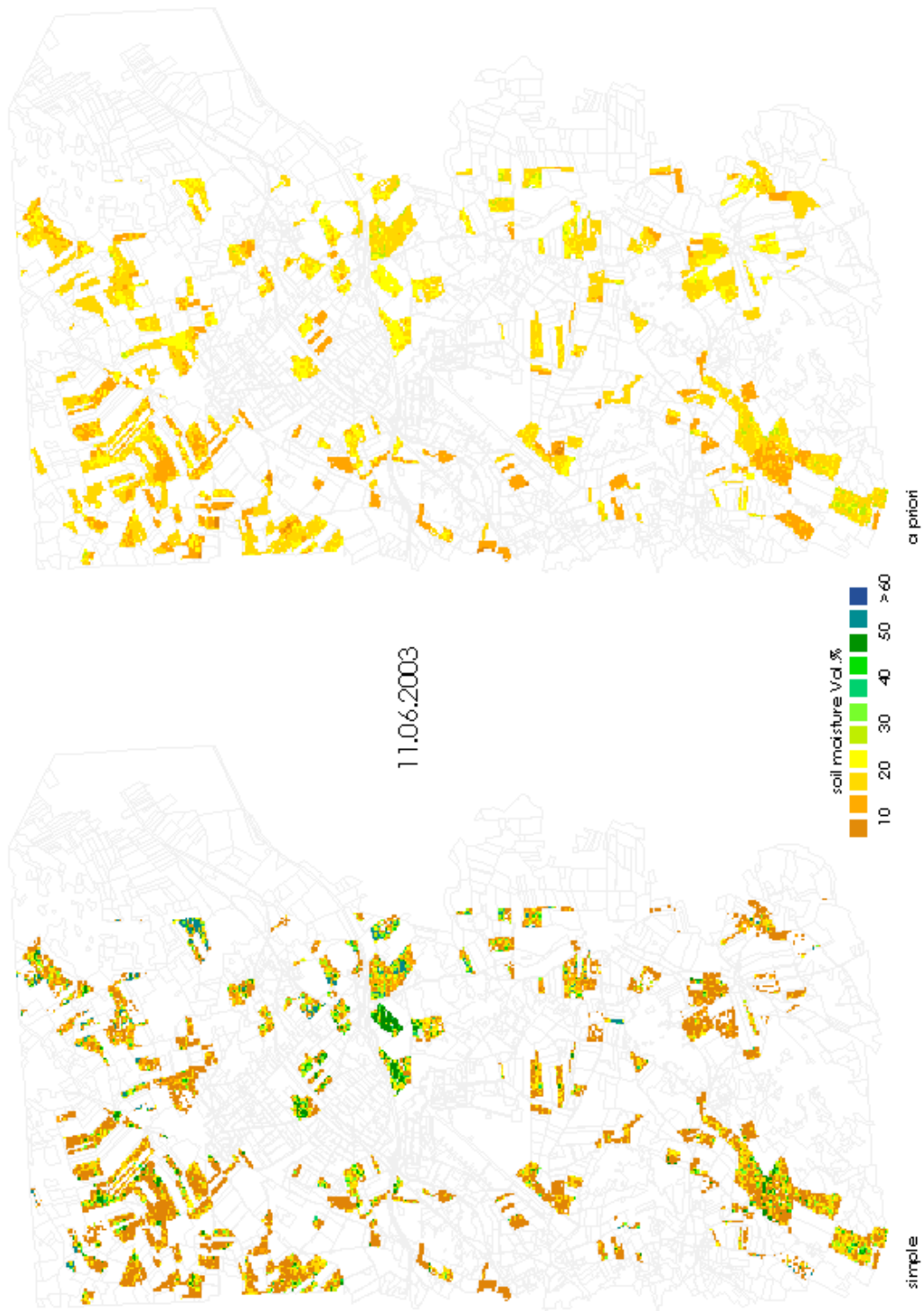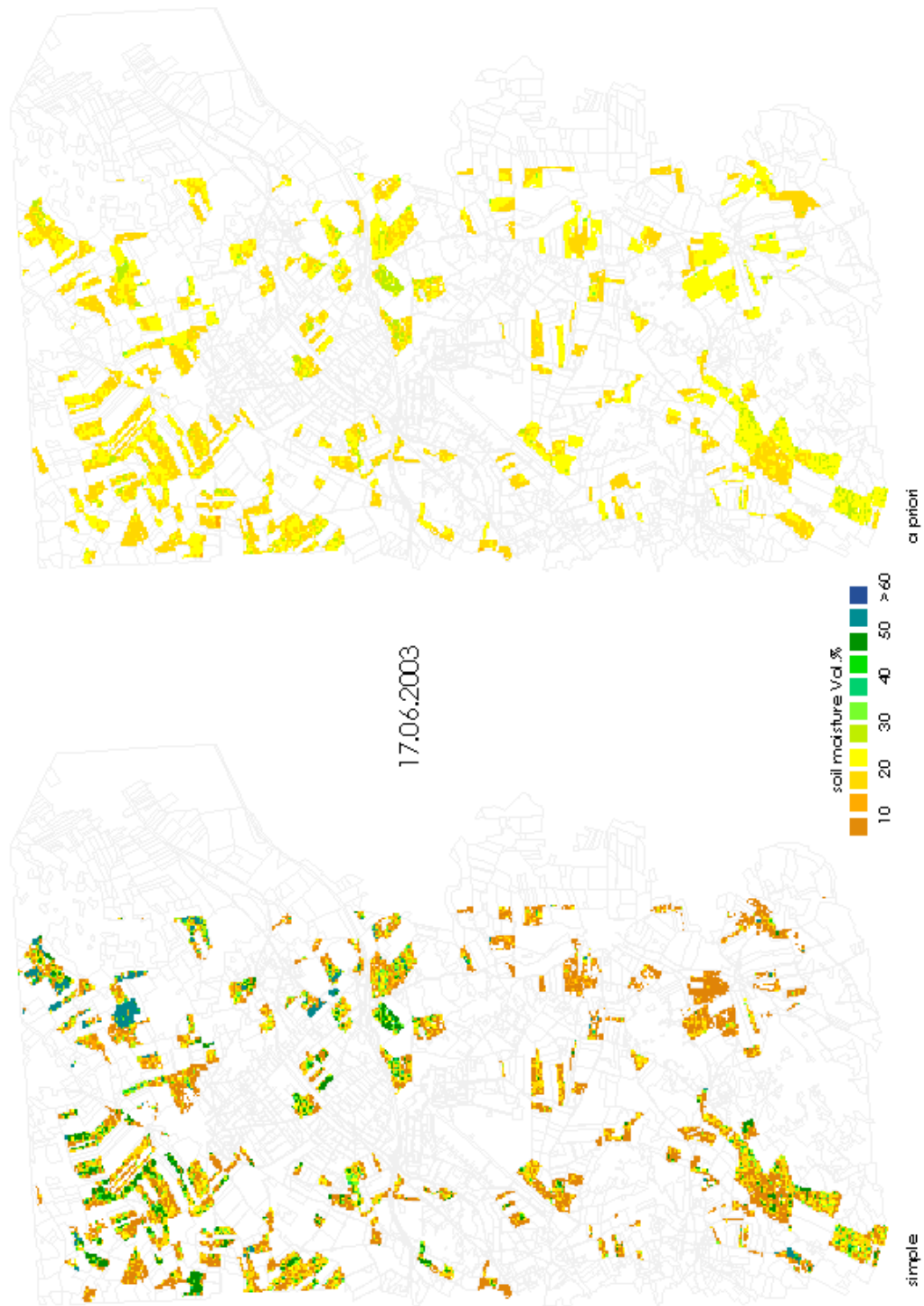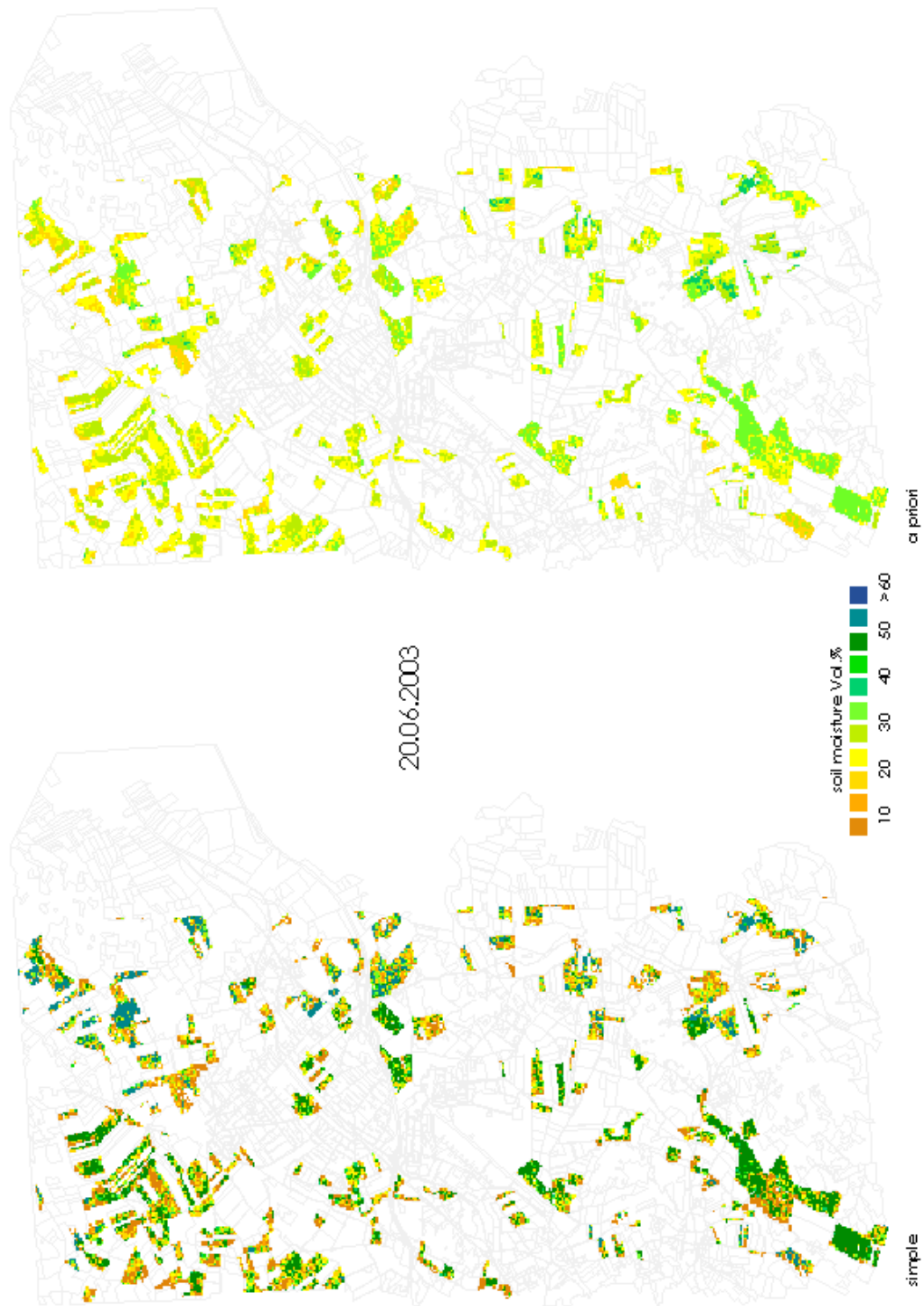
02.04.2003

soil moisture Vol.%

10 20 30 40 50 >60

a priori

simple

11.04.2003

a priori

simple

soil moisture Vol.%

10 20 30 40 50 >60

24.04.2003

soil moisture Vol.%

10 20 30 40 50 >60

a priori

simple

05.06.2003

soil moisture Vol.%

10 20 30 40 50 >60

a priori

simple

17.06.2003

soil moisture Vol.%

10 20 30 40 50 >60

a priori

simple

20.06.2003

a priori

simple

soil moisture Vol.%

10 20 30 40 50 >60

Soil moisture frequency distributions

The following diagrams show the frequency distributions of the soil moisture values for the test fields. Different soil moisture values are shown as follows:

- white: inverted using the *simple* inversion approach

- light grey: inverted with *a priori* information

- dark grey: initial soil moisture values, provided by the landsurface model
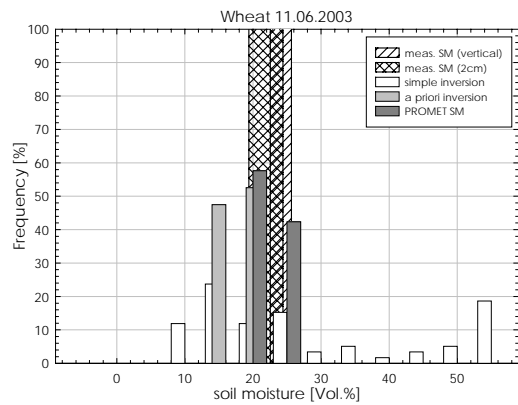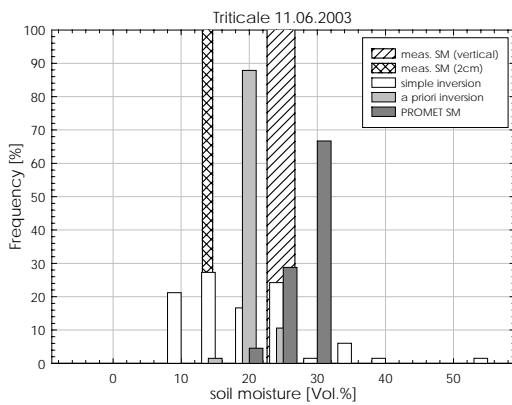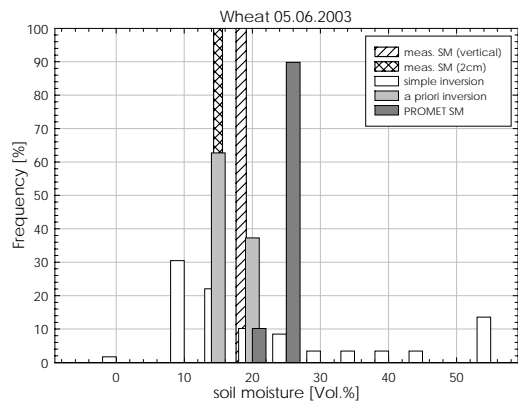
The *in situ* soil moisture measurement results for 2 cm sampling depth and vertical probe are also given. The space between the corresponding lines is equal to twice the standard deviation estimated from the ground measurements. It shows the inner field variance of the measured soil moisture values.
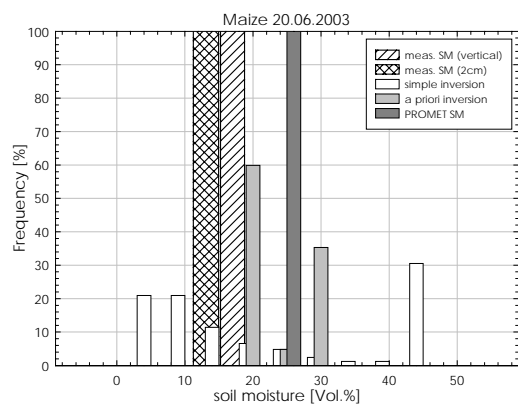
Triticale 24.04.2003

Wheat 24.04.2003

Triticale 01.05.2003

Wheat 01.05.2003
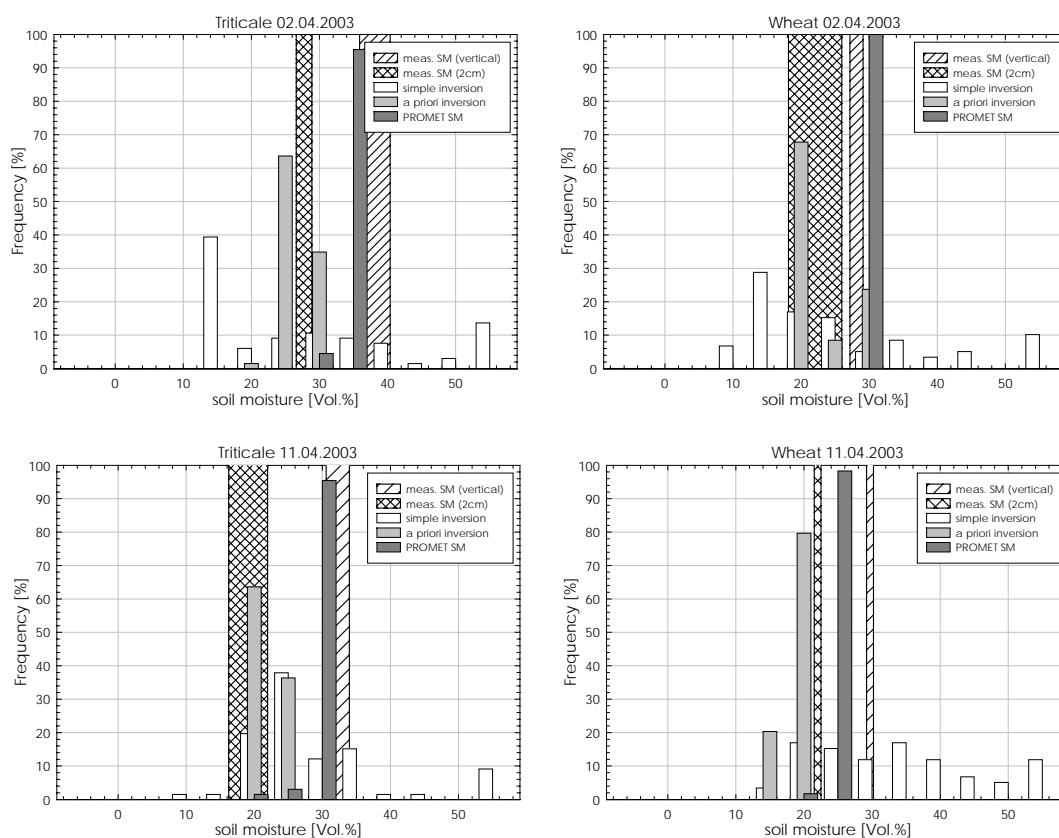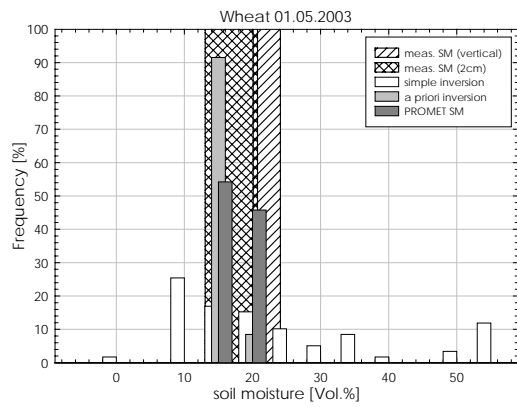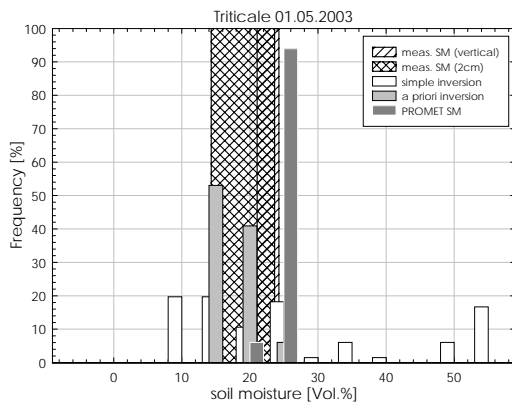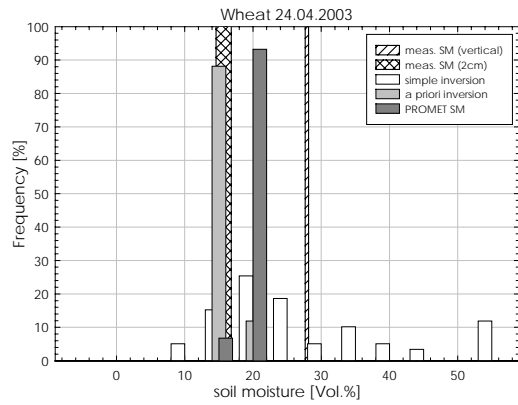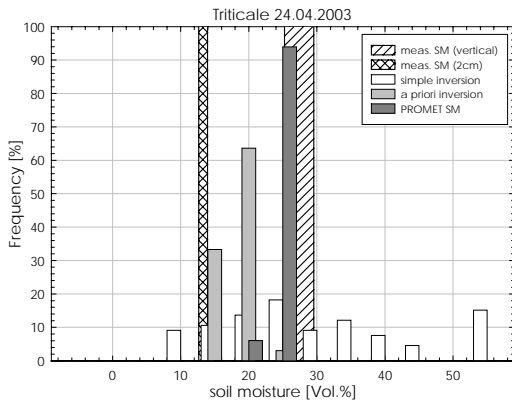
Triticale 05.06.2004

NO in situ SM DATA

Wheat 05.06.2003

Triticale 11.06.2003

Wheat 11.06.2003

Triticale 17.06.2003

Wheat 17.06.2003

Triticale 20.06.2003

Wheat 20.06.2003

Maize 17.06.2003

Maize 20.06.2003
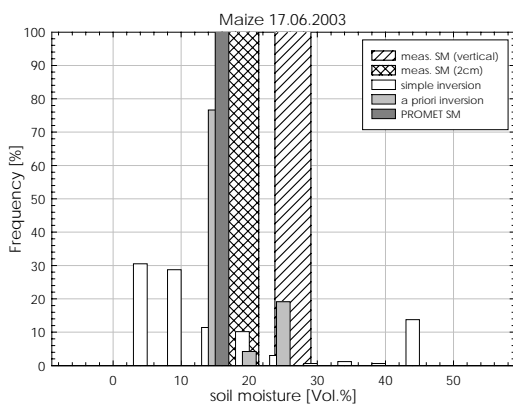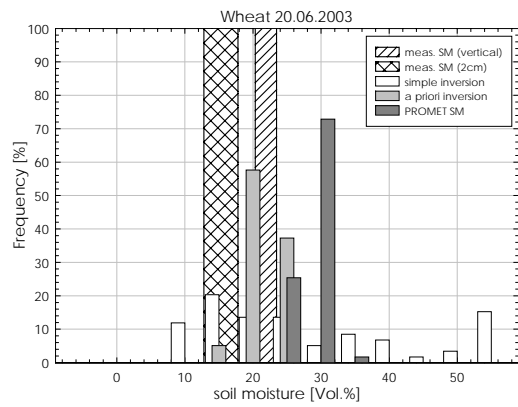
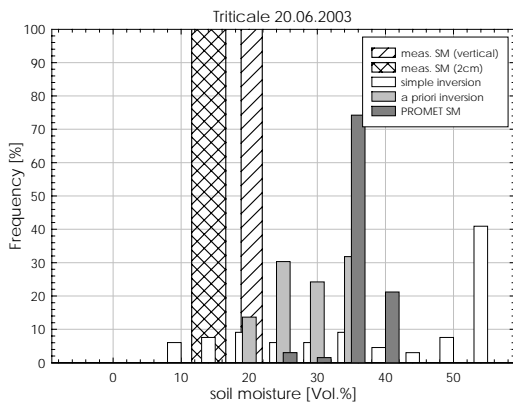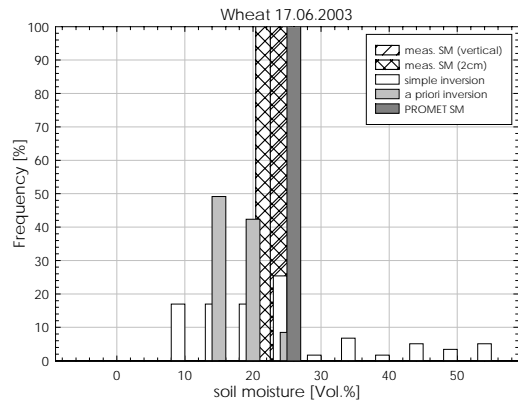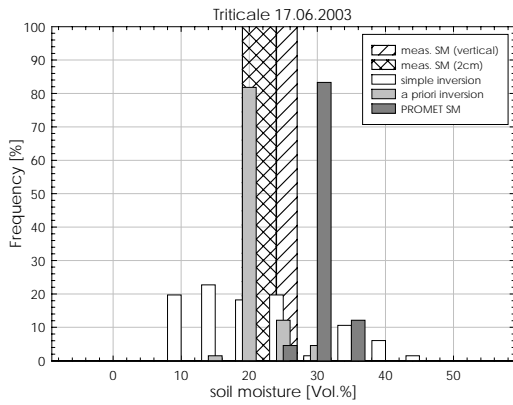## Field based soil moisture inversion results

The following table shows the in situ measured, field based averaged, soil moisture values, compared to the inverted soil moisture values, using the two inversion approaches. The values for the inversion results are field based median values, as discussed in the appropriate section.

DATE	FIELD	IN SITU MEASUREMENTS		INVERSION RESULTS	
		TDR VERTICAL	TDR 2CM	SIMPLE	A PRIORI
02.04.03	Triticale	38.1	27.7	25.0	23.0
11.04.03	Triticale	32.3	19.1	25.0	20.0
24.04.03	Triticale	27.4	13.3	25.0	18.0
01.05.03	Triticale	22.7	19.0	19.0	15.0
07.05.03	Triticale	-	-	8.0	15.0
05.06.03	Triticale	-	-	17.0	18.0
11.06.03	Triticale	24.7	13.9	17.0	18.0
17.06.03	Triticale	25.5	21.5	17.0	20.0
20.06.03[1]	Triticale	20.4	14.1	38.5	30.0
02.04.03	Wheat	28.1	22.1	21.0	22.0
11.04.03	Wheat	29.7	22.0	32.0	20.0
24.04.03	Wheat	27.9	15.7	21.0	15.0
01.05.03	Wheat	22.1	16.9	17.0	15.0
07.05.03	Wheat	-	-	8.0	11.0
05.06.03	Wheat	18.4	15.0	13.0	15.0
11.06.03	Wheat	24.1	21.9	21.0	18.0
17.06.03	Wheat	24.1	22.9	17.0	16.5
20.06.03	Wheat	21.9	15.3	21.0	18.0
17.06.03	Maize	26.4	18.3	10.0	17.0
20.06.03	Maize	17.0	13.1	15.0	20.0

---

[1] not used in final analysis, due to strong soil moisture overestimation by PROMET-V

Curriculum vitae

Personal

Name	:	Alexander Löw
Date of Birth	:	03.05.1975
Place of Birth	:	Königstein / Ts. (Germany)
Nationality	:	German

School and Education

1981 - 1985	Primary School, Eschborn (Germany)
1985 - 1994	High School, Francfort (Germany)
1995 - 2001	Study of Physical Geography
	Ludwig-Maximilians-Universität, Munich (Germany)
	Subsidiary subjects:
	Landscape ecology, Remote sensing
	Diploma thesis:
	Ableitung forstlicher Parameter aus AeS-1 SAR Daten (Derivation of forest parameters from AeS-1 SAR data)
	Graduation : Diplom-Geograph (Univ.)

Scientific career

since 04/2001	Lecturer at the Department of Earth and Environmental Sciences, Section Geography, University of Munich
since 04/2001	PhD student, University of Munich
04/2001 – 09/2002	Scientific researcher at the Chair of Geography and Geographical Remote Sensing, University of Munich
since 10/2002	Scientific assistant at the Chair of Geography and Geographical Remote Sensing, University of Munich
2001 – 2004	Collaboration in the DLR funded project InFerno+: "Integration von Fernerkundungsdaten in operationelle Wasserhaushalts- und Hochwasservorhersagemodelle"
since 2001	Investigator for the ESA ENVISAT ASAR studies

- Improved surface soil moisture determination using ENVISAT ASAR dual-polarization data (AOE.475)
- Synergistic use of ENVISAT data to model land surface processes (AOE.477)